

STRUCTURE OF IONIC LIQUIDS IN BULK AND AT INTERFACES

by

MAN ZHAO

A dissertation submitted to the

School of Graduate Studies

Rutgers, The State University of New Jersey

In partial fulfillment of the requirements

For the degree of

Doctor of Philosophy

Graduate Program in Chemistry and Chemical Biology

Written under the direction of

Edward W. Castner, Jr.

And approved by

New Brunswick, New Jersey

May, 2020

ABSTRACT OF THE DISSERTATION

Structure of Ionic Liquids in Bulk and at Interfaces

By Man Zhao

Dissertation Director:

Edward W. Castner, Jr.

Ionic liquids (ILs) are salts in the liquid state near room temperature. Composed of molecular anions and cations, ILs can be created as needed by chemically modifying the structure of the ions. Finding the connection between the molecular structures and physical properties of ILs allows us to choose an existing IL or synthesize one based on the task. The current thesis contributes to the understanding of IL structure both in bulk and at interfaces, as well as dynamics properties of ILs. This thesis comprises three major sections. The first section examines the bulk structure of ILs with various cations and fluorinated anions. The second section studies the diffusion behavior of charged cations and anions in ILs and the diffusivity of neutral molecules in IL-solvent mixtures. The third section focuses on the structure of ILs in vacuum studied by molecular dynamics (MD) simulations. Structure factors of the liquids were measured using high energy X-ray scattering (XRS) method and calculated from MD simulations. The diffusivity of molecules in ILs were measured using NMR experiments. It is found that the physical properties and bulk structure of ILs are related to their molecular structures. For ILs with long cationic alkyl tails and anionic fluorinated tails, the tails alternate along the charge network and form nonpolar domains. The diffusivity of ILs can be affected by many factors, including ion's size, shape and conformational

flexibility. The heterogeneity structure of ILs renders that neutral molecules diffuse faster than the hydrodynamic prediction. Structure of ILs in vacuum is very different from their bulk structure, which is affected by the nonpolar tail length, box size and electric fields.

Acknowledgements

I gratefully acknowledge the support from those who have helped me obtain a PhD degree in chemistry.

First I thank my advisor, Prof. Edward Castner. He has not only provided excellent guidance on my research, but also valuable advice regarding my future career and life. He gave me the freedom of working on projects of my own choices. He has always been supportive of all the decisions I made along the way, both in research and life. I could not have done this without his tremendous help.

I thank all the group members whom I had the pleasure to work with. I thank Dr. Min Liang and Dr. Boning Wu for getting me interested in ionic liquids in the first place and teaching me the techniques and skills to initiate my research. I thank my lab mates, Dr. Aleksandra B. Biedron, Mr. Jonathan Fetherolf, Mr. Matthew Emerson, and Ms. Yu Wang for their help with experiments and discussions.

I thank Prof. Claudio Margulis and his students from University of Iowa for sharing their computational resources, and for the useful discussions during online meetings. I thank Dr. James Wishart at Brookhaven National Lab and Prof. Sharon Lall-Ramnarin at Queensborough Community College and their students for providing us the samples for experiments and measuring their physical properties. I especially want to thank Prof. Claudio Margulis and Dr. James Wishart for their time and help with writing manuscripts.

I also want to thank the faculty and staff from the Chemistry and Chemical Biology department. I thank Prof. David Case and Prof. Eric Garfunkel for being my committee and providing valuable opinions all these years. I thank Dr. Robert Hayes for discussions and providing valuable suggestions. I thank Dr. Nagarajan Murali for the assistance with the PG-SE NMR experiments.

I thank NSF and DOE for the research funding.

I thank the scientists Dr. Olaf J. Borkiewicz, Kevin A. Beyer and Dr. Karena W. Chapman at the Advanced Photo Source, Sector 11, beamline 11-ID-B of Argonne National Lab, for their help in high-energy X-ray data collection. I thank all my friends and classmates at Rutgers University.

Finally I thank my friends and family in China, whose love and support travelled a long way to get me this far in my research.

Table of Contents

Abstract	ii
Acknowledgements	iv
List of Abbreviations	x
1. Introduction	2
1.1. Properties	2
1.1.1. Low Melting Point	3
1.1.2. Non-volatility	3
1.1.3. Thermal stability	4
1.1.4. Viscosity	4
1.1.5. Conductivity	5
1.1.6. Diffusivity of IL Anions and Cations	6
1.1.7. ILs as Designer Solvents	8
1.2. Applications of ILs	8
1.2.1. ILs as Solvents	8
1.2.2. Catalysis Using ILs	9
1.2.3. Energy Generation and Storage Using ILs	9
1.2.4. Biomass processing	10
1.3. Structure of ionic liquids	11
1.3.1. The Liquid Structure Factor $S(q)$ for ILs	11
1.3.2. Structure Function $S(q)$ for ILs	12
1.4. The Structure of Ionic Liquids Studied	13
1.5. Summary	14

2. Methods	32
2.1. Preparation of Samples	32
2.2. Physical Property Measurements	33
2.3. High-energy X-ray Scattering Experiments	33
2.4. Diffusivities from PG-SE NMR	34
2.5. Molecular Dynamics (MD) Simulations of ILs	35
2.5.1. Simulations of Bulk IL Structure	36
2.5.2. Static Liquid Structure Function $S(q)$ From MD Simulations	37
2.5.3. MD Simulations of the Vacuum-IL Interface	38
3. Bulk Structure of Ionic Liquids	45
3.1. Structural analysis of ILs with symmetric and asymmetric fluorinated-anion ionic liquids: imidazolium cations	45
3.1.1. Physical properties	47
3.1.2. The structure of $\text{Im}_{2,1}^+$ salts	48
3.1.3. The structure of $\text{Im}_{1,8}^+$ salts	52
3.1.4. Domain aggregation analysis	59
3.1.5. Spatial Distribution Functions (SDFs)	61
3.1.6. Summary of structural studied of ILs with imidazolium cations	66
3.2. Structural analysis of ILs with symmetric and asymmetric fluorinated-anions: pyrrolidinium and phosphonium cations	66
3.2.1. Physical properties	67
3.2.2. Structure of $\text{Pyrr}_{1,8}^+$ salts	70
3.2.3. Structure of $\text{P}_{6,6,6,14}^+$ salts	77
3.2.4. Spatial Distribution Functions (SDFs) for $\text{Pyrr}_{1,8}^+/\text{BSI}_{1,4}^-$ and $\text{P}_{6,6,6,14}^+/\text{BSI}_{1,4}^-$	79
3.2.5. Fluorous domain aggregation analysis	83
3.2.6. Summary of results for BSI-anion ILs with $\text{Pyrr}_{1,8}^+$ and $\text{P}_{6,6,6,14}^+$ cations	84

3.3.	Structure of NTf_2^- -anion ILs with cationic ether tails	85
3.3.1.	Physical properties: viscosity and conductivity	86
3.3.2.	Total structure functions $S(q)$ for NTf_2^- -anion ILs with cation alkyl or ether tails	87
3.3.3.	MD simulations	88
	Total structure factors $S(q)$ and their partitioning into components	89
3.3.4.	Snapshots of the equilibrated simulation boxes	92
3.3.5.	Structure of $\text{Im}_{1,\text{EOEOEOM}}^+/\text{NTf}_2^-$: Radial distribution functions	92
3.3.6.	Structure of $\text{Pyrr}_{1,\text{EOEOEOM}}^+/\text{NTf}_2^-$: Radial distribution functions	97
3.3.7.	Summary of structural studied of ILs with cationic oligoether tails	99
3.4.	Conclusions	100
4.	Diffusivities in Ionic Liquids	110
4.1.	Diffusivity of ILs with the $\text{BSI}_{1,4}^-$ anion	111
4.1.1.	Diffusivities as a function of temperature	111
4.1.2.	Stokes-Einstein fits to IL diffusion	115
4.1.3.	Summary of diffusion behavior in $\text{BSI}_{1,4}^-$ ILs	115
4.2.	Structure and Transport of 1-Octanol in $\text{P}_{6,6,6,14}^+/\text{NTf}_2^-$	118
4.2.1.	Structure functions $S(q)$ of the mixtures	118
4.2.2.	Viscosities of IL-octanol mixtures	119
4.2.3.	Diffusivities of IL-octanol mixtures	122
4.2.4.	Summary of diffusion behavior in IL-solvents mixtures	125
4.3.	Conclusions	126
5.	Structure of ILs at Liquid-Vacuum Interfaces	131
5.1.	Liquid-vacuum interfacial structure of ionic liquids with cation and flu- orinated anions	131
5.1.1.	Bulk structures of $\text{Im}_{1,8}^+/\text{BSI}_{1,n}^-$ salts	133
5.1.2.	Interfacial structures of $\text{Im}_{1,8}^+/\text{BSI}_{1,n}^-$ ILs in vacuum	137
5.1.3.	Structure of $\text{Im}_{1,8}^+/\text{BSI}_{1,8}^-$ in a scaled box	140

5.1.4.	Structure of $\text{Im}_{1,8}^+/\text{BSI}_{1,8}^-$ in Electric field	141
5.1.5.	Summaries of the structure of $\text{Im}_{1,8}^+/\text{BSI}_{1,8}^-$ in rectangular box	144
5.2.	Interfacial Structure Difference Between Alkylated and Fluorinated Tails	146
5.2.1.	Bulk structures of the salts	146
5.2.2.	Interfacial structures of the salts	148
5.2.3.	Structure of the $[\text{Im}_{1,8}^+, \text{Im}_{2,1}^+, \text{NTf}_2^-, \text{BSI}_{1,8}^-]$ mixture	151
5.2.4.	Summary of interfacial structures for fluorinated-anion ILs	156
5.3.	Conclusions	157
6.	Conclusions	169
6.1.	Bulk structure of ILs	169
6.2.	Diffusivities in ILs and IL-octanol mixtures	170
6.3.	Liquid-vacuum interfacial structure of ILs	170
6.4.	Future directions	171
	List of Publications	174

List of Abbreviations

APS:	Advanced Photon Source
COM:	Center of Mass
DFT:	Density Functional Theory
FSDP:	First Sharp Diffraction Peak
IL:	Ionic Liquid
MD:	Molecular Dynamics
NMR:	Nuclear Magnetic Resonance
PG-SE:	pulse-gradient spin echo
PME:	Particle Mesh Ewald
RTIL:	Room temperature ionic liquid
Im _{2,1} ⁺ :	1-ethyl-3-methylimidazolium
Im _{1,8} ⁺ :	1-methyl-3-octylimidazolium
Pyrr _{1,8} ⁺ :	1-methyl-1-octylpyrrolidinium
P _{6,6,6,14} ⁺ :	trihexyltetradecylphosphonium
FSI ⁻ :	bis(fluorosulfonyl)imide
BSI _{0,1} ⁻ :	(trifluoromethylsulfonyl)(fluorosulfonyl)imide
NTf ₂ ⁻ :	bis(trifluoromethylsulfonyl)imide
BETI ⁻ :	bis(pentafluoroethanesulfonyl)imide
BSI _{1,3} ⁻ :	(perfluoropropylsulfonyl)(trifluoromethylsulfonyl)imide
BSI _{1,4} ⁻ :	(perfluorobutylsulfonyl)(trifluoromethylsulfonyl)imide
BSI _{1,5} ⁻ :	(perfluoropentylsulfonyl)(trifluoromethylsulfonyl)imide
BSI _{1,6} ⁻ :	(perfluorohexylsulfonyl)(trifluoromethylsulfonyl)imide
BSI _{1,7} ⁻ :	(perfluoroheptylsulfonyl)(trifluoromethylsulfonyl)imide
BSI _{1,8} ⁻ :	(perfluorooctylsulfonyl)(trifluoromethylsulfonyl)imide
Im _{1,EtHx} ⁺ :	1-methyl-3-(2-ethylhexyl)imidazolium
Pyrr _{1,EtHx} ⁺ :	1-methyl-1-(2-ethylhexyl)pyrrolidinium
Im _{1,EOEOE} ⁺ :	1-methyl-3-(2-(2-ethoxyethoxy)ethyl)imidazolium
Pyrr _{1,EOEOE} ⁺ :	1-methyl-1-(2-(2-ethoxyethoxy)ethyl)pyrrolidinium
Im _{1,EOEOEOM} ⁺ :	1-methyl-3-(2-(2-(2-methoxyethoxy)ethoxy)ethyl)imidazolium
Pyrr _{1,EOEOEOM} ⁺ :	1-methyl-1-(2-(2-(2-methoxyethoxy)ethoxy)ethyl)pyrrolidinium

The structure study of ionic liquids with fluorinated anions part is reproduced from the following article.

M. Zhao, B. Wu, S. I. Lall-Ramnarine, J. D. Ramdihal, K. A. Papacostas, E. D. Fernandez, R. A. Sumner, C. J. Margulis, J. F. Wishart, and E. W. Castner, Jr., “Structural Analysis of Ionic Liquids With Symmetric and Asymmetric Fluorinated Anions.”, *J. Chem. Phys.* 151, 074504, 2019, doi: 10.1063/1.5111643.

The structure of ionic liquids with cationic oligoether chains part is reproduced from the following article.

S. I. Lall-Ramnarine, M. Zhao, C. Rodriguez, R. Fernandez, N. Zmich, E. D. Fernandez, S. B. Dhiman, E. W. Castner, Jr., and J. F. Wishart, “Connecting Structural and Transport Properties of Ionic Liquids with Cationic Oligoether Chains”, *J. Electrochem. Soc.* 164, H5247-H5262, 2017, doi: 10.1149/2.0371708jes.

The diffusivity of ILs with the $\text{BSI}_{1,4}^-$ anion part is reproduced from the following article.

F. Lo Celso, G. B. Appetecchi, E. Simonetti, M. Zhao, E. W. Castner, Jr., U. Keiderling, L. Gontrani, A. Triolo, and O. Russina, “Dynamic Features in Triphilic Room Temperature Ionic Liquids”, *Front. Chem.* 7, 285, 2019, doi: 10.3389/fchem.2019.00285.

Chapter 1

Introduction

Ionic liquids (ILs) are salts in the liquid state. Salts are an assembly of cations and anions, which typically have high melting points due to the strong Coulombic attraction among ions. Ionic liquids, however, have a melting point below 100 °C, with many having melting points well below room temperature. Paul Walden discovered one of the earliest ILs in 1914 - ethylammonium nitrate ($[\text{EtNH}_3][\text{NO}_3]$), which has a melting point of 12 °C.⁽¹⁾

ILs that are liquid at ambient temperature are also called room temperature ionic liquids (RTILs). RTILs usually consist of bulky and asymmetric organic anions and/or cations. Examples of such cations include 1-alkyl-3-methylimidazoliums ($[\text{Im}_{1,n}]$), N-methyl-N-alkylpyrrolidiniums ($[\text{Pyr}_{1,n}]$), and tetraalkylphosphoniums ($[\text{P}_{nnn,m}]$). The larger size and low asymmetry of the ions (relative to monotonic ions) results in charge delocalization, lowering the Coulombic attraction between ions, thus preventing the system from crystallization. This is the reason that ILs can stay in liquid state though despite being salts. Some of the most commonly used cations and anions are shown in Figure 1.1.

1.1 Properties

Renewed interest in ionic liquids started in the 1980s and has been growing rapidly ever since.⁽²⁾ The great interest in ILs has everything to do with their unique properties, such as the low melting point, extremely low vapor pressure, thermal stability, high viscosity and so on. Let us consider those individually.

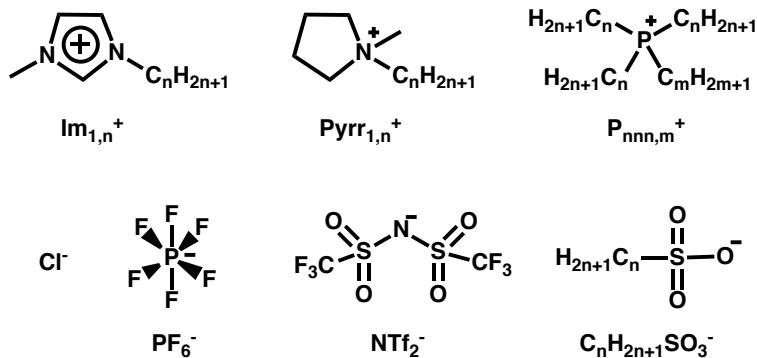


Figure 1.1: Some commonly used cations and anions for ionic liquids.

1.1.1 Low Melting Point

As mentioned above, the larger size, low symmetry, and charge delocalization of ions prevent the cations and anions from close packing. Therefore ILs can be in liquid state with no crystallization. The lower melting points of ILs means that they can be used in ambient environment where molten salts remain solid.(1)

1.1.2 Non-volatility

ILs have negligible vapor pressure because of the Coulombic force among the ions. To evaporate, the IL molecules have to leave the surface of the liquid as ion pairs or larger clusters (like neutral solvents), which only happens at elevated temperatures.(3) As reported, the vapor pressure of 1-butyl-3-methylimidazolium bis(trifluoromethylsulfonyl)imide ([BMIM][NTf₂]) is as low as 10^{-12} mbar at 25 °C.(4) A typical IL vapor pressure could be 10^{-9} Torr at ambient temperatures. As a result, ILs have low flammability and display nearly no vaporization. After being washed by organic solvents during synthesis, ILs can be purified under extremely high vacuum conditions where only the organic solvents will be distilled. This also makes ILs favorable candidates than organic solvents in separations processes, where it can be recycled with minimum loss. For similar reasons, ILs are great materials to be used in green applications, particularly as they are often compatible with water and supercritical fluids.(5)

1.1.3 Thermal stability

ILs are seen as thermally stable because many, but not all, ILs have high thermal stability. There is a growing interest in the elevated temperature applications of ionic liquids, such as heat-transfer fluids and electrolytes for fuel cells, so much work has been done on the thermal stability of ILs.(6–12) Gotz, *et al.* studied approximately 30 ILs with different cations and anions. They found that the NTf₂[−] anion is the most stable anion among those investigated. Two ILs with the NTf₂[−] anion are long-term stable up to 300 °C.(13) In fact, numerous ILs have been reported to be short-term stable in their liquid state to temperatures up to 400 °C or higher.(6) In recent years, James Davis’s group has been successful in finding and designing thermally robust ILs.(8; 11; 14) Siu, *et al.* reported that triarylsulfonium salts constitute ILs are long-term, high-temperature aerobic stable with no mass loss in 90 days at 300 °C in air.(14)

1.1.4 Viscosity

Viscosity is a quantity describing a fluid’s internal flow resistance. In general, ILs are more viscous fluids compared to traditional organic solvent due to the Coulombic forces among ions.(15–17) The viscosity of ILs is highly affected by their molecular structures. Depending on the type of cation-anion combination, their viscosities can range over several orders of magnitude. For example, the viscosity of Im_{2,1}⁺/NTf₂[−] is 33 cP at 25 °C, while the viscosity of P_{6,6,6,14}⁺/NTf₂[−] is 318 cP at 25 °C.(18; 19) These higher viscosities pose one of the major obstacles to successful applications of ILs. The viscosity of ILs could be affected by several factors, like the structure, temperature and mixtures. ILs with bulkier cations and/or anions often have higher viscosity than ILs with smaller ions. For example, increasing the alkyl chain length increases the viscosity of ILs.(15–17; 20) Hydrogen bonding is also an important factor that affects the viscosity of ILs.(21) Fewer hydrogen bonds may lead to lower viscosity of ILs, though it is not always the case. For example, the viscosity of ILs with ether substituted cations are much lower compared to their alkyl analogues.(22; 23) ILs with functional groups such as silicon atom on the cations leads to lower viscosity than their carbon analogues.(24) The

viscosity of ILs is strongly affected by temperature. The higher the temperature, the lower the viscosity is. The relationship between IL viscosity (η) versus temperature (T) could be described by two equations: 1) the Arrhenius equation: $\ln(\eta) = A_0 + \frac{E_a}{R} \times \frac{1}{T}$, where R is the gas constant, and E_a is the Arrhenius activation energy; 2) the Vogel-Fulcher-Tammann (VFT) equation(25; 26): $\ln(\eta) = \eta_0 + \frac{E_0}{R} \times \frac{1}{T-T_0}$, where R is the gas constant and η_0 , E_0 , and T_0 are fitting constants. The viscosity of ILs also increases with increasing pressure due to the decrease of free volume at higher pressure.(27) Another way to “decrease” the viscosity of ILs is by adding a second solvent, either another IL with lower viscosity or miscible organic solvents. Multiple solvents can be added as needed. To this end, much work has been done on the structure and dynamics of IL mixtures.(28–32)

1.1.5 Conductivity

Conductivity is a collective property that characterizes the average flow of ions in the condensed phase. Electrical conductivity quantifies how strongly a material conducts electric current. Conductivity of ILs originates from the inherent motion of cations and anions in ILs under electric potential difference. ILs are expected to possess high conductivity due to their entire ionic structure. Conductivity of aprotic RTILs at room temperature is typically within a broad range of 0.1 - 20 mS/cm and is strongly temperature dependent, and most ILs have conductivities below 10 mS/cm.(33) Meanwhile, conventional aqueous electrolyte solutions used in electrochemistry have conductivities between 500 - 700 mS/cm.(34)

The ionic mobilities are strongly influenced by Coulombic and the van der Waals interactions between the cations and anions. Therefore, the conductivity of ILs depends on properties such as the structure of the ions, their polarizability, and the possibilities for hydrogen bonding.(35–38) For example, for imidazolium based ILs, the increase of the side chain length attached to the imidazolium ring leads to lower conductivity, which could be attributed to the mobility decrease, mass increase, and their higher tendency to form hydrophobic domains between the hydrocarbon tails.(18; 39) The conductivity of ILs is strongly influenced by temperature. Vila, *et al.* reported that the electrical

conductivity of ILs increased more than 200 times for a temperature increase of 180 K.(37) The conductivity of ILs usually obeys the Vogel-Fulcher-Tammann equation: $\ln(\sigma) = \sigma_{\infty} - \frac{B}{T-T_0}$, where B is the temperature dependence of σ in high temperature limit, and T_0 is the Vogel temperature. (37; 39–41) At higher temperature limit, the conductivities of ILs follow the Arrhenius Law: $\sigma = \frac{\sigma_0}{T} - \frac{E_a}{kT}$, where E_a is the Arrhenius activation energy, and k is the Boltzmann constant.

Higher conductivity is desired for ILs as electrolytes for electrochemical application.(42) Walden’s rule states that the product of the shear viscosity (η) and the molar equivalent conductivity (Ω) is a constant for a particular fluid.(35) Therefore, lowering the viscosities of ILs increases their conductivities. The conductivity of ILs is often increased by adding neutral molecular solvents.(31; 43; 44)

1.1.6 Diffusivity of IL Anions and Cations

Brownian motion is the random motion of particles suspended in a fluid resulting from their collision with the fast-moving molecules in the fluid.(45) Take a particle as the 3D random walk, the mean squared displacement (MSD) measures the deviation of the position of the particle with respect to a reference position over time. If no outside force is applied to the system, then MSD over time arises solely from the self-diffusion of the particles. The self-diffusion coefficient of ILs is an important parameter to understand for many applications, such as their use as electrolytes. This requires a knowledge of the dynamics in ILs, which is affected by the molecular structures of the ions. The diffusion of ions in ionic liquids are affected by many factors: ion size, the shape of ions, conformational flexibility, molecular mass, charge distribution between the cations and anions, etc.(46)

Diffusion is characterized as either a translational or orientational process. Electrical conductivity is correlated with translational diffusivity. The translational diffusion is the diffusion coefficient of species when the chemical potential gradient equals zero. Therefore, it is also called “self-diffusion”. The self-diffusion coefficient is expressed in units of area over time (m^2s^{-1} , cm^2s^{-1}).

Diffusivity in ILs can sometimes be predicted using the hydrodynamic theory of the Stokes-Einstein (S-E) equation:

$$D = \frac{k_B T}{c \pi \eta r} \quad (1.1)$$

where D is self-diffusion coefficient, k_B is Boltzmann constant, T is temperature (K), c is 4 or 6, depending on whether slip or stick boundary conditions are imposed at the particle surface (“Stoke’s law”),⁽⁴⁷⁾ r is the effective spherical radius, and η is the shear viscosity. The assumption in the S-E model is that the diffusing molecule has a spherical shape. Harris demonstrated that most molecular fluids show fractional Stokes-Einstein behavior with an average value of fraction $m = 0.90$. Typical exponents for ILs are between $0.79 < m < 1$.⁽⁴⁸⁾

The diffusivity of ILs is temperature dependent. In addition to the S-E model, the relationship between diffusivity and temperature can be described by 1) the Arrhenius equation: $\ln(D) = D_0 + \frac{E_a}{RT}$, where R is the gas constant, D_0 is a pre-exponential factor and E_a is the Arrhenius activation energy; 2) the Vogel-Fulcher-Tammann (VFT) equation^(25; 26): $\ln(D) = D_{VFT} + \frac{B}{T-T_0}$, where T_0 is the critical temperatures for diffusion coefficients.

The Watanabe group demonstrated that in general diffusion in ILs agrees with the hydrodynamic theory.^(36; 49; 50) The cationic self-diffusion coefficients for the cation are higher compared to those for the anion over a wide temperature range, even if the cationic radius is larger than that of the anion.⁽⁵⁰⁾ Thus, the diffusion in pure ILs or in IL/solute systems deviates from the S-E model.⁽¹⁹⁾ A number of factors can be attributed to the deviation. For example, the real shape of ions are not spherical as assumed. The strong Coulombic attraction force between ions, the formation of nonpolar nanoscale domains in the system, or the addition of low viscosity solvents are also possible reasons.

1.1.7 ILs as Designer Solvents

It is time to introduce the tunability of the chemical and physical properties of ILs. One notes that the physical and chemical properties of ILs can easily be adjusted by varying the structure of constituent anions and cations. This in turn provides control of the IL like increasing thermal stability or lowering the viscosity. Therefore, ionic liquids are also called “designer solvents” in the sense that large number of possible ionic liquids (even up to 10^{18})(51) can be synthesized based on the existing wide selection of cations and anions, from which the desired ionic liquid for any application can be selected.(52) Prof. James Davis introduced the term “task-specific ionic liquids” by optimizing the solubility of CO_2 in ILs by selection of different anionic and cationic chemical properties.(53) Not to mention that mixtures of ionic liquids offer the opportunity for more IL systems with fine-tuned properties.

Besides the above mentioned properties, ILs also have wide electrochemical window, high electrochemical stability, polarity and polarizability, *etc.* It is these properties that makes ILs solvents of the future.

1.2 Applications of ILs

With so many superior properties and unlimited combinations, ILs can be used in many fields: catalysis, electrochemistry, fuel cells, drug delivery, lubrication, and coatings.

1.2.1 ILs as Solvents

As solvents, ILs can be used in many fields like surfactant, separation, and gas absorption. Ionic liquids can act as polar and thermally stable stationary phases for gas chromatography.(54; 55) ILs are used in liquid-liquid extraction process to preconcentrate analytes of interest from aqueous phase.(56) ILs can be used as solvents in nuclear waste reprocessing.(54; 57) ILs are able to dissolve high volumes of gases including but not limited to CO_2 , CH_4 , N_2 , and H_2S , which offers more applications for ILs.(58–60)

The ability of ILs to capture CO_2 makes them excellent solvents for the conversion of CO_2 .(61–63) Phosphonium cation ILs and fluorinated anion ILs have high N_2 gas solubility, the first step towards N_2 conversion.(64; 65) ILs are also used for the storage and delivery of highly toxic, flammable, and/or reactive gases. Air Products and Chemicals has developed an ionic-liquid-based technology for storing and delivering gases, including reversible complexation with phosphine.(66)

1.2.2 Catalysis Using ILs

Catalysis is one of the major uses of ionic liquids with regard to synthetic applications.(67–69) Ionic liquids can remain in liquid state over a broad range of temperatures with negligible vapor pressure, so they are considered as green alternatives to volatile organic solvents. ILs are able to solvate a range of polar and non-polar compounds. The miscibility of solvents in ILs could be modified via the choice of anions and cations, the side chain length on the ions, and more. ILs can be functionalized to act as acids, bases, or ligands depending on the reaction requirements.(67; 69; 70) Many classes of organic reactions, such as Diels-Alder reactions and Friedel-Crafts reactions, can be performed using ionic liquids as solvents.(67) ILs are used in transition-metal-mediated catalysis as IL-organic biphasic systems.(71; 72) Electron transfer reactions in ILs also receive considerable attention. As demonstrated by Maroncelli, *et al.*, in ILs the electron transfer rate between neutral donors and acceptors is typically 1 - 2 orders of magnitude faster than the simple diffusion-limited rate predicted by the Smoluchowski equation.(73–75) In recent years, ILs are being investigated as additives to modulate enzyme activities. They can serve as solvents for biocatalysis and enzyme catalysis.(76; 77)

1.2.3 Energy Generation and Storage Using ILs

Because ILs display broad windows of electrochemical stability, non-flammability and thermal stability, ILs are promising materials in applications for energy generation and storage.(78; 79) One of the first applications considered for ILs is using them as battery electrolytes.(80) ILs show good stability to various electrode materials and good

discharge ability and cycle ability as electrolytes. ILs can act as electrolytes for high-efficiency dye-sensitized solar cells,(81), for carbon nanotube electrodes,(82) electrochemical double layer capacitors,(83) lithium batteries,(84) sodium batteries,(43) and fuel cells,(85) to just name a few. It is well known that lithium batteries are flammable because organic carbonates are added to the electrolyte. Considering their thermal and electrical stability, ILs have been proposed as safer electrolytes.(84) However, despite the advantages of ILs as electrolytes, the high viscosity and low conductivity hold back the industrial application of ILs in batteries. ILs that overcome the disadvantages while maintaining their thermal and electrochemical stabilities are to be developed.

1.2.4 Biomass processing

Biomass is a widely available and renewable resource that could be converted to starting materials for chemical and fuel production. Cellulose, lignocellulose and hemicelluloses are the most abundant renewable carbon sources on Earth. However, these polymers are insoluble in water and most organic solvents due to intermolecular forces like hydrogen bonding, making separations difficult. Therefore, pretreatments that could break apart these complex interactions and enable efficient conversion of the raw materials are greatly demanded.

Traditional pretreatments using steam at high temperatures, or using organic solvents are neither energy inefficient nor environmentally friendly.(86) After the discovery that some ionic liquids could be used to dissolve and regenerate cellulose,(87) the simple, efficient and “green” pretreatments with ILs of biomass have become a highly active area of research.(88–90) The dissolution of cellulose and extraction of lignin in ILs have seen great success.(88; 91–93) Kilpeläinen, *et al.* demonstrated that both hardwood and softwood are readily soluble in imidazolium-based ILs under gentle conditions.(91) Achinivu, *et al.* developed a highly effective method for the simple extraction of lignin from lignocellulostic biomass using protic ionic liquids.(93) Researchers are also working on biomass conversion with ILs in a one-pot process, which is simple and has lower operating and capital costs.(94–96) In addition to seeking efficient and recyclable ILs for biomass conversion, researchers are working on generating ILs from biomass, which

are called bio-ionic liquids (Bio-ILs).(97–99) In this way, one can dissolve biomass with ILs and use the substances to generate ILs with enhanced biocompatibility, an excellent example of “green chemistry”.

Much corporate attention has been given to applications of ILs – from startup companies that include IoLiTec, ProIonics, 525 Solutions as well as multinational companies such as BASF, Dupont and Merck. Ionic liquids would be seen more and more in industry fields and serve their purposes as needed.

1.3 Structure of ionic liquids

The unlimited combinations of ILs both a blessing and a curse. The vast number of ILs means that it is not plausible to find the desired ILs by trial and error. It is clear that the applications of ILs rely on their physical, chemical and biological properties, which are essentially determined by the molecular structure of the anions and cations of the ILs. Because ILs are highly structured liquids, it is crucial that we understand the relationship between the molecular structures of ILs and their fundamental properties and structures.

1.3.1 The Liquid Structure Factor $S(q)$ for ILs

The static liquid structure factor $S(q)$ is a critical tool in the interpretation of scattering patterns. Assuming that the material under study is isotropic, like a powder or a simple liquid, and a beam of wavelength λ is being scattered by the material. The magnitude of the scattering vector q is defined as $q = 4\pi \sin(\theta)/\lambda$, where 2θ is the scattering angle. So q is defined in reciprocal space. A peak in $S(q)$ at a particular q indicates periodicity in the system at real space distance d by Bragg’s law $d = 2\pi/q$.(100) $S(q)$ is also related to the radial distribution function $g(r)$ via an inverse Fourier sine transform.

The structure of ionic liquids can be studied in many ways, including high-energy X-ray scattering, neutron scattering, atomic force spectroscopy (AFM), X-ray photoemission spectroscopy (XPS), and MD simulations.(18; 30; 32; 101–122)

In this work, we used two methods to obtain the $S(q)$, high-energy X-ray scattering and MD simulations. The left graph of Figure 1.2 shows the typical 2-D scattering pattern of an IL. The observable in the scattering experiment is the coherent X-ray scattering intensity, $I(q)$. The raw data could be integrated and converted to X-ray intensities $I(q)$ vs q . Structure functions $S(q)$ are derived from $I(q)$. The $S(q)$ obtained from X-ray experiments for the IL $\text{Im}_{2,1}^+/\text{BSI}_{1,4}^-$ (see Figure 1.3) is plotted in the right graph as the red curve. $S(q)$ can also be calculated from MD simulations. The radial distribution functions $g(r)$ between pairs of atoms are computed using the MD simulation trajectories. $S(q)$ is calculated from the MD-derived $g(r)$ a Fourier transform. The $S(q)$ obtained from MD simulations is also plotted in the right graph as the black curve. We could see that the two curves are in very good agreement, which confirms the accuracy of the simulations.

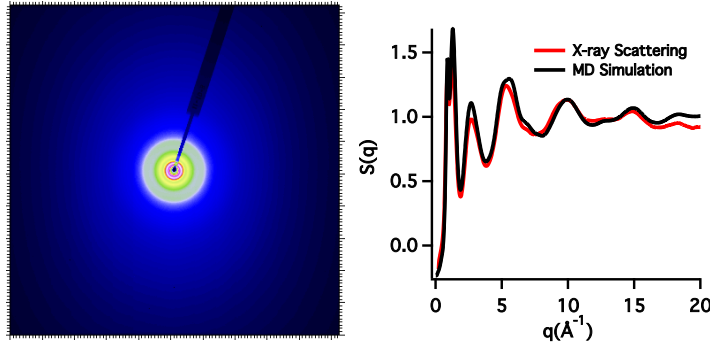


Figure 1.2: Left: 2-D scattering pattern of the ionic liquid $\text{Im}_{2,1}^+/\text{BSI}_{1,4}^-$. (See Figure 1.3 for its molecular structure). Right: $S(q)$ of same IL obtained from X-ray scattering and MD simulation.

1.3.2 Structure Function $S(q)$ for ILs

The total liquid structure function $S(q)$ is divided into two parts: inter-molecular interactions for $q < 2 \text{ \AA}^{-1}$ and intra-molecular interactions for $q > 2 \text{ \AA}^{-1}$ for ILs having

the NTf_2^- anion.(123) Two or three peaks are usually observed in the inter-molecular region for ionic liquids, an *adjacency peak* near $q = 1.4 \text{ \AA}^{-1}$ due to the correlations between neighboring ions, and a *charge-charge correlation peak* near $q = 0.8 \text{ \AA}^{-1}$ arising from repeating charge alternations.(102; 103; 123–126) The $S(q)$ for $\text{Im}_{2,1}^+/\text{BSI}_{1,4}^-$ in Figure 1.2 displays two peaks for $q < 2 \text{ \AA}^{-1}$, just as expected. For ILs with long hydrophobic function groups on the cation and/or anions, a third peak or *first sharp diffraction peak* (FSDP, also called a *pre-peak*) can be observed for $q < 0.5 \text{ \AA}^{-1}$, arising mostly from the nano-domain aggregation of the nonpolar groups.(101; 106; 127–131) Such a feature is evidence of intermediate range order in the system. The position of the FSDP depends largely on the length and volume of the hydrophobic groups. FSDPs can also be observed when more polar groups are present, such as a pentamethyldisiloxy tail on an imidazolium cation.(24) Atkin, *et al.* explained that it was the H-bonding networks in ionic liquids such as ethyl- and propyl-ammonium nitrate that lead to such intermediate range order.(101; 108; 132; 133) It also happens that no FSDPs are observed in the total structure function $S(q)$ even when the IL contains long hydrophobic groups due to peak and anti-peak cancellations of the subcomponents, such as for ILs with short alkyl chains on the cation and long fluoroalkyl chains on the anion.(18) Therefore, the total structure factor $S(q)$ should be interpreted with care as to the existence of nanoscale domains.

1.4 The Structure of Ionic Liquids Studied

Figure 1.3 shows all the cations and anions that are used for this work. Imidazolium and pyrrolidinium based ionic liquids have been widely studied in the development of ionic liquids.(134; 135) Phosphonium-based ionic liquids have also become an important sub-class of ionic liquids, especially in the application of gas absorption.(136; 137) The introduction of NTf_2^- anion broadened the range of cations used, which makes it one of the most popular ions. The ten anions shown are all from the bis(perfluoroalkylsulfonyl)imide (BSI) family, including five anions (colored gray) that have not been synthesized yet. In this work, we would focus on the study of structures of ILs in bulk and at interfaces. We would also talk about the diffusivities of ILs with four cations (colored

red: $\text{Im}_{2,1}^+$, $\text{Im}_{1,8}^+$, $\text{Pyrr}_{1,8}^+$, and $\text{P}_{6,6,6,14}^+$) paired with the $\text{BSI}_{1,4}^-$ anion, and the diffusivities of $\text{P}_{6,6,6,14}^+/\text{NTf}_2^-$ and 1-octanol mixtures.

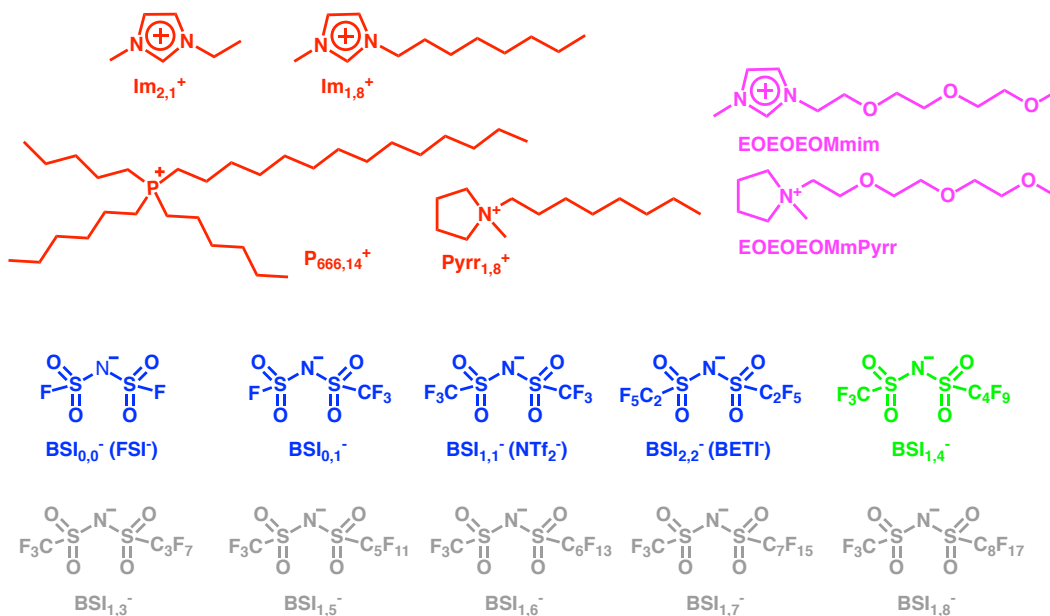


Figure 1.3: All the cations and anions used in this work. Synthesis for the anions that are colored gray have not been reported in the chemical literature as of mid-2019.

1.5 Summary

Though ionic liquids have been reported for more than a century, ILs did not receive major attention from the scientific community until the 1990s. As relatively new solvents, the study of ILs has spread from basic physical properties to the liquid structure down to the atomic level. The application of IL ranges from use in extraction for their physical properties to biomass conversion to nuclear research. Within only two decades, ionic liquids have become a major subject of study for modern chemistry, and the trend continues. With their unique properties and possibility of unlimited combinations, ILs can be used in many ways. To efficiently select the desired ILs for a specific application, it is crucial that we understand the relation between their molecular structures and properties. This dissertation is dedicated to investigation of the structure of ILs,

especially fluorinated ILs, both in bulk and at interfaces. We hope this work would help with the understanding of not only the ILs studied but also other IL systems.

Bibliography

- [1] P. Walden. “Molecular Weights and Electrical Conductivity of Several Fused Salts.” *Bulletin of the Russian Academy of Sciences*, 8, 405–422, 1914. Bull. Acad. Imper. Sci. St. Petersburg.
- [2] T. Welton. “Ionic liquids: a brief history.” *Biophys. Rev.*, 10, 691–706, 2018. doi:10.1007/s12551-018-0419-2.
- [3] J. P. Armstrong, C. Hurst, R. G. Jones, P. Licence, K. R. J. Lovelock, C. J. Satterley, and I. J. Villar-Garcia. “Vapourisation of ionic liquids.” *Phys. Chem. Chem. Phys.*, 9, 982–990, 2007. doi:10.1039/B615137J.
- [4] Y. U. Paulechka, G. J. Kabo, A. V. Blokhin, O. A. Vydrov, J. W. Magee, and M. Frenkel. “Thermodynamic properties of 1-butyl-3-methylimidazolium hexafluorophosphate in the ideal gas state.” *J. Chem. Eng. Data*, 48, 457–462, 2003. doi:10.1021/je025591i.
- [5] T. Welton. “Ionic liquids in green chemistry.” *Green Chem.*, 13, 225–225, 2011. doi:10.1039/C0GC90047H.
- [6] C. Maton, N. De Vos, and C. V. Stevens. “Ionic liquid thermal stabilities: decomposition mechanisms and analysis tools.” *Chem. Soc. Rev.*, 42, 5963–5977, 2013. doi:10.1039/C3CS60071H.
- [7] M. Villanueva, A. Coronas, J. García, and J. Salgado. “Thermal stability of ionic liquids for their application as new absorbents.” *Ind. Eng. Chem. Res.*, 52, 15718–15727, 2013. doi:10.1021/ie401656e.
- [8] C. G. Cassity, A. Mirjafari, N. Mobarrez, K. J. Strickland, R. A. O’Brien, and J. H. Davis. “Ionic liquids of superior thermal stability.” *Chem. Commun.*, 49, 7590–7592, 2013. doi:10.1039/C3CC44118K.

- [9] W. Feng, Y. Lu, Y. Chen, Y. Lu, and T. Yang. “Thermal stability of imidazolium-based ionic liquids investigated by tg and ftir techniques.” *J. Therm. Anal. Calorim.*, 125, 143–154, 2016. doi:10.1007/s10973-016-5267-3.
- [10] C. Francis, R. Louey, K. Sammut, and A. S. Best. “Thermal stability of pyrrolidinium-fsi ionic liquid electrolyte and lithium-ion electrodes at elevated temperatures.” 165, A1204–A1221, 2018. doi:10.1149/2.0281807jes.
- [11] B. D. Rabideau, K. N. West, and J. H. Davis. “Making good on a promise: ionic liquids with genuinely high degrees of thermal stability.” *Chem. Commun.*, 54, 5019–5031, 2018. doi:10.1039/C8CC01716F.
- [12] G. Huang, W. Lin, P. He, Y. Pan, and C. Shu. “Thermal decomposition of imidazolium-based ionic liquid binary mixture: Processes and mechanisms.” *J. Mol. Liq.*, 272, 37–42, 2018. doi:10.1016/j.molliq.2018.09.058.
- [13] M. Götz, R. Reimert, S. Bajohr, H. Schnetzer, J. Wimberg, and T. J. Schubert. “Long-term thermal stability of selected ionic liquids in nitrogen and hydrogen atmosphere.” *Thermochim. Acta*, 600, 82 – 88, 2015. doi:10.1016/j.tca.2014.11.005.
- [14] B. Siu, C. G. Cassity, A. Benchea, T. Hamby, J. Hendrich, K. J. Strickland, A. Wierzbicki, R. E. Sykora, E. A. Salter, R. A. O’Brien, K. N. West, and J. H. Davis. “Thermally robust: triarylsulfonium ionic liquids stable in air for 90 days at 300 °C.” *RSC Adv.*, 7, 7623 – 7630, 2017. doi : 10.1039/C6RA25774G.
- [15] K. Paduszyński and U. Domańska. “Viscosity of ionic liquids: An extensive database and a new group contribution model based on a feed-forward artificial neural network.” *J. Chem. Inf. Model.*, 54, 1311–1324, 2014. doi:10.1021/ci500206u.
- [16] R. Alcalde, G. García, M. Atilhan, and S. Aparicio. “Systematic study on the viscosity of ionic liquids: Measurement and prediction.” *Ind. Eng. Chem. Res.*, 54, 10918–10924, 2015. doi:10.1021/acs.iecr.5b02713.

- [17] H. Li, M. Ibrahim, I. Agberemi, and M. N. Kobrak. “The relationship between ionic structure and viscosity in room-temperature ionic liquids.” *J. Chem. Phys.*, 129, 124507, 2008. doi:10.1063/1.2978378.
- [18] M. Zhao, B. Wu, S. I. Lall-Ramnarine, J. D. Ramdihal, K. A. Papacostas, E. D. Fernandez, R. A. Sumner, C. J. Margulis, J. F. Wishart, and E. W. Castner. “Structural analysis of ionic liquids with symmetric and asymmetric fluorinated anions.” *J. Chem. Phys.*, 151, 074504, 2019. doi:10.1063/1.5111643.
- [19] M. Liang, S. Khatun, and E. W. Castner, Jr. “Communication: Unusual Structure and Transport in Ionic Liquid-Hexane Mixtures.” *J. Chem. Phys.*, 142, 121101, 2015. doi:10.1063/1.4916388.
- [20] S. Zhang, N. Sun, X. He, X. Lu, and X. Zhang. “Physical properties of ionic liquids: Database and evaluation.” *J. Phys. Chem. Ref. Data*, 35, 1475–1517, 2006. doi:10.1063/1.2204959.
- [21] P. A. Hunt, C. R. Ashworth, and R. P. Matthews. “Hydrogen bonding in ionic liquids.” *Chem. Soc. Rev.*, 44, 2015. doi:10.1039/C4CS00278D.
- [22] S. I. Lall-Ramnarine, C. Rodriguez, R. Fernandez, N. Zmich, E. D. Fernandez, S. B. Dhiman, and J. F. Wishart. “The Effect of Lengthening Cation Ether Tails On Ionic Liquid Properties.” *ECS Trans.*, 2016. doi:10.1149/07515.0215ecst. In press.
- [23] S. I. Lall-Ramnarine, M. Zhao, C. Rodriguez, R. Fernandez, N. Zmich, E. D. Fernandez, S. B. Dhiman, E. W. Castner, Jr., and J. F. Wishart. “Connecting structural and transport properties of ionic liquids with cationic oligoether chains.” *J. Electrochem. Soc.*, 164, H5247–H5262, 2017. doi:10.1149/2.0371708jes.
- [24] B. Wu, H. Shirota, and E. W. Castner, Jr. “Structure of Ionic Liquids with Cationic Silicon-Substitutions.” *J. Chem. Phys.*, 145, 114501, 2016. doi:10.1063/1.4962257.
- [25] G. S. Fulcher. “Analysis of recent measurements of the viscosity of glasses.” *J. Am. Ceram. Soc.*, 8, 339–355, 1925. doi:10.1111/j.1151-2916.1925.tb16731.x.

- [26] G. Tammann and W. Hesse. “Die abhängigkeit der viscosität von der temperatur bie unterkühlten flüssigkeiten.” *Z. Anorg. Allg. Chem.*, 156, 245–257, 1926. doi: 10.1002/zaac.19261560121.
- [27] S. N. Suarez, A. Rúa, D. Cuffari, K. Pilar, J. L. Hatcher, S. Ramati, and J. F. Wishart. “Do TFSA Anions Slither? Pressure Exposes the Role of TFSA Conformational Exchange in Self-Diffusion.” *J. Phys. Chem. B*, 119, 14756–14765, 2015. doi: 10.1021/acs.jpcb.5b08658.
- [28] B. Docampo-Alvarez, V. Gomez-Gonzalez, T. Mendez-Morales, J. R. Rodriguez, O. Cabeza, M. Turmine, L. J. Gallego, and L. M. Varela. “The effect of alkyl chain length on the structure and thermodynamics of protic-aprotic ionic liquid mixtures: a molecular dynamics study.” *Phys. Chem. Chem. Phys.*, 9938–9949, 2018. doi: 10.1039/C8CP00575C.
- [29] M. Campetella, A. Mariani, C. Sadun, B. Wu, E. W. CastnerJr., and L. Gontrani. “Structure and dynamics of propylammonium nitrate-acetonitrile mixtures: An intricate multi-scale system probed with experimental and theoretical techniques.” *J. Chem. Phys.*, 148, 134507, 2018. doi:10.1063/1.5021868.
- [30] O. Borodin, D. L. Price, B. Aoun, M. A. Gonzalez, J. B. Hooper, M. Kofu, S. Kohara, O. Yamamuro, and M.-L. Saboungi. “Effect of water on the structure of a prototype ionic liquid.” *Phys. Chem. Chem. Phys.*, 18, 23474–23481, 2016. doi: 10.1039/C6CP02191C.
- [31] K. Ueno, J. Mura, K. Ikeda, S. Tsuzuki, M. Tsuchiya, R. Tatara, T. Mandai, Y. Umebayashi, K. Dokko, and M. Watanabe. “Li⁺ Solvation and Ionic Transport in Lithium Solvate Ionic Liquids Diluted by Molecular Solvents.” *J. Phys. Chem. C*, 120, 15792–15802, 2016. doi:10.1021/acs.jpcc.5b11642.
- [32] A. Mariani, M. Campetella, C. Fasolato, M. Daniele, F. Capitani, L. Bencivenni, P. Postorino, S. Lupi, R. Caminiti, and L. Gontrani. “A joint experimental and computational study on ethylammonium nitrate-ethylene glycol 1:1 mixture. structural,

- kinetic, dynamic and spectroscopic properties.” *J. Mol. Liq.*, 226, 2 – 8, 2017. doi:10.1016/j.molliq.2016.08.043.
- [33] A. Lewandowski and A. Swiderska-Mocek. “Ionic liquids as electrolytes for Li-ion batteries: An overview of electrochemical studies.” *J. Power Sources*, 194, 601–609, 2009. doi:10.1016/j.jpowsour.2009.06.089.
- [34] M. Galinski, A. Lewandowski, and I. Stepniak. “Ionic liquids as electrolytes.” *Electrochim. Acta*, 51, 5567 – 5580, 2006.
- [35] W. Xu, E. I. Cooper, and C. A. Angell. “Ionic Liquids: Ion Mobilities, Glass Temperatures, and Fragilities.” *J. Phys. Chem. B*, 107, 6170–6178, 2003. doi:10.1021/jp0275894.
- [36] H. Tokuda, K. Ishii, M. A. B. H. Susan, S. Tsuzuki, K. Hayamizu, and M. Watanabe. “Physicochemical Properties and Structures of Room-Temperature Ionic Liquids. 3. Variation of Cationic Structures.” *J. Phys. Chem. B*, 110, 2833–2839, 2006. doi:10.1021/jp053396f.
- [37] J. Vila, P. Ginés, J. Pico, C. Franjo, E. Jiménez, L. Varela, and O. Cabeza. “Temperature dependence of the electrical conductivity in emim-based ionic liquids: Evidence of vogel-tamman-fulcher behavior.” *Fluid Phase Equilib.*, 242, 141 – 146, 2006. doi:10.1016/j.fluid.2006.01.022.
- [38] K. Ghandi. “A review of ionic liquids, their limits and applications.” *Green Sustainable Chem.*, 4, 44–53, 2014. doi:10.4236/gsc.2014.41008.
- [39] A. Stoppa, O. Zech, W. Kunz, and R. Buchner. “The conductivity of imidazolium-based ionic liquids from (–35 to 195) °C. A. variation of cation’s alkyl chain.” *J. Chem. Eng. Data*, 55, 1768–1773, 2010. doi:10.1021/je900789j.
- [40] O. Zech, A. Stoppa, R. Buchner, and W. Kunz. “The conductivity of imidazolium-based ionic liquids from (248 to 468) K. B. variation of the anion.” *J. Chem. Eng. Data*, 55, 1774–1778, 2010. doi:10.1021/je900793r.

- [41] J. Nilsson-Hallén, B. Ahlström, M. Marczewski, and P. Johansson. “Ionic liquids: A simple model to predict ion conductivity based on dft derived physical parameters.” *Front. Chem.*, 7, 126, 2019. doi:10.3389/fchem.2019.00126.
- [42] H. Jin, B. O’Hare, J. Dong, S. Arzhantsev, G. A. Baker, J. F. Wishart, A. J. Benesi, and M. Maroncelli. “Physical Properties of Ionic Liquids Consisting of the 1-Butyl-3-Methylimidazolium Cation with Various Anions and the Bis(trifluoromethylsulfonyl)imide Anion with Various Cations.” *J. Phys. Chem. B*, 112, 81–92, 2008. doi:10.1021/jp076462h.
- [43] S. Terada, H. Susa, S. Tsuzuki, T. Mandai, K. Ueno, Y. Umebayashi, K. Dokko, and M. Watanabe. “Dissociation and Diffusion of Glyme-Sodium Bis(trifluoromethanesulfonyl)amide Complexes in Hydrofluoroether-Based Electrolytes for Sodium Batteries.” *J. Phys. Chem. C*, 120, 23339–23350, 2016. doi:10.1021/acs.jpcc.6b06804.
- [44] A. S. Ivanova, T. Brinzer, E. A. Roth, V. A. Kusuma, J. D. Watkins, X. Zhou, D. Luebke, D. Hopkinson, N. R. Washburn, S. Garrett-Roe, and H. B. Nulwala. “Eutectic ionic liquid mixtures and their effect on CO₂ solubility and conductivity.” *RSC Adv.*, 5, 51407–51412, 2015. doi:10.1039/c5ra06561e.
- [45] R. Brown. “Xxvii. a brief account of microscopical observations made in the months of june, july and august 1827, on the particles contained in the pollen of plants; and on the general existence of active molecules in organic and inorganic bodies.” *Philos. Mag.*, 4, 161–173, 1828. doi:10.1080/14786442808674769.
- [46] S. Tsuzuki. “Factors controlling the diffusion of ions in ionic liquids.” *ChemPhysChem.*, 13, 1664–1670, 2012. doi:10.1002/cphc.201100870.
- [47] A. J. Masters and P. A. Madden. “A molecular theory of stokes-einstein behavior. i. translational brownian motion.” *J. Chem. Phys.*, 74, 2450–2459, 1981. doi:10.1063/1.441368.
- [48] K. R. Harris. “The fractional Stokes-Einstein equation: Application to Lennard-Jones, molecular, and ionic liquids.” *J. Chem. Phys.*, 131, 054503, 2009. doi:10.1063/1.3183951.

- [49] H. Tokuda, H. Kikuko, K. Ishii, M. A. B. H. Susan, and M. Watanabe. “Physicochemical Properties and Structures of Room Temperature Ionic Liquids. 1. Variation of Anionic Species.” *J. Phys. Chem. B*, 108, 16593–16600, 2004. doi:10.1021/jp047480r.
- [50] H. Tokuda, K. Hayamizu, K. Ishii, M. A. B. H. Susan, and M. Watanabe. “Physicochemical Properties and Structures of Room Temperature Ionic Liquids. 2. Variation of Alkyl Chain Length in Imidazolium Cation.” *J. Phys. Chem. B*, 109, 6103–6110, 2005. doi:10.1021/jp044626d.
- [51] N. V. Plechkova and K. R. Seddon. “Applications of ionic liquids in the chemical industry.” *Chem. Soc. Rev.*, 37, 123–150, 2008. doi:10.1039/B006677J.
- [52] M. Freemantle. “Designer solvents.” *Chem. Eng. News Archive*, 76, 32–37, 1998. doi:10.1021/cen-v076n013.p032.
- [53] E. D. Bates, R. D. Mayton, I. Ntai, and J. H. D. Jr. “CO₂ Capture by a Task-Specific Ionic Liquid.” *J. Am. Chem. Soc.*, 124, 926–927, 2002. doi:10.1021/ja017593d.
- [54] A. Berthod, M. Ruiz-Ángel, and S. Carda-Broch. “Recent advances on ionic liquid uses in separation techniques.” *J. Chromatogr. A*, 1559, 2–16, 2018. doi:10.1016/j.chroma.2017.09.044.
- [55] A. Berthod, M. Ruiz-Ángel, and S. Carda-Broch. “Ionic liquids in separation techniques.” *J. Chromatogr. A*, 1184, 6–18, 2008. doi:10.1016/j.chroma.2007.11.109.
- [56] M. D. Joshi and J. L. Anderson. “Recent advances of ionic liquids in separation science and mass spectrometry.” *RSC Adv.*, 2, 5470–5484, 2012. doi:10.1039/C2RA20142A.
- [57] X. Sun, H. Luo, and S. Dai. “Ionic liquids-based extraction: A promising strategy for the advanced nuclear fuel cycle.” *Chem. Rev.*, 112, 2100–2128, 2012. doi:10.1021/cr200193x.
- [58] Z. Lei, C. Dai, and B. Chen. “Gas solubility in ionic liquids.” *Chem. Rev.*, 114, 1289–1326, 2014. doi:10.1021/cr300497a.
- [59] Y. Zhao, R. Gani, R. M. Afzal, X. Zhang, and S. Zhang. “Ionic liquids for absorption and separation of gases: An extensive database and a systematic screening method.” *AIChE J.*, 63, 1353–1367, 2017. doi:10.1002/aic.15618.

- [60] M. B. Shiflett and E. J. Maginn. “The solubility of gases in ionic liquids.” *AIChE J.*, 63, 4722–4737, 2017. doi:10.1002/aic.15957.
- [61] L. A. Blanchard, D. Hancu, E. J. Beckman, and J. F. Brennecke. “Green processing using ionic liquids and CO₂.” *Nature*, 399, 28–29, 1999. doi:10.1038/19887.
- [62] Q. He, J. W. O’Brien, K. A. Kitselman, L. E. Tompkins, G. C. T. Curtis, and F. M. Kerton. “Synthesis of cyclic carbonates from CO₂ and epoxides using ionic liquids and related catalysts including choline chloride - metal halide mixtures.” *Catal. Sci. Technol.*, 4, 1513–1528, 2014. doi:10.1039/C3CY00998J.
- [63] R. Babarao, S. Dai, and D.-e. Jiang. “Understanding the High Solubility of CO₂ in an Ionic Liquid with the Tetracyanoborate Anion.” *J. Phys. Chem. B*, 115, 9789–9794, 2011.
- [64] V. S. Kandagal, F. Chen, E. Jánsson, J. M. Pringle, and M. Forsyth. “Molecular simulation study of CO₂ and N₂ absorption in a phosphonium based organic ionic plastic crystal.” *J. Chem. Phys.*, 147, 124703, 2017. doi:10.1063/1.4993654.
- [65] C. Kang, X. Zhang, and D. R. MacFarlane. “Synthesis and physicochemical properties of fluorinated ionic liquids with high nitrogen gas solubility.” *J. Phys. Chem. C*, 122, 24550–24558, 2018. doi:10.1021/acs.jpcc.8b07752.
- [66] D. J. Tempel, P. B. Henderson, J. R. Brzozowski, R. M. Pearlstein, and H. Cheng. “High gas storage capacities for ionic liquids through chemical complexation.” *J. Am. Chem. Soc.*, 130, 400–401, 2008. doi:10.1021/ja077233b.
- [67] T. Welton. “1. Room-Temperature Ionic Liquids. Solvents for Synthesis and Catalysis.” *Chem. Rev.*, 99, 2071–2083, 1999. doi:10.1021/cr980032t.
- [68] A. K. Chakraborti and S. R. Roy. “On catalysis by ionic liquids.” *J. Am. Chem. Soc.*, 131, 6902–6903, 2009. doi:10.1021/ja900076a.
- [69] J. P. Hallett and T. Welton. “Room-temperature ionic liquids: solvents for synthesis and catalysis. 2.” *Chem. Rev.*, 111, 3508–3576, 2011. doi:10.1021/cr1003248.

- [70] V. I. Parvulescu and C. Hardacre. “Catalysis in ionic liquids.” *Chem. Rev.*, 107, 2615–2665, 2007. doi:10.1021/cr050948h.
- [71] P. Wasserscheid and W. Keim. “Ionic liquids - New “solutions” for transition metal catalysis.” *Angew. Chem.-Int. Edit.*, 39, 3772–3789, 2000. doi:10.1002/1521-3773(20001103)39:21<3772::AID-ANIE3772>3.0.CO;2-5.
- [72] J. Dupont, R. de Souza, and P. Suarez. “Ionic liquid (molten salt) phase organometallic catalysis.” *Chem. Rev.*, 102, 3667–3691, 2002. doi:10.1021/cr010338r.
- [73] M. Liang, A. Kaintz, G. A. Baker, and M. Maroncelli. “Bimolecular electron transfer in ionic liquids: Are reaction rates anomalously high?” *J. Phys. Chem. B*, 116, 1370–1384, 2012. doi:10.1021/jp210892c.
- [74] B. Wu, M. Liang, M. Maroncelli, and E. W. Castner. “Photoinduced bimolecular electron transfer from cyano anions in ionic liquids.” *J. Phys. Chem. B*, 119, 14790–14799, 2015. doi:10.1021/acs.jpcc.5b09216.
- [75] B. Wu, M. Liang, N. Zmich, J. Hatcher, S. I. Lall-Ramnarin, J. F. Wishart, M. Maroncelli, and E. W. Castner. “Photoinduced bimolecular electron transfer in ionic liquids: Cationic electron donors.” *J. Phys. Chem. B*, 122, 2379–2388, 2018. doi:10.1021/acs.jpcc.7b12542.
- [76] A. J. Walker and N. C. Bruce. “Cofactor-dependent enzyme catalysis in functionalized ionic solvents.” *Chem. Commun.*, 2570–2571, 2004. doi:10.1039/B410467F.
- [77] M. Goldfeder and A. Fishman. “Modulating enzyme activity using ionic liquids or surfactants.” *Appl. Microbiol. Biotechnol.*, 98, 545–554, 2014. doi:10.1007/s00253-013-5395-7.
- [78] M. Watanabe, M. L. Thomas, S. Zhang, K. Ueno, T. Yasuda, and K. Dokko. “Application of ionic liquids to energy storage and conversion materials and devices.” *Chem. Rev.*, 117, 7190–7239, 2017. doi:10.1021/acs.chemrev.6b00504.

- [79] D. R. MacFarlane, N. Tachikawa, M. Forsyth, J. M. Pringle, P. C. Howlett, G. D. Elliott, J. James H. Davis, M. Watanabe, P. Simon, and C. A. Angell. “Energy applications of ionic liquids.” *Energy Environ. Sci.*, 7, 232–250, 2014. doi:10.1039/c3ee42099j.
- [80] G. Reynolds and C. Dymek. “Primary and secondary room temperature molten salt electrochemical cells.” *J. Power Sources*, 15, 109 – 118, 1985. doi:10.1016/0378-7753(85)80066-5.
- [81] P. Wang, S. M. Zakeeruddin, J. E. Moser, R. Humphry-Baker, and M. Gratzel. “A solvent-free, SeCN-/SeCN₃- based ionic liquid electrolyte for high-efficiency dye-sensitized nanocrystalline solar cells.” *J. Am. Chem. Soc.*, 126, 7164–7165, 2004.
- [82] J. N. Barisci, G. G. Wallace, D. R. MacFarlane, and R. H. Baughman. “Investigation of ionic liquids as electrolytes for carbon nanotube electrodes.” *Electrochem. Comm.*, 6, 22 – 27, 2004.
- [83] G. Sun, K. Li, and C. Sun. “Application of 1-ethyl-3-methylimidazolium thiocyanate to the electrolyte of electrochemical double layer capacitors.” *J. Power Sour.*, 162, 1444–1450, 2006.
- [84] M. A. Navarra. “Ionic liquids as safe electrolyte components for Li-metal and Li-ion batteries.” *MRS Bull.*, 38, 548–553, 2013. doi:10.1557/mrs.2013.152.
- [85] M. Díaz, A. Ortiz, and I. Ortiz. “Progress in the use of ionic liquids as electrolyte membranes in fuel cells.” *J. Membr. Sci.*, 469, 379–396, 2014. doi:10.1016/j.memsci.2014.06.033.
- [86] V. B. Agbor, N. Cicek, R. Sparling, A. Berlin, and D. B. Levin. “Biomass pretreatment: Fundamentals toward application.” *Biotechnol. Adv.*, 29, 675 – 685, 2011. doi:10.1016/j.biotechadv.2011.05.005.
- [87] R. Swatloski, S. Spear, J. Holbrey, and R. Rogers. “Dissolution of cellulose with ionic liquids.” *J. Am. Chem. Soc.*, 124, 4974–4975, 2002. doi:10.1021/ja025790m.
- [88] H. Tadesse and R. Luque. “Advances on biomass pretreatment using ionic liquids: An overview.” *Energy Environ. Sci.*, 4, 3913–3929, 2011. doi:10.1039/C0EE00667J.

- [89] Q. Hou, M. Ju, W. Li, L. Liu, Y. Chen, and Q. Yang. “Pretreatment of lignocellulosic biomass with ionic liquids and ionic liquid-based solvent systems.” *Molecules*, 22, 2017. doi:10.3390/molecules22030490.
- [90] Z. Zhang, J. Song, and B. Han. “Catalytic transformation of lignocellulose into chemicals and fuel products in ionic liquids.” *Chem. Rev.*, 117, 6834–6880, 2017. doi:10.1021/acs.chemrev.6b00457.
- [91] I. Kilpeläinen, H. Xie, A. King, M. Granstrom, S. Heikkinen, and D. S. Argyropoulos. “Dissolution of wood in ionic liquids.” *J. Agric. Food Chem.*, 55, 9142–9148, 2007. doi:10.1021/jf071692e.
- [92] A. Pinkert, K. N. Marsh, S. Pang, and M. P. Staiger. “Ionic Liquids and Their Interaction with Cellulose.” *Chem. Rev.*, 109, 6712–6728, 2009. doi:10.1021/cr9001947.
- [93] E. C. Achinivu, R. M. Howard, G. Li, H. Gracz, and W. A. Henderson. “Lignin extraction from biomass with protic ionic liquids.” *Green Chem.*, 16, 1114–1119, 2014. doi:10.1039/C3GC42306A.
- [94] J. Shi, J. M. Gladden, N. Sathitsuksanoh, P. Kambam, L. Sandoval, D. Mitra, S. Zhang, A. George, S. W. Singer, B. A. Simmons, and S. Singh. “One-pot ionic liquid pretreatment and saccharification of switchgrass.” *Green Chem.*, 15, 2579–2589, 2013. doi:10.1039/C3GC40545A.
- [95] S. De, S. Dutta, and B. Saha. “One-pot conversions of lignocellulosic and algal biomass into liquid fuels.” *ChemSusChem*, 5, 1826–1833, 2012. doi:10.1002/cssc.201200031.
- [96] C. Xu and C. J. Margulis. “Solvation of an Excess Electron in Pyrrolidinium Dicyanamide Based Ionic Liquids.” *J. Phys. Chem. B*, 119, 532–542, 2015.
- [97] T. Klejdysz, B. Łęgosz, D. Czurylskiewicz, K. Czerniak, and J. Pernak. “Biobased ionic liquids with abietate anion.” *ACS Sustain. Chem. Eng.*, 4, 6543–6550, 2016. doi:10.1021/acssuschemeng.6b01381.

- [98] W. Zhao, X. Chi, H. Li, J. He, J. Long, Y. Xu, and S. Yang. “Eco-friendly acetylcholine-carboxylate bio-ionic liquids for controllable n-methylation and n-formylation using ambient co₂ at low temperatures.” *Green Chem.*, 21, 567–577, 2019. doi:10.1039/C8GC03549K.
- [99] I. Noshadi, B. W. Walker, R. Portillo-Lara, E. Shirzaei Sani, N. Gomes, M. R. Aziziyan, and N. Annabi. “Engineering biodegradable and biocompatible bio-ionic liquid conjugated hydrogels with tunable conductivity and mechanical properties.” *Sci. Rep.*, 7, 4345–4345, 2017. doi:10.1038/s41598-017-04280-w.
- [100] W. H. Bragg and W. L. Bragg. “The reflection of x-rays by crystals.” *Proc. Royal Soc. Lond. A*, 88, 428–438, 1913. doi:10.1098/rspa.1913.0040.
- [101] R. Hayes, G. G. Warr, and R. Atkin. “Structure and Nanostructure in Ionic Liquids.” *Chem. Rev.*, 115, 6357–6426, 2015. doi:10.1021/cr500411q.
- [102] H. K. Kashyap, J. J. Hettige, H. V. R. Annapureddy, and C. J. Margulis. “SAXS anti-peaks reveal the length-scales of dual positive-negative and polar-apolar ordering in room-temperature ionic liquids.” *Chem. Commun.*, 48, 5103–5105, 2012. doi:10.1039/C2CC30609C.
- [103] J. C. Araque, S. K. Yadav, M. Shadeck, M. Maroncelli, and C. J. Margulis. “How Is Diffusion of Neutral and Charged Tracers Related to the Structure and Dynamics of a Room-Temperature Ionic Liquid? Large Deviations from Stokes-Einstein Behavior Explained.” *J. Phys. Chem. B*, 119, 7015–7029, 2015. doi:10.1021/acs.jpcc.5b01093.
- [104] A. Triolo, O. Russina, R. Caminiti, H. Shirota, H. Y. Lee, C. S. Santos, N. S. Murthy, and E. W. Castner, Jr. “Comparing intermediate range order for alkyl- vs. ether-substituted cations in ionic liquids.” *Chem. Commun.*, 48, 4959–4961, 2012. doi:10.1039/C2CC31550E.
- [105] O. Russina and A. Triolo. “New experimental evidence supporting the mesoscopic segregation model in room temperature ionic liquids.” *Faraday Discuss.*, 154, 97–109, 2012. doi:10.1039/C1FD00073J.

- [106] O. Russina, A. Triolo, L. Gontrani, R. Caminiti, D. Xiao, J. Hines, Larry G., R. A. Bartsch, E. L. Quitevis, N. Plechkova, and K. R. Seddon. “Morphology and intermolecular dynamics of 1-alkyl-3-methylimidazolium bis(trifluoromethane)sulfonylamide ionic liquids: structural and dynamic evidence of nanoscale segregation.” *J. Phys.: Condens. Matter*, 21, 424121, 2009. doi:10.1088/0953-8984/21/42/424121.
- [107] K. Fujii, R. Kanzaki, T. Takamuku, Y. Kameda, S. Kohara, M. Kanakubo, M. Shibayama, S.-i. Ishiguro, and Y. Umebayashi. “Experimental evidences for molecular origin of low-Q peak in neutron/X-ray scattering of 1-alkyl-3-methylimidazolium bis(trifluoromethanesulfonyl)amide ionic liquids.” *J. Chem. Phys.*, 135, 244502, 2011. doi:10.1063/1.3672097.
- [108] Y. Umebayashi, W.-L. Chung, T. Mitsugi, S. Fukuda, M. Takeuchi, K. Fujii, T. Takamuku, R. Kanzaki, and S.-i. Ishiguro. “Liquid Structure and the Ion-Ion Interactions of Ethylammonium Nitrate Ionic Liquid Studied by Large Angle X-Ray Scattering and Molecular Dynamics Simulations.” *J. Comput. Chem. Jpn*, 7, 125–134, 2008.
- [109] K. Fujii, S. Seki, S. Fukuda, T. Takamuku, S. Kohara, Y. Kameda, Y. Umebayashi, and S.-i. Ishiguro. “Liquid structure and conformation of a low-viscosity ionic liquid, N-methyl-N-propyl-pyrrolidinium bis(fluorosulfonyl) imide studied by high-energy X-ray scattering.” *J. Mol. Liq.*, 143, 64–69, 2008. doi:10.1016/j.molliq.2008.05.011.
- [110] S. Fukuda, M. Takeuchi, K. Fujii, R. Kanzaki, T. Takamuku, K. Chiba, H. Yamamoto, Y. Umebayashi, and S.-i. Ishiguro. “Liquid structure of N-butyl-N-methylpyrrolidinium bis(trifluoromethanesulfonyl) amide ionic liquid studied by large angle X-ray scattering and molecular dynamics simulations.” *J. Mol. Liq.*, 143, 2–7, 2008. doi:10.1016/j.molliq.2008.02.012.
- [111] R. Kanzaki, T. Mitsugi, S. Fukuda, K. Fujii, M. Takeuchi, Y. Soejima, T. Takamuku, T. Yamaguchi, Y. Umebayashi, and S. Ishiguro. “Ion-ion interaction in room temperature ionic liquid 1-ethyl-3-methylimidazolium tetrafluoroborate studied by large angle X-ray scattering experiment and molecular dynamics simulations.” *J. Mol. Liq.*, 147, 77–82, 2009. doi:10.1016/j.molliq.2008.10.003.

- [112] M. Kofu, M. Nagao, T. Ueki, Y. Kitazawa, Y. Nakamura, S. Sawamura, M. Watanabe, and O. Yamamuro. “Heterogeneous Slow Dynamics of Imidazolium-Based Ionic Liquids Studied by Neutron Spin Echo.” *J. Phys. Chem. B*, 117, 2773–2781, 2013. doi:10.1021/jp312608r.
- [113] K. B. Dhungana, L. F. O. Faria, B. Wu, M. Liang, M. C. C. Ribeiro, C. J. Margulis, and E. W. Castner, Jr. “Structure of cyano-anion ionic liquids: X-ray scattering and simulations.” *J. Chem. Phys.*, 145, 024503, 2016. doi:10.1063/1.4955186.
- [114] M. G. D. Pópolo, R. M. Lynden-Bell, and J. Kohanoff. “Ab Initio Molecular Dynamics Simulation of a Room Temperature Ionic Liquid.” *J. Phys. Chem. B*, 109, 5895–5902, 2005. doi:10.1021/jp044414g.
- [115] A. B. Biedron, E. L. Garfunkel, E. W. Castner, Jr., and S. Rangan. “Ionic Liquid Ultrathin Films at the surface of Cu(100) and Au(111).” *J. Chem. Phys.*, 146, 054704, 2017. doi:10.1063/1.4975101.
- [116] J. J. Hettige, W. D. Amith, E. W. Castner, Jr., and C. J. Margulis. “Ionic Liquids with Symmetric Diether Tails: Bulk and Vacuum-Liquid Interfacial Structures.” *J. Phys. Chem. B*, ASAP; doi: 10.1021/acs.jpcb.6b09148, 2016. doi:10.1021/acs.jpcb.6b09148.
- [117] K. Shimizu, M. F. Costa Gomes, A. A. H. Pádua, L. P. Rebelo, and J. N. C. Lopes. “Three commentaries on the nano-segregated structure of ionic liquids.” *J. Mol. Struct.: TheoChem*, 946, 70–76, 2010. doi:10.1016/j.theochem.2009.11.034.
- [118] K. Shimizu, J. N. Canongia Lopes, and A. M. P. S. Gonçalves da Silva. “Ionic liquid films at the water-air interface: Langmuir isotherms of tetra-alkylphosphonium-based ionic liquids.” *Langmuir*, 31, 8371–8378, 2015. doi:10.1021/acs.langmuir.5b01977.
- [119] K. Shimizu, M. Tariq, A. A. Freitas, A. A. H. Pádua, and J. N. Canongia Lopes. “Self-Organization in Ionic Liquids: From Bulk to Interfaces and Films.” *Journal of the Brazilian Chemical Society*, 27, 349 – 362, 2016. doi:10.5935/0103-5053.20150274.

- [120] O. Russina, S. De Santis, and L. Gontrani. “Micro- and mesoscopic structural features of a bio-based choline-amino acid ionic liquid.” *RSC Adv.*, 6, 34737–34743, 2016. doi:10.1039/C6RA02142E.
- [121] S. Sharma, A. Gupta, and H. K. Kashyap. “How the Structure of Pyrrolidinium Ionic Liquids Is Susceptible to High Pressure.” *J. Phys. Chem. B*, 120, 3206–3214, 2016. doi:10.1021/acs.jpcc.6b01133.
- [122] A. Mariani, O. Russina, R. Caminiti, and A. Triolo. “Structural organization in a methanol:ethylammonium nitrate (1:4) mixture: A joint X-ray/Neutron diffraction and computational study.” *J. Mol. Liq.*, 212, 947–956, 2015.
- [123] C. S. Santos, H. V. R. Annapureddy, N. S. Murthy, H. K. Kashyap, E. W. Castner, Jr., and C. J. Margulis. “Temperature-dependent structure of methyltributylammonium bis(trifluoromethylsulfonyl)amide: X ray scattering and simulations.” *J. Chem. Phys.*, 134, 064517, 2011. doi:10.1063/1.3526958.
- [124] H. V. R. Annapureddy, H. K. Kashyap, P. M. De Biase, and C. J. Margulis. “What is the Origin of the Prepeak in the X-ray Scattering of Imidazolium-Based Room-Temperature Ionic Liquids?” *J. Phys. Chem. B*, 114, 16838–16846, 2010. doi:10.1021/jp108545z.
- [125] H. K. Kashyap, C. S. Santos, H. V. R. Annapureddy, N. S. Murthy, C. J. Margulis, and E. W. Castner, Jr. “Temperature-Dependent Structure of Ionic Liquids: X-ray Scattering and Simulations.” *Faraday Discuss.*, 154, 133–143, 2012. doi:10.1039/C1FD00059D.
- [126] E. W. Castner, Jr., C. J. Margulis, M. Maroncelli, and J. F. Wishart. “Ionic Liquids: Structure and Photochemical Reactions.” *Annu. Rev. Phys. Chem.*, 62, 85–105, 2011. doi:10.1146/annurev-physchem-032210-103421.
- [127] J. N. Canongia Lopes and A. A. H. Padua. “Molecular Force Field for Ionic Liquids III: Imidazolium, Pyridinium, and Phosphonium Cations; Chloride, Bromide, and Dicyanamide Anions.” *J. Phys. Chem. B*, 110, 19586–19592, 2006. doi:10.1021/jp063901o.
- [128] A. Triolo, O. Russina, H.-J. Bleif, and E. Di Cola. “Nanoscale segregation in room temperature ionic liquids.” *J. Phys. Chem. B*, 111, 4641–4644, 2007. doi:10.1021/jp067705t.

- [129] H. K. Kashyap, C. S. Santos, R. P. Daly, J. J. Hettige, N. S. Murthy, H. Shirota, E. W. Castner, Jr., and C. J. Margulis. “How Does the Ionic Liquid Organizational Landscape Change when Nonpolar Cationic Alkyl Groups Are Replaced by Polar Isoelectronic Diethers?” *J. Phys. Chem. B*, 117, 1130–1135, 2013. doi:10.1021/jp311032p.
- [130] O. Russina, L. Gontrani, B. Fazio, D. Lombardo, A. Triolo, and R. Caminiti. “Selected chemical-physical properties and structural heterogeneities in 1-ethyl-3-methylimidazolium alkyl-sulfate room temperature ionic liquids.” *Chem. Phys. Lett.*, 493, 259–262, 2010. doi:10.1016/j.cplett.2010.05.042.
- [131] M. Macchiagodena, F. Ramondo, A. Triolo, L. Gontrani, and R. Caminiti. “Liquid Structure of 1-Ethyl-3-methylimidazolium Alkyl Sulfates by X-ray Scattering and Molecular Dynamics.” *J. Phys. Chem. B*, 116, 13448–13458, 2012. doi:10.1021/jp306982e.
- [132] T. L. Greaves, D. F. Kennedy, S. T. Mudie, and C. J. Drummond. “Diversity Observed in the Nanostructure of Protic Ionic Liquids.” *J. Phys. Chem. B*, 114, 10022–10031, 2010. doi:10.1021/jp103863z.
- [133] R. Hayes, S. Imberti, G. G. Warr, and R. Atkin. “Pronounced sponge-like nanostructure in propylammonium nitrate.” *Phys. Chem. Chem. Phys.*, 13, 13544–13551, 2011. doi:10.1039/C1CP21080G.
- [134] C. E. S. Bernardes, K. Shimizu, A. I. M. C. Lobo Ferreira, L. M. N. B. F. Santos, and J. N. Canongia Lopes. “Structure and Aggregation in the 1,3-Dialkyl-imidazolium Bis(trifluoromethylsulfonyl)imide Ionic Liquid Family: 2. From Single to Double Long Alkyl Side Chains.” *J. Phys. Chem. B*, 118, 6885–6895, 2014. doi:10.1021/jp502968u.
- [135] J. S. Wilkes and M. J. Zaworotko. “Air and water stable 1-ethyl-3-methylimidazolium based ionic liquids.” *J. Chem. Soc., Chem. Commun.*, 965–967, 1992. doi:10.1039/C39920000965.
- [136] K. J. Fraser, E. I. Izgorodina, M. Forsyth, J. L. Scott, and D. R. MacFarlane. “Liquids intermediate between “molecular” and “ionic” liquids: Liquid ion pairs?” *Chem. Comm.*, 3817–3819, 2007. doi:10.1039/b710014k.

- [137] D. R. MacFarlane, M. Forsyth, E. I. Izgorodina, A. P. Abbott, G. Annat, and K. Fraser.
“On the concept of ionicity in ionic liquids.” *Phys. Chem. Chem. Phys.*, 11, 4962–4967,
2009. doi:10.1039/b900201d.

Chapter 2

Methods

2.1 Preparation of Samples

ILs are often prepared by creating an organic cation via quaternization of a nitrogen or phosphorus atom. This is frequently accomplished by an S_N2 reaction with, e.g., an alkyl halide, followed by exchange of the halide for the desired anion. This leads to the molecular structures of compounds shown in Figures 1.3. Ultra-high pure trihexyltetradecylphosphonium bis(trifluoromethylsulfonyl)imide ($P_{6,6,6,14}^+ / NTf_2^-$) ionic liquid was purchased from Sigma-Aldrich or IoLiTec and was dried under vacuum for 24 h before use. Neat anhydrous 1-octanol was purchased from Sigma-Aldrich and used as received.

ILs with cations 1-ethyl-3-methylimidazolium ($Im_{2,1}^+$), 1-methyl-3-octylimidazolium ($Im_{1,8}^+$), N-methyl-N-octylpyrrolidinium ($Pyrr_{1,8}^+$) and trihexyltetradecylphosphonium ($P_{6,6,6,14}^+$) paired with anions bis(fluorosulfonyl)imide (FSI^-), (fluorosulfonyl)(trifluoromethylsulfonyl)imide ($BSI_{0,1}^-$), bis(trifluoromethylsulfonyl)imide (NTf_2^-), bis(perfluoroethylsulfonyl)imide ($BETI^-$), and (trifluoromethylsulfonyl)(perfluorobutylsulfonyl)imide ($BSI_{1,4}^-$) were synthesized by our research collaborators Prof. Sharon Lall-Ramnarine, *et al.*, as described in reference [1].

ILs with cationic oligoether chains N-(2-ethoxyethoxyethyl)-N-methyl pyrrolidinium ($Pyrr_{1,EOEOE}^+$), 1-(2-(2-ethoxyethoxy)ethyl)-3-methylimidazolium ($Im_{1,EOEOE}^+$), N-methyl-N-(2-(2-(2-methoxyethoxy)ethoxy)ethyl)pyrrolidinium ($Pyrr_{1,EOEOEOM}^+$), and 1-(2-(2-(2-methoxyethoxy)ethoxy)ethyl)-3-methylimidazolium ($Im_{1,EOEOEOM}^+$) paired with the NTf_2^- anion were also synthesized by Prof. Sharon Lall-Ramnarine, *et al.*, see reference [2].

2.2 Physical Property Measurements

The physical property measurements were carried out by our research collaborators Prof. Sharon Lall-Ramnarin, *et al.*, in the laboratory of Dr. James Wishart at Brookhaven National Laboratory, see references [1] and [2].

Water contents of the dried ionic liquid samples were measured using a Mettler Toledo DL39 coulometric Karl Fischer titrator and an analytical balance. The water contents of the samples used for the physical property measurements ranged from 48-214 ppm.

Shear viscosities were measured with a Cambridge Applied Systems ViscoLab 4100 electromagnetic reciprocating piston viscometer that was temperature regulated to ± 0.1 K by a Lauda RM-6 recirculating water bath. Viscosities for each of the ILs were recorded at intervals between 9 and 90 °C in ascending and descending order within their liquid ranges.

Heat capacities as a function of T were measured using a TA Instruments Q100 Differential Scanning Calorimeter (DSC) to determine melting points and glass transition onset temperatures (T_g). Scan rates were 5 °C/min. A minimum of three scans were recorded. The data were analyzed using TA Universal Analysis 2000 software.

Ionic conductivities were determined using a Yellow Springs Instruments (YSI) 3200 conductivity meter using a YSI 3253 probe that was temperature regulated by a Lauda RM-6 recirculating water bath and housed in a moisture controlled dry box. 1 M aqueous KCl was used as the reference solution.

2.3 High-energy X-ray Scattering Experiments

High-energy X-ray scattering experiments were performed at the Advanced Photon Sources (APS) beamline 11-ID-B for pair distribution function analysis. The X-ray beam wavelength was set to 0.2114 Å or a photon energy of 58.66 keV. The sample-to-detector distance was calibrated from the powder diffraction pattern of CeO₂, and ranged from 18-26 cm, which corresponds to a range of scattering vectors q between

0.2 to 20 \AA^{-1} . The 2-D X-ray scattering pattern was recorded at 25 °C using a Perkin-Elmer amorphous silicon 2D area detector. The Fit2D software package was used to integrate the raw data to obtain X-ray intensities $I(q)$ vs. q .⁽³⁾ Structure functions $S(q)$ were calculated from $I(q)$ using PDFgetX2 software.⁽⁴⁾

The prepared ionic liquid samples used in the X-ray experiments were dried under vacuum at 2×10^{-2} mbar for 48 hours at ambient temperature, then immediately transferred to a glovebox under argon atmosphere. The oxygen and water concentration in the glovebox were below 0.1 ppm and 0.4 ppm, respectively. While in the glovebox, the samples were loaded into 3 mm NMR tubes (Sigma-Aldrich) that were temporarily sealed with beeswax. Subsequently the sample tubes were flame-sealed after removal from the glovebox.

For the $\text{P}_{6,6,14}^+/\text{NTf}_2^-$ - 1-octanol mixtures, the samples were flame sealed in 2 mm quartz capillaries and used for the high-energy X-ray scattering (XRS) experiments directly. The experiments were performed at the Advanced Photon Sources (APS) beamline 11-ID-B for pair distribution function analysis. The X-ray beam wavelength was again set to 0.2114 \AA , corresponding to a photon energy of 58.66 keV. The sample-to-detector distance is calibrated using CeO_2 and calculated to be 22.7 cm. Fit2D ⁽³⁾ and PDFgetX2 ⁽⁴⁾ softwares are used to transform the raw data into total structure factors $S(q)$ vs. q .

2.4 Diffusivities from PG-SE NMR

Self-diffusion coefficients for the anions and cations were measured using pulsed gradient spin-echo (PG-SE) NMR methods. NMR samples were prepared from ionic liquids dried for 48 h on a Schlenk vacuum line, and prepared in an argon glovebox with water and oxygen levels below 0.1 and 0.4 ppm, respectively. Samples were prepared in 3 mm O.D. NMR tubes, capped in the glovebox, and flame-sealed immediately after removal from the glovebox. The 3mm NMR tubes were placed in another 5 mm diameter NMR tube, which was filled with D_2O for gradient shimming. The Diffusion-ordered bipolar pulse pair stimulated echo (DBPPSTE) pulse sequence was used.⁽⁵⁾ A Doty Scientific (model

16-38) diffusion probe was installed on the 400 MHz Varian DirectDrive spectrometer for the PG-SE NMR measurements. PG-SE intensities were measured as a function of the field gradient field strength g , which was varied from 5 to 350 G/cm. The self-diffusion coefficient D is obtained by fitting the spin echo intensities to the following equation:

$$I_g = I_0 e^{-D\gamma^2 g^2 \delta^2 (\Delta - \delta/3)} \quad (2.1)$$

where I_g is the intensity of the signal, I_0 the intensity of the signal at $g=0$, γ is the gyromagnetic constant, δ is the duration of the gradient pulse (s), Δ is diffusion delay (s), and D is the diffusion coefficient.

The magnetic field gradient was calibrated using a standard D_2O sample, from which the diffusion of D_2O was calibrated to be $1.9 \times 10^{-9} \text{ m}^2/\text{s}$ at 298 K.(6) In the measurement of diffusivities for $P_{6,6,6,14}^+/\text{NTf}_2^-$ and 1-octanol mixtures, the diffusivities of the $P_{6,6,6,14}^+$ cation and 1-octanol were measured using ^1H signal, and that of NTf_2^- anion was measured using ^{19}F signal. The temperature was set to 298 K, 308 K and 318K. In the measurement of diffusivities for ILs with the four cations ($\text{Im}_{2,1}^+$, $\text{Im}_{1,8}^+$, $\text{Pyrr}_{1,8}^+$, and $P_{6,6,6,14}^+$) paired with $\text{BSI}_{1,4}^-$ anion, anionic diffusivities were measured from ^{19}F NMR signals, and cationic diffusivities and 1-octanol diffusivities were obtained from ^1H signals. The measurements were done at temperatures: 280 K, 285 K, 298 K, 308 K, 318 K, 328 K, 338 K, and 348 K. PG-SE experiments had temperature uncertainties of ± 1 K. Sample temperatures were re-equilibrated for at least 10 min after each temperature change. Additional details of our NMR diffusion protocols have been described previously in detail.(7-9)

2.5 Molecular Dynamics (MD) Simulations of ILs

The total structure functions $S(q)$ can be obtained by both high energy X-ray scattering experiments and molecular dynamics (MD) simulations. The accuracy of the simulated $S(q)$ can be verified by the experimental results. Though total $S(q)$ can tell us the averaged structure of all components in ILs, it is important to understand the internal

structural organization in ILs. MD simulations allow us to analyze the structure of ILs on an atomic level. For example, repetitive patterns of organization in real space result in interfering structural correlations that selective theoretical partitioning schemes of the total liquid structure function $S(q)$ can help reveal.

2.5.1 Simulations of Bulk IL Structure

Molecular dynamics simulations were performed using the GROMACS package (version 2016.1).(10; 11) CL&P force fields were used for topology parameters to obtain the best match with structural data. The CL&P transferable force field for ILs reported by Canongia Lopes and Pádua,(12–15) in itself a generalization of Jorgensen’s Optimized Potentials for Liquid Simulations, All-Atom (OPLS-AA) force field,(16) has provided very good predictive capability for the structural properties of ILs.(17–22)

In this work, the initial structures of cations and anions were optimized at the HF/6-31G(d,p) level of theory using the Gaussian16 electronic structure package.(23) Each simulation box was packed with 1,000 ion pairs using Packmol(24). The following protocol was used to equilibrate all periodically replicated simulation boxes. All equilibrations were carried out using the NPT ensemble.(25–27) After energy minimization, the box was equilibrated for 50 ps while the charges of all atoms were scaled to 10% of full values at 298 K and 1 bar. The temperature and pressure were controlled using the Berendsen pressure and temperature coupling schemes.(11) The system was then equilibrated for another 200 ps using the V-rescale temperature coupling method at 298 K and the Berendsen pressure coupling method at 1 bar.(11) Next the charges were scaled to 50% of full values and the box was equilibrated for 500 ps without changing any settings. Finally with full charges the system was equilibrated using the V-rescale temperature coupling(11) and the Berendsen pressure coupling at 298 K and 1 bar for 2 ns. A simulated annealing protocol was used next where T was controlled by the Nosé-Hoover thermostat(25; 26) and pressure was regulated with the Parrinello-Rahman barostat(27). The system was heated from 298 to 598 K over 500 ps, and stayed at 598 K for 2 ns. After this, the temperature was decreased from 598 K to 298 K over 5 ns. The annealed simulation boxes were equilibrated at 1 bar and 298 K for

another 10 ns, using the Nosé-Hoover thermostat(25; 26) and the Parrinello-Rahman barostat.(27) The final production runs were carried out at 298 K and 1 bar for 2 ns with coordinates saved every 1 ps. During the equilibration and final production runs, the Verlet leap-frog algorithm was used to integrate the equations of motion with a time step of 1 fs using the default Verlet cutoff scheme in GROMACS(10; 28) with neighboring list radii and cutoffs for Coulomb and Lennard-Jones interactions all set to 1.5 nm. Long range electrostatic potentials were calculated using the Particle Mesh Ewald (PME) summation method(29; 30) with an interpolation order of 6 and a FFT grid spacing of 0.08 nm in a 3D periodic geometry.

2.5.2 Static Liquid Structure Function $S(q)$ From MD Simulations

The radial distribution functions $g(r)$ between all atom pairs were calculated from the trajectory of the production run over 2 ns with 200 frames. The structure function $S(q)$ is then calculated using Eqn 2.2: (18; 21; 31)

$$S(q) = \frac{\rho_0 \sum_i \sum_j x_i x_j f_i(q) f_j(q) \int_0^\infty 4\pi r^2 (g_{ij}(r) - 1) \frac{\sin(qr)}{qr} W(r) dr}{[\sum_i x_i f_i(q)]^2} \quad (2.2)$$

where ρ_0 is the total number density of the box, $g_{ij}(r)$ is the partial radial distribution function (RDF) between atom type i and atom type j , respectively. Specifically, the indices i and j span the set of the constituent atoms that include C, O, N, H, S, and F. x_i and x_j are the fractions of atoms of type i and j , $f_i(q)$ and $f_j(q)$ are the x ray atomic form factors (32–34), and $W(r) = \sin(2\pi r/L)/(2\pi r/L)$ is a Lorch-type function and L is the smallest box length, introduced to reduce the effect of finite truncation of r .(18; 19; 21; 22; 35–37)

To interpret the experimental structure functions, it is useful to deconstruct the calculated $S(q)$ obtained from molecular simulations.(18; 38; 39) One can select from several useful ways to partition $S(q)$. Ionic partitioning of $S(q)$ is achieved by grouping sets of molecular ions as anion-anion, anion-cation and cation-cation contributions as described by Santos, *et al.*:(18)

$$S(q) = S_{a-a}(q) + S_{c-a}(q) + S_{a-c}(q) + S_{c-c}(q) \quad (2.3)$$

A sub-ionic partitioning of $S(q)$ results in more detailed information. (22) In this case one can split contributions to $S(q)$ from the cations into head and tail, and those for the anions into anion head and fluoruous alkyl tail. The equation for sub-ionic partitioning is as follows:

$$\begin{aligned} S(q) = & S_{h^+,h^+}(q) + S_{h^+,t}(q) + S_{t,t}(q) + S_{h^+,h^-}(q) + S_{h^+,f}(q) \\ & + S_{t,h^-}(q) + S_{t,f}(q) + S_{h^-,h^-}(q) + S_{h^-,f}(q) + S_{f,f}(q) \end{aligned} \quad (2.4)$$

where h^+ indicates the cationic head group, t denotes the cationic alkyl tail, h^- denotes the anionic head group, and f denotes the anionic perfluoroalkyl tail. In Eq. 2.4, note that while the self-terms $S_{ii}(q)$ are unique, the cross-terms $S_{ij}(q)$ are symmetric. We have summed each of the symmetric cross-terms to shorten Eq. (3) from 16 to 10 terms.

2.5.3 MD Simulations of the Vacuum-IL Interface

The vacuum-IL simulations followed the protocol provided by Amith, *et al.*(40) Since our bulk structure analysis was carried out at 298 K, we first increased the system temperature from 298 to 425 K under NPT ensemble using an annealing process: the temperature was increased from 298 to 500 K over 1 ns and stayed at 500 K for 1 ns; then the temperature was decreased from 500 to 425 K over 1 ns and stayed at 425 K for another 3 ns. The well-equilibrated simulation box was further extended in the NVT ensemble using Nosé-Hoover thermostat(25; 26) for 5 ns prior to introducing the vacuum interfaces. For the IL in the slab configuration, electrostatic interactions were computed by using the PME Ewald summations together with the Yeh-Berkowitz correction (EW3DC).(41) The last configuration was then placed at the center of a tetragonal supercell of dimensions l nm x l nm x $4l$ nm (l is the length of the box from bulk simulation), which is reported as relevant to the successful application of EW3DC.(41; 42) An 8 ns simulated annealing protocol was carried out to initially equilibrate the slab configuration. The slab was heated to 725 K over 500 ps, and

stayed at 725 K for 2 ns. Then the temperature was decreased to 425 K over 5 ns and stayed at 425 K for another 500 ps. After this, the system was thoroughly equilibrated for 116 ns at 425 K in the NVT ensemble. The final 16 ns was used for analysis of the liquid-vacuum structures.

Bibliography

- [1] M. Zhao, B. Wu, S. I. Lall-Ramnarine, J. D. Ramdihal, K. A. Papacostas, E. D. Fernandez, R. A. Sumner, C. J. Margulis, J. F. Wishart, and E. W. Castner. “Structural analysis of ionic liquids with symmetric and asymmetric fluorinated anions.” *J. Chem. Phys.*, 151, 074504, 2019. doi:10.1063/1.5111643.
- [2] S. I. Lall-Ramnarine, M. Zhao, C. Rodriguez, R. Fernandez, N. Zmich, E. D. Fernandez, S. B. Dhiman, E. W. Castner, Jr., and J. F. Wishart. “Connecting structural and transport properties of ionic liquids with cationic oligoether chains.” *J. Electrochem. Soc.*, 164, H5247–H5262, 2017. doi:10.1149/2.0371708jes.
- [3] A. Hammersley, S. Svensson, M. Hanfland, A. Fitch, and D. Hausermann. “Two-dimensional detector software: From real detector to idealised image or two-theta scan.” *High Pressure Res.*, 14, 235–248, 1996. doi:10.1080/08957959608201408.
- [4] X. Qiu, J. W. Thompson, and S. J. L. Billinge. “PDFgetX2: a GUI-driven program to obtain the pair distribution function from X-ray powder diffraction data.” *J. Appl. Cryst.*, 37, 678, 2004. doi:10.1107/S0021889804011744.
- [5] D. Wu, A. Chen, and C. Johnson. “An Improved Diffusion-Ordered Spectroscopy Experiment Incorporating Bipolar-Gradient Pulses.” *J. Magn. Reson.*, A115, 260–264, 1995. doi:10.1006/jmra.1995.1176.
- [6] B. Antalek. “Using pulsed gradient spin echo nmr for chemical mixture analysis: How to obtain optimum results.” *Concepts. Magn. Reson.*, 14, 225–258, 2002. doi:10.1002/cmr.10026.

- [7] M. Liang, S. Khatun, and E. W. Castner, Jr. “Communication: Unusual Structure and Transport in Ionic Liquid-Hexane Mixtures.” *J. Chem. Phys.*, 142, 121101, 2015. doi:10.1063/1.4916388.
- [8] T. A. Fadeeva, P. Husson, J. A. DeVine, M. F. Costa Gomes, S. G. Greenbaum, and E. W. Castner, Jr. “Interactions Between Water and 1-butyl-1-methylpyrrolidinium Ionic Liquids.” *J. Chem. Phys.*, 143, 064503, 2015. doi:10.1063/1.4928065.
- [9] B. Wu, K. Kuroda, K. Takahashi, and E. W. Castner, Jr. “Structural analysis of zwitterionic liquids vs. homologous ionic liquids.” *J. Chem. Phys.*, 148, 193807, 2018. doi:10.1063/1.5010983.
- [10] M. J. Abraham, T. Murtola, R. Schulz, S. Páll, J. C. Smith, B. Hess, and E. Lindahl. “GROMACS: High performance molecular simulations through multi-level parallelism from laptops to supercomputers.” *SoftwareX*, 1-2, 19–25, 2015. doi:10.1016/j.softx.2015.06.001.
- [11] H. J. C. Berendsen, D. van der Spoel, and R. van Drunen. “GROMACS: A message-passing parallel molecular dynamics implementation.” *Comp. Phys. Comm.*, 91, 43–56, 1995. doi:10.1016/0010-4655(95)00042-E.
- [12] J. N. Canongia Lopes, J. Deschamps, and A. A. H. Pádua. “Modeling Ionic Liquids Using a Systematic All-Atom Force Field.” *J. Phys. Chem. B*, 108, 2038–2047, 2004. doi:10.1021/jp0362133.
- [13] J. N. Canongia Lopes and A. A. H. Pádua. “Molecular Force Field for Ionic Liquids Composed of Triflate or Bistriflylimide Anions.” *J. Phys. Chem. B*, 108, 16893–16898, 2004. doi:10.1021/jp0476545.
- [14] J. N. Canongia Lopes and A. A. H. Padua. “Molecular Force Field for Ionic Liquids III: Imidazolium, Pyridinium, and Phosphonium Cations; Chloride, Bromide, and Dicyanamide Anions.” *J. Phys. Chem. B*, 110, 19586–19592, 2006. doi:10.1021/jp063901o.

- [15] J. N. Canongia Lopes and A. A. H. Pádua. “CL&P: A generic and systematic force field for ionic liquids modeling.” *Theor. Chem. Acc.*, 131, 1129, 2012. doi: 10.1007/s00214-012-1129-7.
- [16] R. C. Rizzo and W. L. Jorgensen. “OPLS All-Atom Model for Amines: Resolution of the Amine Hydration Problem.” *J. Am. Chem Soc.*, 121, 4827–4836, 1999.
- [17] J. C. Araque, J. J. Hettige, and C. J. Margulis. “Modern Room Temperature Ionic Liquids, a Simple Guide to Understanding Their Structure and How It May Relate to Dynamics.” *J. Phys. Chem. B*, 119, 12727–12740, 2015. doi: 10.1021/acs.jpcc.5b05506.
- [18] C. S. Santos, H. V. R. Annapureddy, N. S. Murthy, H. K. Kashyap, E. W. Castner, Jr., and C. J. Margulis. “Temperature-dependent structure of methyltributylammonium bis(trifluoromethylsulfonyl)amide: X ray scattering and simulations.” *J. Chem. Phys.*, 134, 064517, 2011. doi:10.1063/1.3526958.
- [19] H. K. Kashyap, C. S. Santos, H. V. R. Annapureddy, N. S. Murthy, C. J. Margulis, and E. W. Castner, Jr. “Temperature-Dependent Structure of Ionic Liquids: X-ray Scattering and Simulations.” *Faraday Discuss.*, 154, 133–143, 2012. doi: 10.1039/C1FD00059D.
- [20] H. K. Kashyap, J. J. Hettige, H. V. R. Annapureddy, and C. J. Margulis. “SAXS anti-peaks reveal the length-scales of dual positive-negative and polar-apolar ordering in room-temperature ionic liquids.” *Chem. Commun.*, 48, 5103–5105, 2012. doi:10.1039/C2CC30609C.
- [21] H. K. Kashyap, C. S. Santos, R. P. Daly, J. J. Hettige, N. S. Murthy, H. Shirota, E. W. Castner, Jr., and C. J. Margulis. “How Does the Ionic Liquid Organizational Landscape Change when Nonpolar Cationic Alkyl Groups Are Replaced by Polar Isoelectronic Diethers?” *J. Phys. Chem. B*, 117, 1130–1135, 2013. doi: 10.1021/jp311032p.

- [22] H. K. Kashyap, C. S. Santos, N. S. Murthy, J. J. Hettige, K. Kerr, S. Ramati, J. Gwon, M. Gohdo, S. I. Lall-Ramnarine, J. F. Wishart, C. J. Margulis, and E. W. Castner, Jr. “Structure of 1-Alkyl-1-methylpyrrolidinium Bis(trifluoromethylsulfonyl)amide Ionic Liquids with Linear, Branched, and Cyclic Alkyl Groups.” *J. Phys. Chem. B*, 117, 15328–15337, 2013. doi:10.1021/jp403518j.
- [23] M. J. Frisch, G. W. Trucks, H. B. Schlegel, and et al., Gaussian 16, Revision B.01, Gaussian, Inc., Wallingford, CT, 2016.
- [24] L. Martinez, R. Andrade, E. G. Birgin, and J. M. Martinez. “Packmol: A package for building initial configurations for molecular dynamics simulations.” *J. Comput. Chem.*, 30, 2157–2164, 2009. doi:10.1002/jcc.21224.
- [25] S. Nosé. “A unified formulation of the constant temperature molecular dynamics methods.” *J. Chem. Phys.*, 81, 511–519, 1984. doi:10.1063/1.447334.
- [26] S. Nosé. “A molecular dynamics method for simulations in the canonical ensemble.” *Mol. Phys.*, 52, 255–268, 1984. doi:10.1080/00268978400101201.
- [27] M. Parrinello and A. Rahman. “Polymorphic transitions in single crystals: A new molecular dynamics method.” *J. Appl. Phys.*, 52, 7182–7190, 1981. doi:10.1063/1.328693.
- [28] S. Pronk, S. Pall, R. Schulz, P. Larsson, P. Bjelkmar, R. Apostolov, M. R. Shirts, J. C. Smith, P. M. Kasson, D. van der Spoel, B. Hess, and E. Lindahl. “GROMACS 4.5: a high- throughput and highly parallel open source molecular simulation toolkit.” *Bioinformatics*, 29, 845–854, 2013.
- [29] T. Darden, D. York, and L. Pedersen. “Particle mesh Ewald: An $N \cdot \log(N)$ method for Ewald sums in large systems.” *J. Chem. Phys.*, 98, 10089–10092, 1993. doi:10.1063/1.464397.
- [30] U. Essmann, L. Perera, M. L. Berkowitz, T. Darden, H. Lee, and L. G. Pedersen. “A smooth particle mesh Ewald method.” *J. Chem. Phys.*, 103, 8577–8593, 1995. doi:10.1063/1.470117.

- [31] E. W. Castner, Jr., C. J. Margulis, M. Maroncelli, and J. F. Wishart. “Ionic Liquids: Structure and Photochemical Reactions.” *Annu. Rev. Phys. Chem.*, 62, 85–105, 2011. doi:10.1146/annurev-physchem-032210-103421.
- [32] P. A. Doyle and P. S. Turner. “Relativistic Hartree-Fock X-ray and Electron Scattering Factors.” *Acta Cryst.*, A24, 390–397, 1968. doi:10.1107/S0567739468000756.
- [33] D. T. Cromer and J. B. Mann. “X-ray scattering factors computed from numerical Hartree-Fock wave functions.” *Acta Cryst.*, A24, 321–324, 1968. doi:10.1107/S0567739468000550.
- [34] E. Prince. *International Tables for Crystallography : Volume C: Mathematical, Physical and Chemical Tables, Third Edition*. 2004.
- [35] E. Lorch. “Neutron Diffraction by Germania, Silica and Radiation-damaged Silica Glasses.” *J. Phys. C: Solid State Phys.*, 2, 229–237, 1969. doi:10.1088/0022-3719/2/2/305.
- [36] J. Du, C. J. Benmore, R. Corrales, R. T. Hart, and J. K. R. Weber. “A molecular dynamics simulation interpretation of neutron and x-ray diffraction measurements on single phase Y_2O_3 - Al_2O_3 glasses.” *J. Phys.: Condens. Matter*, 21, 205102, 2009. doi:10.1088/0953-8984/21/20/205102.
- [37] K. B. Dhungana, L. F. O. Faria, B. Wu, M. Liang, M. C. C. Ribeiro, C. J. Margulis, and E. W. Castner, Jr. “Structure of cyano-anion ionic liquids: X-ray scattering and simulations.” *J. Chem. Phys.*, 145, 024503, 2016. doi:10.1063/1.4955186.
- [38] J. L. Lebowitz. “Exact Solution of Generalized Percus-Yevick Equation for a Mixture of Hard Spheres.” *Phys. Rev.*, 133, A895–A899, 1964. doi:10.1103/PhysRev.133.A895.
- [39] N. W. Ashcroft and D. C. Langreth. “Structure of Binary Liquid Mixtures. I.” *Phys. Rev.*, 156, 685–692, 1967. doi:10.1103/PhysRev.156.685.
- [40] W. D. Amith, J. J. Hettige, E. W. Castner, Jr., and C. J. Margulis. “Structures of Ionic Liquids Having Both Anionic and Cationic Octyl Tails: Lamellar Vacuum

Interface vs Sponge-Like Bulk Order.” *J. Phys. Chem. Lett.*, 7, 3785–3790, 2016. doi:10.1021/acs.jpcllett.6b01763.

- [41] I.-C. Yeh and M. L. Berkowitz. “Ewald summation for systems with slab geometry.” *J. Chem. Phys.*, 111, 3155–3162, 1999. doi:10.1063/1.479595.
- [42] I.-C. Yeh and A. Wallqvist. “On the proper calculation of electrostatic interactions in solid-supported bilayer systems.” *J. Chem. Phys.*, 134, 055109, 2011. doi:10.1063/1.3548836.

Chapter 3

Bulk Structure of Ionic Liquids

Ionic liquids are salts in the liquid state. ILs are often composed of large and flexible cations and anions, which not only delocalizes the charges and lowers the Coulombic attraction among the ions, but also prevents the ions from close packing. Therefore, they can remain in the liquid state even below room temperature. The structures of ILs are well known. IL systems are heterogeneous with a polar network composed of cationic and anionic heads, and typically have a nonpolar network composed of alkyl tails. The bulk structure of ILs can easily be modified by the changing of the ionic liquid molecular structure. If both the cations and anions are smaller, as for the IL $\text{Im}_{2,1}^+/\text{FSI}^-$, the systems predominantly comprise a polar network. When the cations or anions contain longer alkyl tails, like $\text{Im}_{2,1}^+/\text{BSI}_{1,4}^-$ or $\text{Im}_{1,8}^+/\text{FSI}^-$, then nonpolar domains can be formed by the tails. If the alkyl tails are more polar and flexible, like oligoether tails, then nonpolar domains can still be formed but with less structural definition than the alkylated analogues. In this chapter, we discuss the study of the bulk structure for three kinds of ILs: ILs with fluorinated anions paired with aromatic alkyl imidazolium cations; the same fluorinated anions with non-aromatic cations; and ILs with cationic oligoether tails paired with the NTf_2^- anion.

3.1 Structural analysis of ILs with symmetric and asymmetric fluorinated-anion ionic liquids: imidazolium cations

The structures of ILs with imidazolium cations paired with NTf_2^- have been well studied. Russina, *et al.* studied the nanoscale segregation of 1-alkyl-3-methylimidazolium bis(trifluoromethylsulfonyl)imide ($\text{Im}_{1,n}^+/\text{NTf}_2^-$) ILs.(1) They found that the nanoscale structural aggregation only occurred for $n \geq 5$ based on the X-ray scattering data.

The first sharp diffraction peaks (FSDPs) in $S(q)$ also shifted to lower q value as the length of the alkyl chain increased, indicating a growth of the domain sizes. Xiao, *et al.* studied the effect of cation symmetry and alkyl chain length on the structure of 1,3-dialkylimidazolium bis(trifluoromethylsulfonyl)imide ($\text{Im}_{n,n}^+/\text{NTf}_2^-$) ILs.(2) The X-ray scattering data showed that the FSDPs were observable only for $n \geq 5$, despite the fact that the $\text{Im}_{n,n}^+$ cations have twice the length of alkylated tails on the $\text{Im}_{1,n}^+$ cations.

Having gained so much insight on ILs with imidazolium cations, we can now focus on the study of the fluorinated bis(perfluoroalkanesulfonyl)imide (BSI) anions. In this section, the following ILs are studied: 1-ethyl-3-methylimidazolium ($\text{Im}_{2,1}^+$) or 1-octyl-3-methylimidazolium ($\text{Im}_{1,8}^+$) cations paired with fluorinated anions bis(fluorosulfonyl)imide (FSI^-), (fluorosulfonyl)(trifluoromethylsulfonyl)imide ($\text{BSI}_{0,1}^-$), bis(trifluoromethylsulfonyl)imide (NTf_2^-), bis(perfluoroethylsulfonyl)imide (BETI^-), and (trifluoromethylsulfonyl)(perfluorobutylsulfonyl)imide ($\text{BSI}_{1,4}^-$). The molecular structures of these ions are presented in Figure 3.1.

ILs with these fluorinated BSI anions have good thermal stability, wide electrochemical windows, low viscosities and high conductivities.(3; 4) Apart from the symmetric FSI^- , NTf_2^- , and BETI^- anions, we also want to explore the consequences of asymmetric anions $\text{BSI}_{0,1}^-$ and $\text{BSI}_{1,4}^-$ on IL structural and physical properties. To study the effect on structure of fluorinated anions, $\text{Im}_{2,1}^+$ is a good cation since it is small and should not interfere with non-polar domain aggregation if there is any.(5) $\text{Im}_{1,8}^+$ is selected to probe the effects of polar, aliphatic and fluorous interactions on IL structure and domain formation. For a deeper understanding of the interaction between alkyl and fluorous tails, We extended our study by simulating three additional anions in the same series with longer fluorinated tails: (trifluoromethylsulfonyl)(perfluoropropylsulfonyl)imide ($\text{BSI}_{1,3}^-$), (trifluoromethylsulfonyl)(perfluoropentylsulfonyl)imide ($\text{BSI}_{1,5}^-$), and (trifluoromethylsulfonyl)(perfluoroheptylsulfonyl)imide ($\text{BSI}_{1,7}^-$).

The following sections 3.1.1 to 3.1.6 are adapted from the article published by Zhao, *et al.*,(6) used with the permission of AIP Publishing.

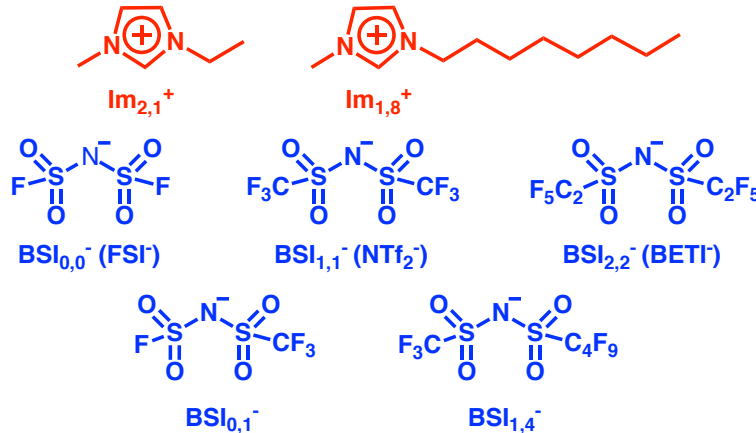


Figure 3.1: Chemical structures of the cations (red) and anions (blue) used for X-ray scattering, viscosity, conductivity and thermochemical experiments. Figure was published by Zhao, *et al.*,⁽⁶⁾ used with the permission of AIP Publishing.

3.1.1 Physical properties

The physical properties, including densities, viscosities, glass transition temperatures, melting points and conductivities of the ILs, are listed in Table 3.1. The data was measured by our collaborators Prof. Sharon Lall-Ramnarine, *et al.*⁽⁶⁾ For the same cation, the ionic liquid density increases as the anion size increases. For the same anion, The ionic liquid density decreases as the cation size increases. The glass transition temperatures (T_g) generally increase with anion size in both cation families. The T_g values in Table 3.1 for $\text{Im}_{2,1}^+/\text{BSI}_{1,4}^-$ and $\text{Im}_{1,8}^+/\text{BSI}_{1,4}^-$ are 190 and 193 K, respectively. The T_g values were measured by DSC with a scan rate of 5 K/min. They are consistent with the $T_{g,\text{diel}}$ values of 187 and 190 K obtained from dielectric spectroscopy by Lo Celso, *et al.* ⁽⁷⁾

The viscosities at 298 K for the $\text{Im}_{2,1}^+$ salts are each lower than the corresponding one for the $\text{Im}_{1,8}^+$ cation paired with the same anion, and among both cation series the viscosities increase as the anion gets larger.

$$\ln(\eta_T) = \ln(\eta_0) + D/((T/T_0) - 1) \quad (3.1)$$

Table 3.1: Physical properties of ionic liquids measured at 298 K. Data was published by Zhao, *et al.*,⁽⁶⁾ used with the permission of AIP Publishing.

IL	Exp. Density (g/cm ⁻³)	Sim. Density (g/cm ⁻³)	Viscosity ^a (cP)	T _g ^b (K)	Melting Pt. ^b (K)	Conductivity (mS/cm)
Im _{2,1} ⁺ /FSI ⁻	1.39	1.53	19	c	254	15
Im _{2,1} ⁺ /BSI _{0,1} ⁻	1.46	1.56	23	166	241 ^d	16.9
Im _{2,1} ⁺ /NTf ₂ ⁻	1.52 (8)	1.60	33	186 (9)	255 (9)	9.2 (8)
Im _{2,1} ⁺ /BETI ⁻	1.52	1.67	81	188	268 ^d	3.1
Im _{2,1} ⁺ /BSI _{1,4} ⁻	1.59	1.70	114	190	c	2.3
Im _{1,8} ⁺ /FSI ⁻	1.18	1.30	66	179	271 ^d	2.5
Im _{1,8} ⁺ /BSI _{0,1} ⁻	1.25	1.34	69	176	243 ^d	2.0
Im _{1,8} ⁺ /NTf ₂ ⁻	1.28 @ 22 °C (10)	1.39	93	187 (10)	250 (11)	1.41 (10)
Im _{1,8} ⁺ /BETI ⁻		1.46	180	191	c	0.34
Im _{1,8} ⁺ /BSI _{1,4} ⁻		1.37	222	193	c	0.39

^aCalculated from the VFT parameters in this table according to Eqn. 3.1; ^bOnset temperature; ^cnot observed;

^dMelting after cold crystallization.

3.1.2 The structure of Im_{2,1}⁺ salts

The liquid structure functions for ILs with the Im_{2,1}⁺ cation from high-energy X-ray scattering experiments and MD simulations are shown in Figure 3.2. The simulated $S(q)$ functions are in good agreement with the measured ones.

From empirical observations of the experimental and simulated $S(q)$ in Figure 3.2, we see that the adjacency peak, which appears around $q \sim 1.4 \text{ \AA}^{-1}$, shifts to a smaller q when the anion size increases. The charge correlation peak, which is near $q \sim 0.8 \text{ \AA}^{-1}$, appears as a shoulder in Im_{2,1}⁺/FSI⁻, while it is clearly apparent in the other four Im_{2,1}⁺ ILs. No FSDPs are observed in the total structure functions $S(q)$ of these Im_{2,1}⁺ ILs; this is to be expected for systems where neither the cationic nor the anionic tails are sufficiently large.^(1; 5; 12) However, this does not mean that partitions of $S(q)$ will not show intermediate range order.

The ionic partitioning of $S(q)$ for the Im_{2,1}⁺ ILs as defined by Eqn. 2.3 is shown in Figure 3.3, with q displayed up to 2 \AA^{-1} . Figure 3.3 shows that the charge correlation intensities are large when compared to the adjacency peaks, but the charge correlation intensities are diminished in Figure 3.2 due to peak and anti-peak cancellations.⁽¹³⁾ As the anion size increases, the charge correlation interactions shift to smaller q values and smaller amplitudes. A smaller q value indicates a larger distance, which follows the trend of increasing anion size.

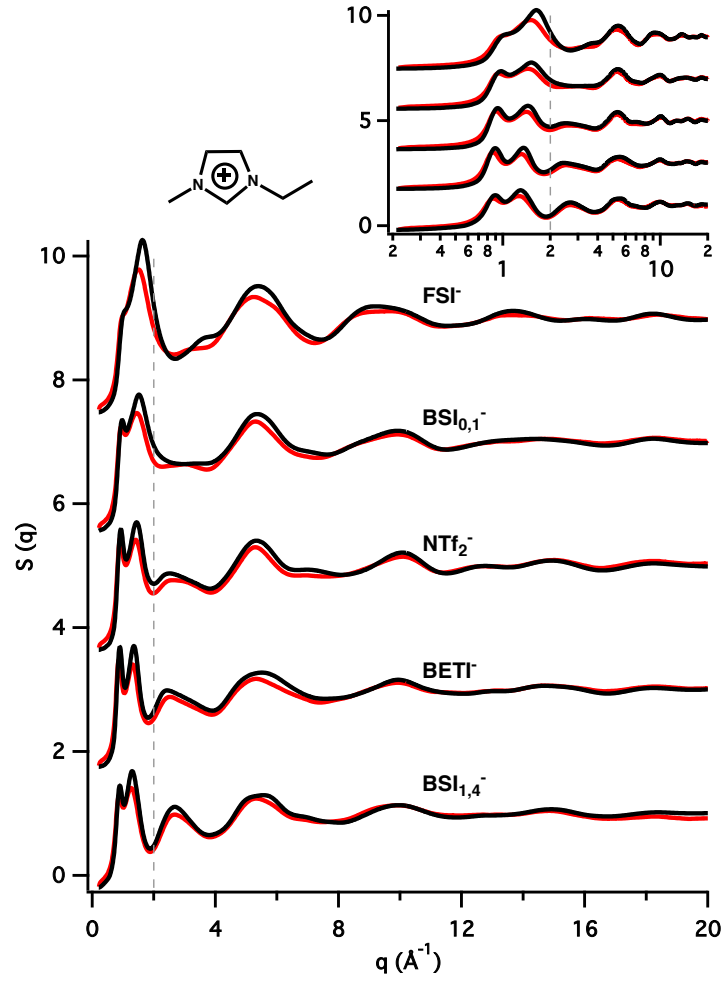


Figure 3.2: The experimental (red) and simulated (black) structure functions $S(q)$ for ILs with the $\text{Im}_{2,1}^+$ cation and five BSI anions. The dashed vertical line at 2 \AA^{-1} is the approximate boundary between intermolecular ($q < 2 \text{ \AA}^{-1}$) and intramolecular ($q > 2 \text{ \AA}^{-1}$) interactions. In the inset, a logarithmic x-axis is used to emphasize the intermolecular part of $S(q)$. Figure was published by Zhao, *et al.*,⁽⁶⁾ used with the permission of AIP Publishing.

As with the nonpolar domains formed by alkyl tails, fluorous domains can also give rise to FSDPs. (14–16) Russina, *et al.* (17) found a FSDP in the total $S(q)$ of $\text{Im}_{2,1}^+/\text{BSI}_{1,4}^-$ below 223 K by X-ray scattering. Lo Celso, *et al.* also found fluorous domains in ILs with symmetric bis(perfluoroalkylsulfonyl)imide anions paired with the diethylmethyl(2-methoxyethyl)ammonium (DEME^+) cation using neutron scattering methods, while X-ray cross sections did not provide enough contrast to reveal the existence of fluorous domains in the same ILs. (18) In a study by Shimizu, *et al.*, MD simulations were performed along the 1-alkyl-3-methylimidazolium perfluorobutylsulfonate homologous series ($\text{Im}_{m,1}^+/\text{C}_4\text{F}_9\text{SO}_3^-$, $2 \leq m \leq 12$). (19) All of the studied ILs displayed significant FSDPs in the total structure functions $S(q)$ at room temperature, including $\text{Im}_{2,1}^+/\text{C}_4\text{F}_9\text{SO}_3^-$.

Figure 3.3 shows broad low- q peaks and anti-peaks in the ionic subcomponents of $S(q)$ near 0.42 \AA^{-1} for $\text{Im}_{2,1}^+/\text{BSI}_{1,4}^-$ and 0.54 \AA^{-1} for $\text{Im}_{2,1}^+/\text{BETI}^-$, indicating the formation of intermediate range order on that scale. (The domain aggregation analysis discussed in a later section is consistent with this observation.) However, the FSDP is missing in the total $S(q)$ of these two ILs due to the completely interference of different ionic components. Since the ethyl group on the $\text{Im}_{2,1}^+$ cation is too short to permit the formation of significant non-polar domains, (5; 12) the peaks and anti-peaks predominantly arise from the segregation between the charge network and the anionic fluorous tails. A FSDP at a higher q value corresponds to a smaller domain size, which correlates with the shorter and symmetric perfluorinated tails of BETI^- relative to $\text{BSI}_{1,4}^-$.

To further investigate the aggregation of perfluorinated tails in bulk ILs, we carried out MD simulations on three ILs with perfluoroalkyl tails *in silico*, containing BSI anions with $n = 3$ ($\text{BSI}_{1,3}^-$), 5 ($\text{BSI}_{1,5}^-$) and 7 ($\text{BSI}_{1,7}^-$), paired with the $\text{Im}_{2,1}^+$ cation. The *in silico* results for the liquid structure functions $S(q)$ and the ionic partitioning of these $S(q)$ are shown in Figure 3.4, together with the molecular structures of these anions. Low-intensity FSDPs are observed in the total $S(q)$ for $\text{Im}_{2,1}^+/\text{BSI}_{1,5}^-$ and $\text{Im}_{2,1}^+/\text{BSI}_{1,7}^-$, which become more sharp and intense when analyzing the ionic partitions. Even in the case of the partitions for $\text{Im}_{2,1}^+/\text{BSI}_{1,3}^-$, we observe broad FSDPs

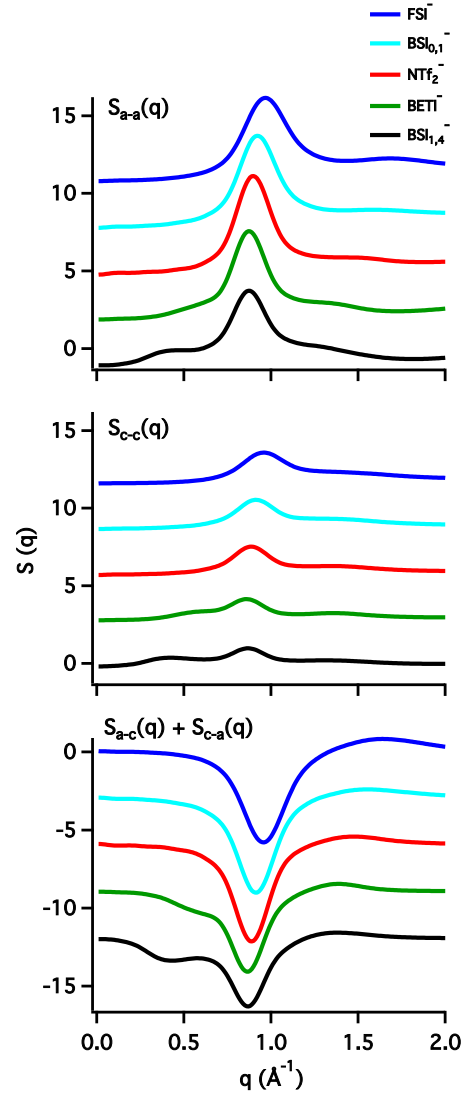


Figure 3.3: Ionic partitioning of $S(q)$ for the five BSI ILs with $\text{Im}_{2,1}^+$ cation. Top: anion-anion; center: cation-cation; bottom: anion-cation. From top to bottom, the curves represent the partial $S(q)$ for $\text{Im}_{2,1}^+$ with FSI^- (blue), $\text{BSI}_{0,1}^-$ (cyan), NTf_2^- (red), BETI^- (green), and $\text{BSI}_{1,4}^-$ (black). For clarity, an offset of 3 units is applied to each subsequent curve. Figure was published by Zhao, *et al.*,⁽⁶⁾ used with the permission of AIP Publishing.

in the low q region. These ionic partitioning peaks and anti-peaks are at $q = 0.50 \text{ \AA}^{-1}$ for $\text{Im}_{2,1}^+/\text{BSI}_{1,3}^-$, 0.37 \AA^{-1} for $\text{Im}_{2,1}^+/\text{BSI}_{1,5}^-$, and 0.30 \AA^{-1} for $\text{Im}_{2,1}^+/\text{BSI}_{1,7}^-$. Converting the q values for these FSDPs into apparent domain sizes results in good correlation with the length of perfluorinated alkyl tails, and the slope of L_{domain} vs. n is about $2.2 \text{ \AA}/\text{CF}_2$. For increased anion (or fluorous domain) sizes, this peak gets more intense and shifts to a lower q value.

For these $\text{Im}_{2,1}^+$ -cation ILs, snapshots of equilibrated periodic boxes from the end of the MD trajectories are shown in Figure 3.5. The boxes are visualized using the Visual Molecular Dynamics (VMD) program.⁽²⁰⁾ The three simulation snapshots in the left column of Figure 3.5 display green fragments distributed throughout the box, with no clear evidence of fluorous domains; the red and blue charged polar network appears to span the box. The simulation boxes for the $\text{Im}_{2,1}^+/\text{BETI}^-$ and $\text{Im}_{2,1}^+/\text{BSI}_{1,4}^-$ ILs are displayed in the middle column of Figure 3.5, and show nanoscale domains corresponding to the FSDPs observed in the ionic partitioning of $S(q)$ for $\text{Im}_{2,1}^+/\text{BETI}^-$ and $\text{Im}_{2,1}^+/\text{BSI}_{1,4}^-$. The three snapshots in the right column of Figure 3.5 are for the three ILs studied *in silico*. For $\text{Im}_{2,1}^+/\text{BSI}_{1,7}^-$, the fluorous domains occupy a relatively larger fraction of the total volume. Figure 3.5 shows that as the length of anionic perfluoroalkyl tail increases, the size of the fluorous green domain grows.

3.1.3 The structure of $\text{Im}_{1,8}^+$ salts

In the previous section, we showed that $\text{Im}_{2,1}^+/\text{BETI}^-$ and $\text{Im}_{2,1}^+/\text{BSI}_{1,4}^-$ have polar networks and nonpolar fluorous domains. This section details the structural effects of the cationic octyl tail on the ILs.

The total structure functions $S(q)$ for the five $\text{Im}_{1,8}^+$ ILs are shown in Figure 3.6. Except for $\text{Im}_{1,8}^+/\text{FSI}^-$ where agreement is only adequate, good agreement is observed between the X-ray experiment results and MD simulations. In Figure 3.6, FSDPs are observed for all five ILs in the q range from $0.3 - 0.35 \text{ \AA}^{-1}$. The charge-charge alternation peaks shift to lower q , with increasing amplitude, as the anion size increases from FSI^- to $\text{BSI}_{1,4}^-$. This charge-charge alternation peak for $\text{Im}_{1,8}^+/\text{FSI}^-$ appears as a shoulder next to the adjacency peak, as is also observed in $\text{Im}_{2,1}^+/\text{FSI}^-$. The adjacency peak

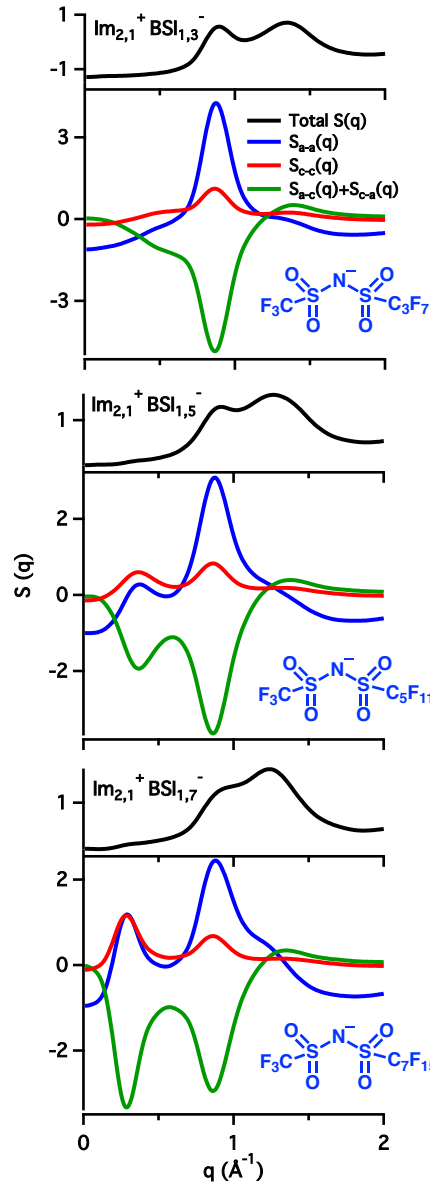


Figure 3.4: *In silico* ionic partitioning of the liquid structure function $S(q)$ from MD simulations of ILs having $\text{Im}_{2,1}^+$ cations paired with the fluorosulfonate anions $\text{BSI}_{1,3}^-$, $\text{BSI}_{1,5}^-$, and $\text{BSI}_{1,7}^-$. The anions are shown in the lower right in each of the three graphs above. The ionic partitioning of the total $S(q)$ (black curves) is shown as anion-anion (blue), cation-cation (red) and anion-cation/cation-anion (green) contributions. Figure was published by Zhao, *et al.*,⁽⁶⁾ used with the permission of AIP Publishing.

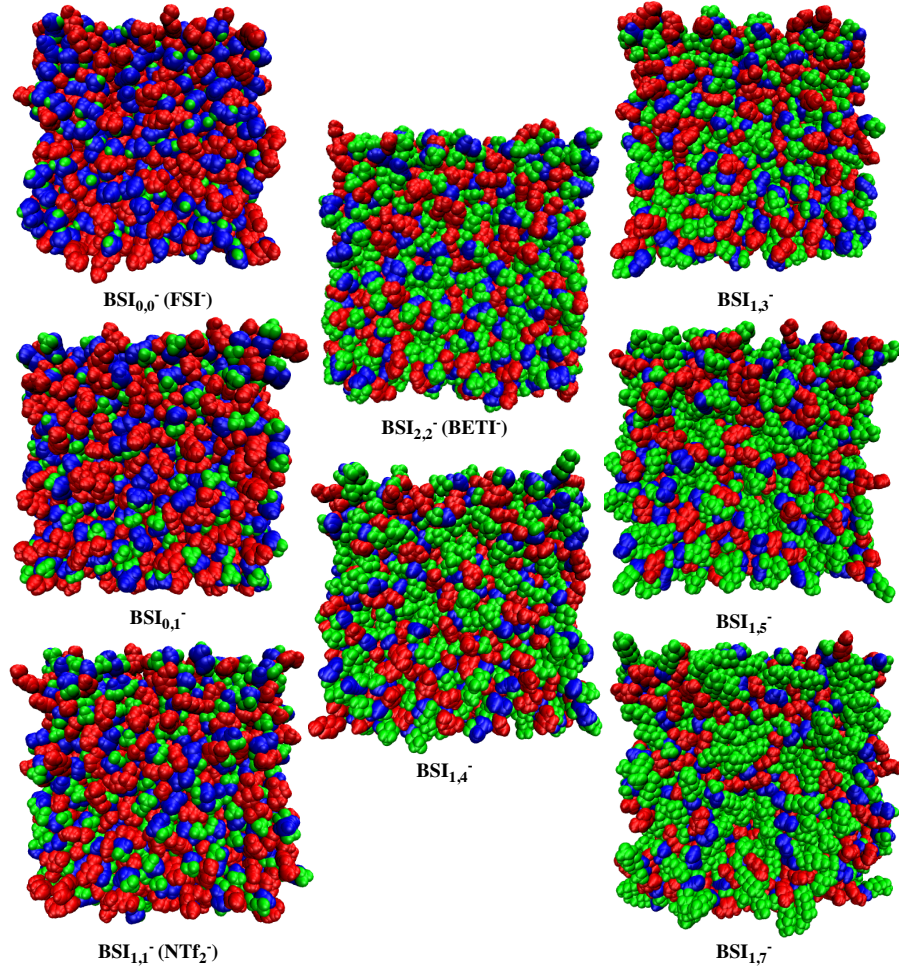


Figure 3.5: Snapshots from the equilibrated simulation boxes for ILs with $\text{Im}_{2,1}^+$ cations. The set of ILs that were investigated experimentally are shown in the left and center columns, while the *in-silico-only* set of ILs is shown in the right column. The color coding is red for the entire $\text{Im}_{2,1}^+$ cation, including the ethyl group; blue for the five central $\text{N}(\text{SO}_2)_2$ atoms on the anion; and green for all fluororous moieties, ranging from the F atoms on FSI $^-$ to the C_7F_{15} tails on BSI $_{1,7}^-$. Figure was published by Zhao, *et al.*,⁽⁶⁾ used with the permission of AIP Publishing.

($q \approx 1.5 \text{ \AA}^{-1}$) also shifts to lower q values, but the peak amplitude decreases as the anion size increases.

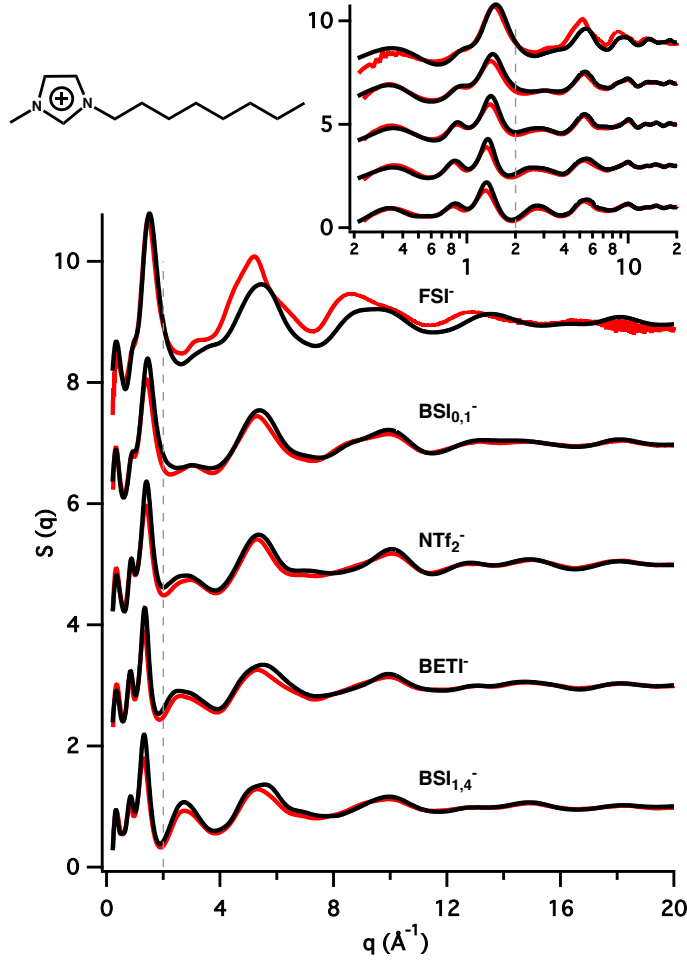


Figure 3.6: The experimental (red) and simulated (black) structure functions $S(q)$ for the five ILs that pair the BSI-anions and the $\text{Im}_{1,8}^+$ cation, sequentially offset by 2 units each for clarity. The dashed vertical line at 2 \AA^{-1} marks the approximate boundary between q values associated with intermolecular and intramolecular distances. In the inset, a semilog horizontal axis is also used to emphasize the intermolecular part of $S(q)$. Figure was published by Zhao, *et al.*,⁽⁶⁾ used with the permission of AIP Publishing.

To investigate the effect of alkyl and fluorinated tails as well as that of the different charged heads separately, sub-ionic partitioning as defined by Eqn. 2.4 is performed for $\text{Im}_{1,8}^+$ ILs.

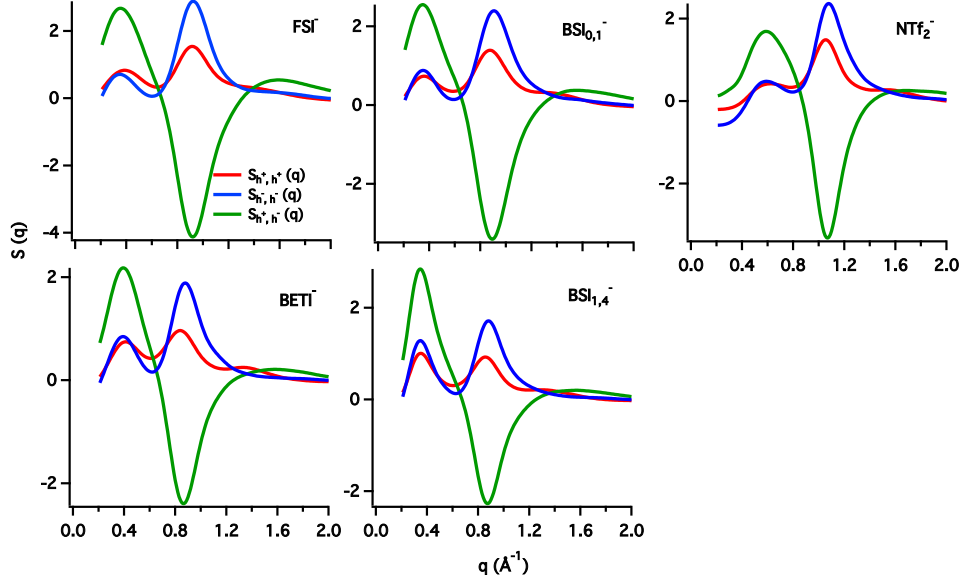


Figure 3.7: Contribution of charged subcomponents in the sub-ionic partitioning of $S(q)$ for the five BSI ILs with $\text{Im}_{1,8}^+$ cation. Figure was published by Zhao, *et al.*, (6) used with the permission of AIP Publishing.

For the family of fluorinated anions paired with $\text{Im}_{1,8}^+$, Figure 3.7 displays positive-positive, negative-negative and positive-negative structural correlations contributing to $S(q)$. At low q region associated with intermediate-range order ($q < 0.5 \text{ \AA}^{-1}$), positive and negative components as well as their cross terms contribute as peaks. This is because in this q region charges – independent of their sign – behave as “same-type” species; they are all polar. Instead, in the charge alternation region ($q \sim 0.9 \text{ \AA}^{-1}$) positive-negative correlations contribute as antipeaks. This is to be expected since here they behave as “opposite-type” species that alternate in space to form the charge network.

We are interested in the contribution to $S(q)$ of alkylated and fluorinated tails, Figure 3.8 (left) shows fluorinated and alkylated subcomponents of $S(q)$ as well as their cross contributions for $\text{BSI}_{1,4}^-$, $\text{BSI}_{1,5}^-$, and $\text{BSI}_{1,7}^-$. It is clear from this figure that the fluorinated tail - tail peaks ($S_{f,f}(q)$) in the low q region are dominant and broad. Two peaks are observed in the low q region, one at $q \sim 0.35 \text{ \AA}^{-1}$ and one at $q \sim 0.6 \text{ \AA}^{-1}$. These two fluorinated prepeaks result from different structural origins.

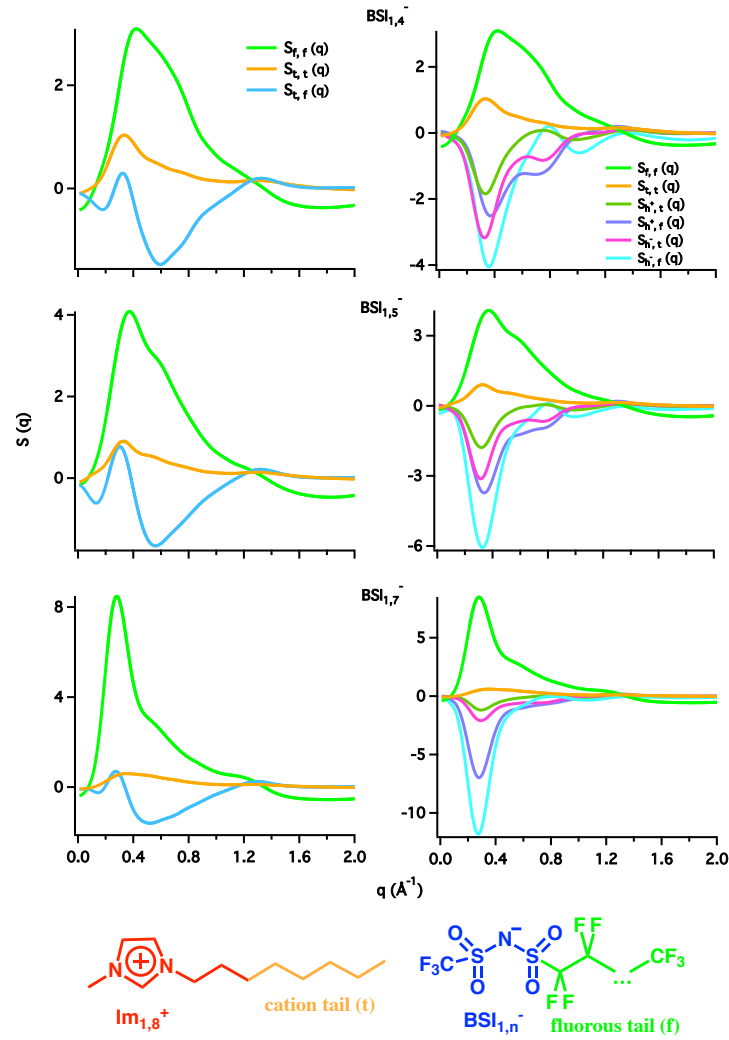


Figure 3.8: Sub-ionic partitioning of the total liquid structure function $S(q)$ for: $\text{Im}_{1,8}^+/\text{BSI}_{1,4}^-$, $\text{Im}_{1,8}^+/\text{BSI}_{1,5}^-$, and $\text{Im}_{1,8}^+/\text{BSI}_{1,7}^-$. “t” refers to the non-polar section (C_6H_{13}) of the cationic octyl tail. “f” refers only to the longer anionic perfluoroalkyl tails. Due to simulation box size limitations, features below 0.2 \AA^{-1} will not be discussed. Figure was published by Zhao, *et al.*,⁽⁶⁾ used with the permission of AIP Publishing.

The prepeak at $q \sim 0.35 \text{ \AA}^{-1}$ is associated with intermediate-range segregation of charged heads and nonpolar tail domains. As the fluorinated tails become longer and comparable in size with the alkylated tails, it becomes significantly larger as the anion size increases and shifts to lower q values. At this q value, the cationic alkyl tail subcomponent ($S_{t,t}(q)$) and the fluorinated-alkylated tail cross-subcomponent ($S_{f,t}(q)$) both contribute as peaks. This means that in this region, alkyl and fluorinated tails are behaving as “same-type” species, forming the nonpolar domains together. Regardless of whether tails are alkylated or fluorinated, the charge-tail subcomponents at $q \sim 0.35 \text{ \AA}^{-1}$ in Figure 3.8 (right) all contribute as anti-peaks. The nonpolar tails behave as “opposite-type” species of charged cationic and anionic heads. This is expected since the tail domains separate the charged networks, which is the origin for the intermediate range order commonly found in ILs.

For the prepeak at $q \sim 0.6 \text{ \AA}^{-1}$, the fluorinated-alkylated tail subcomponents contribute as antipeaks instead. This means that at this q value, alkylated and fluorinated tails behave as “opposite-type” species that alternate. This alternation likely occurs along charge networks and not across them; for a thorough discussion on this for a similar set of systems see Figures 11 and 12 in reference [21].

Figure 3.9 shows a typical cluster found in $\text{Im}_{1,8}^+/\text{BSI}_{1,7}^-$. It demonstrates several features of IL structures. There is a typical length scale across charge networks for this IL and we clearly see that both alkylated and fluorinated tails contribute to this spacing. There is also a pattern of alternation for tails decorating each individual charge network. Because cationic heads and anionic heads must alternate, the respective cationic hydrocarbon and anionic fluorocarbon tails must also alternate.

In a way, this alternation manifests in $S(q)$ as a structural recurrence. The feature near $q \sim 0.6 \text{ \AA}^{-1}$, associated with the fluorinated/alkylated alternation, occurs only because charge alternation exists. The charge alternation peak occurs at $q \sim 0.9 \text{ \AA}^{-1}$ (see Figure 3.7) while the fluorinated-alkylated tail alternation occurs at $q \sim 0.6 \text{ \AA}^{-1}$, though the real origin of both features is the same. This is because tails are separated by a larger distance than the charge heads.

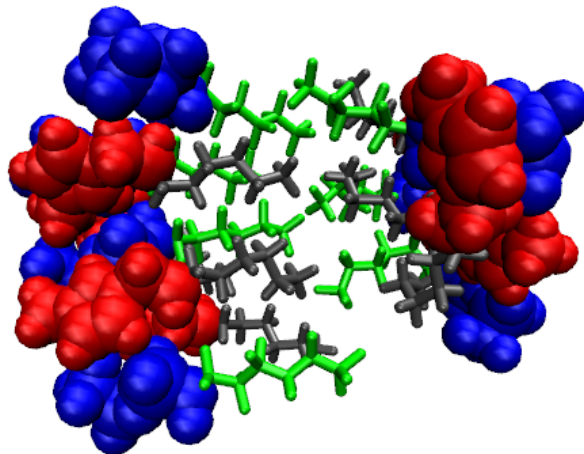


Figure 3.9: Typical nanostructure found in the case of $\text{Im}_{1,8}^+/\text{BSI}_{1,7}^-$. Blue and red volumes represent the anion and cation heads, respectively. The gray and green sticks represent the configuration of the cationic and anionic tails, respectively. Figure was published by Zhao, *et al.*,⁽⁶⁾ used with the permission of AIP Publishing.

Figure 3.8 (right) shows that another set of peaks and antipeaks occur near $q \sim 0.8 \text{ \AA}^{-1}$, where cationic head-tail correlations and anionic head-tail correlations show a peak, and the corresponding cationic head-anionic tail and anionic head-cationic tail correlations show antipeaks. This means that at this typical distance in real space, it is unlikely to find fluorinated tails next to cationic heads or alkyl tails next to anionic heads.

3.1.4 Domain aggregation analysis

In Figures 3.11 and 3.12, an analysis of the connectivity between different moieties was performed based on the algorithms introduced by Bernardes, *et al.*⁽²²⁾ and Shimizu, *et al.*⁽²³⁾ As in prior work,⁽²³⁾ the cutoff distance is determined based on a decomposition of the first peak in the radial distribution function of the terminal tail carbon atom for alkyl and fluoroalkyl groups, as in Figure 3.10. The cutoff distance defines whether residues are connected and form an aggregate of size n_a with probability of aggregate $P(n_a)$.

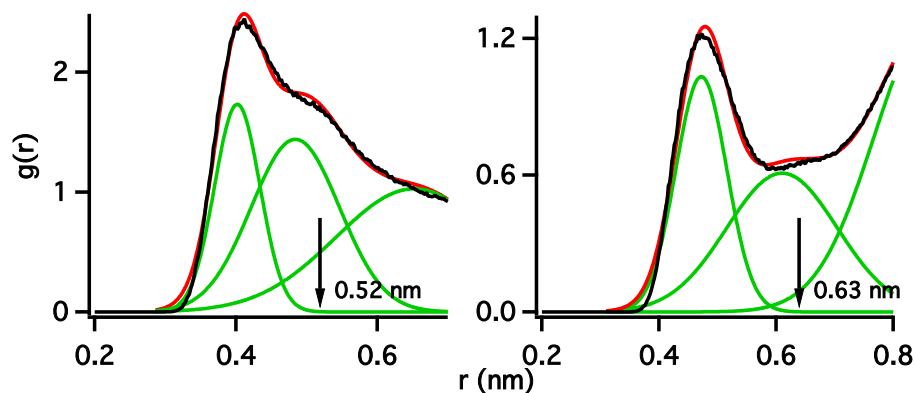


Figure 3.10: Radial distribution functions (RDFs) used in the determination of the connectivity criteria for the aggregation analysis. The RDF on the left is calculated for the terminal C - C on the $\text{Im}_{1,8}^+$ cation in $\text{Im}_{1,8}^+/\text{BSI}_{1,5}^-$, and the RDF on the right is calculated for the C - C on the NTf_2^- anion in $\text{Im}_{2,1}^+/\text{NTf}_2^-$. Because the cutoff distances determined varied only slightly with changes of anion, the values of 0.52 and 0.63 nm were used for all of the ILs analyzed. The green curves are the result of the deconvolution of the first RDF peak by using a series of Gaussian functions; the red curves are the sums of the corresponding Gaussian functions. Figure was published by Zhao, *et al.*,⁽⁶⁾ used with the permission of AIP Publishing.

For the different ILs, the top graph in Figures 3.11 and 3.12 shows the hydrocarbon domain analysis, and the bottom graph shows the fluororous domain analysis. Since there are 1000 ion pairs in each simulation box, the domain size n_a ranges from 0 to 1000.

We can see that for the $\text{Im}_{2,1}^+$ -based ILs, hydrocarbon tails are disconnected but fluororous domains start to form for BETI^- and highly continuous for $\text{BSI}_{1,3}^-$ and the larger anions. This is consistent with the appearance of FSDP features in the partitioned liquid structure functions in Figure 3.3. For $\text{Im}_{1,8}^+$ -based liquids the alkyl tails are for the most part connected. As the anionic tail size increases there is a transition between disconnected to connected fluororous tails that occurs for $n = 4, 5$ and 7 . For $\text{Im}_{1,8}^+/\text{BSI}_{1,7}^-$, the fluororous connectivity is dominant across the whole simulation box and we start seeing a high probability of disconnected alkyl tails (significant probability at low n_a) implying a disruption in alkyl tail connectivity due to the presence of the fluorinated tails. Whereas this analysis provides a clear view of tail connectivity it does not imply that alkyl and fluororous moieties form spatially separated environments. While different box sizes and cutoff values make the absolute scales different, the results of Lo Celso, *et al.* show qualitatively the same trends in the cluster analysis.(7)

3.1.5 Spatial Distribution Functions (SDFs)

Spatial distribution functions (SDFs) can be used to get an idea of the average 3-D environment around different ionic types in the simulation. For this, we use the TRAVIS (trajectory visualization) program from Brehm and Kirchner(24) to obtain the SDFs and Visual Molecular Dynamics (VMD) program to view the results.(20) From this analysis, we learn mostly about the adjacency correlations.

To calculate SDFs, a reference molecule is selected and three atoms must be selected from the reference molecule to define its orientation. Every instance of the reference molecule (cation or anion in our case) in every time step is then aligned in a way that the set of three atoms can best overlap. SDFs result from the averaging in space around these reference atoms.(24) Different distributions can be obtained by changing these three reference atoms, and doing this for multiple combinations of reference points can

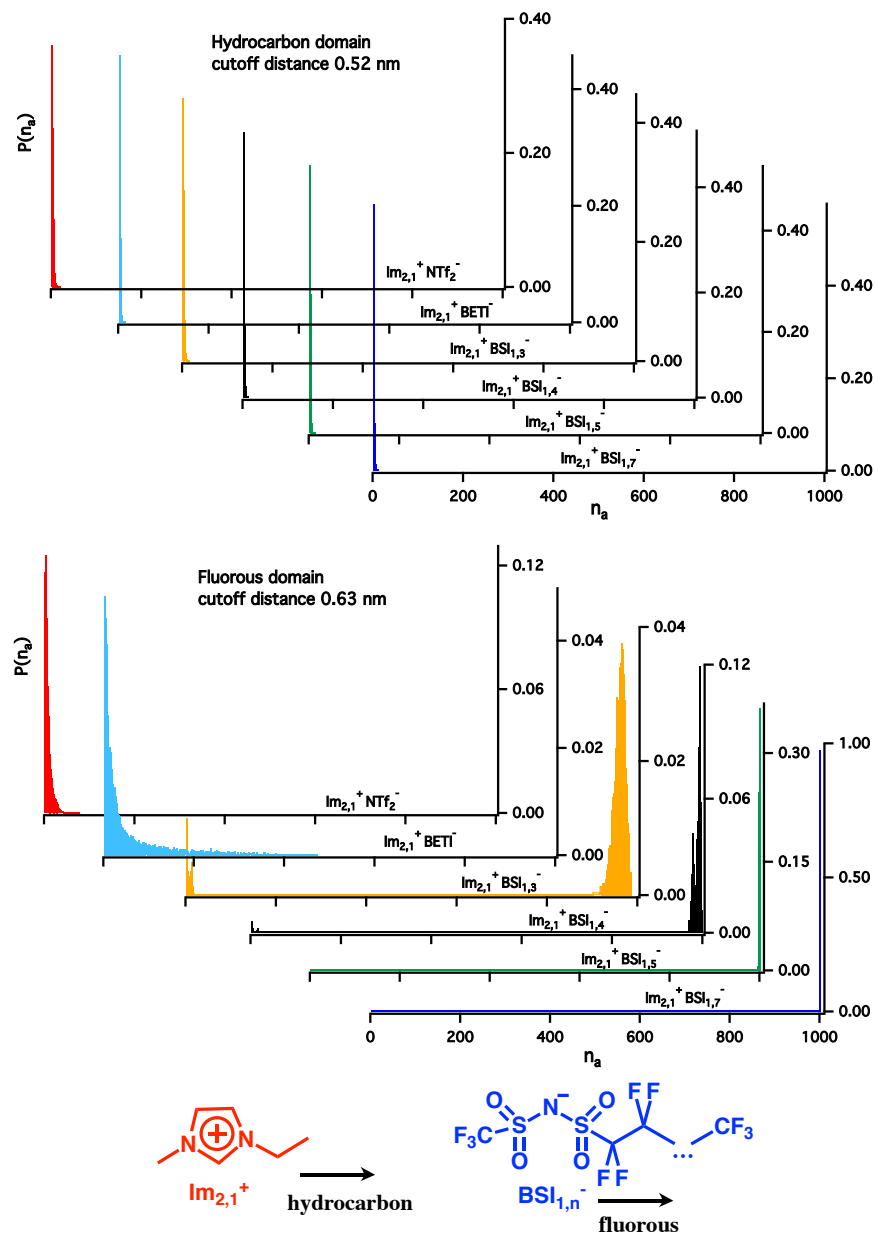


Figure 3.11: Discrete probability distribution of aggregation sizes, $P(n_a)$, as a function of aggregate size number, n_a , for six BSI-anion ILs with the $\text{Im}_{2,1}^+$ cation. For each system, the top subfigure shows the domain aggregate analysis for hydrocarbons, and the bottom shows that for fluorous tails. The terminal cationic C atom in the ethyl tail is used in the analysis of hydrocarbon domains, and all C atoms of the longest anionic perfluoroalkyl tail are used in the analysis of fluorous domains. In the case of $\text{Im}_{2,1}^+/\text{BETI}^-$, only C atoms in one of the C_2F_5 tails are used for the analysis. Figure was published by Zhao, *et al.*,⁽⁶⁾ used with the permission of AIP Publishing.

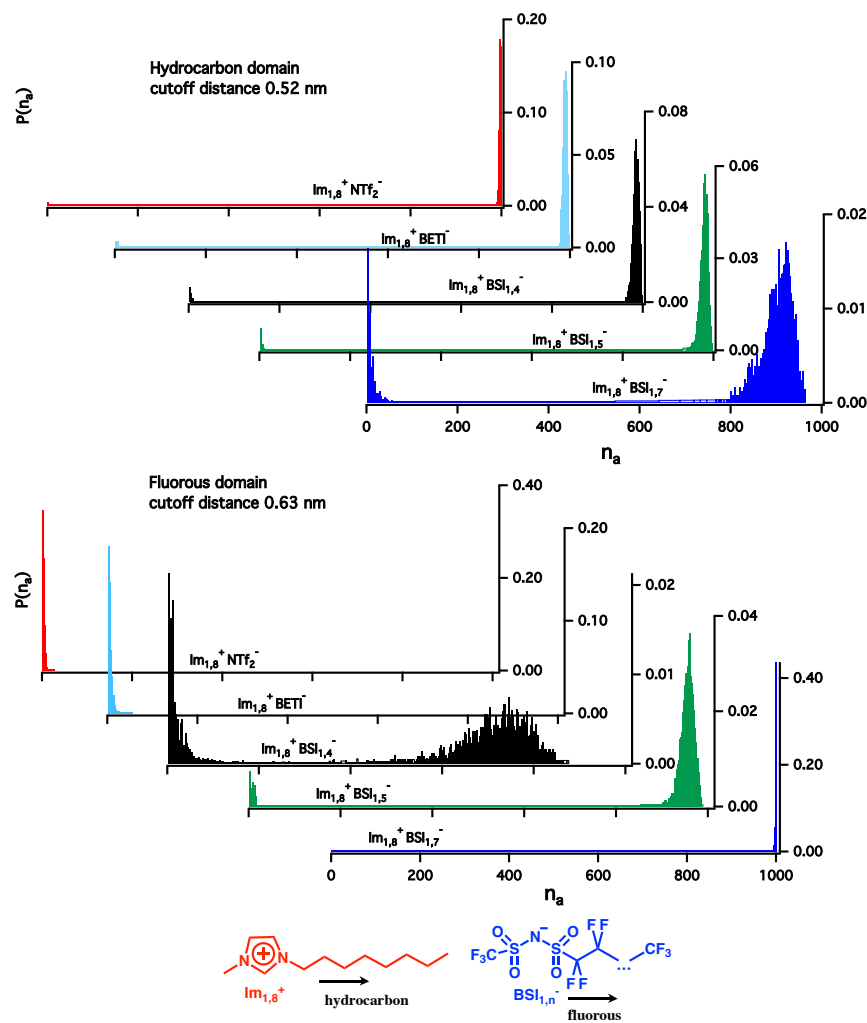


Figure 3.12: Discrete probability distribution of aggregation sizes, $P(n_a)$, as a function of aggregate size number, n_a , for five BSI-anion ILs with the $\text{Im}_{1,8}^+$ cation. The top shows the hydrocarbon domain aggregate analysis for each system, and the bottom shows the fluorous domain aggregate analysis. C atoms in the cationic $-\text{C}_7\text{H}_{15}$ chain are used in the analysis of hydrocarbon domains, and all C atoms of the longest anionic perfluoroalkyl tail are used in the analysis of fluorous domains. In the case of $\text{Im}_{1,8}^+/\text{BETI}^-$, only C atoms in one of the C_2F_5 tails are used for the analysis. Figure was published by Zhao, *et al.*,⁽⁶⁾ used with the permission of AIP Publishing.

provide very instructive 3-D perspectives of the solvation environment of the central molecule.

Figure 3.13 shows SDFs for $\text{Im}_{1,8}^+/\text{BSI}_{1,4}^-$, with various sets of reference atoms. The top row shows a range of SDFs for a central $\text{Im}_{1,8}^+$ cation, while the bottom row does the same for a central $\text{BSI}_{1,4}^-$ anion. As indicated by squares in this figure, the reference atoms are chosen for the cationic (SDF-1) and anionic head groups (SDF-5), the central atoms on the alkyl (SDF-2) or perfluoroalkyl tails (SDF-6), atoms defining the full spatial extent of the cation (SDF-3) or anion (SDF-7) and the terminal methyl (SDF-4) or trifluoromethyl groups (SDF-8).

The spatial distribution SDF-1 in Figure 3.13 emphasizes the interactions around the charged and H-bond-donating part of the imidazolium cation. The density arising from the anionic polar head (blue) is centered around the cationic ring, concentrated next to the three H-bond donating H atoms. Although yellow lobes are located right next to the blue lobes in similar shapes, the green lobe (terminal CF_3) can only be found to the right side; the same holds true for the orange and gray lobes, which lie to the right where the cationic tail is. A similar distribution for ionic moieties surrounding the anionic head group is shown in SDF-5 where CF_3 groups (green) and CH_3 groups (gray) are on the opposite end to the anionic head. These two figures emphasize what is depicted in Figure 3.9 where adjacent alkylated and fluorinated tails alternate along a charge network.

The spatial distributions SDF-2 and SDF-3 display the distributions relative to the cationic alkyl tails and the full spatial extent of the cation, respectively. The anion heads (blue lobes) lie in a circle around the cation head, with the red lobe of cation heads surrounding outside. This is consistent with the fact that ionic heads belong to the charge network. The anionic fluorinated tails and cationic alkylated tails once again follow the pattern depicted in Figure 3.9. The fluorocarbon tails and hydrocarbon tails lie close, constrained by the cation and anion alternating heads along the charge network.

SDF-4 shows the spatial distribution with respect to the reference frame defined by the three H-atoms on the terminal methyl group. Umbrella-shaped lobes formed by

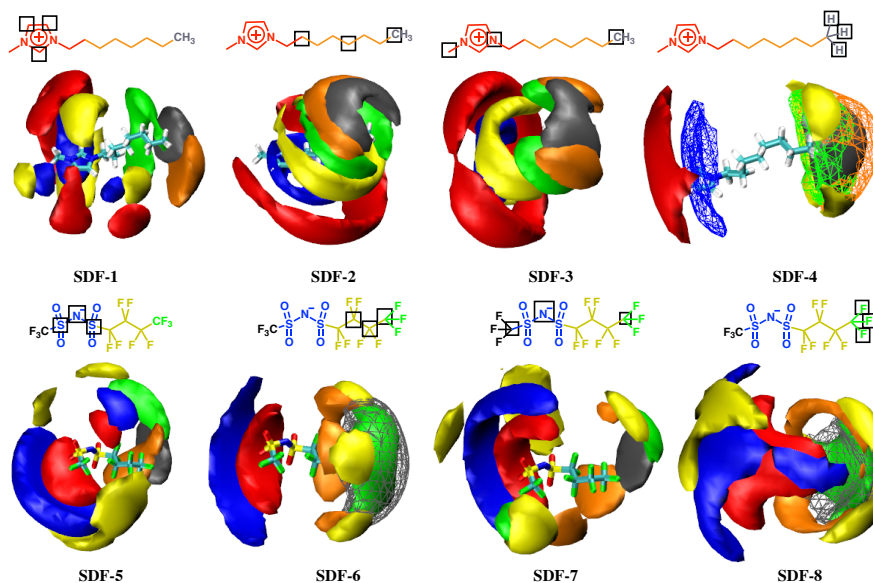


Figure 3.13: SDFs for $\text{Im}_{1,8}^+/\text{BSI}_{1,4}^-$ using different sets of reference atoms. The three specific reference atoms used to calculate these SDFs are shown in the boxes surrounding the atoms in the molecular structures, which are in turn shown above the SDFs. Top row: anion and cation probabilities surrounding a reference cation. Bottom row: anion and cation probabilities surrounding a reference anion. The color coding used in generating the SDFs is: red for the polar head group of imidazolium; orange for the five carbons at the 3 - 7 positions of the octyl tail; gray for the terminal CH_3 group on the octyl tail; blue for the anionic polar head group; yellow for the three CF_2 groups on $\text{BSI}_{1,4}^-$; and green for the anionic CF_3 groups. The isodensity values used can be found in Table 3.2. Figure was published by Zhao, *et al.*,⁽⁶⁾ used with the permission of AIP Publishing.

fluorocarbon tails and hydrocarbons tails often cross with each other showing from a different perspective that the ordering of tails is a result of the charge network organization; in other words, charge alternation causes tail alternation.

Table 3.2: Isodensity values used in Fig. 13 (nm^{-3}). Data was published by Zhao, *et al.*,⁽⁶⁾ used with the permission of AIP Publishing.

Color Code	Red	Orange	Grey	Blue	Yellow	Green
SDF-1	1.991	1.921	2.093	3.135	2.139	2.187
SDF-2	1.915	2.010	2.258	2.661	2.089	2.391
SDF-3	1.991	1.969	2.240	3.133	2.155	2.300
SDF-4	1.767	1.857	2.092	1.932	1.904	2.243
SDF-5	2.888	2.065	2.268	2.167	1.860	1.986
SDF-6	2.915	2.175	2.428	2.188	1.876	2.200
SDF-7	3.212	2.088	2.465	2.382	1.853	2.130
SDF-8	2.390	2.137	2.343	1.960	1.752	2.113

3.1.6 Summary of structural studied of ILs with imidazolium cations

This section quantitatively describes the structural and physical properties of ILs containing anions in the $\text{BSI}_{n,m}^-$ family paired with short- and long-tail imidazolium cations. ILs containing these anions may be promising candidates for applications including energy storage devices and tribology, but they are less well understood than those containing the extremely popular anion NTf_2^- . X-ray measurements and MD simulations provide an interesting perspective on the arrangement of fluorinated and alkylated moieties on an ionic level. From distribution of tail aggregation sizes we find that, when they are sufficiently long, both alkylated and fluorinated components can form large intermediate aggregates. However, positive-negative charge alternation results in the formation of charge networks, tails in cations and anions must necessarily decorate them. This decoration results in ionic-level tail alternation between cationic and anionic tails, which precludes separation of the fluorinated and alkylated components.

3.2 Structural analysis of ILs with symmetric and asymmetric fluorinated-anions: pyrrolidinium and phosphonium cations

Besides imidazolium based ILs, there is increasing interest in using pyrrolidinium-based RTILs in electrochemical devices,⁽²⁵⁾ and using phosphonium-based ILs as thermally

stable and viscous liquids.(26–29) Therefore, we studied the structure of ILs with two non-aromatic cations: 1-octyl-1-methylpyrrolidinium ($\text{Pyrr}_{1,8}^+$) and trihexyltetradecylphosphonium ($\text{P}_{6,6,6,14}^+$) paired with the above mentioned five BSI-anions from Section 3: FSI^- , $\text{BSI}_{0,1}^-$, NTf_2^- , BETI^- and $\text{BSI}_{1,4}^-$. The molecular structures of studied ILs are presented in Figure 3.14 Both X-ray scattering experiments and MD simulations are used to study the structure of these ILs.

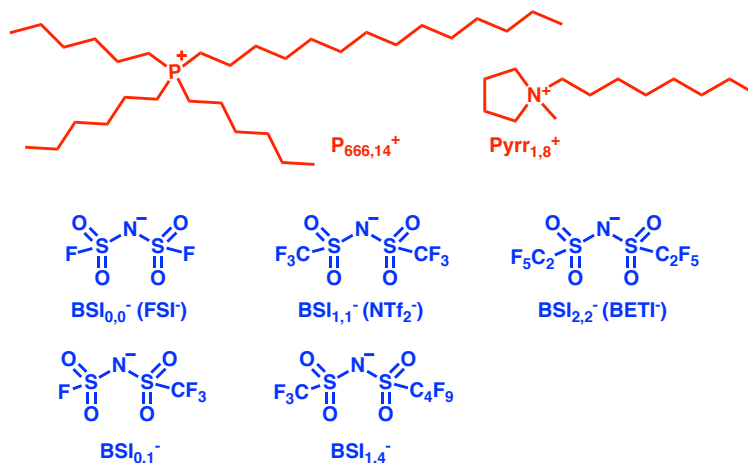


Figure 3.14: Chemical structures of the cations (red) and anions (blue) used for X-ray scattering, viscosity, conductivity and thermochemical experiments.

3.2.1 Physical properties

The physical properties of ILs in Figure 3.14 are listed in Table 3.1. The densities calculated from the simulations are close to those measured from experiments. For the same cation, the densities increase as the BSI anion size increases as a result of an increasing contribution from fluorinated tail components. For the same anion, the densities for the $\text{P}_{6,6,6,14}^+$ ILs are lower than those for the $\text{Pyrr}_{1,8}^+$ ILs. This is because the larger size of the $\text{P}_{6,6,6,14}^+$ cation prevents close packing among ions in the systems. The glass transition temperatures (T_g) increase with anion size for the $\text{Pyrr}_{1,8}^+$ -cation ILs. Due to facile crystallization, even at low temperatures, glass transitions can only be observed for three of the five $\text{P}_{6,6,6,14}^+$ ILs. The glass transitions for the three ILs occur at about the same temperature, indicating that anion is not a major influence

on the low-temperature dynamics for the $P_{6,6,6,14}^+$ ILs. When observed, the melting points for $Pyrr_{1,8}^+$ ILs increase with anion size. The melting points for $P_{6,6,6,14}^+$ ILs are very close except for $P_{6,6,6,14}^+/NTf_2^-$, whose melting point is much lower than the other four ILs. The viscosities as functions of temperature for all the ILs except $Pyrr_{1,8}^+/NTf_2^-$ were measured by our collaborator Prof. Sharon Lall-Ramnarine. The viscosities for $Pyrr_{1,8}^+/NTf_2^-$ were reported previously by Lall-Ramnarine, *et al.*(10) The experimental viscosities vs. temperatures are plotted in Figure 3.15.

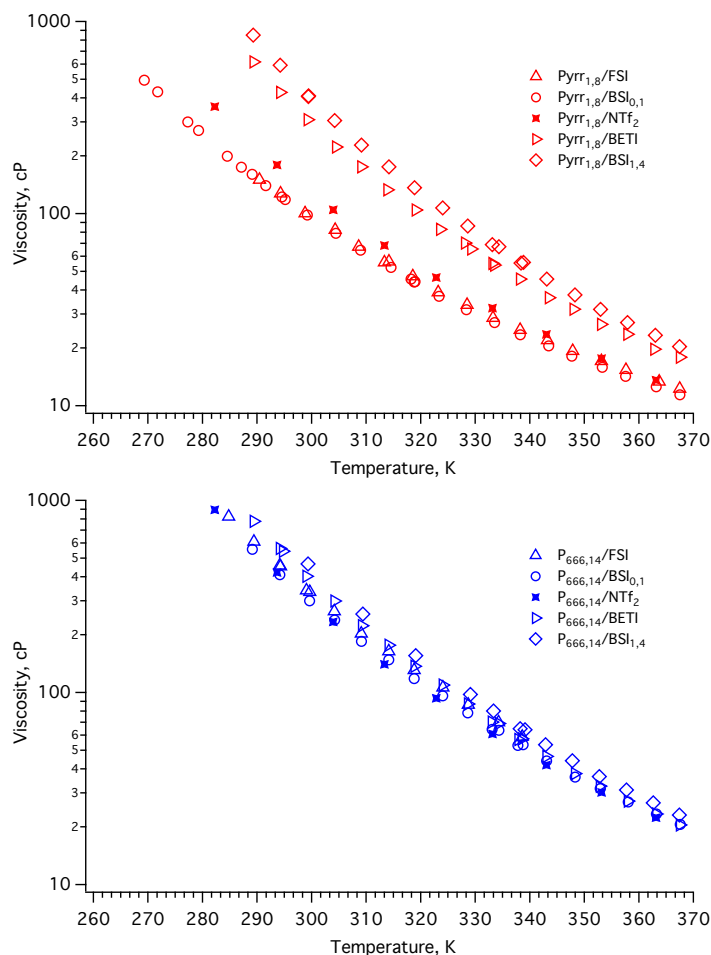


Figure 3.15: Measured viscosities of the ten ionic liquids at various temperatures. Data for $Pyrr_{1,8}^+/NTf_2^-$ is generated based on the VFT parameters from Lall-Ramnarine, *et al.*(10)

The logarithmic form of the Vogel-Fulcher-Tamann (VFT) equation (Eqn. 3.1) was used to fit the temperature-dependent experimental viscosity data. When glass transition onset temperature T_g is observed, a viscosity value of 10^{13} cP was included for each IL following the practice of Angell.(30) Fixing this low-temperature point for the viscosity curve is critical in obtaining consistent results for comparison amongst a series of similar liquids. Note that for $P_{6,6,6,14}^+ / BSI_{0,1}^-$ and $P_{6,6,6,14}^+ / NTf_2^-$, the T_g values are not observed. Thus, while the VFT equation provides an excellent fit to the data, the fit parameter are subject to a large uncertainty. The VFT fitting results are presented in Table 3.3.

Table 3.3: Physical properties of ILs measured at 298 K.

ILs	Exp. Density (g/cm ³)	Sim. Density (g/cm ³)	Viscosity ^a (cP)	T_g^b (K)	Melting Point (K)	Conductivity (mS/cm)	Walden product (P S cm ² /mol)	$\ln(\eta_0/\text{cP})$	D	T_0 (K)
$Pyrr_{1,8}^+ / FSI^-$	1.10	1.25	105	174	243	2.05	0.73	-2.43	8.06	139.4
$Pyrr_{1,8}^+ / BSI_{0,1}^-$	1.24	1.30	102	173	247	1.38	0.49	-2.70	8.62	137.0
$Pyrr_{1,8}^+ / NTf_2^-$	1.27	1.34	140	190	257	1.10	0.58	-2.43(10)	6.55(10)	157.9(10)
$Pyrr_{1,8}^+ / BETf^-$	1.32	1.41	331	196	c	0.17	0.25	-3.09	7.83	158.6
$Pyrr_{1,8}^+ / BSI_{1,4}^-$	1.38	1.45	451	193	c	0.167	0.34	-3.64	9.61	150.1
$P_{6,6,6,14}^+ / FSI^-$	0.995	1.05	362	188	253	0.100	0.25	-2.48	8.29	149.8
$P_{6,6,6,14}^+ / BSI_{0,1}^-$	1.00	1.08	328	c	241	0.093	0.22	-4.33	16.08	115.2
$P_{6,6,6,14}^+ / NTf_2^-$	1.065	1.11	318	c	198	0.081	0.26	-3.24	9.71	143.4
$P_{6,6,6,14}^+ / BETf^-$	1.08	1.17	436	191	255	0.058	0.19	-3.60	9.86	147.7
$P_{6,6,6,14}^+ / BSI_{1,4}^-$	1.15	1.20	507	188	253	0.045	0.17	-3.89	11.25	141.2

^aCalculated from the VFT parameters in this table according to equation 4; ^bOnset temperature; ^cnot observed

The D parameter in VFT fits is associated with the deviation from the Arrhenius law. Smaller D values indicate greater deviation from Arrhenius behavior, which has been described as the “fragility” of the liquid.(31) The more fragile a liquid is (smaller D), the faster its viscosity will decrease as the temperature increases above its T_g . As can be seen in Figure 3.15, the viscosity for $Pyrr_{1,8}^+ / NTf_2^-$ decreases faster than the other $Pyrr_{1,8}^+$ ILs, and it has the lowest D value.

More insight about the transport behavior of these ILs can be obtained by calculating the Walden product, which is the product of the molar conductivity and the viscosity.(30) A Walden product of $1.0 \text{ P S cm}^2 \text{ mol}^{-1}$ (typical for 1 M KCl) represents “ideal” conductive behavior for an electrolyte, while values above one are described as “superionic” and values below one represent a decrease in “ionicity”. The Walden products, all fall below one, indicating a decrease in “ionicity” for these ILs. The ionicities of the $Pyrr_{1,8}^+$ salts are significantly greater than the ionicities of the corresponding $P_{6,6,6,14}^+$ salts for each of the five anions. Ion pairing(32–34) has been invoked to explain the extremely low ionicity for the $P_{6,6,6,14}^+$ ILs, where the anions are practically

nested in the cations.(35) From energetic considerations,(36) ionic diffusion is primarily confined to the polar domain. As the relative spatial extent of the polar domain decreases, the correlations between the movement of ions are expected to increase. This can explain the decreasing of ionicities as the anion size increases, and the lower ionicity of $P_{6,6,6,14}^{+}$ ILs compared to the $Pyrr_{1,8}^{+}$ ILs.

3.2.2 Structure of $Pyrr_{1,8}^{+}$ salts

The liquid structure functions $S(q)$ for ILs with the $Pyrr_{1,8}^{+}$ cation from high-energy XRS experiments and MD simulations are shown in Figure 3.16. Good agreements are achieved between the simulated $S(q)$ functions and the experimental $S(q)$ functions and the experimental results.

In Figure 3.16, we see that a FSDP is observed for each of the five $Pyrr_{1,8}^{+}$ ILs at $q \sim 0.37 \text{ \AA}^{-1}$. Previous studies on N-alkyl-N-methylpyrrolidinium cation ($Pyrr_{1,n}^{+}$) paired with NTf_2^{-} showed that FSDPs are only observed for $n \geq 6$ with X-ray scattering measurements.(37; 38) Since the $Pyrr_{1,8}^{+}$ cation includes an octyl tail, which is long enough to aggregate into nano-scale domains, it is expected to see FSDPs for the $Pyrr_{1,8}^{+}$ ILs. Studies on $BSI_{1,4}^{-}$ - ILs showed that the fluorinated butyl tails can form nano segregated fluorine domains when no long alkyl tails are present in the system.(6; 7) We may argue that the FSDP for $Pyrr_{1,8}^{+}/BSI_{1,4}^{-}$ points to the existence of nonpolar domains associated with both the alkyl tails and fluorinated tails. However, considering that changing anions does not affect the position of the FSDP peaks, and that fluorinated ILs often show no FSDPs in X-ray scattering results due to peaks and antipeaks cancellation,(6; 7; 18; 38) it is the cationic alkyl tails that are responsible for the display of the FSDP for $Pyrr_{1,8}^{+}/BSI_{1,4}^{-}$.

From empirical observations, the adjacency peak around $q \sim 1.4 \text{ \AA}^{-1}$ shifts to smaller q value as the anion size increases; the peak shape becomes sharper and the peak amplitude slightly decreases. The charge correlation peak, which appears around $q \sim 0.8 \text{ \AA}^{-1}$, also shifts to smaller q value as the anion size increases. The peak amplitude, however, significantly increases.

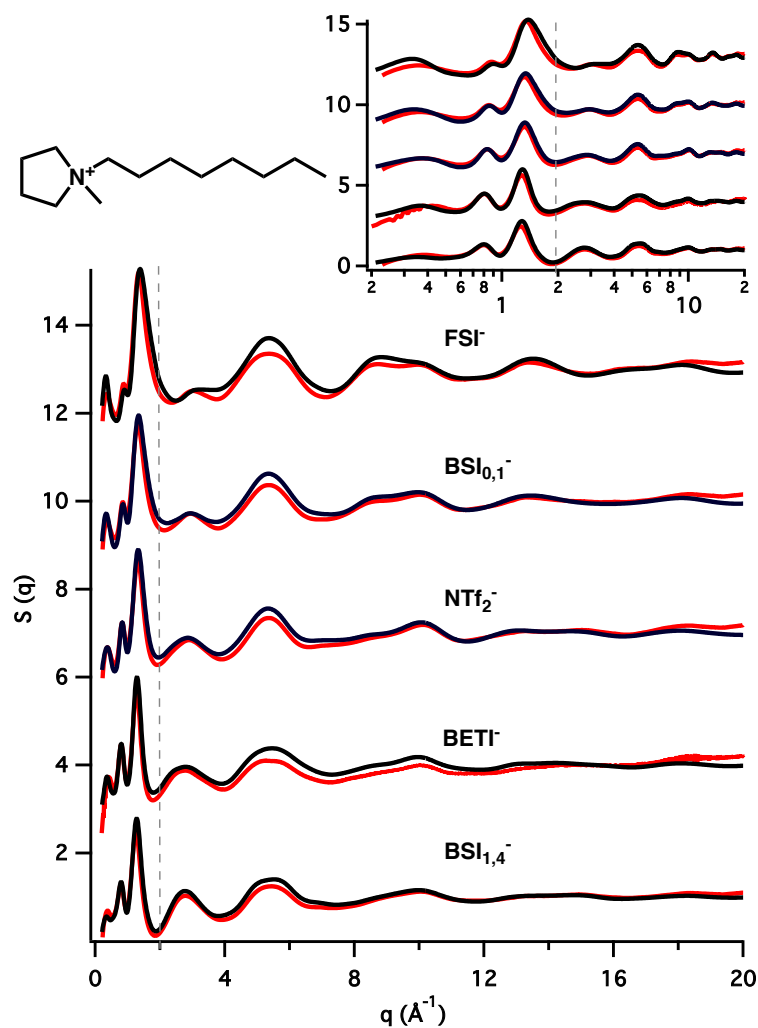


Figure 3.16: The experimental (red) and simulated (black) structure functions $S(q)$ for the five ILs that pair the BSI-anions and the $\text{Pyr}_{1,8}^+$ cation, sequentially offset by 3 units each for clarity. The dashed vertical line at 2 \AA^{-1} marks the approximate boundary between q values associated with intermolecular and intramolecular distances. In the inset, a semilog horizontal axis is also used to emphasize the intermolecular part of $S(q)$.

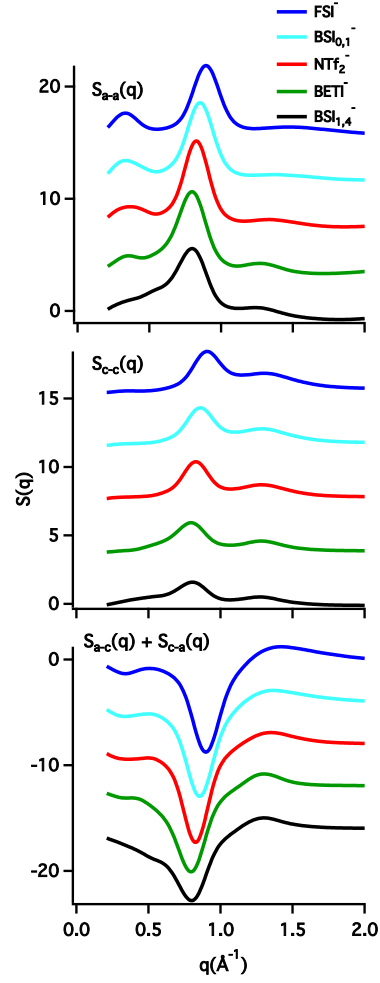


Figure 3.17: Ionic partitioning of $S(q)$ for the five BSI ILs with $\text{Pyrr}_{1,8}^+$ cation. Top: anion-anion; center: cation-cation; bottom: anion-cation. From top to bottom, the curves represent the partial $S(q)$ for $\text{Pyrr}_{1,8}^+$ with FSI^- (blue), $\text{BSI}_{0,1}^-$ (cyan), NTf_2^- (red), BETI^- (green), and $\text{BSI}_{1,4}^-$ (black). For clarity, an offset of 3 units is applied to each subsequent curve.

The ionic partitioning for the five $\text{Pyrr}_{1,8}^+$ ILs is shown in Figure 3.17. In total $S(q)$, the adjacency peaks appear to be the main peak in the inter-molecular region. In the ionic partitioning, the charge-charge alternation peak turn out to be the most interesting peak. It is noticed that the charge-charge alternation peak shifts to lower q values as the anions size increases from FSI^- to $\text{BSI}_{1,4}^-$. This indicates that as the anion gets larger, the distances between cationic heads and anionic heads are increasing. The amplitude of the FSDPs in $S(q)$ is significantly decreases as the anion size increases from FSI^- to $\text{BSI}_{1,4}^-$. This may have to do with the increasing volume of fluorinated moieties in the system. For $\text{Pyrr}_{1,8}^+/\text{BSI}_{1,4}^-$, the FSDP in $S(q)$ is very weak and broad, and it is barely observable for $q = 0.37 \text{ \AA}^{-1}$. Moreover, there is a second shoulder peak near $q = 0.52 \text{ \AA}^{-1}$ in anion-anion and anion-cation interactions, which is absent for the other ILs in this set. This may be attributed to the presence of a long fluorinated butyl tail on the $\text{BSI}_{1,4}^-$ anion, which can form fluorous nonpolar domains.

To investigate the effect of changing anion size on the structure, the sub-ionic partitioning of the structure factor $S(q)$ is performed as defined by Eqn. 2.4. Figure 3.18 displays positive-positive, negative-negative, and positive-negative structural correlations contributing to $S(q)$. At low q values where the intermediate-range order occurs, all three components contribute as peaks in $S(q)$. This is because in the sense of separating the alkyl tails, both the positive and negative components behave as “same-type” species, independent of their sign. In the charge alternation region, on the other hand, the positive-positive and negative-negative interactions appear as peaks whereas their cross terms appear as antipeaks. This is because the cationic and anionic heads behave as “opposite-type” species that alternate to form the charge network. When the anion is small, like FSI^- , the cationic heads and anionic heads are closer to each other than when the anion is large, like $\text{BSI}_{1,4}^-$. Therefore, the charge-charge alternation peaks for $\text{Pyrr}_{1,8}^+/\text{FSI}^-$ have the highest amplitude among all five anions, while those for $\text{Pyrr}_{1,8}^+/\text{BSI}_{1,4}^-$ have the lowest amplitude.

Apart from the interaction of the positive and negative components, we are most interested in the interaction of alkylated and fluorinated tails. To amplify the effect of fluorinated tails, we simulated the IL system $\text{Pyrr}_{1,8}^+/\text{BSI}_{1,7}^-$ using MD simulations.

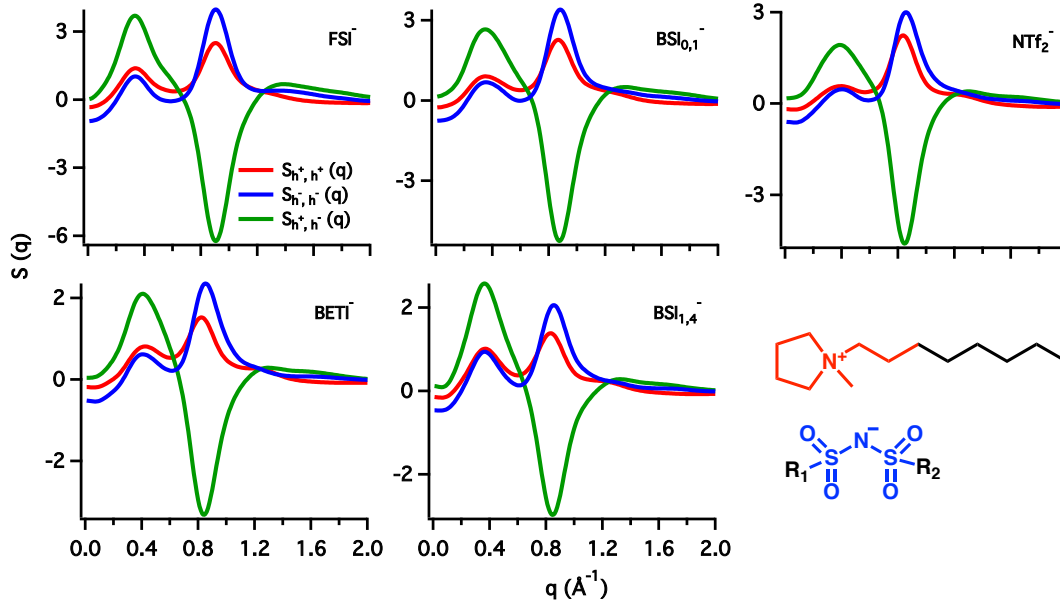


Figure 3.18: Contribution of charged subcomponents in the sub-ionic partitioning of $S(q)$ for the five BSI ILs with the $\text{Pyrr}_{1,8}^+$ cation. h^+ refers to the cationic head (colored red) and h^- refers to the anionic head (colored blue).

Figure 3.19 (left) shows the fluorinated and alkylated subcomponents of $S(q)$ as well as their cross contributions for $\text{Pyrr}_{1,8}^+/\text{BSI}_{1,4}^-$ and $\text{Pyrr}_{1,8}^+/\text{BSI}_{1,7}^-$. In the prepeak region of $S(q)$, the fluorinated tail contribution dominates. The peaks are broad in the case of $\text{BSI}_{1,4}^-$, but extremely sharp and intense in the case of $\text{BSI}_{1,7}^-$. The alkylated-alkylated tail subcomponent and the fluorinated-alkylated tail cross-subcomponent of $S(q)$ also contribute as peak in $S(q)$ for this q region, indicating that the alkylated tails and fluorinated tails act as “same-type” species. They serve the same purpose as to form the nonpolar domains.⁽⁶⁾ All charge-tail subcomponents at this q value in Figure 3.19 (right) contribute as antipeaks in $S(q)$. This means in the low q region, the charged cationic and anionic head groups act as “opposite-type” species of the tails. This is expected since tails form the intermediate range order while the cationic and anionic heads form the charged network that separates the nonpolar domains formed by the tails.

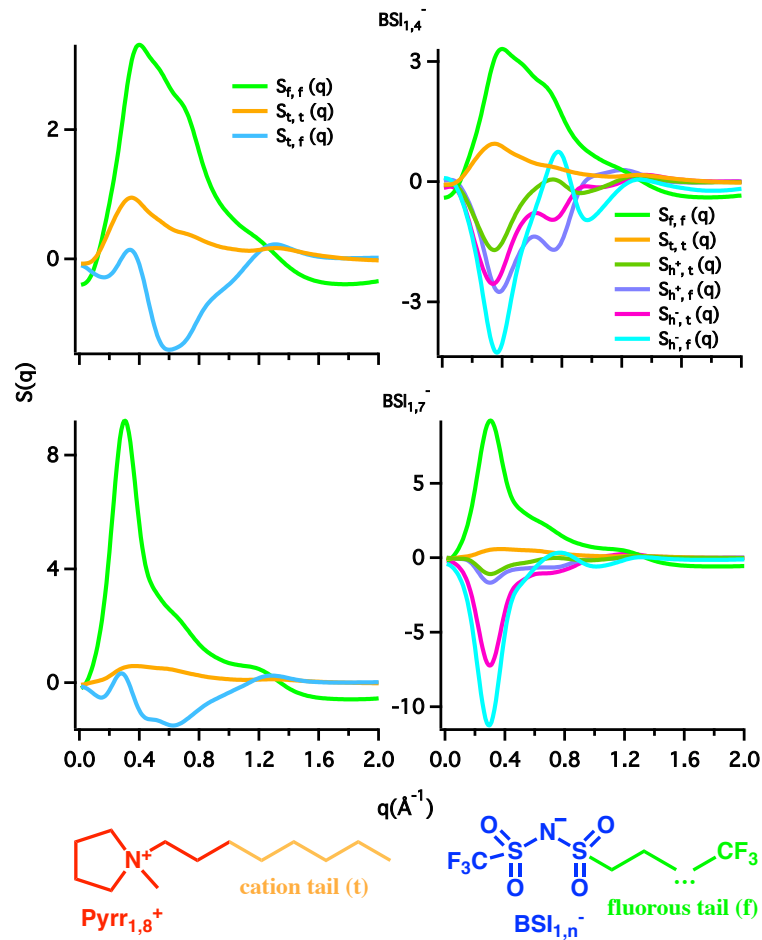


Figure 3.19: Sub-ionic partitioning of the total liquid structure function $S(q)$ for: $\text{Pyrr}_{1,8}^+/\text{BSI}_{1,4}^-$ and $\text{Pyrr}_{1,8}^+/\text{BSI}_{1,7}^-$. “t” refers to the non-polar section (C_6H_{13}) of the cationic octyl tail. “f” refers only to the longer anionic perfluoroalkyl tails. Due to simulation box size limitations, features below 0.2\AA^{-1} will not be discussed.

In the left two graphs in Figure. 3.19, there is another fluorinated tail prepeak in $S(q)$ at $q \sim 0.6 \text{ \AA}^{-1}$, which coincides with an antipeak of the fluorinated-alkylated tail sub-component. At this q value, alkylated and fluorinated tails behave as “opposite-type” species that alternate. This alternation most likely occurs along the charged network.(6; 21) To see this, a typical nanostructure found in the case of $\text{Pyrr}_{1,8}^+/\text{BSI}_{1,7}^-$ is shown in Figure 3.20. Since the alkylated tail is attached to the cationic head and the fluorinated tail is attached to anionic head, the charge alternation of cationic and anionic heads inevitably leads to the alternation of the tails. Thus, the tails behave as “opposite-type” species, like the positive-negative component that contributes to an antipeak around 0.8 \AA^{-1} in Figure 3.18. Though the origin of these two peaks is the same, they occur at different q values because tails are not as closely packed as the heads in the system. Figure 3.20 shows that for a pair of adjacent cationic head and anionic head, the attached alkylated tail and fluorinated tail are not necessarily parallel. The tails are more flexible than the charged heads and can point to different directions, thus there is larger distance among the tails than the charged heads.

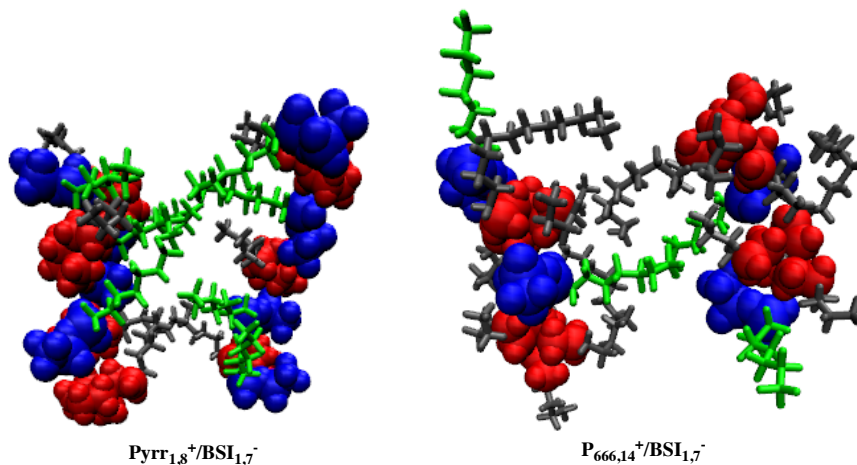


Figure 3.20: Typical nanostructure found in the case of $\text{Pyrr}_{1,8}^+/\text{BSI}_{1,7}^-$ (left) and $\text{P}_{6,6,6,14}^+/\text{BSI}_{1,7}^-$ (right). Blue and red volumes represent the anion and cation heads, respectively. The gray and green sticks represent the configuration of the cationic and anionic tails, respectively.

3.2.3 Structure of $P_{6,6,6,14}^+$ salts

The total structure functions $S(q)$ for the five $P_{6,6,6,14}^+$ ILs are shown in Figure 3.21.

Good agreement is achieved between the experiments and simulation results.

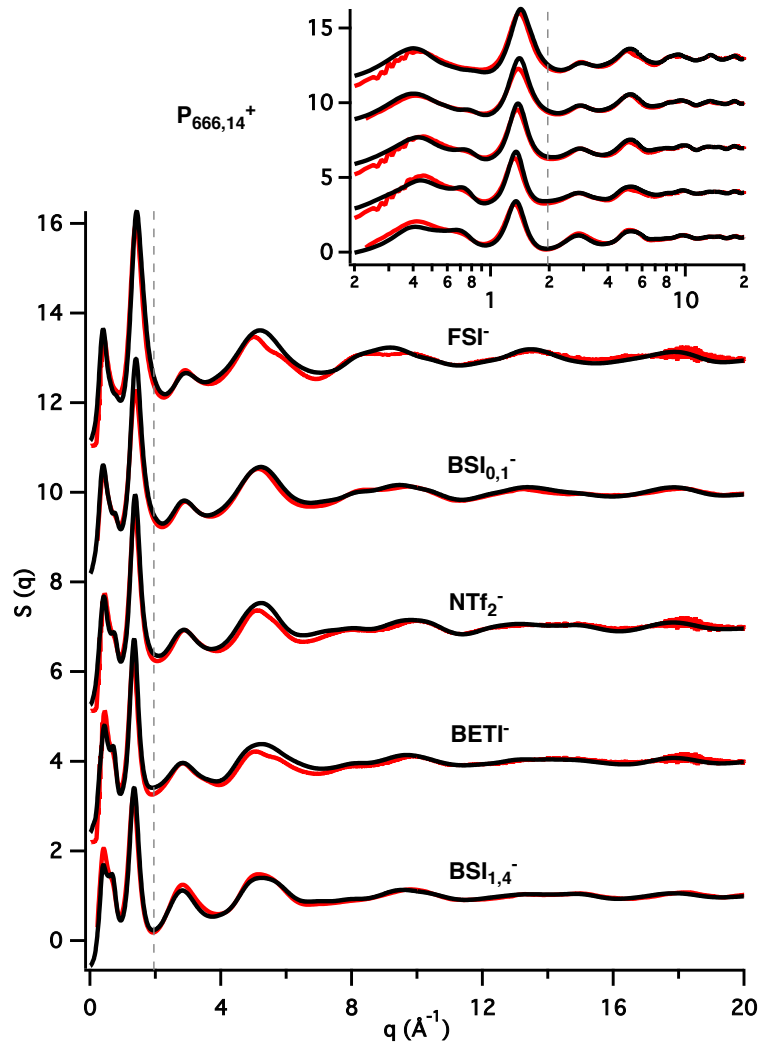


Figure 3.21: The experimental (red) and simulated (black) structure functions $S(q)$ for the five ILs that pair the BSI-anions and the $P_{6,6,6,14}^+$ cation, sequentially offset by 3 units each for clarity. The dashed vertical line at 2 \AA^{-1} marks the approximate boundary between q values associated with intermolecular and intramolecular distances. In the inset, a semilog horizontal axis is also used to emphasize the intermolecular part of $S(q)$.

FSDPs are observed for all five ILs at $q \sim 0.4 \text{ \AA}^{-1}$. Due to the relatively large size of the $\text{P}_{6,6,6,14}^+$ cation, the aggregation of nonpolar domains is dominated by the alkyl tails on the cations. Therefore, the FSDPs locate around the same q value despite the change of anion size. It is noticed that the FSDPs for ILs with the $\text{P}_{6,6,6,14}^+$ cation are at a higher q value than those for $\text{Pyrr}_{1,8}^+$ ILs. A lower q value indicates larger nano-scale aggregations in the system. Therefore, the nonpolar domains in the $\text{P}_{6,6,6,14}^+$ systems are smaller than those in the $\text{Pyrr}_{1,8}^+$ systems. This may seem counterintuitive considering that the $\text{P}_{6,6,6,14}^+$ cation has a tetradecyl tail that is much longer than the octyl tail on the $\text{Pyrr}_{1,8}^+$ cation. This can be explained by the structure differences of the two cations. The $\text{P}_{6,6,6,14}^+$ cation includes three hexyl tails and one tetradecyl tail, all of which are long enough to aggregate and form nonpolar domains.(1; 5; 12) The three hexyl tails are the main contribution to the nonpolar domain formation. Due to the unique structure of the quaternary phosphonium cation, the three hexyl tails are not able to aggregate in the same way as single alkyl tails do, such as for $\text{Im}_{1,8}^+$ and $\text{Pyrr}_{1,8}^+$ ILs. In addition, The tetradecyl tail typically displays multiple local conformations, leading to an effective tail length that is shorter than the linear tetradecyl chain. For ILs with the $\text{Pyrr}_{1,8}^+$ cation, the octyl tails dominate the aggregation and the tails are able to align freely next to the charged network. Therefore, the nonpolar domains in $\text{P}_{6,6,6,14}^+$ systems are smaller than those in the $\text{Pyrr}_{1,8}^+$ systems, despite that the $\text{P}_{6,6,6,14}^+$ cation has multiple alkyl tails. A similar phenomenon was observed in the study by Cosby, *et al.* (39) With the same NTf_2^- anion, the FSDP in $S(q)$ for triethyloctylphosphonium is at a lower q value than that for tributylloctylphosphonium; and the FSDP for triethyldodecylphosphonium is at a lower q value than that for tributylldodecylphosphonium. This is because the tetrahedral structure of phosphonium cations obstruct the aggregation of cationic alkyl tails. Instead, shorter trialkyl tails facilitate the aggregation of the longer alkyl tails.

The charge-charge alternation peaks in $S(q)$ again appear as shoulder peaks. Cation-anion ionic partitioning of $S(q)$ are shown in Figure 3.22. In anion-anion interactions, the amplitude of FSDPs decreases as the anion size increases from FSI^- to $\text{BSI}_{1,4}^-$. There are no FSDPs observed in $S(q)$ for cation-cation interactions. In anion-cation

interactions, however, the amplitude of FSDPs increases with the increased anion size. The adjacency peak ($q \approx 1.4 \text{ \AA}^{-1}$) and charge-charge alternation peak both shift to lower q values as the anion size increases from FSI^- to $\text{BSI}_{1,4}^-$. Though the charge-charge alternation peaks appear as weak shoulder peaks in total $S(q)$, they appear as main peaks in the ionic partitioning.

The sub-ionic partitioning of $S(q)$ to investigate the effect of changing anion size is shown in Figure 3.23. Clearly, the positive and negative cross item components act as “same-type” species at lower q region, and “opposite-type” species at the charge-charge alternation region.

To study the interaction of alkylated tails on the $\text{P}_{6,6,6,14}^+$ cation and the fluorinated tail on the anion, $\text{P}_{6,6,6,14}^+/\text{BSI}_{1,7}^-$ is simulated. Figure 3.20 displays a typical cluster that can be found in the $\text{P}_{6,6,6,14}^+/\text{BSI}_{1,7}^-$ system. We observe the folding of the tetradecyl alkyl tails, and that the three hexyl tails point to different directions and can not align close to each other. The fluorinated tails lie next to either the tetradecyl tails or the hexyl tails, depending on how the anionic heads align with the cationic heads.

3.2.4 Spatial Distribution Functions (SDFs) for $\text{Pyrr}_{1,8}^+/\text{BSI}_{1,4}^-$ and $\text{P}_{6,6,6,14}^+/\text{BSI}_{1,4}^-$

Compared to the sub-ionic peaks for ILs with the $\text{Pyrr}_{1,8}^+$ cation in Figure 3.18, the peaks for $\text{P}_{6,6,6,14}^+$ ILs in Figure 3.23 are at higher q values, which indicates smaller nonpolar domain sizes. The sub-ionic peaks for $\text{P}_{6,6,6,14}^+$ ILs also have higher amplitude, indicating a narrower distribution of inter-ionic spatial configurations. As a tool to look at the average 3-D environment around the molecules, spatial distribution functions (SDFs) are calculated to seek explanations for the higher amplitude of sub-ionic peaks of $S(q)$ for $\text{P}_{6,6,6,14}^+$ ILs compared to $\text{Pyrr}_{1,8}^+$ ILs. SDFs are calculated for $\text{Pyrr}_{1,8}^+/\text{BSI}_{1,4}^-$ and $\text{P}_{6,6,6,14}^+/\text{BSI}_{1,4}^-$, as shown in Figure 3.24. We learn mostly about the adjacency correlations from the SDFs, which is sufficient for the analysis of charge-charge alternation peaks. On the left side of Figure 3.24, there are three sites (blue lobes) of strong H-bonding between the anionic head and the cationic protons.

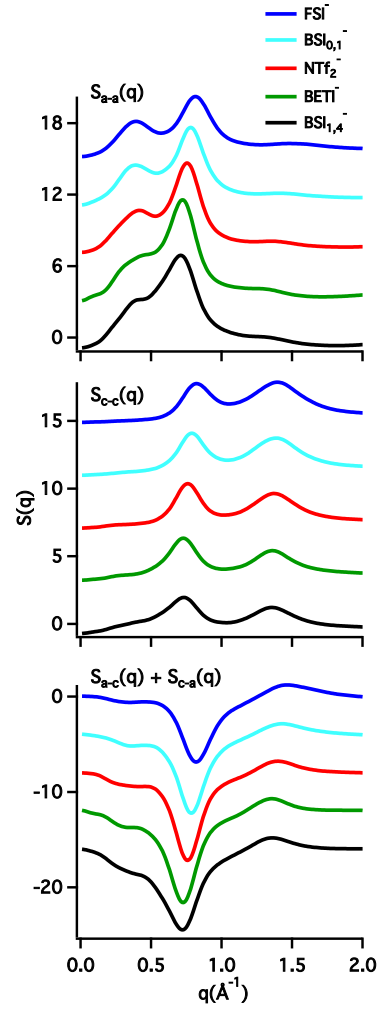


Figure 3.22: Ionic partitioning of $S(q)$ for the five BSI ILs with $P_{6,6,6,14}^+$ cation. Top: anion-anion; center: cation-cation; bottom: anion-cation. From top to bottom, the curves represent the partial $S(q)$ for $P_{6,6,6,14}^+$ with FSI^- (blue), $BSI_{0,1}^-$ (cyan), NTf_2^- (red), $BETI^-$ (green), and $BSI_{1,4}^-$ (black). For clarity, an offset of 3 units is applied to each subsequent curve.

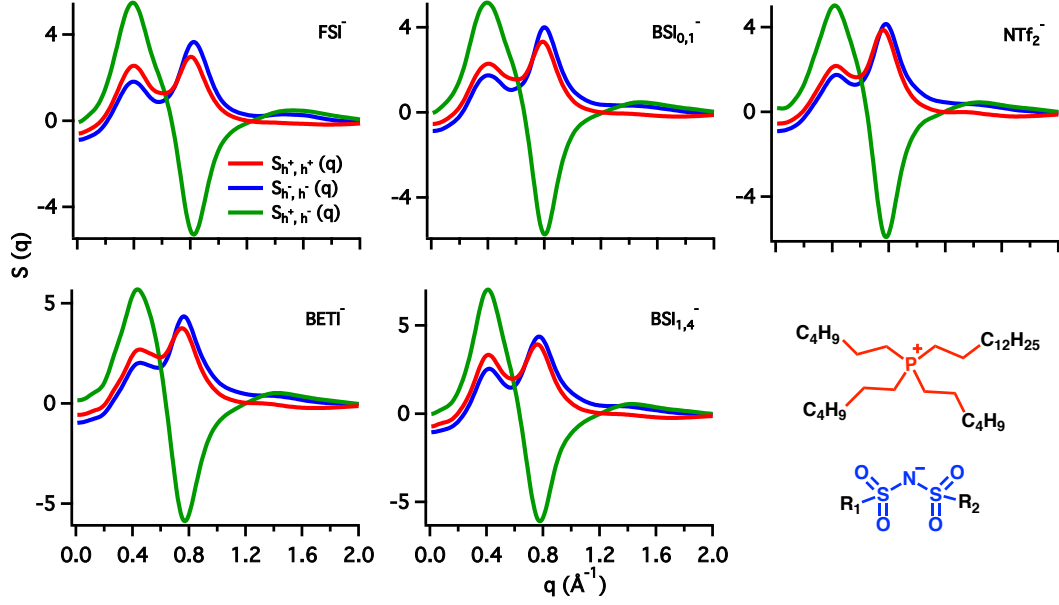


Figure 3.23: Contribution of charged subcomponents in the sub-ionic partitioning of $S(q)$ for the six BSI ILs with $P_{6,6,6,14}^+$ cation. h^+ refers to the cationic head (colored red) and h^- refers to the anionic head (colored blue).

The fluorinated tails (green lobes) are mainly found between the cationic and anionic heads. The cationic heads (red lobes) surround the anions at the outer layer. The alkyl tails (gray lobes) are located right next to the octyl tails, indicating the nonpolar domain aggregation by alkylated tails.

The SDFs for $P_{6,6,6,14}^+/\text{BSI}_{1,4}^-$ on the right side are very different. There are four sites (blue lobes) of H-bonding between the anionic head and the cationic head protons. This can explain the higher amplitude of peaks in the sub-ionic positive-negative component interactions for $P_{6,6,6,14}^+$ ILs. The cationic head probability isosurfaces (red lobes) are of the same shape as the blue lobes and occupy the same positions at an outer layer. The fluorinated tails (green lobes) are found right in between the cationic and anionic heads, whose probability isosurfaces are of the same shape. The fluorinated tails on the $\text{Pyrr}_{1,8}^+/\text{BSI}_{1,4}^-$ can be found outside the cationic and anionic head pairs, while the fluorinated tails on $P_{6,6,6,14}^+/\text{BSI}_{1,4}^-$ are strictly confined between the charged pairs. The alkyl tails (gray lobes) on the $P_{6,6,6,14}^+$ cation locate in between the space of the red lobes. we can see that the red lobes and gray lobes perfectly enclosed the anionic

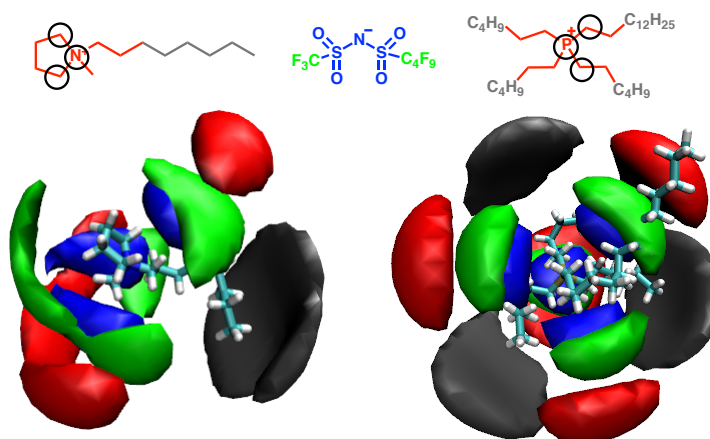


Figure 3.24: Spatial distribution functions for $\text{Pyrr}_{1,8}^+/\text{BSI}_{1,4}^-$ and $\text{P}_{6,6,6,14}^+/\text{BSI}_{1,4}^-$. The probabilities are calculated surrounding the reference cationic head, and the reference atoms are circled. SDFs for the cationic heads are colored red; SDFs for the cationic alkyl tails are colored gray; SDFs for the anionic heads are colored blue; and SDFs for the anionic fluorinated tails are colored green. The cationic head (anionic head) isodensity values are: 2.05 (3.15) for $\text{Pyrr}_{1,8}^+/\text{BSI}_{1,4}^-$, and 1.05 (1.70) for $\text{P}_{6,6,6,14}^+/\text{BSI}_{1,4}^-$; The cationic tail (anionic tail) isodensity values are: 0.95 (1.21) for $\text{Pyrr}_{1,8}^+/\text{BSI}_{1,4}^-$, and 1.82 (2.05) for $\text{P}_{6,6,6,14}^+/\text{BSI}_{1,4}^-$.

components. This is in consistent with the description that the anions are embedded in the cations for $P_{6,6,6,14}^+$ ILs due to its unique structure. The dispersion of alkyl domains in $P_{6,6,6,14}^+/\text{BSI}_{1,4}^-$ explains why the nonpolar domains in $P_{6,6,6,14}^+/\text{BSI}_{1,4}^-$ are smaller than those in $\text{Pyrr}_{1,8}^+/\text{BSI}_{1,4}^-$. The intermediate tails and the quaternary structure of phosphonium cations disturb the mesoscale hydrophobic aggregates.

3.2.5 Fluorous domain aggregation analysis

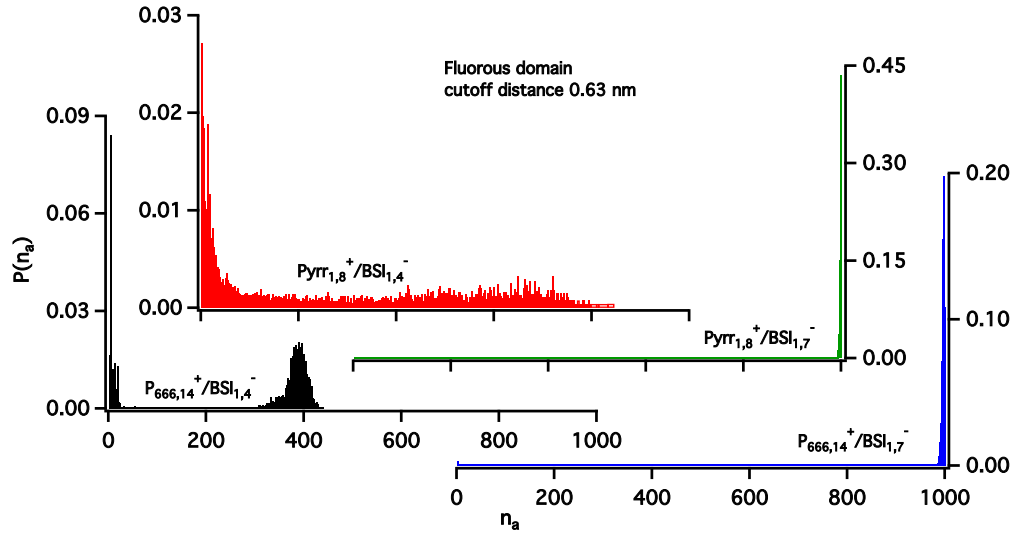


Figure 3.25: Discrete probability distribution of aggregation sizes, $P(n_a)$, as a function of aggregate size number, n_a , for ILs with $\text{Pyrr}_{1,8}^+$ and $P_{6,6,6,14}^+$ cations paired with $\text{BSI}_{1,4}^-$ and $\text{BSI}_{1,7}^-$ anions. All C atoms of the longest perfluoroalkyl tail are used in the analysis of fluorous domains.

Another way to look at the connectivity between fluorinated tails was performed based on the algorithm introduced by Bernardes and Shimizu.(22; 23) The cutoff distance defining whether residues are connected and form an fluorous aggregate is determined to be 0.63 nm, which is consistent with previously calculated value for ILs with the BSI anions.(6; 23) Since there are 1000 ion pairs in each simulation box, the domain size n_a ranges from 0 to 1000.

For the $\text{BSI}_{1,4}^-$ -based ILs in Figure 3.25, the fluorous tails are mostly disconnected but partially connected for $\text{Pyrr}_{1,8}^+/\text{BSI}_{1,4}^-$, while the fluorous tails are primarily

disconnected for $P_{6,6,6,14}^+ / BSI_{1,4}^-$. For $BSI_{1,7}^-$ -based ILs, the fluorinated tails are highly connected both for $Pyrr_{1,8}^+ / BSI_{1,7}^-$ and $P_{6,6,6,14}^+ / BSI_{1,7}^-$. It is expected that the fluorinated tails are more scattered for $P_{6,6,6,14}^+$ ILs because alkyl tails have a disruption effect on the fluorinated tail connectivity.⁽⁶⁾ Figure 3.20 shows that alkylated and fluorinated tails alternate along a charge network, and the alkylated tails together with the fluorinated tails form the hydrophobic domains.

3.2.6 Summary of results for BSI-anion ILs with $Pyrr_{1,8}^+$ and $P_{6,6,6,14}^+$ cations

This section quantitatively describes the structural and physical properties of ILs containing anions in the $BSI_{n,m}^-$ family coupled with pyrrolidinium ($Pyrr_{1,8}^+$) and phosphonium ($P_{6,6,6,14}^+$) cations. These ILs are promising candidates for many applications including energy storage devices and gas absorption, but they are less well understood than those imidazolium based ILs. Through analysis of temperature-dependent viscosity behavior, we noticed the extremely high viscosities and low conductivities of $P_{6,6,6,14}^+$ ILs compared to the $Pyrr_{1,8}^+$ ILs. From conductivity measurements and Walden products we observed that ionicities were quite low for ILs with the $P_{6,6,6,14}^+$ cation, which can be explained by ion pairing and ionic diffusion confined in polar domains. X-ray measurements and MD simulations provide an interesting perspective on the arrangement of fluorinated and alkylated moieties on an ionic level. From the analysis of sub-ionic partitioning of $S(q)$ peaks, we confirm that positive-negative charge alternation results in the formation of charge network, and the tails on cations and anions must decorate them. From the distribution of fluorinated tail aggregate sizes, we find that for cations like $P_{6,6,6,14}^+$, there is an interrupting effect of the cationic tails on the aggregation of fluorinated domains. The differences in physical properties and bulk structure ordering between $Pyrr_{1,8}^+$ ILs and $P_{6,6,6,14}^+$ ILs can be explained by their fundamental structure differences.

3.3 Structure of NTf₂⁻-anion ILs with cationic ether tails

Ether and polyether groups have been exploited for their water-compatibility liquefying and transport-improving properties for many years, including their incorporation into cations and anions to yield liquid ion conductive polymers(40) and zwitterionic liquids(41). Ether tails are more polar and flexible than their alkyl analogues, thus the presence of ether tails interrupts the ordering of nonpolar domains in the system. Relative to alkyl-functionalized ILs, ether-functionalized ILs exhibit lower viscosities and melting points and higher conductivities, making them significantly more useful for practical applications. There are numerous reports of ether functionalized ILs as electrolytes for lithium ion batteries,(42–45) in electrochemical double layer capacitors and in dye sensitized solar cells.(46; 47) In many cases ether or polyether functionalities have been incorporated into IL cations to increase their affinity for CO₂ absorption,(48; 49) SO₂ absorption,(50; 51) extraction of metal ions such as Hg²⁺ and La³⁺,(52; 53) dissolution of carbohydrates, glycolipids and glycoproteins(54–56) and for enzyme stabilization and activation.(44)

To study the effect of ether tails on the bulk structure of ILs, the ILs shown in Figure 3.26 were studied: two imidazolium cations 1-methyl-3-octylimidazolium (Im_{1,8}⁺) and 1-methyl-3-decylimidazolium (Im_{1,10}⁺) and their oligoether analogues 1-methyl-3-(2-(2-ethoxyethoxy)ethyl)imidazolium (Im_{1,EOEOE}⁺) and 1-methyl-1-(2-(2-ethoxyethoxy)ethyl)pyrrolidinium (Pyrr_{1,EOEOE}⁺) paired with NTf₂⁻; two pyrrolidinium cations N-methyl-N-octylpyrrolidinium (Pyrr_{1,8}⁺) and N-methyl-N-decylpyrrolidinium (Pyrr_{1,10}⁺) and their oligoether analogues 1-methyl-3-(2-(2-(2-methoxyethoxy)ethoxy)-ethyl)imidazolium (Im_{1,EOEOEOM}⁺) and 1-methyl-1-(2-(2-(2-methoxyethoxy)ethoxy)-ethyl)pyrrolidinium (Pyrr_{1,EOEOEOM}⁺) paired with NTf₂⁻.

The following Sections 3.3.1 to 3.3.7 are adapted from our research article by Lall-Ramnarine, published in 2017.(10)

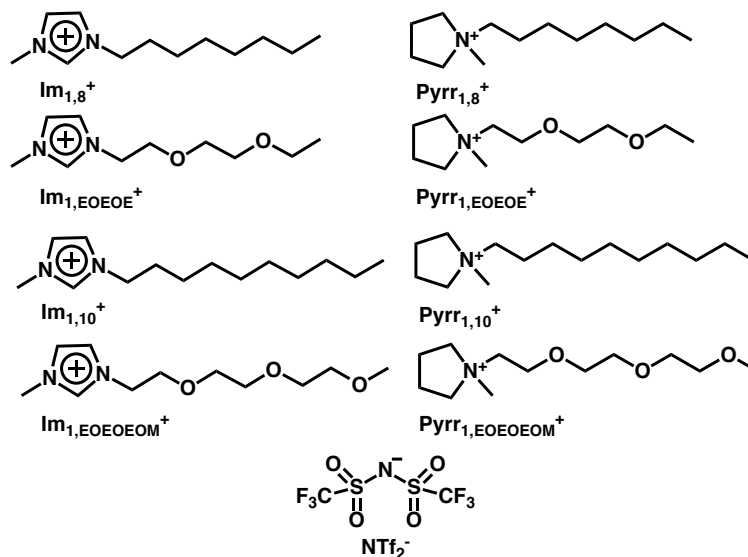


Figure 3.26: Chemical structures of the cations (red) and anions (blue) used for X-ray scattering experiments.

3.3.1 Physical properties: viscosity and conductivity

The viscosities and conductivities of the studied ILs were measured by our collaborators Prof. Sharon Lall-Ramnarine,(10) as shown in Table 3.4. The effect of increasing alkyl chain length on the viscosities within IL families has been well documented in the literature.(57) Viscosities increase with increasing alkyl chain length. The viscosities of the ether-substituted salts are much lower compared to their alkyl analogues, especially for the pyrrolidinium salts. The conductivities of ILs generally decrease as the length of the alkyl chain increases, corresponding with increased viscosities.

Table 3.4: Conductivities and viscosities of NTf₂⁻ ionic liquids at 25 °C. Data was published by Lall-Ramnarine, *et al.*(10).

Cation	Conductivity mS/cm	Viscosity cP
Im _{1,EOEOE} ⁺	1.78	61
Im _{1,8} ⁺	1.41	93
Im _{1,EOEOEOM} ⁺	1.28	80
Im _{1,10} ⁺	0.55	119
Pyr _{1,EOEOE} ⁺	2.0	56
Pyr _{1,8} ⁺	1.1	140
Pyr _{1,EOEOEOM} ⁺	1.5	64
Pyr _{1,10} ⁺	0.69	150

3.3.2 Total structure functions $S(q)$ for NTf_2^- -anion ILs with cation alkyl or ether tails

Transport properties of ionic liquids are highly connected to their nanoscale structure. Previous structural and molecular dynamics studies of imidazolium, ammonium and phosphonium ILs with ether groups have shown that their organization on the molecular scale is different than their normal alkyl chain analogues.(36; 38; 58–61) While alkyl chains tend to exist in extended conformations, ether chains have a large fraction of gauche conformations, particularly across C-C bonds connected to ether oxygens.(38; 58–60) The gauche conformations cause the ether tails to curl around the cations and remain adjacent to the polar, ionic domain of the IL rather than extend to form a separate nonpolar domain, as occurs for long enough alkyl chains.(23; 36; 38; 62) When there is nanosegregation of the nonpolar domains ILs, a first sharp diffraction peak (FSDP, also called “prepeak”) is observed in the X-ray scattering structure function $S(q)$ for $q < 0.5 \text{ \AA}^{-1}$. Existing X-ray scattering results for ether ILs show no evidence of a prepeak, consistent with the tendency of the tails to curl rather than extend to create separate domains.(38; 58; 61; 63)

Figure 3.27 depicts X-ray structure functions for the sets of ether and alkyl imidazolium and pyrrolidinium ILs. The data is consistent with earlier X-ray and MD results.(1; 23; 61) For the alkyylimidazolium ILs, the prepeak is sharp and intense and shifts to lower q values as the alkyl chain extends from octyl to decyl. For the ether-substituted imidazolium ILs, there is no sign of such a prepeak except for a weak, broad shoulder peak in the case of $\text{Im}_{1,EOEOE}^+/\text{NTf}_2^-$. This is also consistent with previous X-ray results on ether ILs.(38; 61; 63) Shimizu, *et al.* have observed that “the suppression of the prepeak in the ether-substituted ILs is not caused by structural changes in the polar network but rather by the (re-)organization around it of the non-polar domains.”(58) It is also clear from the scattering data that the polar network is increasingly perturbed as the ether side chains get longer. Compared to the alkyl imidazolium ILs, the “adjacency peak” ($q \sim 1.4 \text{ \AA}^{-1}$) and “charge-charge alternation peak” ($q \sim 0.86 \text{ \AA}^{-1}$) in $S(q)$ for ether imidazolium ILs become broader and shift to higher q values.

Because the observed experimental structure factors are actually the sums of self- and cross-terms that mostly cancel each other,(64–66) it is easy to over-interpret such peak shifts, but it is clear that the curling of the ether cation tails is having an effect on the polar network structure. The nature of this effect is more easily interpreted through MD simulations, as discussed below and in the literature.(58; 59)

The $S(q)$'s for the pyrrolidinium ILs have similar features as the imidazolium ones, with a minor variation regarding the adjacency peak. The prepeak is evident for alkylpyrrolidinium ILs. Just as in the imidazolium case, there are no prepeaks for the ether pyrrolidinium ILs and the “charge-charge alternation peaks” shift to higher q values as chain length increases. The ether pyrrolidinium adjacency peaks shift slightly to higher q but remain in the same range as the corresponding alkyl ones.

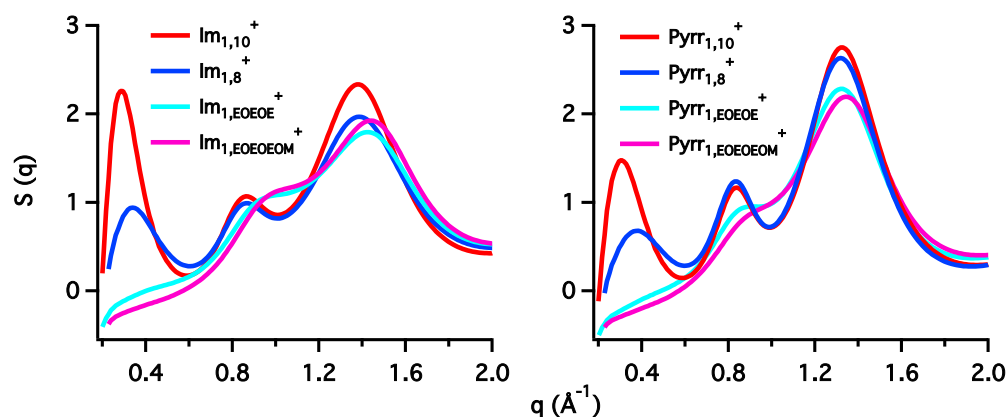


Figure 3.27: Experimental X-ray scattering structure functions $S(q)$ for the studied ILs in Figure 3.26. Figure was published by Lall-Ramnarine, *et al.*(10)

3.3.3 MD simulations

As discussed above, a number of MD simulations have investigated the structure of alkyl and ether imidazolium NTf₂[−] ILs, and alkylpyrrolidinium NTf₂[−] ILs.(13; 23; 38; 58; 59; 62) Since those results were well established, here only ILs with the longest ether chains, Im_{1,EOEOEOM}⁺/NTf₂[−] and Pyr_{1,EOEOEOM}⁺/NTf₂[−], were simulated.

Total structure factors $S(q)$ and their partitioning into components

The liquid structure functions $S(q)$ obtained from the X-ray scattering experiments and MD simulations on $\text{Im}_{1,\text{EOEOEOM}}^+/\text{NTf}_2^-$ and $\text{Pyrr}_{1,\text{EOEOEOM}}^+/\text{NTf}_2^-$ are compared in Figure 3.28. Though no prepeak is observed in the range of $0.25 < q < 0.50 \text{ \AA}^{-1}$ in the X-ray experimental data for the oligoethers, small shoulders in the simulated $S(q)$ are observed for $\text{Im}_{1,\text{EOEOEOM}}^+/\text{NTf}_2^-$.

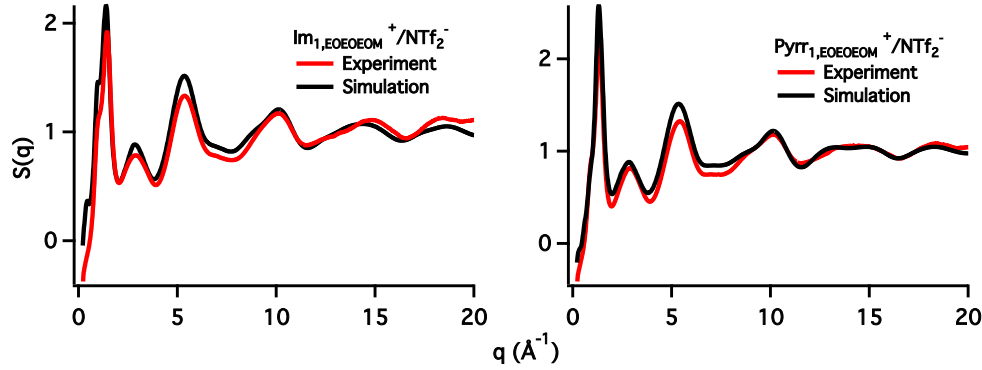


Figure 3.28: Comparisons of the liquid structure functions $S(q)$ for the $\text{Im}_{1,\text{EOEOEOM}}^+/\text{NTf}_2^-$ and $\text{Pyrr}_{1,\text{EOEOEOM}}^+/\text{NTf}_2^-$ ILs obtained from high energy X-ray scattering experiments (red) and from MD simulations (black). Figure was published by Lall-Ramnarine, *et al.*(10)

In the analysis of the experimental scattering $S(q)$, it is noticed that there were shifts and changes in the charge alternation peaks for both families of ILs as the length of the ether chain increased, indicating a disruption of the polar network. However, the nature of the disruption is obscured in the total $S(q)$ due to the effects of massive cancellations among the ionic scattering terms. MD simulations allow us partition the total structure functions into meaningful correlation-based components. The top panel of Figure 3.29 shows the ionic partitioning of $S(q)$ defined by Eqn. 2.3.

At first glance the partitioned $S(q)$ contributions for $\text{Im}_{1,\text{EOEOEOM}}^+/\text{NTf}_2^-$ and $\text{Pyrr}_{1,\text{EOEOEOM}}^+/\text{NTf}_2^-$ appear very similar in shape, with a slight difference below $q = 0.4 \text{ \AA}^{-1}$. Though the “charge-charge alternation peak” in total $S(q)$ appears around $q = 0.86 \text{ \AA}^{-1}$, the ionic components are at a much lower q value around 0.6 \AA^{-1} . The

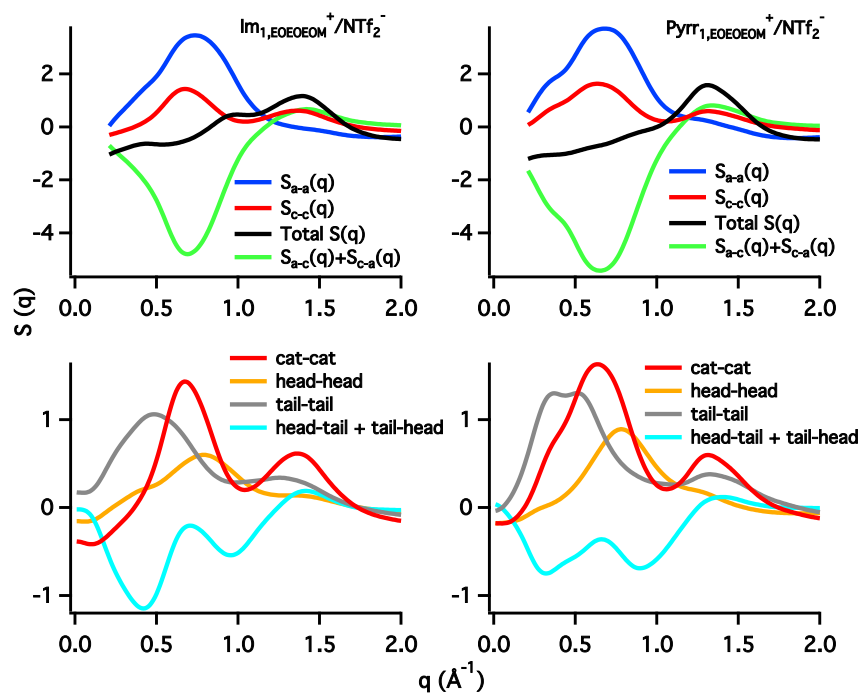


Figure 3.29: Ionic and sub-ionic partitioning of the simulated structure factors $S(q)$ for $\text{Im1,EOEOEOM}^+/\text{NTf}_2^-$ and $\text{Pyrr1,EOEOEOM}^+/\text{NTf}_2^-$. Figure was published by Lall-Ramnarine, *et al.*(10)

positive contributions from anion-anion and cation-cation correlations are offset by the negative contributions of the anion-cation/cation-anion correlations, giving rise to the features in the observed total $S(q)$. However, the effects of oligoether substitution on the structure of the ILs only become clear when comparison is made with the partitioned structure factors of a corresponding alkyl IL, $\text{Pyrr}_{1,10}^+/\text{NTf}_2^-$, as shown in Figure 3.30. The partitioned adjacency peaks ($q \sim 1.3 - 1.4 \text{ \AA}^{-1}$) in the ether and alkyl ILs are similar in shape, but there are enormous differences for the charge alternation peaks ($q \sim 0.8 - 0.9 \text{ \AA}^{-1}$) and prepeaks ($q < 0.5 \text{ \AA}^{-1}$) between the ether and alkyl ILs. For $\text{Pyrr}_{1,10}^+/\text{NTf}_2^-$, all of the ionic correlations show narrow, well-resolved and strong peaks and anti-peaks, indicating a high degree of nanostructural organization. The opposite is true for the oligoethers, where there are only single, broad peaks in each of the ionic correlations over the range $0.3 < q < 1.0 \text{ \AA}^{-1}$. The broad charge alternation peaks of ether ILs are at lower q values compared to the charge alternation peaks in $\text{Pyrr}_{1,10}^+/\text{NTf}_2^-$, indicating an increase in spacing within the polar network due to the curling of the ether tails around and among the ions.

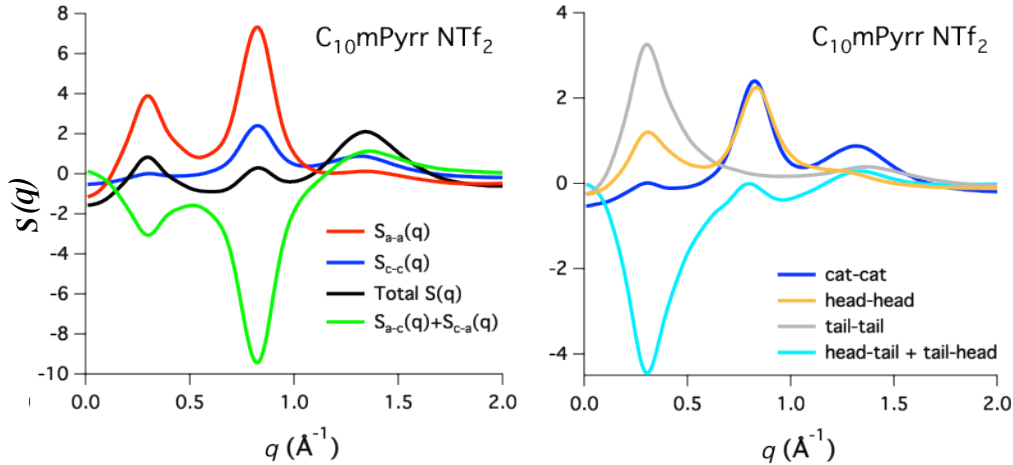


Figure 3.30: Ionic and sub-ionic partitioning of $S(q)$ for N-decyl-N-methylpyrrolidinium bis(trifluoromethylsulfonyl)imide ($\text{C}_{10}\text{mPyrr NTf}_2$). Data is from Refs. [38] and [37], and the figure is replotted using the data published in Ref. [10].

The effect of ether tail curling into the polar network is also apparent when the partial $S(q)$ for cation-cation correlation is further decomposed into correlations for the

cationic head groups and ether tails, as shown in the bottom panel of Figure 3.29. For $\text{Pyrr}_{1,10}^+/\text{NTf}_2^-$, as shown in Figure 3.30, there is a strong self-correlation for the cation heads in the charge alternation region, and another one in the polarity alternation region. When the decyl group is replaced by the oligoether as in $\text{Pyrr}_{1,\text{EOEOEOM}}^+/\text{NTf}_2^-$, the head-head correlation peak in the charge alternation region shifts to lower q value, suggesting an increase in spacing between cation heads as the ether tails curl around them. Moreover, the head-head prepeak disappears for $\text{Pyrr}_{1,\text{EOEOEOM}}^+/\text{NTf}_2^-$, indicating the absence of separate nonpolar domains in the system. $\text{Im}_{1,\text{EOEOEOM}}^+/\text{NTf}_2^-$ shows the same behavior.

3.3.4 Snapshots of the equilibrated simulation boxes

Figure 3.32 shows the snapshots of the equilibrated simulation boxes for $\text{Pyrr}_{1,\text{EOEOEOM}}^+/\text{NTf}_2^-$ and $\text{Im}_{1,\text{EOEOEOM}}^+/\text{NTf}_2^-$. The color scheme is given in Figure 3.31. We observe a sponge-like structure with charge network composed of cationic heads (red) and anionic head (blue), accommodated with ether tails. As for ILs with long alkyl tails, (1; 5; 23; 36; 58) the ether chains do have their own network of connectivity. While the ether chains are more polar than alkyl analogues, they still induce a degree of local nanophase segregation. The same effect were observed for more strongly polar alkylsilyl and alkylsiloxy tails on the same cations.(41; 67) In the case of the ethers, however, this segregation is incomplete and disordered, as shown by the partitioned structure factors discussed above. The absent of a distinct prepeak in the low q region indicates the incomplete segregation in ether IL systems. Further understanding of the local environment can be obtained by studying selected radial distribution functions to identify specific structural interactions among the components of the ILs.

3.3.5 Structure of $\text{Im}_{1,\text{EOEOEOM}}^+/\text{NTf}_2^-$: Radial distribution functions

Shimizu, *et al.* performed simulations on ether imidazolium ILs where the ether groups are connected by a methylene (CH_2) group between the imidazolium nitrogen and the first ether oxygen.(58) Whereas in our ether ILs, an ethylene (CH_2CH_2) group connects the cation nitrogen and the first ether oxygen. This difference is critical because

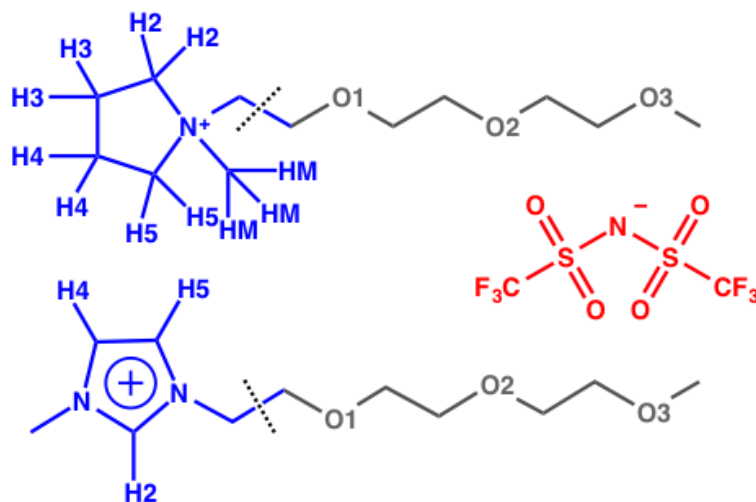


Figure 3.31: Color scheme for Figures 3.32. The labeling scheme follows the precedent of Smith, *et al.* (59) Figure was published by Lall-Ramnarine, *et al.*(10)

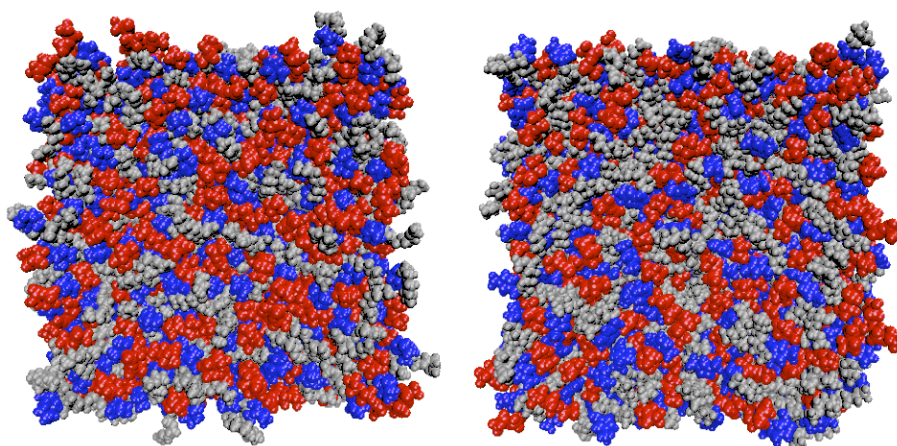


Figure 3.32: sub-ionic partitioning of the equilibrated simulation boxes for $\text{Pyrr1,EOEOEOM}^+/\text{NTf}_2^-$ (left) and $\text{Im1,EOEOEOM}^+/\text{NTf}_2^-$ (right). The dimensions of the two boxes are 8.54 and 8.66 nm, respectively, on each side. The color scheme is explained in Figure 3.31. Figure was published by Lall-Ramnarine, *et al.*(10)

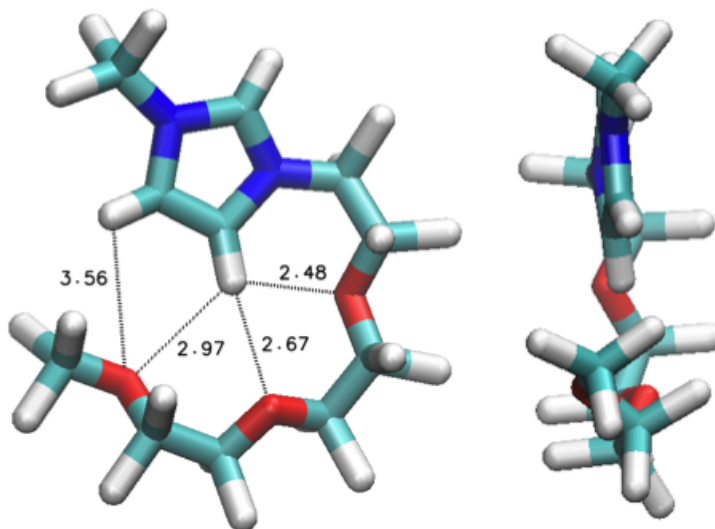


Figure 3.33: Two views of the structure of an $\text{Im}_{1,\text{EOEOEOM}}^+$ cation selected from our MD simulation showing the ether chain conformation close to the plane of the imidazolium ring. Distances between atoms are given in Å. Figure was published by Lall-Ramnarine, *et al.*(10)

the extra CH_2 group enables enough conformational freedom for the first ether oxygen (labeled O1 in Figure 3.31) to interact with the nearest hydrogens of the cation head group to form a 6-member ring (counting from the H2 or H5 atom to O1). Such a configuration is shown in Figure 3.33. This kind of intramolecular interaction from the first oxygen to the imidazolium ring is sterically precluded for the shorter methylene-linked ether ILs such as $\text{Im}_{1,\text{MOM}}^+/\text{NTf}_2^-$ and $\text{Im}_{1,\text{MOEOM}}^+/\text{NTf}_2^-$, as the oxygen atoms cannot approach the imidazolium ring.(58; 61; 63) Smith, *et al.* performed MD simulations on two shorter ethylene-linked ether ILs ($\text{Im}_{1,\text{EOM}}^+/\text{NTf}_2^-$ and $\text{Im}_{1,\text{EOEOM}}^+/\text{NTf}_2^-$ as well as the corresponding BF_4^- -salts). They observed strong intramolecular correlations between O1 and the ring protons, while the correlations for O2 were primarily intermolecular.(59) In their ethylene-linked imidazolium oligoether ILs, Smith, *et al.* found that the nearest ether oxygen (O1) is most likely to interact with the protons on the imidazolium ring, while in the methylene-linked ILs studied by Shimizu, *et al.*, it is the terminal oxygen that is mostly likely to interact with the ring protons.(58; 59)

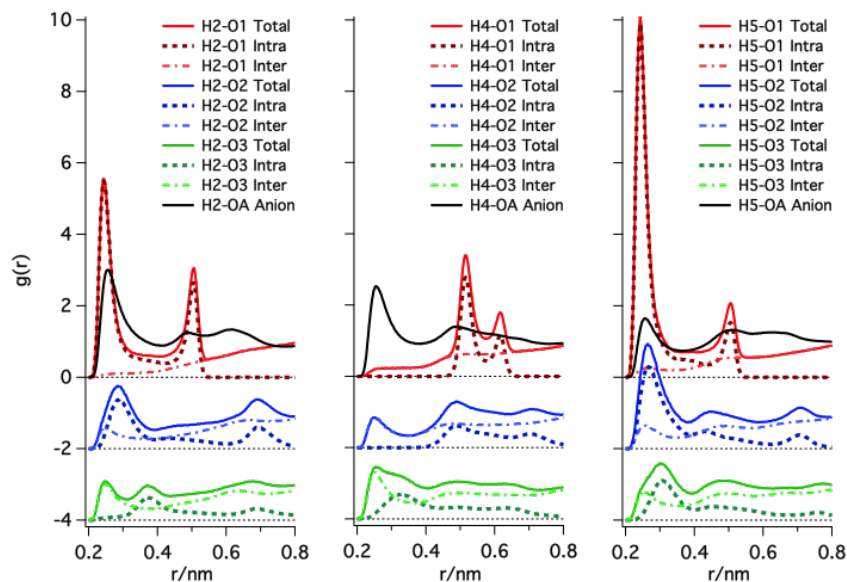


Figure 3.34: Radial distribution functions among the hydrogen atoms on the cation ring in $\text{Im}_{1,\text{EOEOEOM}}^+/\text{NTf}_2^-$ and the oxygen atoms in the oligoether and anion moieties. The labels are explained in Figure 3.31. The total RDFs for each interaction are partitioned into intramolecular and intermolecular correlations. Note that the four oxygen atoms of the anion are labeled together as OA. For clarity, the RDFs for O2 and O3 are offset by -2 and -4 units, respectively. Figure was published by Lall-Ramnarine, *et al.*(10)

Figure 3.34 shows the RDFs between the imidazolium ring hydrogen atoms and the ether and anion oxygen atoms for $\text{Im}_{1,\text{EOEOEOM}}^+/\text{NTf}_2^-$. The RDFs are also partitioned into intramolecular and intermolecular components. The interaction is intramolecular if both atoms are on the same ion. All the graphs are presented on the same vertical scale. We can see that the first ether oxygen O1 has a very high probability of interacting with H5 proton and a high probability of being near H2. O1 has a very low probability of being located near the H4 proton, since H4 is on the far side of the ring relative to the ether tails. It also shows in Figure 3.34 that the interaction between O1 and the ring protons is intermolecular for steric reasons, and would require the unlikely close approach of two cations. The middle oxygen in the ether chain, O2, has lower probabilities of interaction with the ring hydrogens but they still rank in the same order, $\text{H5} > \text{H2} > \text{H4}$. Again, the interaction between O2 and H2 and H5 are mainly intramolecular while the interaction between O2 and H4 is intermolecular, for the same steric reasons. The terminal oxygen O3 has the highest probability of interacting with H4 among all the ether oxygens. The partitioned RDFs are in accord with the partitioned analysis by Smith for the shorter ethylene-linked ether chains, although they did not distinguish between H4 and H5.⁽⁵⁹⁾ The partitioned RDFs indicate that the interactions of O1 and O2 with H2 and H5 are predominantly intramolecular, while the interactions of O3 are mostly intermolecular, although there are weaker (longer) intramolecular interactions between O1 and the ring protons.⁽⁵⁹⁾ The RDFs indicate that association of the oxygens (OA) on the NTf_2^- -anion with the ring hydrogens is strongest for H2, which is more acidic than H4 and H5. Despite the fact that H4 and H5 have essentially the same acidity, the anion oxygens associate more with H4 than H5. This is likely due to the competition from the intramolecular O2 oxygen for the H5 site and the lack of such competition for the H4 site.

The hydrogen-oxygen radial distribution functions for $\text{Im}_{1,\text{EOEOEOM}}^+/\text{NTf}_2^-$ point to a large extent of interactions between the ether tails and the imidazolium head groups, which disrupt the structure of the polar network as noted earlier. The analysis of the methylene-linked imidazolium ether ILs ($\text{Im}_{1,\text{MOM}}^+/\text{NTf}_2^-$, $\text{Im}_{1,\text{MOEOM}}^+/\text{NTf}_2^-$ and $\text{Im}_{1,\text{MOEOEOM}}^+/\text{NTf}_2^-$) by Shimizu described a situation where the curling ether

tails form a thin sheath around the polar network of the IL but do not disrupt it.(58) Between this work and theirs, the description of the RDFs for the terminal oxygen (O8 in Figure 8 in Ref. [58] and O3 in our case) is consistent, but it is very different for the nearest oxygens. The structural, dynamical and transport consequences of this minor modification in side chain structure requires further investigation.

3.3.6 Structure of $\text{Pyrr}_{1,\text{EOEOEOM}}^+/\text{NTf}_2^-$: Radial distribution functions

The corresponding H-O radial distribution functions for $\text{Pyrr}_{1,\text{EOEOEOM}}^+/\text{NTf}_2^-$ are calculated to compare with the imidazolium system, as shown in Figure 3.35. The protons on alpha carbons bonded to the nitrogen center are very weakly acidic. We found that O1 ether oxygens have a very high probability of interacting with the methyl protons (HM), followed by H(2,5) and then H(3,4). Although O1 has the same degree of adjacency to HM and H(2,5), the methyl protons (HM) are free to rotate around the methyl carbon to optimize their interaction with O1 while the methylene protons (H2 and H5) cannot, thus the O1-HM interactions are predominant. Interactions of O2 with HM (at slightly longer distances) are equally intramolecular and intermolecular, while those with the ring protons H2 and H5 are mostly intermolecular. Interactions of O3 with the methyl protons (HM) and ring protons (H2, H3, H4, H5) are primarily intermolecular with equal probabilities. Interactions of anion oxygens (OA) with the ring protons are slightly more probable than the those with the HM protons. This is to be expected considering the strong competition for the HM site by the O1 ether oxygens. For all the ring protons (H2, H3, H4 and H5), the nearest neighbors were most likely to be NTf_2^- - anions. As in the imidazolium case, it would be interesting to examine the structural consequences of using methylene-bridged ether groups and the consequences for diffusivity and viscosity.

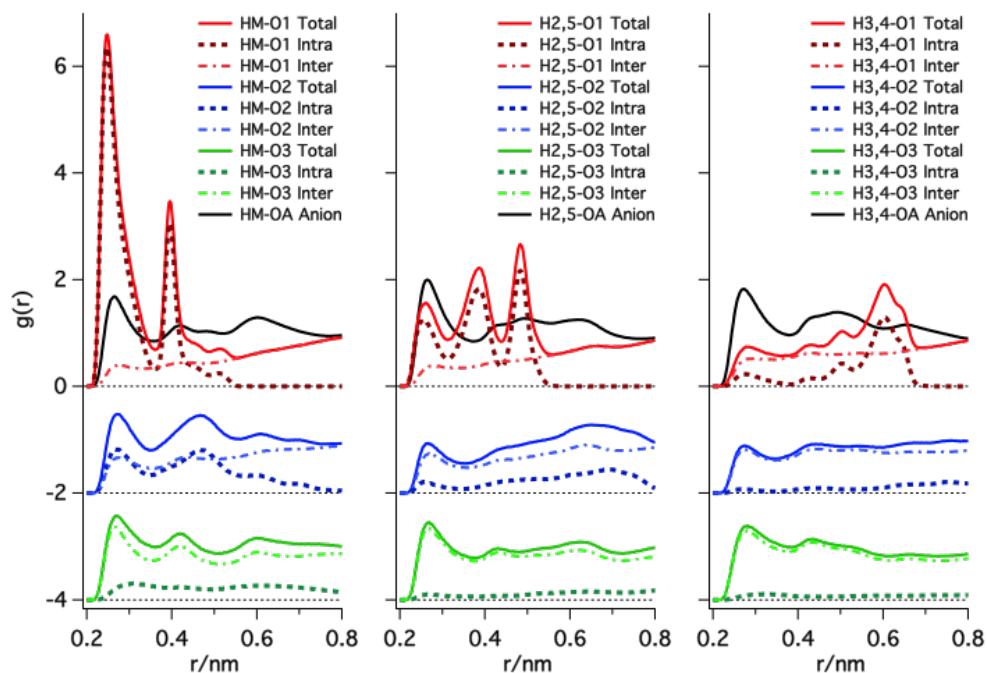


Figure 3.35: Radial distribution functions among hydrogen atoms on the cationic head group in $\text{Pyr}_{11}\text{EOEOEOM}^+/\text{NTf}_2^-$ and the oxygen atoms in the oligoether and anion moieties. The labels are explained in Figure 3.31. The total RDFs for each interaction are partitioned into intramolecular and intermolecular correlations. Note that the four oxygen atoms of the anion are labeled together as OA. For clarity, the RDFs for O2 and O3 are offset by -2 and -4 units, respectively. Figure was published by Lall-Ramnarine, *et al.*(10)

3.3.7 Summary of structural studied of ILs with cationic oligoether tails

For the ILs studied in this section, the viscosities of ether-substituted ILs are much lower than their alkyl analogues, especially for pyrrolidinium based ILs. X-ray scattering data shows that the polar networks of imidazolium and pyrrolidinium IL families become disrupted when the oligoether chains are present. There are plenty of evidence pointing to ether chain curling and disruptive interaction with the polar parts of the IL, particularly the cations. The weakened polar network interactions, combined with less segregation of the cation side chains, improve the mobility of the ions in the ether ILs and reduce their viscosities compared to the alkyl cases.

The interactions between the imidazolium cation heads and their oligoether tails may provide a mechanism for such disruption of the polar network. Notably, an important fraction of these specific interactions are intramolecular and operate via the first and second oxygens in the ether chain, through favorable interactions in the case of O1 and hydrogen bonds in the case of O2. This is because the ether chains are linked by ethylene groups that provide the conformational flexibility for the first oxygen to closely approach the H2 and H5 protons of the imidazolium ring, and also likely provide an optimal configuration for H-bonding of O2 with the same protons. Other groups have done X-ray scattering and MD simulations on imidazolium ILs with methylene-linked oligoether tails that are sterically restricted from having such intramolecular interactions involving the first oxygen, and simulations showed that their structures are different on the molecular scale.(58; 61; 63) Shimizu, *et al.* compared the methylene-linked imidazolium ether cations to scorpions because they curl their tails above their bodies.(58) We think an apt comparison for the ethylene-linked imidazolium ether cations would be with lizards, since some species can curl their tails from side-to-side. It remains to be seen whether such distinctions lead to exploitable differences in structural, physical or dynamical properties between methylene- and ethylene-linked ether ILs.

3.4 Conclusions

In this chapter, the bulk structure of ILs was examined. The studied ILs belong to three families: the fluorinated-anion ILs with imidazolium cations, the fluorinated-anion ILs with non-aromatic pyrrolidinium and phosphonium cations, and the NTf_2^- -anion ILs with cationic oligoether tails. The physical properties and bulk structure of ILs are related to their molecular structures. It is found that long anionic fluorinated tails can form nanoscale nonpolar domains in the system, just as the alkyl tails do. When both long alkyl and fluorinated tails are present, they form into nonpolar domains together instead of spatially separated domains due to charge alternations. When the cationic alkyl tails are replaced by more polar oligoether analogues, the viscosities of the ILs are reduced significantly and their conductivities increase. The ether chains curl and interact with the polar parts of the IL. The ether oxygens form inter- and intra-molecular hydrogen bonding with ring protons, which disrupts the charge network formed by the cationic and anionic heads. As a result, a prepeak is often absent for ILs with oligoether tails.

Bibliography

- [1] A. Triolo, O. Russina, H.-J. Bleif, and E. Di Cola. “Nanoscale segregation in room temperature ionic liquids.” *J. Phys. Chem. B*, 111, 4641–4644, 2007. doi:10.1021/jp067705t.
- [2] D. Xiao, L. G. Hines, S. Li, R. A. Bartsch, E. L. Quitevis, O. Russina, and A. Triolo. “Effect of cation symmetry and alkyl chain length on the structure and intermolecular dynamics of 1,3-dialkylimidazolium bis(trifluoromethanesulfonyl)amide ionic liquids.” *J. Phys. Chem. B*, 113, 6426–6433, 2009. doi:10.1021/jp8102595.
- [3] K. Fujii, S. Seki, S. Fukuda, T. Takamuku, S. Kohara, Y. Kameda, Y. Umebayashi, and S.-i. Ishiguro. “Liquid structure and conformation of a low-viscosity ionic liquid, N-methyl-N-propyl-pyrrolidinium bis(fluorosulfonyl) imide

- studied by high-energy X-ray scattering.” *J. Mol. Liq.*, 143, 64–69, 2008. doi:10.1016/j.molliq.2008.05.011.
- [4] J. Huang and A. F. Hollenkamp. “Thermal behavior of ionic liquids containing the FSI anion and the Li^+ cation.” *J. Phys. Chem. C*, 114, 21840–21847, 2010. doi:10.1021/jp107740p.
- [5] O. Russina, A. Triolo, L. Gontrani, R. Caminiti, D. Xiao, J. Hines, Larry G., R. A. Bartsch, E. L. Quitevis, N. Plekhova, and K. R. Seddon. “Morphology and intermolecular dynamics of 1-alkyl-3-methylimidazolium bis(trifluoromethane)sulfonylamide ionic liquids: structural and dynamic evidence of nanoscale segregation.” *J. Phys.: Condens. Matter*, 21, 424121, 2009. doi:10.1088/0953-8984/21/42/424121.
- [6] M. Zhao, B. Wu, S. I. Lall-Ramnarine, J. D. Ramdihal, K. A. Papacostas, E. D. Fernandez, R. A. Sumner, C. J. Margulis, J. F. Wishart, and E. W. Castner. “Structural analysis of ionic liquids with symmetric and asymmetric fluorinated anions.” *J. Chem. Phys.*, 151, 074504, 2019. doi:10.1063/1.5111643.
- [7] F. Lo Celso, G. B. Appetecchi, E. Simonetti, M. Zhao, E. W. Castner, Jr., U. Keiderling, L. Gontrani, A. Triolo, and O. Russina. “Microscopic Structural and Dynamic Features in Triphilic Room Temperature Ionic Liquids.” *Front. Chem.*, 7, 285, 2019. doi:10.3389/fchem.2019.00285.
- [8] H. Shirota and H. Fukazawa. “Atom Substitution Effects in Ionic Liquids: A Microscopic View by Femtosecond Raman-Induced Kerr Effect Spectroscopy.” chapter 9, 201–224. Intech. Open, 2011. doi:10.5772/14817.
- [9] H. Tokuda, S. Tsuzuki, M. A. B. H. Susan, K. Hayamizu, and M. Watanabe. “How Ionic Are Room-Temperature Ionic Liquids? An Indicator of the Physicochemical Properties.” *J. Phys. Chem. B*, 110, 19593–19600, 2006. doi:10.1021/jp064159v.
- [10] S. I. Lall-Ramnarine, M. Zhao, C. Rodriguez, R. Fernandez, N. Zmich, E. D. Fernandez, S. B. Dhiman, E. W. Castner, Jr., and J. F. Wishart. “Connecting

- structural and transport properties of ionic liquids with cationic oligoether chains.” *J. Electrochem. Soc.*, 164, H5247–H5262, 2017. doi:10.1149/2.0371708jes.
- [11] T. J. Hughes, T. Syed, B. F. Graham, K. N. Marsh, and E. F. May. “Heat capacities and low temperature thermal transitions of 1-hexyl and 1-octyl-3-methylimidazolium bis(trifluoromethylsulfonyl)amide.” *J. Chem. Eng. Data*, 56, 2153–2159, 2011. doi:10.1021/je101213p.
- [12] K. B. Dhungana, L. F. O. Faria, B. Wu, M. Liang, M. C. C. Ribeiro, C. J. Margulis, and E. W. Castner, Jr. “Structure of cyano-anion ionic liquids: X-ray scattering and simulations.” *J. Chem. Phys.*, 145, 024503, 2016. doi:10.1063/1.4955186.
- [13] H. K. Kashyap, C. S. Santos, N. S. Murthy, J. J. Hettige, K. Kerr, S. Ramati, J. Gwon, M. Gohdo, S. I. Lall-Ramnarine, J. F. Wishart, C. J. Margulis, and E. W. Castner, Jr. “Structure of 1-Alkyl-1-methylpyrrolidinium Bis(trifluoromethylsulfonyl)amide Ionic Liquids with Linear, Branched, and Cyclic Alkyl Groups.” *J. Phys. Chem. B*, 117, 15328–15337, 2013. doi:10.1021/jp403518j.
- [14] T. L. Greaves, D. F. Kennedy, Y. Shen, A. Weerawardena, A. Hawley, G. Song, and C. J. Drummond. “Fluorous protic ionic liquid exhibits a series of lyotropic liquid crystalline mesophases upon water addition.” *J. Mol. Liq.*, 210, 279–285, 2015. doi:10.1016/j.molliq.2015.03.037.
- [15] T. L. Greaves and C. J. Drummond. “Solvent nanostructure, the solvophobic effect and amphiphile self-assembly in ionic liquids.” *Chem. Soc. Rev.*, 42, 1096–1120, 2013. doi:10.1039/C2CS35339C.
- [16] Y. Shen, D. F. Kennedy, T. L. Greaves, A. Weerawardena, R. J. Mulder, N. Kirby, G. Song, and C. J. Drummond. “Protic ionic liquids with fluorous anions: physicochemical properties and self-assembly nanostructure.” *Phys. Chem. Chem. Phys.*, 14, 7981–7992, 2012. doi:10.1039/C2CP40463J.
- [17] O. Russina, F. Lo Celso, M. Di Michiel, S. Passerini, G. B. Appetecchi, F. Castiglione, A. Mele, R. Caminiti, and A. Triolo. “Mesoscopic structural organization

- in triphilic room temperature ionic liquids.” *Faraday Discuss.*, 167, 499–513, 2013. doi:10.1039/C3FD00056G.
- [18] F. Lo Celso, Y. Yoshida, R. Lombardo, C. Jafta, L. Gontrani, A. Triolo, and O. Russina. “Mesoscopic structural organization in fluorinated room temperature ionic liquids.” *C. R. Chim.*, 21, 757–770, 2018. doi:10.1016/j.crci.2018.02.001.
- [19] K. Shimizu, A. A. Freitas, and J. N. Canongia Lopes. “Structural characterization of the $[C_nC_{1im}][C_4F_9SO_3]$ ionic liquid series: Alkyl versus perfluoroalkyl side chains.” *J. Mol. Liq.*, 226, 28–34, 2017. doi:10.1016/j.molliq.2016.08.014.
- [20] W. Humphrey, A. Dalke, and K. Schulten. “VMD – Visual Molecular Dynamics.” *J. Mol. Graph. Model.*, 14, 33–38, 1996. doi:10.1016/0263-7855(96)00018-5.
- [21] J. J. Hettige, J. C. Araque, and C. J. Margulis. “Bicontinuity and Multiple Length Scale Ordering in Triphilic Hydrogen-Bonding Ionic Liquids.” *J. Phys. Chem. B*, 118, 12706–12716, 2014.
- [22] C. E. S. Bernardes, M. E. Minas da Piedade, and J. N. Canongia Lopes. “The Structure of Aqueous Solutions of a Hydrophilic Ionic Liquid: The Full Concentration Range of 1-Ethyl-3-methylimidazolium Ethylsulfate and Water.” *J. Phys. Chem. B*, 115, 2067–2074, 2011. doi:10.1021/jp1113202.
- [23] K. Shimizu, C. E. S. Bernardes, and J. N. Canongia Lopes. “Structure and Aggregation in the 1-Alkyl-3-Methylimidazolium Bis(trifluoromethylsulfonyl)imide Ionic Liquid Homologous Series.” *J. Phys. Chem. B*, 118, 567–576, 2014. doi:10.1021/jp409987d.
- [24] M. Brehm and B. Kirchner. “TRAVIS - A Free Analyzer and Visualizer for Monte Carlo and Molecular Dynamics Trajectories.” *J. Chem. Inf. Model.*, 51, 2007–2023, 2011. doi:10.1021/ci200217w.
- [25] F. Castiglione, M. Moreno, G. Raos, A. Famulari, A. Mele, G. B. Appetecchi, and S. Passerini. “Structural Organization and Transport Properties of Novel

- Pyrrolidinium-Based Ionic Liquids with Perfluoroalkyl Sulfonylimide Anions.” *J. Phys. Chem. B*, 113, 10750–10759, 2009. doi:10.1021/jp811434e.
- [26] L. Sanchez-Cupido, J. M. Pringle, A. L. Siriwardana, A. Unzurrunzaga, M. Hilder, M. Forsyth, and C. Pozo-Gonzalo. “Water-facilitated electrodeposition of neodymium in a phosphonium-based ionic liquid.” *J. Phys. Chem. Lett.*, 10, 289–294, 2019. doi:10.1021/acs.jpcclett.8b03203.
- [27] R. Yunis, G. M. Girard, X. Wang, H. Zhu, A. J. Bhattacharyya, P. Howlett, D. R. MacFarlane, and M. Forsyth. “The anion effect in ternary electrolyte systems using poly(diallyldimethylammonium) and phosphonium-based ionic liquid with high lithium salt concentration.” *Solid State Ion.*, 327, 83–92, 2018. doi:10.1016/j.ssi.2018.10.018.
- [28] V. S. Kandagal, F. Chen, E. Jansson, J. M. Pringle, and M. Forsyth. “Molecular simulation study of CO₂ and N₂ absorption in a phosphonium based organic ionic plastic crystal.” *J. Chem. Phys.*, 147, 124703, 2017. doi:10.1063/1.4993654.
- [29] F. Philippi, D. Rauber, J. Zapp, and R. Hempelmann. “Transport properties and ionicity of phosphonium ionic liquids.” *Phys. Chem. Chem. Phys.*, 19, 23015–23023, 2017. doi:10.1039/C7CP04552B.
- [30] W. Xu, E. I. Cooper, and C. A. Angell. “Ionic Liquids: Ion Mobilities, Glass Temperatures, and Fragilities.” *J. Phys. Chem. B*, 107, 6170–6178, 2003. doi:10.1021/jp0275894.
- [31] C. A. Angell. *Ionic Liquids in the Temperature Range 150 - 1500 K: Patterns and Problems*, chapter 1, 1–24. Wiley, 2010.
- [32] H. Tokuda, K. Ishii, M. A. B. H. Susan, S. Tsuzuki, K. Hayamizu, and M. Watanabe. “Physicochemical Properties and Structures of Room-Temperature Ionic Liquids. 3. Variation of Cationic Structures.” *J. Phys. Chem. B*, 110, 2833–2839, 2006. doi:10.1021/jp053396f.

- [33] D. R. MacFarlane, M. Forsyth, E. I. Izgorodina, A. P. Abbott, G. Annat, and K. Fraser. “On the concept of ionicity in ionic liquids.” *Phys. Chem. Chem. Phys.*, 11, 4962–4967, 2009. doi:10.1039/b900201d.
- [34] K. Ueno, H. Tokuda, and M. Watanabe. “Ionicity in ionic liquids: correlation with ionic structure and physicochemical properties.” *Phys. Chem. Chem. Phys.*, 12, 1649–1658, 2010. doi:10.1039/b921462n.
- [35] K. J. Fraser, E. I. Izgorodina, M. Forsyth, J. L. Scott, and D. R. MacFarlane. “Liquids intermediate between “molecular” and “ionic” liquids: Liquid ion pairs?” *Chem. Comm.*, 3817–3819, 2007. doi:10.1039/b710014k.
- [36] J. N. A. Canongia Lopes and A. A. H. Pádua. “Nanostructural Organization in Ionic Liquids.” *J. Phys. Chem. B*, 110, 3330–3335, 2006. doi:10.1021/jp056006y.
- [37] C. S. Santos, H. V. R. Annapureddy, N. S. Murthy, H. K. Kashyap, E. W. Castner, Jr., and C. J. Margulis. “Temperature-dependent structure of methyltributylammonium bis(trifluoromethylsulfonyl)amide: X ray scattering and simulations.” *J. Chem. Phys.*, 134, 064517, 2011. doi:10.1063/1.3526958.
- [38] H. K. Kashyap, C. S. Santos, R. P. Daly, J. J. Hettige, N. S. Murthy, H. Shirota, E. W. Castner, Jr., and C. J. Margulis. “How Does the Ionic Liquid Organizational Landscape Change when Nonpolar Cationic Alkyl Groups Are Replaced by Polar Isoelectronic Diethers?” *J. Phys. Chem. B*, 117, 1130–1135, 2013. doi:10.1021/jp311032p.
- [39] T. Cosby, Z. Vicars, M. Heres, K. Tsunashima, and J. Sangoro. “Dynamic and structural evidence of mesoscopic aggregation in phosphonium ionic liquids.” *J. Chem. Phys.*, 148, 193815, 2018. doi:10.1063/1.5009765.
- [40] S. Tang, G. A. Baker, and H. Zhao. “Ether- and alcohol-functionalized task-specific ionic liquids: attractive properties and applications.” *Chem. Soc. Rev.*, 41, 4030–4066, 2012. doi:10.1039/C2CS15362A.

- [41] B. Wu, H. Shirota, and E. W. Castner, Jr. “Structure of Ionic Liquids with Cationic Silicon-Substitutions.” *J. Chem. Phys.*, 145, 114501, 2016. doi:10.1063/1.4962257.
- [42] Y. Jin, S. Fang, L. Yang, S. ichi Hirano, and K. Tachibana. “Functionalized ionic liquids based on guanidinium cations with two ether groups as new electrolytes for lithium battery.” *J. Power Sources*, 196, 10658 – 10666, 2011. doi:10.1016/j.jpowsour.2011.08.008.
- [43] S. Fang, Y. Jin, L. Yang, S. ichi Hirano, K. Tachibana, and S. Katayama. “Functionalized ionic liquids based on quaternary ammonium cations with three or four ether groups as new electrolytes for lithium battery.” *Electrochim. Acta*, 56, 4663 – 4671, 2011. doi:10.1016/j.electacta.2011.02.107.
- [44] S. Luo, S. Zhang, Y. Wang, A. Xia, G. Zhang, X. Du, and D. Xu. “Complexes of ionic liquids with poly(ethylene glycol)s.” *J. Org. Chem.*, 75, 1888–1891, 2010. doi:10.1021/jo902521w.
- [45] L. Carbone, M. Gobet, J. Peng, M. Devany, B. Scrosati, S. Greenbaum, and J. Hassoun. “Comparative study of ether-based electrolytes for application in lithium-sulfur battery.” *ACS Appl. Mater. Interfaces*, 7, 13859–13865, 2015. doi:10.1021/acsami.5b02160.
- [46] T. Sato, G. Masuda, and K. Takagi. “Electrochemical properties of novel ionic liquids for electric double layer capacitor applications.” *Electrochim. Acta*, 49, 3603 – 3611, 2004. doi:10.1016/j.electacta.2004.03.030.
- [47] M. Wang, X. Xiao, X. Zhou, X. Li, and Y. Lin. “Investigation of peo-imidazole ionic liquid oligomer electrolytes for dye-sensitized solar cells.” *Sol. Energ. Mat. Sol. C.*, 91, 785 – 790, 2007. doi:10.1016/j.solmat.2007.01.009.
- [48] S. Sharma, A. Gupta, and H. K. Kashyap. “How the Structure of Pyrrolidinium Ionic Liquids Is Susceptible to High Pressure.” *J. Phys. Chem. B*, 120, 3206–3214, 2016. doi:10.1021/acs.jpcc.6b01133.

- [49] M. Kanakubo, T. Makino, T. Taniguchi, T. Nokami, and T. Itoh. “Co₂ solubility in ether functionalized ionic liquids on mole fraction and molarity scales.” *ACS Sustainable Chem. Eng.*, 4, 525–535, 2016. doi:10.1021/acssuschemeng.5b00960.
- [50] Y. Zhao, J. Wang, H. Jiang, and Y. Hu. “Desulfurization performance of ether-functionalized imidazolium-based ionic liquids supported on porous silica gel.” *Energy Fuels*, 29, 1941–1945, 2015. doi:10.1021/ef502682v.
- [51] H. Wang, W. Chen, R. A. Bartynski, P. Kaghazchi, and T. Jacob. “Nitrogen-induced reconstruction and faceting of Re(11 $\bar{2}$ 1).” *J. Chem. Phys.*, 140, 024707, 2014. doi:10.1063/1.4861046.
- [52] L. C. Branco, J. a. N. Rosa, J. J. Moura Ramos, and C. A. M. Afonso. “Preparation and characterization of new room temperature ionic liquids.” *Chem.: Eur. J.*, 8, 3671–3677, 2002. doi:10.1002/1521-3765(20020816)8:16<3671::AID-CHEM3671>3.0.CO;2-9.
- [53] J. D. Holbrey, A. E. Visser, S. K. Spear, W. M. Reichert, R. P. Swatloski, G. A. Broker, and R. D. Rogers. “Mercury(ii) partitioning from aqueous solutions with a new, hydrophobic ethylene-glycol functionalized bis-imidazolium ionic liquid.” *Green Chem.*, 5, 129–135, 2003. doi:10.1039/B300971H.
- [54] N. Kimizuka and T. Nakashima. “Spontaneous self-assembly of glycolipid bilayer membranes in sugar-philic ionic liquids and formation of ionogels.” *Langmuir*, 17, 6759–6761, 2001. doi:10.1021/la015523e.
- [55] S. Park and R. J. Kazlauskas. “Improved preparation and use of room-temperature ionic liquids in lipase-catalyzed enantio- and regioselective acylations.” *J. Org. Chem.*, 66, 8395–8401, 2001. doi:10.1021/jo015761e.
- [56] Z. Wang, Y. Pei, J. Zhao, Z. Li, Y. Chen, and K. Zhuo. “Formation of ether-functionalized ionic-liquid-based aqueous two-phase systems and their application in separation of protein and saccharides.” *J. Phys. Chem. B*, 119, 4471–4478, 2015. doi:10.1021/jp510984d.

- [57] S. Zhang, N. Sun, X. He, X. Lu, and X. Zhang. “Physical properties of ionic liquids: Database and evaluation.” *J. Phys. Chem. Ref. Data*, 35, 1475–1517, 2006. doi:10.1063/1.2204959.
- [58] K. Shimizu, C. E. S. Bernardes, A. Triolo, and J. N. Canongia Lopes. “Nano-segregation in ionic liquids: scorpions and vanishing chains.” *Phys. Chem. Chem. Phys.*, 15, 16256–16262, 2013. doi:10.1039/C3CP52357H.
- [59] G. D. Smith, O. Borodin, L. Li, H. Kim, Q. Liu, J. E. Bara, D. L. Ginc, and R. Nobel. “A comparison of ether- and alkyl-derivatized imidazolium-based room-temperature ionic liquids: a molecular dynamics simulation study.” *Phys. Chem. Chem. Phys.*, 10, 6301–6312, 2008.
- [60] Z. Fei, W. H. Ang, D. Zhao, R. Scopelliti, E. E. Zvereva, S. A. Katsyuba, and P. J. Dyson. “Revisiting ether-derivatized imidazolium-based ionic liquids.” *J. Phys. Chem. B*, 111, 10095–10108, 2007. doi:10.1021/jp073419l.
- [61] O. Russina and A. Triolo. “New experimental evidence supporting the mesoscopic segregation model in room temperature ionic liquids.” *Faraday Discuss.*, 154, 97–109, 2012. doi:10.1039/C1FD00073J.
- [62] K. Shimizu, D. Almantariotis, M. F. Costa Gomes, A. A. H. Pádua, and J. N. Canongia Lopes. “Molecular Force Field for Ionic Liquids V: Hydroxyethylimidazolium, Dimethoxy-2- Methylimidazolium, and Fluoroalkylimidazolium Cations and Bis(Fluorosulfonyl)Amide, Perfluoroalkanesulfonylamide, and Fluoroalkylfluorophosphate Anions.” *J. Phys. Chem. B*, 114, 3592–3600, 2010. doi:10.1021/jp9120468.
- [63] A. Triolo, O. Russina, R. Caminiti, H. Shirota, H. Y. Lee, C. S. Santos, N. S. Murthy, and E. W. Castner, Jr. “Comparing intermediate range order for alkyl- vs. ether-substituted cations in ionic liquids.” *Chem. Commun.*, 48, 4959–4961, 2012. doi:10.1039/C2CC31550E.
- [64] N. W. Ashcroft and D. C. Langreth. “Structure of Binary Liquid Mixtures. I.” *Phys. Rev.*, 156, 685–692, 1967. doi:10.1103/PhysRev.156.685.

- [65] H. V. R. Annapureddy, H. K. Kashyap, P. M. De Biase, and C. J. Margulis. “What is the Origin of the Prepeak in the X-ray Scattering of Imidazolium-Based Room-Temperature Ionic Liquids?” *J. Phys. Chem. B*, 114, 16838–16846, 2010. doi:10.1021/jp108545z.
- [66] H. K. Kashyap, C. S. Santos, H. V. R. Annapureddy, N. S. Murthy, C. J. Margulis, and E. W. Castner, Jr. “Temperature-Dependent Structure of Ionic Liquids: X-ray Scattering and Simulations.” *Faraday Discuss.*, 154, 133–143, 2012. doi: 10.1039/C1FD00059D.
- [67] B. Wu, Y. Yamashita, T. Endo, K. Takahashi, and E. W. Castner, Jr. “Structure and Dynamics of Ionic Liquids: Trimethylsilylpropyl-Substituted Cations and Bis(sulfonyl)amide Anions.” *J. Chem. Phys.*, 145, 244506, 2016. doi: 10.1063/1.4972410.

Chapter 4

Diffusivities in Ionic Liquids

All fluids can be broken down into two basic types, Newtonian and non-Newtonian. A Newtonian fluid's viscosity remains constant, no matter the amount of shear applied for a constant temperature. A non-Newtonian fluid is a fluid that does not follow Newton's law of viscosity. The viscosity of non-Newtonian fluids changes when shear is applied, to either more fluid or more solid. Thermal motion in these non-Newtonian complex fluids is a complex stochastic process. It is challenging to achieve a quantitative understanding of the transport dynamics of disordered fluidic systems, including ionic liquids.(1) Smith, *et al.* reported that ammonium based ILs displayed Newtonian behavior at low shear rates but shear thin at higher shear rates.(2) Rauber, *et al.* studied the rheological behaviour of trioctylphosphonium ILs with perfluorinated groups and reported that all the investigated fluorinated ILs displayed Newtonian behavior at low shear rates, linear shear thinning at higher shear rates and a transition zone in between. For all the investigated tetraalkylphosphonium ILs only Newtonian flow behavior is observed.(3)

Diffusion is the thermal motion of all particles at temperatures above glass transition temperature (T_g) or melting point (T_m), in the gas or liquid phases. When there is concentration gradient, a driving force for diffusion, the particles diffuse from a region of higher concentration to lower concentration following Fick's Law.(4) Once the concentrations are equal, the molecules continue to move due to the random motion of the molecules. This is the process of "self-diffusion". In the end, the system reaches a "dynamic equilibrium" state. Diffusivities in ionic liquids are affected by many factors including ion size, the shape of ions, conformational flexibility, and external electric fields, *etc.*(5)

In this chapter, we study how the diffusion coefficient changes with cations, and how it is affected by adding a second neutral solvent. Section 4.1 is adapted from the paper published by Lo Celso, *et al.* (6)

4.1 Diffusivity of ILs with the $\text{BSI}_{1,4}^-$ anion

ILs are binary liquids composed of cations and anions. The differences in size, shape, molecular mass and charge distribution between the cation and anion can lead to different diffusivities of the ions. Four $\text{BSI}_{1,4}^-$ -anion ILs were selected with cations: $\text{Im}_{2,1}^+$, $\text{Im}_{1,8}^+$, $\text{Pyrr}_{1,8}^+$, and $\text{P}_{6,6,6,14}^+$. Their molecular structures are shown in Figure 4.1. The inclusion of a perfluorinated butyl tail on the anion is expected to bring a third fluorine domain into the system.(7–10) It has been demonstrated that while it is true for $\text{Im}_{2,1}^+/\text{BSI}_{1,4}^-$, for systems like $\text{Im}_{1,8}^+/\text{BSI}_{1,4}^-$ and $\text{Pyrr}_{1,8}^+/\text{BSI}_{1,4}^-$, where long alkyl tails are also included, the hydrocarbon and fluorinated tails together form the nonpolar domains and cannot be separated.(11) The diffusion differences in these ILs are studied.

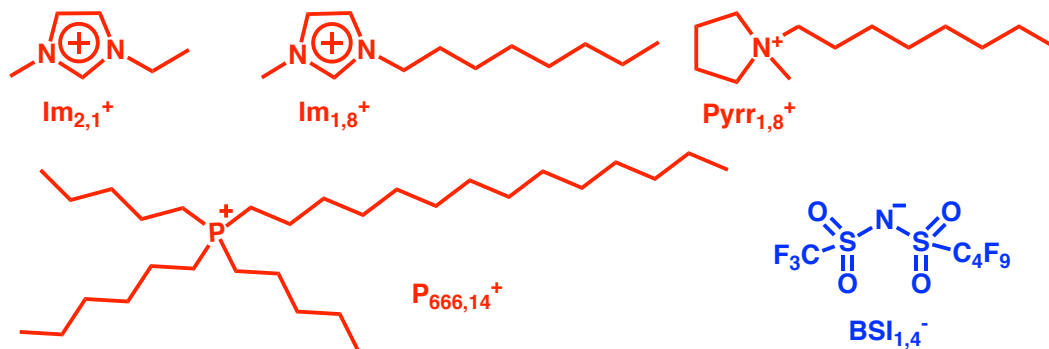


Figure 4.1: The molecular structures of ILs studied in this section. The cations are colored red, and the anion is colored blue.

4.1.1 Diffusivities as a function of temperature

While a first look at diffusivities in ILs might suggest that they obey hydrodynamic laws for transport, more detailed study shows that this is not the case. To this end, the diffusivities of the ILs were measured under a set of temperatures. For ILs the viscosity

is best fit by the Vogel-Fulcher-Tammann (VFT) equation(12; 13) as they are "fragile" liquids, which means that ILs show deviations from Arrhenius behaviour.(14) Fragility reflects the degree of deviation of the temperature dependent viscosity from the Arrhenius behavior.(14) The fitting curves and fitted parameters based on Eqn. 4.1 are shown in Figure 4.2 and Table 4.1, respectively. For the same temperature, the diffusivity of the four ILs are in the order of $\text{Im}_{2,1}^+/\text{BSI}_{1,4}^- > \text{Im}_{1,8}^+/\text{BSI}_{1,4}^- > \text{Pyrr}_{1,8}^+/\text{BSI}_{1,4}^- > \text{P}_{6,6,6,14}^+/\text{BSI}_{1,4}^-$, which is the same order as their fluidity or inverse viscosity. For $\text{Im}_{2,1}^+/\text{BSI}_{1,4}^-$, the cation diffuses much faster than the anion, due to their size differences. For $\text{Im}_{1,8}^+/\text{BSI}_{1,4}^-$ and $\text{Pyrr}_{1,8}^+/\text{BSI}_{1,4}^-$, where the cation size is slightly smaller than the anion size, the cation still diffuses slightly faster than the anion. For $\text{P}_{6,6,6,14}^+/\text{BSI}_{1,4}^-$, where the cation is much larger than the anion, the anion diffuses slightly faster than the cation.

$$D = \exp(D_{VFT} + B/(T - T_0)) \quad (4.1)$$

IL	cation			anion		
	D_{VFT}	B	T_0 (K)	D_{VFT}	B	T_0 (K)
$\text{Im}_{2,1}^+/\text{BSI}_{1,4}^-$	-15.974	-1585.2	120.68	-10.440	-4072.4	31.341
$\text{Im}_{1,8}^+/\text{BSI}_{1,4}^-$	-3.640	-3125.3	61.44	-7.189	-1485.3	149.76
$\text{Pyrr}_{1,8}^+/\text{BSI}_{1,4}^-$	-15.444	-2027.2	117.09	-15.750	-1945.3	122.52
$\text{P}_{6,6,6,14}^+/\text{BSI}_{1,4}^-$	-7.540	-1934.3	116.21	-7.768	-1752.1	127.77

Table 4.1: Parameters calculated from the VFT equation for the set of four ILs in Figure 4.2. Data was reproduced from the paper by Lo Celso, *et al.*(6)

While the VFT model provides the best fits to viscosity and diffusivity, at elevated temperatures, the Arrhenius equation can also be used to fit the viscosity and diffusivity. The Arrhenius fitting of $\ln(D)$ vs $1/T$ is shown in Figure 4.3, and the fitted parameters are listed in Table 4.2. In Arrhenius equation, E_a is the (diffusion) activation energy. A lower diffusion activation energy usually indicates higher diffusivities. In this case, the diffusion activation energy E_a value is calculated to be highest for $\text{Pyrr}_{1,8}^+/\text{BSI}_{1,4}^-$ and lowest for $\text{Im}_{2,1}^+/\text{BSI}_{1,4}^-$. While $\text{Im}_{2,1}^+/\text{BSI}_{1,4}^-$ has the highest diffusivity among the four ILs, the diffusivity of $\text{Pyrr}_{1,8}^+/\text{BSI}_{1,4}^-$ is not the smallest. Note that the E_a value depends on the goodness of the fitting and the range of data sets. Therefore, we

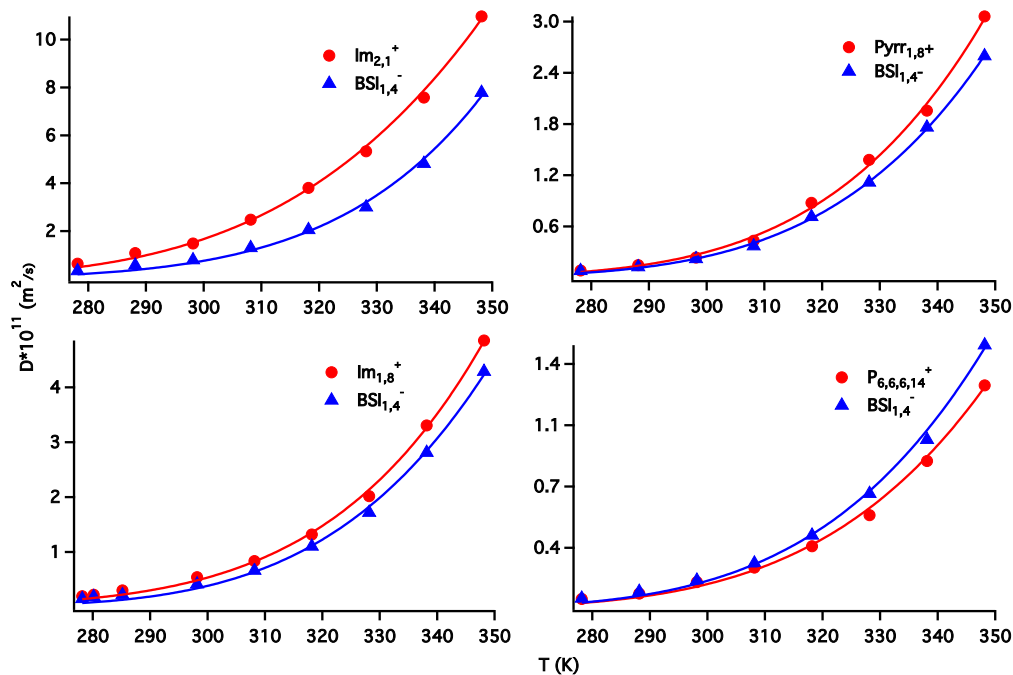


Figure 4.2: VFT plots of temperature-dependent diffusivity for the set of four ILs with the $\text{BSI}_{1,4}^-$ anion: $\text{Im}_{2,1}^+/\text{BSI}_{1,4}^-$, $\text{Im}_{1,8}^+/\text{BSI}_{1,4}^-$, $\text{Pyrr}_{1,8}^+/\text{BSI}_{1,4}^-$, and $\text{P}_{6,6,6,14}^+/\text{BSI}_{1,4}^-$. Figure was reproduced from the paper by Lo Celso, *et al.*(6)

can use it as a general rule to compare the diffusivities of different species, but should be aware that exceptions exist.

$$\ln(D) = D_0 + E_a/(RT) \quad (4.2)$$

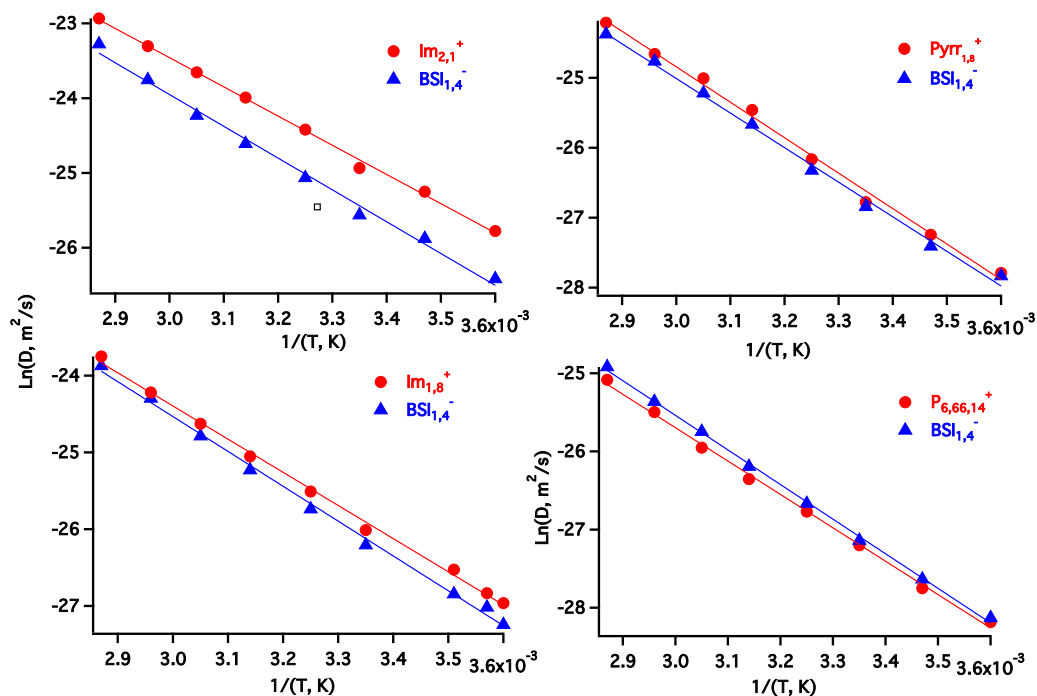


Figure 4.3: Arrhenius plots of temperature-dependent diffusivity for the set of four ILs with the $\text{BSI}_{1,4}^-$ anion: $\text{Im}_{2,1}^+/\text{BSI}_{1,4}^-$, $\text{Im}_{1,8}^+/\text{BSI}_{1,4}^-$, $\text{Pyr}_{1,8}^+/\text{BSI}_{1,4}^-$, and $\text{P}_{6,6,6,14}^+/\text{BSI}_{1,4}^-$. Figure was reproduced from the paper by Lo Celso, *et al.* (6)

IL	cation		anion	
	D_0	E_a (kJ/mol)	D_0	E_a (kJ/mol)
$\text{Im}_{2,1}^+/\text{BSI}_{1,4}^-$	-11.742	32.469	-11.192	35.359
$\text{Im}_{1,8}^+/\text{BSI}_{1,4}^-$	-11.435	35.916	-10.912	37.747
$\text{Pyr}_{1,8}^+/\text{BSI}_{1,4}^-$	-9.632	42.152	-10.175	41.109
$\text{P}_{6,6,6,14}^+/\text{BSI}_{1,4}^-$	-12.250	36.824	-12.878	35.522

Table 4.2: Parameters calculated from the Arrhenius equation for the set of four ILs in Figure 4.3. Data was reproduced from the paper by Lo Celso, *et al.* (6)

4.1.2 Stokes-Einstein fits to IL diffusion

The diffusivities of ILs are measured at several temperatures. Stokes-Einstein (S-E) equation, $D = k_B T / (c \pi \eta R)$ is used to fit D vs. T/η , where c is 4. A fractional SE equation given by $m = 0.9$ is used to predict the diffusivity for $\text{Im}_{2,1}^+/\text{BSI}_{1,4}^-$ and $\text{P}_{6,6,6,14}^+/\text{BSI}_{1,4}^-$. The results are shown in Figure 4.4. We can see that for $\text{Im}_{2,1}^+/\text{BSI}_{1,4}^-$, the diffusivity for anion is slightly higher than the hydrodynamic prediction, and the diffusivity for $\text{Im}_{2,1}^+$ cation is about 3 times faster than the prediction. Such a deviation from hydrodynamic predictions is very common. Chung reported a difference between experimental data and the S-E prediction of up to 10 times.⁽¹⁵⁾ For the other three ILs, the experimental data fits well with the hydrodynamic predictions, especially at high temperatures. At lower temperatures, the diffusivity of ions is usually faster than the S-E prediction. We notice that for $\text{P}_{6,6,6,14}^+/\text{BSI}_{1,4}^-$, the $\text{BSI}_{1,4}^-$ anion actually diffuses slower than the prediction. This may be attributed to the unusual structure of the $\text{P}_{6,6,6,14}^+$ cation. The $\text{BSI}_{1,4}^-$ anions tend to stay close to the cationic heads and are “trapped” there by the alkyl tails on the cations, making it hard for them to move around in the charged network.

Finally, a comparison of the diffusivity of the $\text{BSI}_{1,4}^-$ anion in the four ILs is shown in Figure 4.5. The S-E prediction fits well with the experimental data at elevated temperatures and smaller than the experimental diffusivities at low temperatures for $\text{Im}_{2,1}^+/\text{BSI}_{1,4}^-$, $\text{Im}_{1,8}^+/\text{BSI}_{1,4}^-$, and $\text{Pyrr}_{1,8}^+/\text{BSI}_{1,4}^-$. For $\text{P}_{6,6,6,14}^+/\text{BSI}_{1,4}^-$, the diffusivity of $\text{BSI}_{1,4}^-$ is lower than the prediction at elevated temperatures.

4.1.3 Summary of diffusion behavior in $\text{BSI}_{1,4}^-$ ILs

The diffusivity of ILs is affected by many factors. As expected, for the ILs studied in this section, low viscosity ILs diffuse faster than high viscosity ILs. In these systems, small ions diffuse faster than the large ions. The self-diffusion coefficients are affected by the structure of ions as well. Ions in general diffuse faster than the hydrodynamic predictions based on the Stokes-Einstein equation. For ILs like $\text{P}_{6,6,6,14}^+/\text{NTf}_2^-$, where the cations are extremely large and the anions are embedded in the cations, the ions

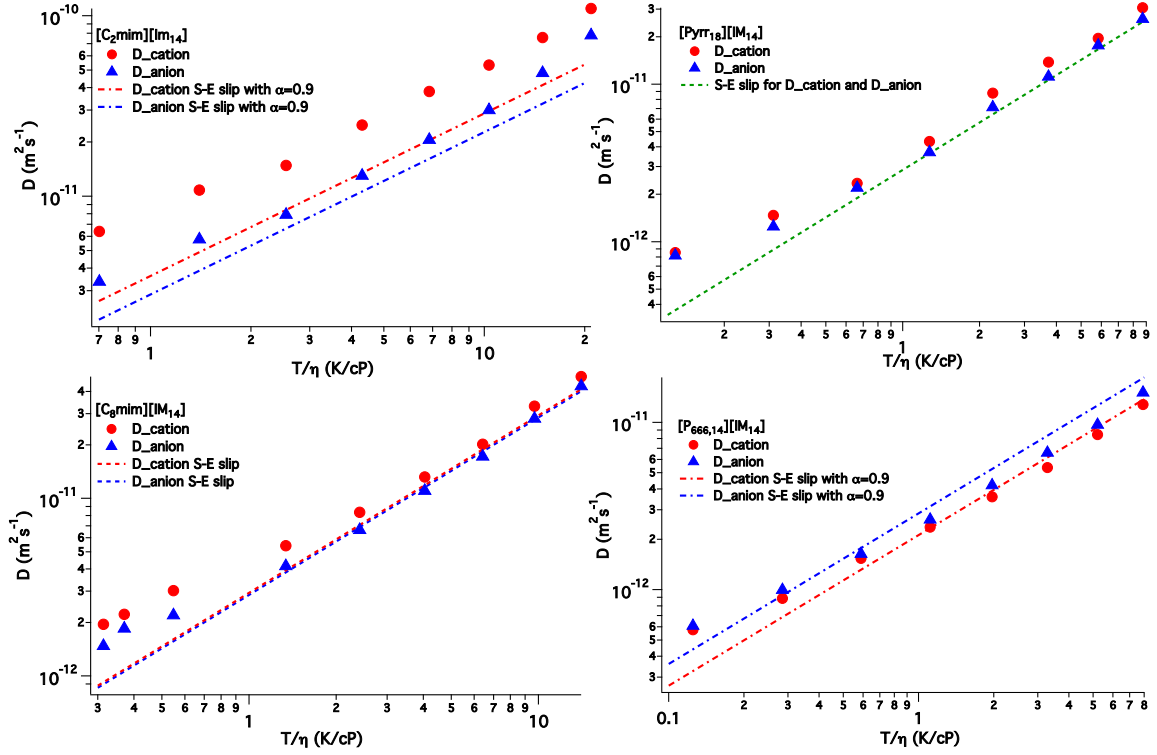


Figure 4.4: Plots of self-diffusion coefficients for the set of four ILs with the $\text{BSI}_{1,4}^-$ anion: $\text{Im}_{2,1}^+/\text{BSI}_{1,4}^-$, $\text{Im}_{1,8}^+/\text{BSI}_{1,4}^-$, $\text{Pyrr}_{1,8}^+/\text{BSI}_{1,4}^-$, and $\text{P}_{6,6,6,14}^+/\text{BSI}_{1,4}^-$. Dashed lines denote the predictions from the Stokes-Einstein equation. Figure was reproduced from the paper by Lo Celso, *et al.*(6)

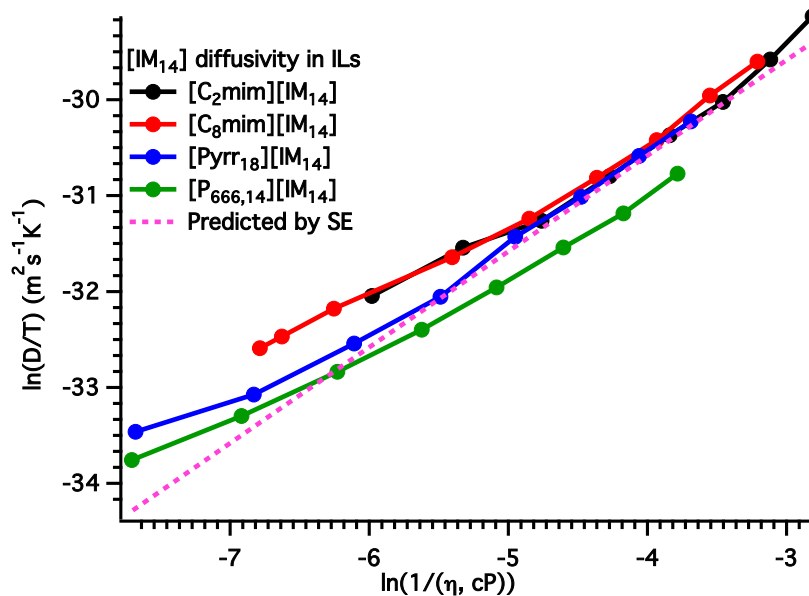


Figure 4.5: Self-diffusion coefficients of $\text{BSI}_{1,4}^-$ anion in the set of four ILs: $\text{Im}_{2,1}^+/\text{BSI}_{1,4}^-$, $\text{Im}_{1,8}^+/\text{BSI}_{1,4}^-$, $\text{Pyrr}_{1,8}^+/\text{BSI}_{1,4}^-$, and $\text{P}_{6,6,6,14}^+/\text{BSI}_{1,4}^-$. Dashed line denotes the predictions from the Stokes-Einstein equation for $\text{BSI}_{1,4}^-$. Figure was reproduced from the paper by Lo Celso, *et al.*(6)

diffuse slower than the prediction. Fractional S-E is shown to provide a reasonable alternative to S-E.

4.2 Structure and Transport of 1-Octanol in $P_{6,6,6,14}^+/\text{NTf}_2^-$

It has been established that when the cations or anions have long alkyl tails, nonpolar nanoscale domains form in the systems.(16–19) The existence of nanoscale domains is reflected by the FSDP in the total structure functions $S(q)$.(17–20) The heterogeneity of IL structures is related to the dynamic complexity in ILs.

One particular IL $P_{6,6,6,14}^+/\text{NTf}_2^-$, was shown to have very high solubilities for alkanes and alkanols.(21) Our group showed that the IL structure persists on addition of hydrocarbons, even up to 80% number density of hexane in $P_{6,6,6,14}^+/\text{NTf}_2^-$. The hexane is solubilized in the non-polar domains formed by the hydrocarbon-rich cationic groups. The self-diffusivities of the dissolved hexane were measured to be 21 times larger than for the $P_{6,6,6,14}^+$ cations. Thus, the next step was for us to investigate the same IL for various concentrations of an alcohol, 1-octanol.

In this section, we studied the transportation in $P_{6,6,6,14}^+/\text{NTf}_2^-$ -octanol mixtures. Though the hydroxyl group at the end of 1-octanol helps to increase its solubility in $P_{6,6,6,14}^+/\text{NTf}_2^-$, we expect a lower self-diffusion coefficient of 1-octanol than hexane, considering the possibility of hydrogen bonding between hydroxyl group and the anions. High-energy X-ray scattering experiments were carried out to obtain the total structure function $S(q)$, and Pulsed-Gradient Spin-Echo (PG-SE) NMR experiments were performed to measure the self-diffusion coefficients.

4.2.1 Structure functions $S(q)$ of the mixtures

Figure 4.6 presents the liquid structure functions $S(q)$ for neat $P_{6,6,6,14}^+/\text{NTf}_2^-$, neat 1-octanol and their mixtures measured using high-energy X-ray experiments. For all the $S(q)$'s, there is a sharp separation between intermolecular and intramolecular correlations at $q = 2.0 \text{ \AA}^{-1}$. There are three peaks shown for neat $P_{6,6,6,14}^+/\text{NTf}_2^-$ IL: the adjacency peak at $q = 1.37 \text{ \AA}^{-1}$, the charge-charge alternation peak at $q = 0.75$

\AA^{-1} , and the FSDP at $q = 0.41 \text{ \AA}^{-1}$, resulting from the formation of intermediate range order domains.(16; 22) The adjacency peak and FSDP remain for all the mixtures. The neat $\text{P}_{6,6,6,14}^{+}/\text{NTf}_2^{-}$ shows a weak charge-charge alternation peak, which eventually disappears as the mole fraction of 1-octanol x_{oct} is more than 80 percent.

The adjacency peak for 1-octanol is at a much higher q value than $\text{P}_{6,6,6,14}^{+}/\text{NTf}_2^{-}$, whereas the adjacency peak for neat n- C_6D_{14} is at the same position as the adjacency for $\text{P}_{6,6,6,14}^{+}/\text{NTf}_2^{-}$.(23) This indicates that the natural sizing of the neat n- C_6D_{14} liquid is larger than that of the 1-octanol. As the mole fraction of 1-octanol increases, the adjacency peak shifts to higher q value, while the amplitude of the adjacency peak barely changes.

From $x_{oct} = 0$ to 1, the intensity of the FSDP in $S(q)$ is significantly decreased. The inset shows the intramolecular interactions under $q = 2 \text{ \AA}^{-1}$. The dashed line marks the position change of FSDPs. The FSDPs for neat 1-octanol and $\text{P}_{6,6,6,14}^{+}/\text{NTf}_2^{-}$ are both at $q = 0.41 \text{ \AA}^{-1}$. As the mole fraction of 1-octanol increases, the FSDP first shifts to lower q values and then back to $q = 0.41 \text{ \AA}^{-1}$. The position of the FSDP (q) corresponds to real space domain size ($2\pi/q$). The domain grows from an effective size of 15.4 \AA for the neat IL to 17.0 \AA for the mixtures with $x_{oct} = 0.8$, then shrinks back to 15.4 \AA for neat 1-octanol. At low mole fraction of 1-octanol, the added 1-octanol molecules reside in the nonpolar domains formed by the $\text{P}_{6,6,6,14}^{+}$ cations. The addition of 1-octanol expands the nonpolar domains formed by the $\text{P}_{6,6,6,14}^{+}$ cation, so the FSDP shifts to lower q value. As the mole fraction of 1-octanol increases, the system transfers from 1-octanol molecules surrounded by ions to ions surrounded by the 1-octanol molecules. The nonpolar domains in the system are mainly formed by the octyl tails on the 1-octanol. Therefore, the size of the nanoscale domains starts to decrease as the mole fraction of 1-octanol reaches $x_{oct} = 0.8$ or higher.

4.2.2 Viscosities of IL-octanol mixtures

Temperature-dependent viscosities were measured for 1-octanol, $\text{P}_{6,6,6,14}^{+}/\text{NTf}_2^{-}$ and their mixtures. Though viscosities are best fit to VFT equation, the Arrhenius equation also provides acceptable fits. The Arrhenius fitting is shown in Figure 4.7, and the

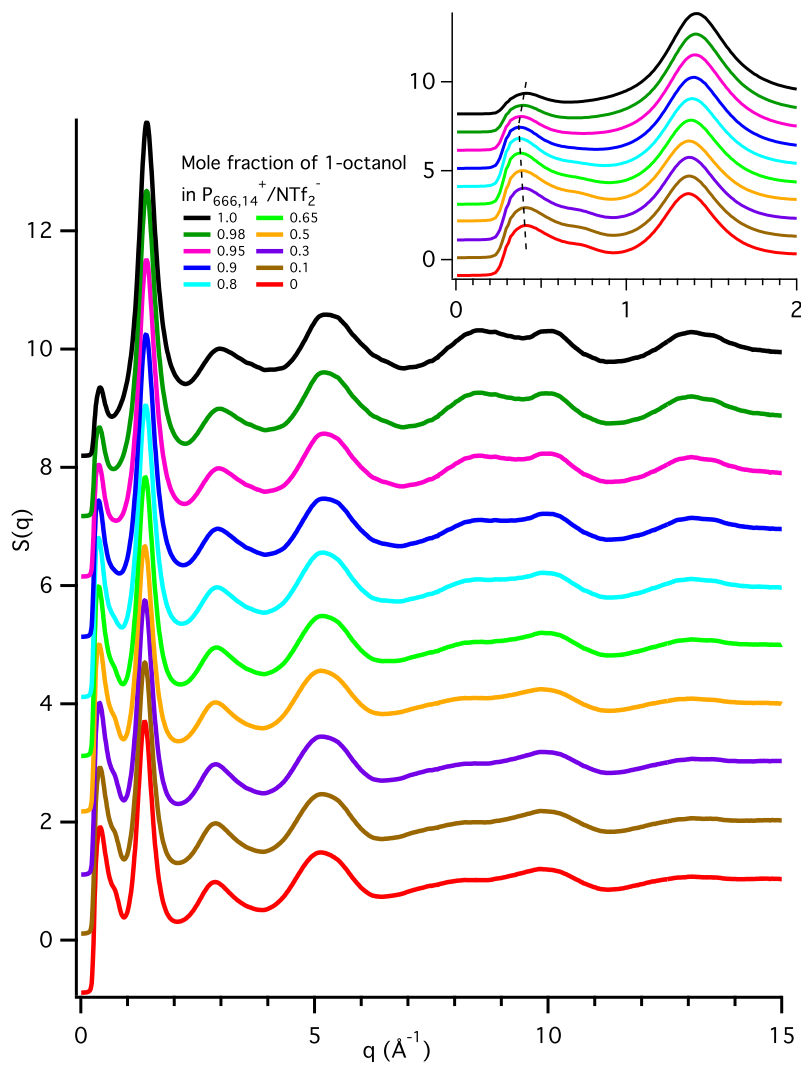


Figure 4.6: Liquid structure functions for mixtures of 1-octanol in $P_{6,6,6,14}^+ / NTf_2^-$; mole fractions range from $x_{oct} = 0.0$ to 1.0. The inset shows the intra-molecular interactions under 2 \AA^{-1} .

fitted parameters are listed in Table 4.3. The viscosity of $P_{6,6,6,14}^+ / NTf_2^-$ is much higher than the viscosity of 1-octanol. Therefore, adding 1-octanol to $P_{6,6,6,14}^+ / NTf_2^-$ decreases the viscosity significantly. For each sample, the viscosity greatly decreases as the temperature increases. Each data set is perfectly fitted with Arrhenius equation: $\ln(\eta) = A + (-E_a/(RT))$, where the slope corresponds to the activation energy E_a . The calculated E_a is listed in Table 4.3, which is a measure of how rapidly viscosities change with increasing temperatures. As the mole fraction of 1-octanol increases, the viscosity of mixtures decreases, as does the activation energy. Note that for 1-octanol, the value of E_a is 27 kJ/mol, which is significantly larger than the value $E_a = 17$ kJ/mol for C_6D_{14} .

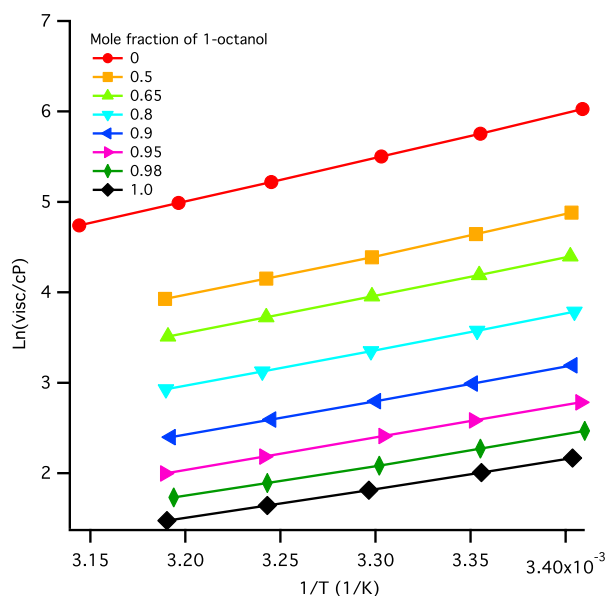


Figure 4.7: Arrhenius plots of temperature-dependent shear viscosity for 1-octanol, $P_{6,6,6,14}^+ / NTf_2^-$ and their mixtures.

The temperature dependent viscosities are best fitted using the VFT equation: $\ln(\eta_T) = \ln(\eta_{VFT}) + B/(T - T_0)$. The fitted plots are shown in Figure 4.8 and the fitted parameters are listed in Table 4.3. The viscosity activation energies can also be calculated based on the VFT equation as shown in Eqn 4.3.(24). The calculated effective activation energies based on the Arrhenius (blue) and VFT equation (red) are plotted versus the mole fraction of 1-octanol in Figure 4.9. We can see that the

activation energies calculated from the Arrhenius equation are slightly smaller than the values calculated from the VFT equation, but they all decrease with increasing mole fraction of 1-octanol.

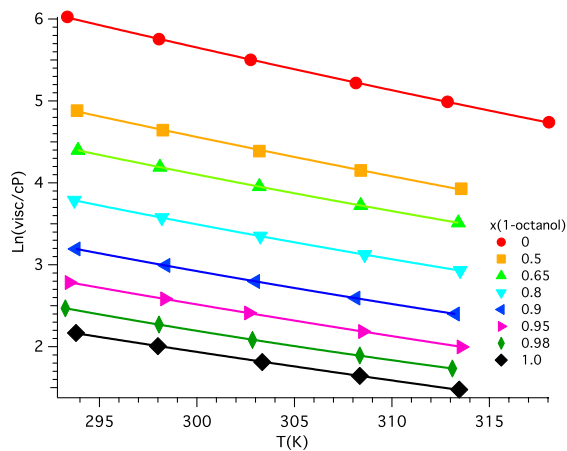


Figure 4.8: The temperature-dependent viscosity data fit to the VFT equation for 1-octanol, $P_{6,6,6,14}^+ / NTf_2^-$ and their mixtures. The mole fraction of 1-octanol is shown in the graph.

$$E_\eta \equiv R \frac{d \ln \eta}{d(1/T)} = RB \left(\frac{T}{T - T_0} \right)^2 \quad (4.3)$$

x(oct)	Arrhenius fits		VFT fits			E_η (kJ/mol)
	η_a	E_a (kJ/mol)	η_{VFT}	B	T_0 (K)	
0	-10.48	40.3	-5.17	2135.2	102.64	41.3
0.5	-10.31	37.0	-1.46	706.4	182.52	39.1
0.65	-9.81	34.7	-5.18	1837.1	102.11	35.3
0.8	-9.80	33.2	-4.41	1388.8	124.29	34.0
0.9	-9.60	31.2	-4.89	1443.3	115.23	31.9
0.95	-9.49	29.9	-7.83	2667.4	42.264	30.1
0.98	-9.13	28.3	-2.69	615.5	173.88	29.5
1	-8.85	26.9	-4.77	1233.5	116.02	27.5

Table 4.3: Parameters calculated from the Arrhenius equation and VFT equation for 1-octanol, $P_{6,6,6,14}^+ / NTf_2^-$ and their mixtures with different mole fractions of 1-octanol.

4.2.3 Diffusivities of IL-octanol mixtures

The slip boundary condition Stokes-Einstein (S-E) or fraction Stokes-Einstein (FSE) equations have been shown to apply well to ionic liquids that has no strong directional

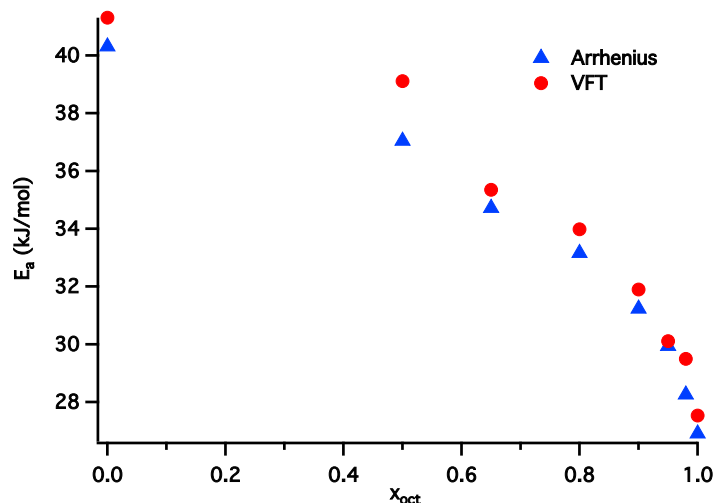


Figure 4.9: Effective activation enthalpies calculated from the VFT (red) and Arrhenius (blue) equations at 298 K.

intermolecular bonding.(25) The equations are given by $D = k_B T / (4\pi\eta r)$ and $D \propto (T/\eta)^m$, respectively. The value for m of ionic liquids is between $0.79 \leq m \leq 1$, though typically in $0.9 \leq m \leq 0.95$. Harris showed that FSE relation describes the self-diffusion behavior more precisely for a variety of liquids with an average value of $m = 0.90$.(25) It proved to be accurate for neat $P_{6,6,6,14}^+ / NTf_2^-$ and $n\text{-C}_6\text{D}_{14}$. However, diffusion behavior for $n\text{-C}_6\text{D}_{14}$ deviates strongly from the FSE predictions in the mixtures.(23)

The results from the PG-SE NMR self-diffusion measurements are analyzed in Figure 4.10, where the self-diffusion coefficients are plotted versus the ratio of absolute temperature to shear viscosity on log-log axes. The self-diffusion coefficients were measured for a set of three temperatures – 298 K, 308 K, and 318 K. From top to bottom, the graphs show self-diffusion coefficients for 1-octanol, $P_{6,6,6,14}^+$, and NTf_2^- , respectively. The predicted diffusion coefficient from the Stokes-Einstein hydrodynamic equation for slip boundary conditions is plotted in the dashed line. The effective spherical radii (r) used were: 5.18, 3.36 and 3.72 Å for $P_{6,6,6,14}^+$, NTf_2^- and 1-octanol, respectively.

The self-diffusivity for the $P_{6,6,6,14}^+$ cation is well described by slip hydrodynamics. The self-diffusion for the NTf_2^- anion fits well with the predictions at low 1-octanol mole fractions. When x_{oct} is larger than 0.65, the NTf_2^- anion shows a diffusivity

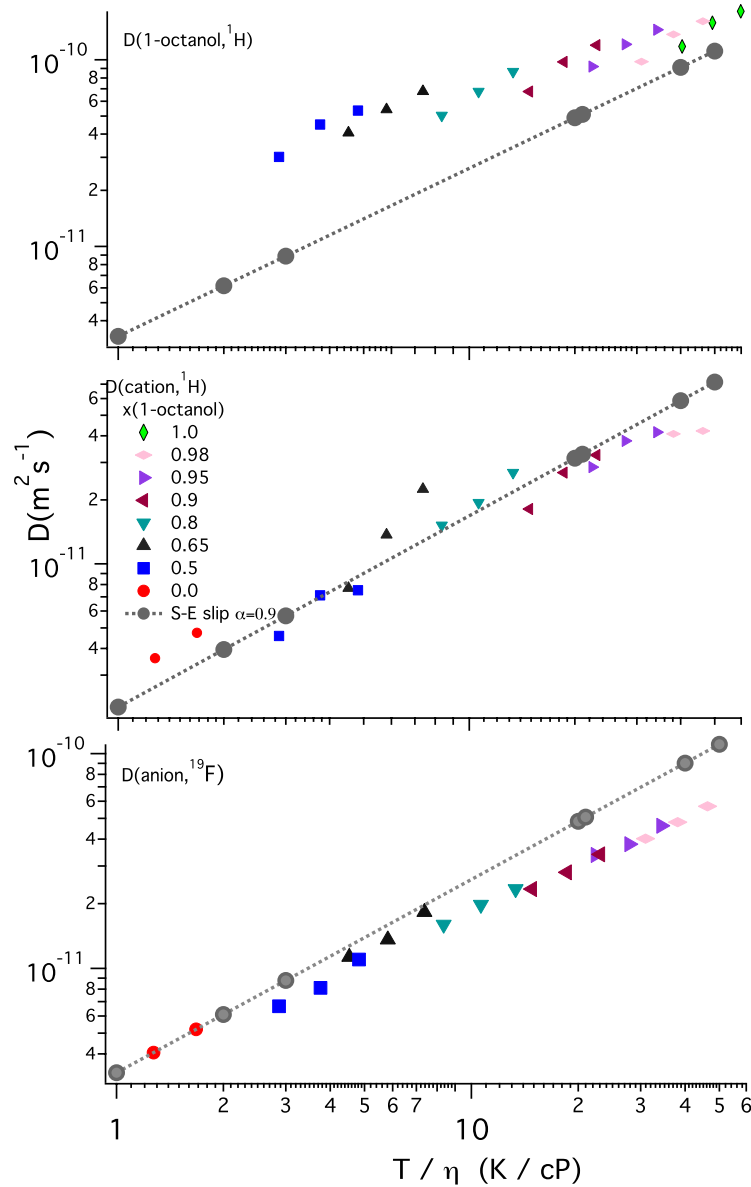


Figure 4.10: Plots of self-diffusion coefficients for mixtures of 1-octanol with NTf_2^- vs. the ratio of temperature to viscosity. Top: 1-octanol; middle: $\text{P}_{6,6,6,14}^+$; bottom: NTf_2^- . Dashed lines denote the predictions from the Stokes-Einstein equation.

lower than predicted by the S-E theory. With higher octanol mole fraction, the total hydrogen bonding between the OH group on the 1-octanol and the NTf₂⁻ anion also increases, which results in slower motion of the NTf₂⁻ anion. This can be testified by MD simulations.

In contrast, the self-diffusion of 1-octanol deviates greatly from the SE hydrodynamic predictions, especially at lower mole fractions of octanol in the mixture. The diffusivity of 1-octanol gets closer to the prediction line at high x_{oct} . This indicates that the 1-octanol experiences a very different environment than the polar regions, pointing to the likelihood of nanophase segregation of 1-octanol in a domain together with the non-polar alkyl tails on the P_{6,6,6,14}⁺ cation. At low x_{oct} , the 1-octanol molecules reside in the nonpolar domains formed by the P_{6,6,6,14}⁺ cations, where they experience smaller resistance moving around in the system. Therefore, they diffuse faster than predicted. For n-C₆D₁₄ in P_{6,6,6,14}⁺/NTf₂⁻, the diffusivity of n-C₆D₁₄ is consistently more than an order of magnitude larger than predicted. The self-diffusion of 1-octanol to the S-E prediction ratio is in the range of 1.3 to 4, which is much lower than the ratio range from 16 to 28 for n-C₆D₁₄. The hydroxyl group on 1-octanol significantly slows down the diffusion of 1-octanol in the mixture. This again can be explained by the formation of H-bonding between 1-octanol and the NTf₂⁻ anion.

4.2.4 Summary of diffusion behavior in IL-solvents mixtures

Addition of 1-octanol to the P_{6,6,6,14}⁺/NTf₂⁻ leads to changes of several physical properties. For liquid structure functions $S(q)$, FSDP shifts to lower q values as the mole fraction of 1-octanol increases. This is consistent with the growth of the domain size from 15.4 to 17.0 Å. Adding a low viscosity solvent to the viscous IL would greatly decrease the viscosity of the solution, which in turn increases the diffusivities of the molecules and ions. The viscosities are well fitted by both the Arrhenius and VFT equations in the measured temperature range. In the 1-octanol and P_{6,6,6,14}⁺/NTf₂⁻ mixtures, the self-diffusion coefficients are in moderately good agreement with hydrodynamic predictions for the P_{6,6,6,14}⁺ cation and NTf₂⁻ anion, while the diffusivity of 1-octanol molecules is much faster than predicted. The fast diffusion of 1-octanol is a

result of the accommodation of 1-octanol in apolar domains formed by the alkyl tails on the $\text{P}_{6,6,6,14}^{+}$ cations. However, the diffusivity of 1-octanol in $\text{P}_{6,6,6,14}^{+}/\text{NTf}_2^{-}$ is much slower compared to hexane, due to the hydrogen bonding between the hydroxyl group on the 1-octanol and the ions.

4.3 Conclusions

The diffusivity of ILs can be affected by many factors, including ion size, the shape of ions, conformational flexibility, and external electric fields, *etc.*(5) In this chapter, we learned that in general low viscosity ILs diffuse faster than high viscosity ILs. The diffusion behavior of some ILs can be well described by hydrodynamic laws, but deviation from the predictions often happens. Adding low viscosity neutral solvents to ILs can greatly decrease the viscosity of the solution, thus increasing the diffusivities of ions in the system. In the case with $\text{P}_{6,6,6,14}^{+}/\text{NTf}_2^{-}$ -octanol mixtures, the diffusion behavior of the ions are moderately fitted by the (fractional) Stokes-Einstein equation, while the diffusivity of neutral octanol molecules deviates greatly from the prediction. The heterogeneity structure of ILs, where intermediate range order domains exist, renders that the neutral molecules experience less friction in the nonpolar regions, thus diffusing faster than the hydrodynamic prediction. We demonstrated that with a trivial adjustment of the concentration of the solvents, or modification of the molecular structure of the solvent, the density, viscosity, size of hydrophobic domains, and transport behaviors of the mixtures can be precisely adjusted. This further reflects the tunability of ionic liquids, which can be useful for the precise tailoring of properties for challenging chemical reactions and separations.

Bibliography

- [1] A. Shakeel, H. Mahmood, U. Farooq, Z. Ullah, S. Yasin, T. Iqbal, C. Chasagne, and M. Moniruzzaman. “Rheology of pure ionic liquids and their complex fluids: A review.” *ACS Sustainable Chem. Eng.*, 7, 13586–13626, 2019. doi: 10.1021/acssuschemeng.9b02232.

- [2] J. A. Smith, G. B. Webber, G. G. Warr, and R. Atkin. “Rheology of protic ionic liquids and their mixtures.” *J. Phys. Chem. B*, 117, 13930–13935, 2013. doi:10.1021/jp407715e.
- [3] D. Rauber, F. Heib, M. Schmitt, and R. Hempelmann. “Trioctylphosphonium room temperature ionic liquids with perfluorinated groups - physical properties and surface behavior in comparison with the nonfluorinated analogues.” *Colloids Surf. A*, 537, 116 – 125, 2018. doi:10.1016/j.colsurfa.2017.10.013.
- [4] A. Fick. “On liquid diffusion.” *J. Membr. Sci.*, 100, 33 – 38, 1995. doi:10.1016/0376-7388(94)00230-V.
- [5] S. Tsuzuki. “Factors controlling the diffusion of ions in ionic liquids.” *ChemPhysChem.*, 13, 1664–1670, 2012. doi:10.1002/cphc.201100870.
- [6] F. L. Celso, G. Appetecchi, E. Simonetti, U. Keiderling, L. Gontrani, A. Triolo, and O. Russina. “Mesoscopic structural organization in fluorinated pyrrolidinium-based room temperature ionic liquids.” *J. Mol. Liq.*, 289, 111110, 2019. doi:10.1016/j.molliq.2019.111110.
- [7] T. L. Greaves, D. F. Kennedy, Y. Shen, A. Hawley, G. Song, and C. J. Drummond. “Fluorous protic ionic liquids exhibit discrete segregated nano-scale solvent domains and form new populations of nano-scale objects upon primary alcohol addition.” *Phys. Chem. Chem. Phys.*, 15, 7592–7598, 2013. doi:10.1039/C3CP44589E.
- [8] T. L. Greaves, D. F. Kennedy, Y. Shen, A. Weerawardena, A. Hawley, G. Song, and C. J. Drummond. “Fluorous protic ionic liquid exhibits a series of lyotropic liquid crystalline mesophases upon water addition.” *J. Mol. Liq.*, 210, 279–285, 2015. doi:10.1016/j.molliq.2015.03.037.
- [9] F. Lo Celso, Y. Yoshida, F. Castiglione, M. Ferro, A. Mele, C. J. Jafta, A. Triolo, and O. Russina. “Direct experimental observation of mesoscopic fluorine domains in fluorinated room temperature ionic liquids.” *Phys. Chem. Chem. Phys.*, 19, 13101–13110, 2017. doi:10.1039/C7CP01971H.

- [10] F. Lo Celso, G. B. Appetecchi, E. Simonetti, M. Zhao, E. W. Castner, Jr., U. Keiderling, L. Gontrani, A. Triolo, and O. Russina. “Microscopic Structural and Dynamic Features in Triphilic Room Temperature Ionic Liquids.” *Front. Chem.*, 7, 285, 2019. doi:10.3389/fchem.2019.00285.
- [11] M. Zhao, B. Wu, S. I. Lall-Ramnarine, J. D. Ramdihal, K. A. Papacostas, E. D. Fernandez, R. A. Sumner, C. J. Margulis, J. F. Wishart, and E. W. Castner. “Structural analysis of ionic liquids with symmetric and asymmetric fluorinated anions.” *J. Chem. Phys.*, 151, 074504, 2019. doi:10.1063/1.5111643.
- [12] G. S. Fulcher. “Analysis of recent measurements of the viscosity of glasses.” *J. Am. Ceram. Soc.*, 8, 339–355, 1925. doi:10.1111/j.1151-2916.1925.tb16731.x.
- [13] G. Tammann and W. Hesse. “Die abhängigkeit der viscosität von der temperatur bie unterkühlten flüssigkeiten.” *Z. Anorg. Allg. Chem.*, 156, 245–257, 1926. doi:10.1002/zaac.19261560121.
- [14] C. A. Angell. *Ionic Liquids in the Temperature Range 150 - 1500 K: Patterns and Problems*, chapter 1, 1–24. Wiley, 2010.
- [15] S. H. Chung, R. Lopato, S. G. Greenbaum, H. Shirota, E. W. Castner, Jr., and J. F. Wishart. “A nuclear magnetic resonance study of room temperature ionic liquids with $\text{CH}_2\text{Si}(\text{CH}_3)_3$ vs. $\text{CH}_2\text{C}(\text{CH}_3)_3$ substitutions on the imidazolium cations.” *J. Phys. Chem. B*, 111, 4885–4893, 2007. doi:10.1021/jp071755w.
- [16] S. M. Urahata and M. C. C. Ribeiro. “Structure of ionic liquids of 1-alkyl-3-methylimidazolium cations: A systematic computer simulation study.” *J. Chem. Phys.*, 120, 1855–1863, 2004. doi:10.1063/1.1635356.
- [17] A. Triolo, O. Russina, H.-J. Bleif, and E. Di Cola. “Nanoscale segregation in room temperature ionic liquids.” *J. Phys. Chem. B*, 111, 4641–4644, 2007. doi:10.1021/jp067705t.

- [18] O. Russina, A. Triolo, L. Gontrani, R. Caminiti, D. Xiao, J. Hines, Larry G., R. A. Bartsch, E. L. Quitevis, N. Pleckhova, and K. R. Seddon. “Morphology and intermolecular dynamics of 1-alkyl-3-methylimidazolium bis(trifluoromethane)sulfonamide ionic liquids: structural and dynamic evidence of nanoscale segregation.” *J. Phys.: Condens. Matter*, 21, 424121, 2009. doi:10.1088/0953-8984/21/42/424121.
- [19] H. K. Kashyap, C. S. Santos, R. P. Daly, J. J. Hettige, N. S. Murthy, H. Shirota, E. W. Castner, Jr., and C. J. Margulis. “How Does the Ionic Liquid Organizational Landscape Change when Nonpolar Cationic Alkyl Groups Are Replaced by Polar Isoelectronic Diethers?” *J. Phys. Chem. B*, 117, 1130–1135, 2013. doi:10.1021/jp311032p.
- [20] J. N. Canongia Lopes and A. A. H. Padua. “Molecular Force Field for Ionic Liquids III: Imidazolium, Pyridinium, and Phosphonium Cations; Chloride, Bromide, and Dicyanamide Anions.” *J. Phys. Chem. B*, 110, 19586–19592, 2006. doi:10.1021/jp063901o.
- [21] M. Blesic, J. N. C. Lopes, M. F. C. Gomes, and L. P. N. Rebelo. “Solubility of alkanes, alkanols and their fluorinated counterparts in tetraalkylphosphonium ionic liquids.” *Phys. Chem. Chem. Phys.*, 12, 9685–9692, 2010. doi:10.1039/C003408H.
- [22] H. K. Kashyap, C. S. Santos, H. V. R. Annapureddy, N. S. Murthy, C. J. Margulis, and E. W. Castner, Jr. “Temperature-Dependent Structure of Ionic Liquids: X-ray Scattering and Simulations.” *Faraday Discuss.*, 154, 133–143, 2012. doi:10.1039/C1FD00059D.
- [23] M. Liang, S. Khatun, and E. W. Castner, Jr. “Communication: Unusual Structure and Transport in Ionic Liquid-Hexane Mixtures.” *J. Chem. Phys.*, 142, 121101, 2015. doi:10.1063/1.4916388.
- [24] H. Jin, B. O’Hare, J. Dong, S. Arzhantsev, G. A. Baker, J. F. Wishart, A. J. Benesi, and M. Maroncelli. “Physical Properties of Ionic Liquids Consisting of the 1-Butyl-3-Methylimidazolium Cation with Various Anions and the

- Bis(trifluoromethylsulfonyl)imide Anion with Various Cations.” *J. Phys. Chem. B*, 112, 81–92, 2008. doi:10.1021/jp076462h.
- [25] K. R. Harris. “The fractional Stokes-Einstein equation: Application to Lennard-Jones, molecular, and ionic liquids.” *J. Chem. Phys.*, 131, 054503, 2009. doi: 10.1063/1.3183951.

Chapter 5

Structure of ILs at Liquid-Vacuum Interfaces

ILs are promising candidates as electrolyte with tunable properties. ILs are widely used in catalysis,(1–3) lubrication,(4–6) batteries and supercapacitors,(7–11), and many other areas.(12) It is immediately noticed that these applications all include heterogeneous systems containing solid-liquid interactions. Therefore, understanding the interfacial behavior of ILs is of significant importance.

So far, we have done a significant amount of work to understand the bulk structure of ILs. Polar domains form in the bulk from the charge abundant cationic and anionic centers. If long nonpolar functional groups are present on the ions, then nonpolar nano-domains would form from the nano-aggregation of these tails.(13–16) The structure of ILs thus depend on the composition of the chosen cations and anions. The solid-liquid interface in ILs is considerably different from its bulk structure due to the solid-solvent interactions, such as electrostatic attraction and van der Waals forces.(17–19)

Various experimental techniques can be used to study the IL-vacuum/solid interfaces including interface tension and viscoelasticity measurements,(20–22) scanning tunneling microscopy (STM),(23; 24) sum frequency harmonic generation,(25–27) neutron reflection, (28) X-ray reflection,(29–31) and atomic force microscopy (AFM),(32–38) Molecular dynamics (MD) simulations are another powerful technique for studying the interfacial structure of ILs on a molecular level.(39–43)

5.1 Liquid-vacuum interfacial structure of ionic liquids with cation and fluorinated anions

Extensive studies on the interactions of ILs with surfaces have been carried out during the past decade.(35; 37; 41–52) We have learned a lot about the structure of ILs

at liquid-vacuum interface, especially ILs with 1-alkyl-3-methylimidazolium ($[C_n\text{mim}]$) cations. When in contact with vacuum, the nonpolar alkyl chains point toward the vacuum side, and polar groups face toward the bulk side, forming a lamellar structure at the interface.(41; 44; 45; 53–55) However, the ordering of lamellar structure only exists a few nanometers thick, and the structure of the bulk is not strongly affected by the presence of the interface.(45; 50; 54) At the outermost layer, the alkyl chains at the vacuum interface do not fully cover the surface. The polar parts of the ILs are still accessible from above the interface.(44; 53) ILs with long side chains behaves like surfactant, with the side chain pointing parallel to the surface, whereas the imidazolium rings perpendicular to the plane of the surface.(35; 44; 52; 56)

As mentioned above, MD simulations show that the lamellar structure observed for all ILs with nonpolar tails on either cations or anions persists only a few nanometers into the bulk. However, experiments show that confined ILs can exhibit pronounced layered structure that is much longer ranged and persistent than simulations suggested.(57; 58) It is not until recently that Amith, *et al.* performed a MD simulation with 1-octyl-3-methylimidazolium octylsulfonate ($[C_8\text{mim}][C_8\text{SO}_4]$) in vacuum, which has both anionic and cationic octyl tails. This IL displayed a lamellar structure that extends across the full 9 nm slab.(59) When the alkyl tails are polar, as in the case of ether functionalities, the vacuum interface affects only the few nanometers beneath the surface.(60) Therefore, having long and nonpolar alkyl tails on both the cation and the anion is critical for the lamellar structure of an IL to persist across the whole slab. Then the question arises as to the size of the box. The lamellar structure may only form due to the small box size, where the two liquid-vacuum interfaces are too close that they are “interacting” with each other. How far would the lamellar structure persist away from the interfaces when the box size is increased? Wu did a study on the effect of box size with a mixture of 1-methyl-3-octylimidazolium octylsulfate and 1-ethyl-3-methylimidazolium ethylsulfate.(61) They found that with a thin film of less than 10 nm, the layers are highly correlated from one interface to the other with no bulk-like liquid in between.

For a thicker film (around 26 nm), the interfacial and bulk-like regions can be distinguished. This indicates that the continuous lamellar structure Amith, *et al.* observed partially results from the small box size.

One of our recent interests lies in ILs with fluorinated anions. The C-F bond is one of the strongest single bonds in organic chemistry due to its partial ionic character.(62–64) This means that fluorine containing compounds exhibit high thermal and oxidative stability, low polarity, and weak inter-molecular interactions. The fluorinated species have the tendency to form a fluorous phase, which is immiscible with both hydrocarbons and water.(65; 66) These properties make them attractive for a wide variety of applications, including surfactants,(67; 68) gas absorption,(69–71) and membranes and conductive polymers.(66; 72) The fluorinated tails are able to aggregate into nanoscale fluorous domains, similar to alkylated tails. (13; 63; 73–75) The combination of ILs and fluorinated moieties can play a major role in developing stable and novel solvents.

To study the structure of fluorinated ILs in vacuum and the effect of fluorous tail length on the interfacial structure, we selected ILs with the $\text{Im}_{1,8}^+$ cation, paired with a series of $\text{BSI}_{1,n}$ anions: (trifluoromethylsulfonyl)(perfluorobutylsulfonyl)imide ($\text{BSI}_{1,4}^-$), (trifluoromethylsulfonyl)(perfluorohexylsulfonyl)imide ($\text{BSI}_{1,6}^-$), and (trifluoromethylsulfonyl)(perfluorooctylsulfonyl)imide ($\text{BSI}_{1,8}^-$), as shown in Figure 5.1. Both bulk structure simulations and liquid-vacuum interfacial simulations were carried out. The total structure functions $S(q)$ for $\text{Im}_{1,8}^+/\text{BSI}_{1,4}^-$ were confirmed by XRS experiment,(13) while the others are simulation based only.

5.1.1 Bulk structures of $\text{Im}_{1,8}^+/\text{BSI}_{1,n}^-$ salts

The total structure functions $S(q)$ of the four are shown in Figure 5.2 (left top). As the fluorinated tail length increases, the *adjacency peak* around $q \sim 1.3 \text{ \AA}^{-1}$ shifts to lower q values, while the *charge-charge alternation peak* around $q \sim 0.8 \text{ \AA}^{-1}$ shifts to higher q values. FSDPs are observed for all ILs, which arise from nonpolar domain aggregation of the hydrophobic tails in the system.(37; 76–79) The FSDPs in $S(q)$ for these three ILs are found the same q value, but with decreasing amplitude as the anion size decreases. For ILs with cation 1-alkyl-3-methylimidazolium ($\text{Im}_{1,n}^+$, $n \geq 4$) paired

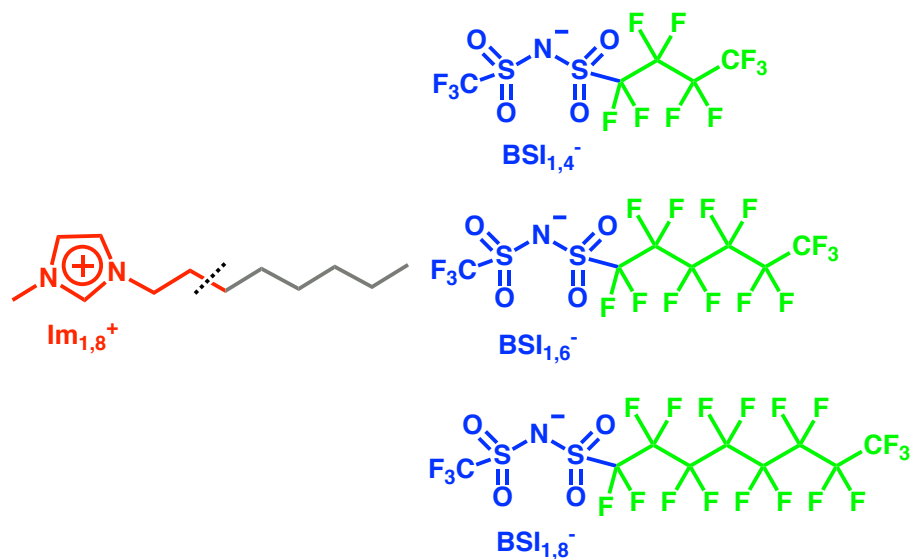


Figure 5.1: The molecular structures of ILs studied in this work. The cationic head is colored red; the cationic tail is colored gray; the anionic head is colored blue; and the anionic tail is colored green, The same coloring scheme is used throughout the manuscript.

with the small anions like Cl^- , the FSDP often shifts to lower q values with increasing amplitude as the alkylated tail increases.(80–83)

Fluorinated ILs often display FSDPs in $S(q)$ with low amplitudes due to destructive interference between peaks and anti-peaks.(13; 84; 85) Since the total $S(q)$ are a sum of multiple subcomponent interactions, we performed sub-ionic partitioning of $S(q)$ according to Eqn. 2.4. Figure. 5.2 displays positive-positive, negative-negative and positive-negative structural correlations contributing to $S(q)$. After partitioning, we observe that the *adjacency peaks* and *charge-charge alternation peaks* for the four ILs are at the same q value and of the same amplitude. This is to be expected since the three ILs have the same cationic and anionic head groups. The FSDPs in the sub-ionic partitioning shift to lower q values with increasing intensities as the fluorinated tail increases. This indicates that the size of nonpolar domains in the system is increasing as a result of increased volume occupancy of the nonpolar tails. Notice that the positive-negative component interactions in the lower q region contribute as peaks. In this region the cationic alkylated tails and anionic fluorinated tails act as “same-type” species.

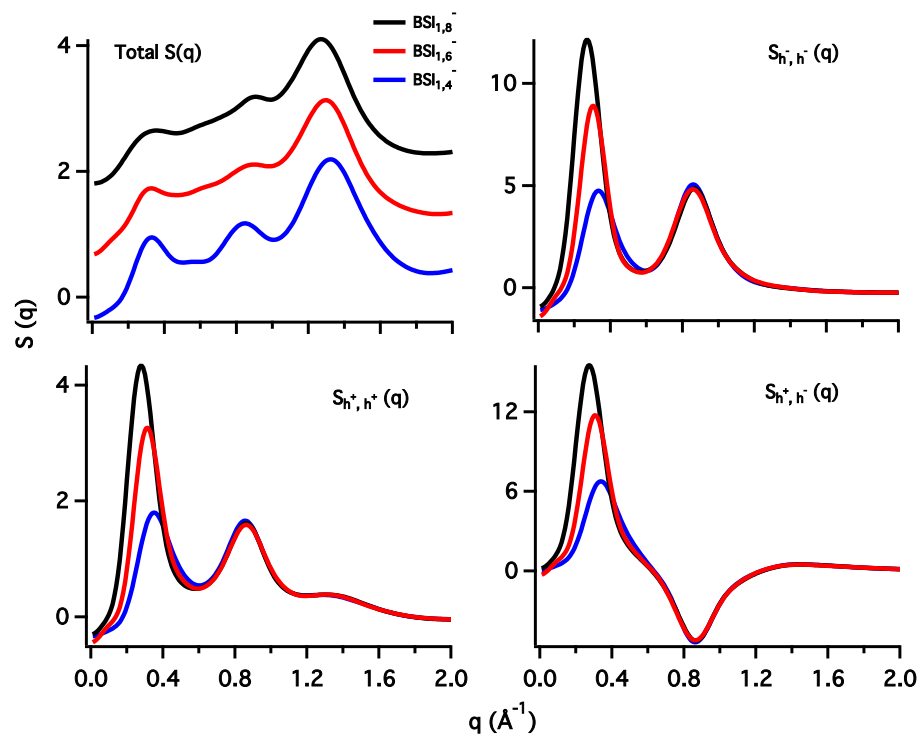


Figure 5.2: Total structure functions $S(q)$ and its sub-ionic partitioning for the $\text{Im}_{1,8}^+/\text{BSI}_{1,n}^-$ ILs. h^+ indicates the cationic head group (colored red in Figure 5.1), and h^- indicates the anionic head group (colored blue in Figure 5.1).

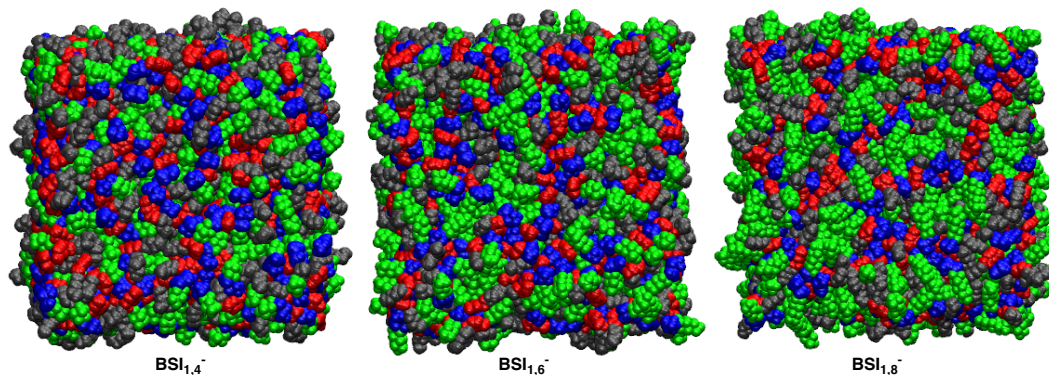


Figure 5.3: Snapshots of the equilibrated bulk systems of $\text{Im}_{1,8}^+$ paired with $\text{BSI}_{1,4}^-$, $\text{BSI}_{1,6}^-$, and $\text{BSI}_{1,8}^-$. The coloring scheme is the same as in Figure 5.1 The cubic box size is around 10 nm.

They form into hydrophobic domains that intercalate the charged work.(13; 86) The domain size corresponding to the q value of FSDPs ($2\pi/q$) has an increase of 1.2 Å per CF_2 unit. This value is much larger for ILs that only include fluorinated nonpolar tails like $\text{Im}_{2,1}^+/\text{BSI}_{1,n}^-$ ($2.2\text{Å}/\text{CF}_2$)(13) or ILs that include only alkylated tails like $\text{Im}_{1,n}^+/\text{NTf}_2^-$ ($2.1\text{Å}/\text{CH}_2$)(80–82). For $\text{Im}_{1,8}^+/\text{BSI}_{1,n}^-$, the nonpolar domains are formed by both the alkylated and fluorinated tails. Since the fluorinated tails occupy about half the hydrophobic volume fraction, it is reasonable that increasing the fluorinated tail length only increases the nonpolar domains with $1.2\text{ Å}/\text{CF}_2$.

The final frame from the production run of the simulated boxes are visualized with the Visual Molecular Dynamics (VMD) program.(87) The snapshots of equilibrated systems in bulk are shown in Figure 5.3. All three systems show a sponge-like structure with a continuous charged network and nonpolar domains. As the anion size increases, the charged network is stretched to accommodate the increased volume fraction the nonpolar moieties. When the fluorinated tail is short, like $\text{BSI}_{1,4}^-$, the nonpolar domains are dominated by the cationic alkyl tails. When the fluorinated tail is long, like $\text{BSI}_{1,8}^-$, the nonpolar domains are mainly formed by the fluorinated species. By changing the fluorinated tail length, the “hydrophobicity” of the nonpolar domains can be modified.

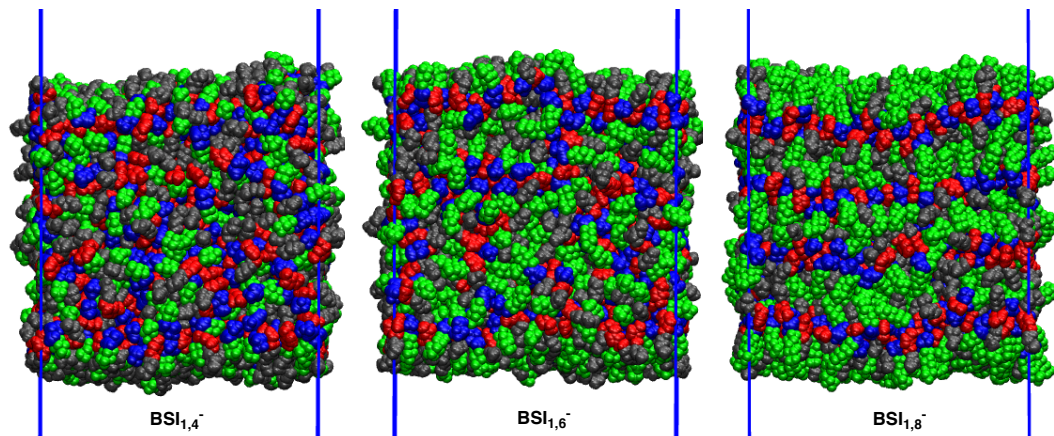


Figure 5.4: Snapshots of the equilibrated systems of $\text{Im}_{1,8}^+$ paired with $\text{BSI}_{1,4}^-$, $\text{BSI}_{1,6}^-$, and $\text{BSI}_{1,8}^-$ in vacuum, looking from the front of the box. The cubic box size is around 10 nm.

5.1.2 Interfacial structures of $\text{Im}_{1,8}^+/\text{BSI}_{1,n}^-$ ILs in vacuum

Since we are interested in the structure of the ILs in vacuum, each box from the bulk structure simulations is placed in the center of a box three time its length, with vacuum above and below. The approximate distance between the two vacuum interfaces is 10 nm. Figure. 5.4 shows the front view of the boxes from the last frame of the production run after thorough equilibration. As expected, the nonpolar tails, both alkylated and fluorinated, point to the vacuum and form the outermost layer. For $\text{Im}_{1,8}^+/\text{BSI}_{1,4}^-$, cationic and anionic heads can still be observed at the interfaces; while for $\text{Im}_{1,8}^+/\text{BSI}_{1,8}^-$, the interfaces are nearly fully covered by the hydrophobic tails. A charged layer of cationic and anionic heads follows next to the interfaces, forming a double layer lamellar structure. From empirical observations, we see that for $\text{Im}_{1,8}^+/\text{BSI}_{1,4}^-$, the middle of the box returns to the sponge-like bulk structure. For $\text{Im}_{1,8}^+/\text{BSI}_{1,6}^-$, we can distinguish another double layer of nonpolar tails and charged heads from the top. For $\text{Im}_{1,8}^+/\text{BSI}_{1,8}^-$, however, the lamellar structure was established across the entire slab.

To analyze the structure of the systems in Figure 5.4 quantitatively, the density profiles of ILs along the z axis are calculated. Figure. 5.5 shows the molecular number density per unit volume for cation head, cation tail, anion head and anion tail across

the slab for the three $\text{Im}_{1,8}^+/\text{BSI}_{1,n}^-$ ILs along z axis. The center of the slab is noted as the coordinate origin. The following observations apply to each of the three systems. The density profiles oscillate along the directions perpendicular to the interface. Density profiles for the cationic and anionic head groups are fully overlapped, while the alkylated and fluorinated tail density profiles oscillate together. The total molecular number density profile oscillates in sync with the cationic and anionic head density profiles. The charged heads are smaller in size than the hydrophobic tails and there is Coulombic attraction between the head groups, which results in the close packing - higher molecular number density per unit volume - of charged layers. The cation-tail and anion-tails peaks are farthest from the origin, as the tails are pointing into the vacuum. Notice that at this position, the densities for cation heads and anion heads are nearly zero, indicating that there is low probability of observing charged heads at the vacuum-IL interfaces. A layer of charged heads naturally follows going inside the slab, as the tails are attached to the heads.

The density profiles clearly show the structure change along the z axis of the slab configuration. The double layer lamellar structure at the interfaces give rise to the set of peaks at around 4 nm from the origin. If the structure returns to bulk liquid phase, then the density profiles flattens ($\text{Im}_{1,8}^+/\text{BSI}_{1,4}^-$). If the lamellar structure persists throughout the whole slab, then the density profiles oscillate with peaks of nearly the same amplitude ($\text{Im}_{1,8}^+/\text{BSI}_{1,8}^-$). For $\text{Im}_{1,8}^+/\text{BSI}_{1,6}^-$, which has a structure in between liquid phase and lamellar structure in the middle of the slab, the amplitude of the density modulation is reduced in the center of the slab.

For $\text{Im}_{1,8}^+/\text{BSI}_{1,4}^-$, the double layer lamellar structure at the interfaces only persists for 2 nm before returning to the bulk liquid structure, with a flat density profile. For $\text{Im}_{1,8}^+/\text{BSI}_{1,6}^-$, the double layer lamellar structure lasts about 3 nm at the interfaces. As pointed out by Wu, *et al.*,⁽⁶¹⁾ the 10 nm film for $\text{Im}_{1,8}^+/\text{BSI}_{1,6}^-$ is highly ordered because the density oscillations from each side do not decay completely but instead meet in the middle and are correlated. Therefore, the density profiles still show peaks in the middle of the slab, instead of flattening out like $\text{Im}_{1,8}^+/\text{BSI}_{1,4}^-$. For $\text{Im}_{1,8}^+/\text{BSI}_{1,6}^-$, the film is essentially two correlated interfaces with no bulk liquid in between. For

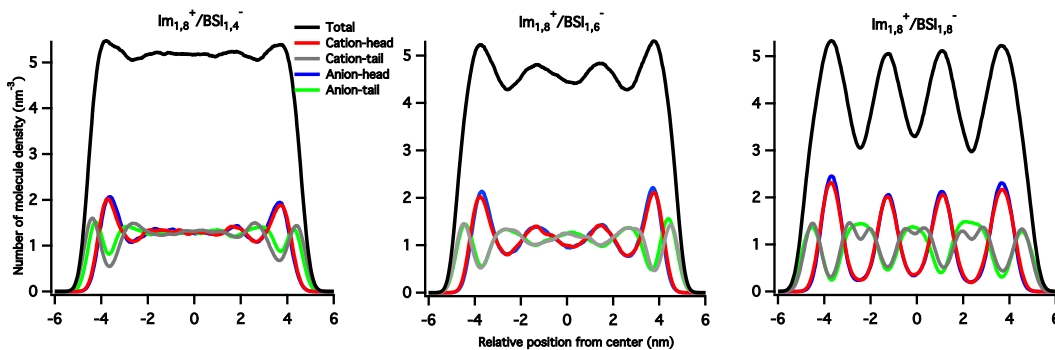


Figure 5.5: Molecular number density profiles for $\text{Im}_{1,8}^+/\text{BSI}_{1,4}^-$, $\text{Im}_{1,8}^+/\text{BSI}_{1,6}^-$, and $\text{Im}_{1,8}^+/\text{BSI}_{1,8}^-$ in the slab configuration. Each line represents the group or molecular number density per unit volume for different groups in the system along the Z axis of the extended simulation box. The total molecular number density is the sum of the four group molecular number densities.

$\text{Im}_{1,8}^+/\text{BSI}_{1,8}^-$, the double layer lamellar structure persists for 3.5 nm at the interfaces. After the double layers, the heads and tails continue to alternate inside the slab, establishing the lamellar phase. For every fluorinated tail peak, there are two alkylated tail peaks. The fluorinated tail on $\text{BSI}_{1,8}^-$ (C_8F_{17}) is longer and bulkier than the alkylated tails on $\text{Im}_{1,8}^+$ (C_6H_{13}). In the nonpolar layer sandwiched between two charged heads layers, the ends of long fluorinated tails are able to contact while the short alkylated tails are not. As a result, the alkylated tails are less possible to be found in the middle area of a nonpolar layer. Therefore, there are two alkylated tail peaks for one fluorinated tail peak.

Out of the three ILs, only $\text{Im}_{1,8}^+/\text{BSI}_{1,8}^-$ forms a lamellar structure across the slab when placed in vacuum. The length of nonpolar tails on the cations and anions is critical for the formation of lamellar structure, which determines the thickness of the double layers. As mentioned above, the thickness of a double layer at the interface is 2 nm for $\text{Im}_{1,8}^+/\text{BSI}_{1,4}^-$ and 3 nm for $\text{Im}_{1,8}^+/\text{BSI}_{1,6}^-$. For $\text{Im}_{1,8}^+/\text{BSI}_{1,8}^-$, the thickness of the double layer reaches 3.5 nm. The length of each of the three boxes is about the same, 12 nm from one interface to the other. For $\text{Im}_{1,8}^+/\text{BSI}_{1,8}^-$, the double layer from each side has no space to relax before meeting in the middle. The layer recurrence

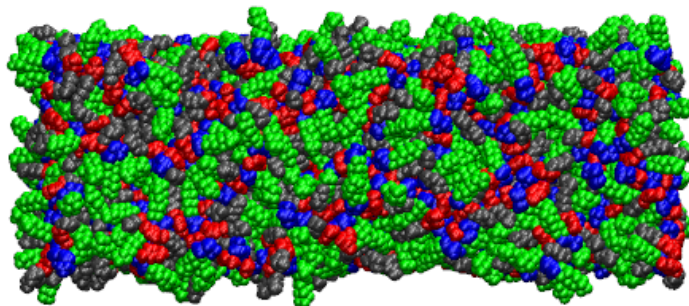


Figure 5.6: Snapshots of the scaled equilibrated box for $\text{Im}_{1,8}^+/\text{BSI}_{1,8}^-$ in bulk. Box size: 6.92403 x 6.92403 x 19.78296 nm.

results in the establishment of lamellar structure across the slab, which occurs only because layer alternation exists at the interface and the nonpolar tails are sufficiently long.(13; 61)

For $\text{Im}_{1,8}^+/\text{BSI}_{1,8}^-$, We notice that the amplitude of the peaks in the middle of the slab is smaller than that of the peaks at the interfaces. This raises the question that if we increase the length of the box along z axis, would the lamellar structure finally merges into a liquid phase in the middle, as shown by Wu.(61) If so, to what extent would the lamellar structure persist?

5.1.3 Structure of $\text{Im}_{1,8}^+/\text{BSI}_{1,8}^-$ in a scaled box

To answer the questions as to the structure of $\text{Im}_{1,8}^+/\text{BSI}_{1,8}^-$ in a larger box, we performed simulations of $\text{Im}_{1,8}^+/\text{BSI}_{1,8}^-$ in a scaled box. The 1,000 ion pairs were placed in a rectangular box with a size of 7 nm x 7 nm x 20 nm. The box length is doubled in z axis. The procedure as described in the “Bulk IL Simulations” section was followed to fully equilibrate the box. The snapshots of the scaled box from the last frame of production run is shown in Figure 5.6. As expected, sponge-like structure is observed regardless of the shape of the box, as the box is periodically replicated in all directions.

Following the procedures described in the “Vacuum-IL Simulations” section, the scaled box was placed in vacuum and went through sufficient equilibration (216 ns)

under 425 K. The last 100 ns is used for analysis. Figure 5.7 shows color-coded density profiles and composite snapshots of the system consisting of 90 frames each spanning from 116 to 216 ns in the equilibration run. The fluorinated and alkylated tail peaks at around 10 nm from the origin show that the vacuum-IL interfaces are fully covered by the nonpolar tails, pointing to the vacuum. For this 20 nm film, about two oscillation cycles of subcomponent density profiles are observed, before the profiles go into flat with random oscillations. The complete decay lengthscale is about 5 nm, which explains the formation of lamellar structure for $\text{Im}_{1,8}^+/\text{BSI}_{1,8}^-$ as observed in Figure 5.4. The lamellar structure, which is formed due to the introduction of vacuum-IL interfaces, can last about two oscillation cycles of “tails - charged heads”. If the box length is large enough, the lamellar structure returns into the sponge-like liquid structure in the middle of the film.

5.1.4 Structure of $\text{Im}_{1,8}^+/\text{BSI}_{1,8}^-$ in Electric field

Is there any way to affect the structure of ILs so that the lamellar structure can be re-established across the 20 nm slab? Considering that ILs are composed of cations and anions, we think of applying an electric field along the Z axis. This was done by setting the first parameter of electric-field-z (E_0) to the desired electric field strength in GROMACS (version 2016.1).^(88; 89) The last configuration of the $\text{Im}_{1,8}^+/\text{BSI}_{1,8}^-$ slab (20 nm) in vacuum after 100 ns equilibration was used as the starting structure for simulations in electric field. We first applied an electric field of $E_0 = 0.5$ V/nm for 60 ns. Next we increased the electric field strength to $E_0 = 1.0$ V/nm for another 60 ns. We name the structure of $\text{Im}_{1,8}^+/\text{BSI}_{1,8}^-$ at this point “structure-0”. After this, with the last configuration of the slab in electric field, we did two things: (1) extend the simulation with $E_0 = 1.0$ V/nm for 60 ns, and “structure-1” was obtained; (2) remove the electric field ($E_0 = 0$ V/nm) and equilibrate for 100 ns, and “structure-2” was obtained;

Structures 0-2 are shown in Figure 5.8. The lamellar structure is re-established across the 20 nm slab for all three structures. The density profiles are shown in Figure 5.9. Note that the time interval used for the density calculation is 100 ps instead of

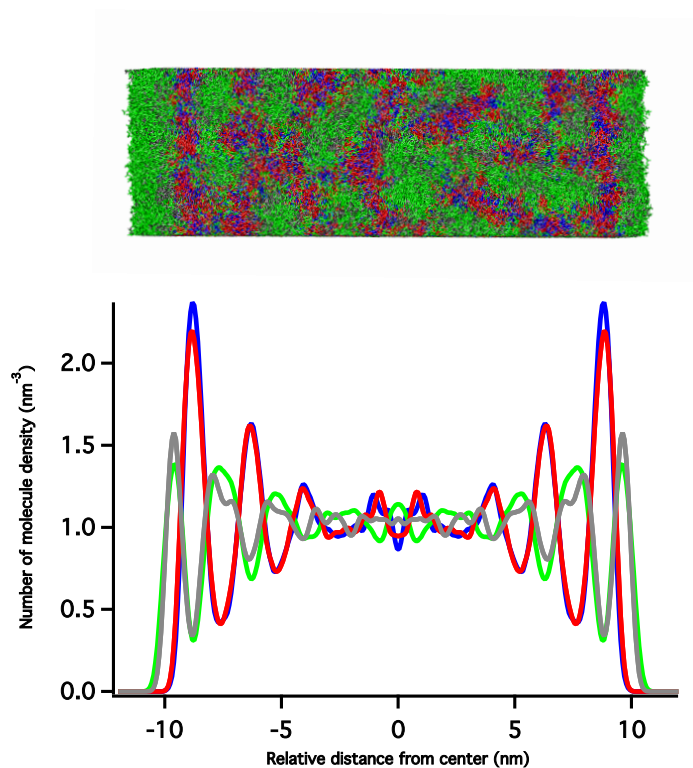


Figure 5.7: Simulation box snapshot and molecule density profiles for $\text{Im}_{1,8}^+/\text{BSI}_{1,8}^-$ in rectangular box after equilibrated in vacuum. On top of the density profiles, we show an overlay of 90 frames across the last 100 ns equilibration trajectory. The density profiles are calculated using trajectories from the last 100 ns equilibration procedure. Box size: 6.92403 x 6.92403 x 19.78296 nm.

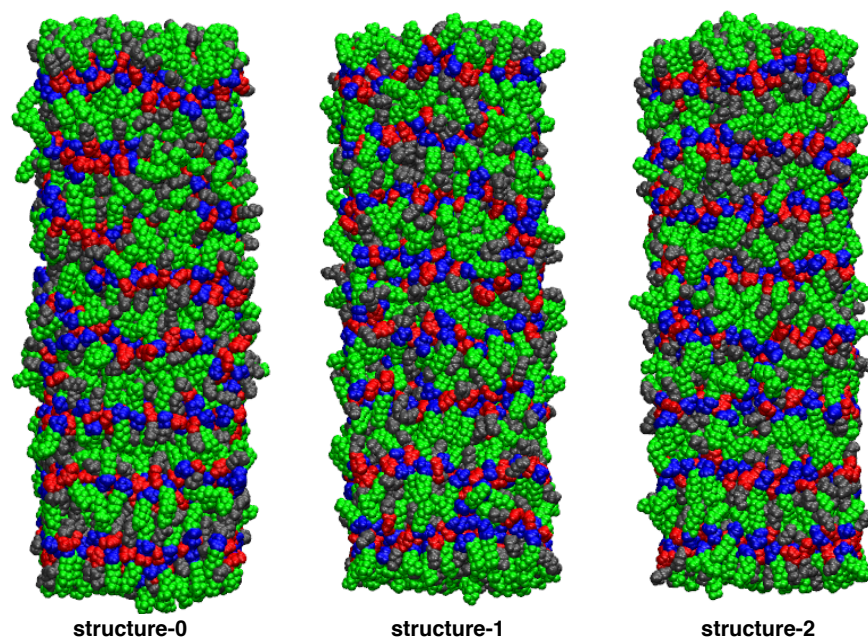


Figure 5.8: Snapshots of structures 0-2 from the last frame of slab configuration. structure-0 was obtained after the slab in vacuum was equilibrated in an electric field of $E_0 = 0.5$ V/nm for 60 ns; structure-1 was obtained after structure-0 was equilibrated in $E_0 = 1.0$ V/nm for 60 ns; and structure-2 was obtained after structure-1 was equilibrated without an electric field for 100 ns.

100 ns, since we are looking at the evolution of structures. From the density profiles, we can see that the full length lamellar structure is re-established after about 40 ns in $E_0 = 1.0$ V/nm. The establishment of lamellar structure starts from each end of the box at the interfaces and moves onto the middle of the slab. The electric field strength is doubled after 60 ns in $E_0 = 1.0$ V/nm to speed up the formation of lamellar structure in the middle, although these fields are well above the experimental limits imposed by dielectric breakdown. Once the lamellar structure is established across the whole slab, the electric field is no longer needed, as shown by the dashed lines in Figure 5.9. In fact, after removing the electric field, the structure becomes more ordered as the equilibration continues. Without the electric field, the lamellar structure may return to the “lamellar structure - liquid - lamellar structure” state as shown in Figure 5.7, but that requires a time scale much longer than 100 ns used in this work.

5.1.5 Summaries of the structure of $\text{Im}_{1,8}^+/\text{BSI}_{1,8}^-$ in rectangular box

Inspired by the exciting work done by Amith and Wu,(59; 61), we carried out interfacial simulations of $\text{Im}_{1,8}^+/\text{BSI}_{1,n}^-$ ILs in vacuum to study the structure change of these fluorinated ILs. It is found that for all the systems studied, the vacuum-IL interfaces are covered by the hydrophobic tails, followed by an inner layer of charged heads. In a cubic box with length of 10 nm, a lamellar structure can be observed across the whole slab when the cationic alkylated tails and anionic fluorinated tails are both sufficiently long, like $\text{Im}_{1,8}^+/\text{BSI}_{1,8}^-$. Otherwise, the middle of the box may be in a liquid phase like the case of $\text{Im}_{1,8}^+/\text{BSI}_{1,4}^-$, or more ordered than bulk liquid structure as in the case of $\text{Im}_{1,8}^+/\text{BSI}_{1,6}^-$. When we increased the box length along the z axis, the lamellar structure only persists about two oscillation cycles of “tails-heads” double layers, before returning to a sponge-like bulk structure. To re-establish the lamellar structure for $\text{Im}_{1,8}^+/\text{BSI}_{1,8}^-$ across the 20 nm slab, we can apply electric field along the z axis. Once the full length lamellar structure is restored, the electric field is not necessary to maintain the established structure. The relaxation time of the newly established structure goes beyond 100 ns. This work demonstrated that the structure of ILs in vacuum is affected by a number of factor, including the length of tails on the cations and anions, the

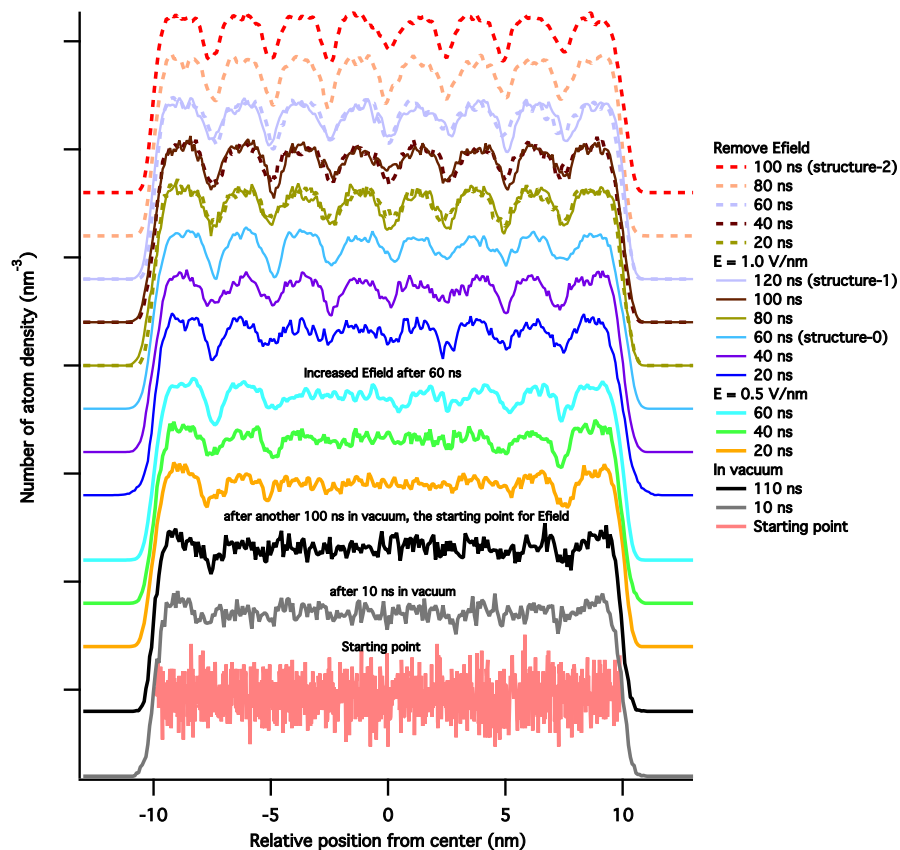


Figure 5.9: Calculate the atom number density profiles along the Z axis of the scaled simulation box for $\text{Im}_{1,8}^+/\text{BSI}_{1,8}^-$ after 110 ns in vacuum, 60 ns in an electric field of 0.5 V/nm, and 60 ns in an electric field of 1.0 V/nm. Next: (1) extend the simulation with $E_0 = 1.0$ V/nm for 60 ns; (2) remove the electric field and equilibrate for 100 ns. The time interval for density analysis is 100 ps.

distance between the interfaces, and electric fields. This provides us several ways to manipulate the structure of ILs as needed, which is one step further towards designing task specific ionic liquids.

5.2 Interfacial Structure Difference Between Alkylated and Fluorinated Tails

During our experience with fluorinated ILs, we find that the fluorinated tails and alkylated tails can not form separate nonpolar domains due to charge alternation. However, when the alkyl tail is replaced by its equivalent perfluorinated tails, the structure of ILs becomes more ordered.

In this section, we aim at studying the structure difference between ILs with long alkyl tails and ILs with long fluorinated tails in vacuum, and how the ions interact in a mixture using MD simulations. The systems include three ILs with the $\text{Im}_{2,1}^+$ cation paired with (trifluoromethylsulfonyl)(perfluorohexylsulfonyl)imide ($\text{BSI}_{1,6}^-$), (trifluoromethylsulfonyl)(perfluoroheptylsulfonyl)imide ($\text{BSI}_{1,7}^-$), and (trifluoromethylsulfonyl)(perfluorooctylsulfonyl)imide ($\text{BSI}_{1,8}^-$); and $\text{Im}_{1,8}^+/\text{NTf}_2^-$. Finally, a 1:1 mixture of $\text{Im}_{1,8}^+/\text{NTf}_2^-$ and $\text{Im}_{2,1}^+/\text{BSI}_{1,8}^-$, which can also be seen as a 1:1 mixture of $\text{Im}_{1,8}^+/\text{BSI}_{1,8}^-$ and $\text{Im}_{2,1}^+/\text{NTf}_2^-$, is simulated to study its structure at the vacuum interface. The chemical molecular structures are shown in Fig. 5.10.

5.2.1 Bulk structures of the salts

The liquid structure functions for ILs from MD simulations are calculated from the production run. The ionic partitioning of $S(q)$ as defined by Eqn. 2.3 is shown in Fig. 5.11. A FSDP is displayed at around 0.4 \AA^{-1} in the total $S(q)$ for $\text{Im}_{1,8}^+/\text{NTf}_2^-$ due to the octyl tails. For the $\text{Im}_{2,1}^+/\text{BSI}_{1,n}^-$ ILs, though the perfluorinated tails on the anions are long enough to form fluorine domains,(13; 74) no FSDPs can be observed in the total $S(q)$. It is after ionic partitioning that the FSDPs are revealed. The fluorinated tails aggregate into nano-scale nonpolar domains in bulk, the same as alkylated tails do, see Fig. 5.12. For $\text{Im}_{2,1}^+/\text{BSI}_{1,n}^-$ ILs, the ionic peaks and antipeaks in the lower q

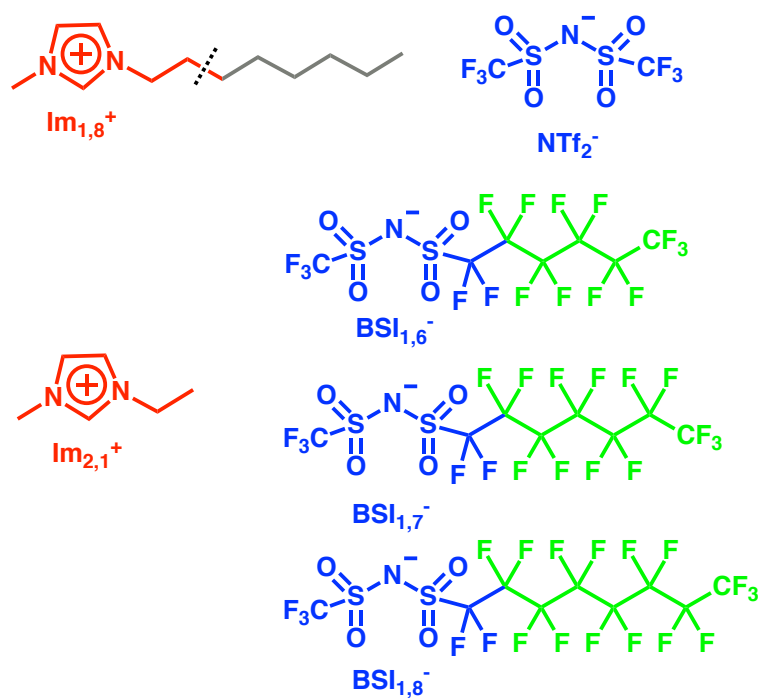


Figure 5.10: The molecular structures of ILs studied in this work. The cationic head is colored red; the cationic tail is colored gray; the anionic head is colored blue; and the anionic tail is colored green. The same coloring scheme is used throughout the manuscript unless indicated otherwise.

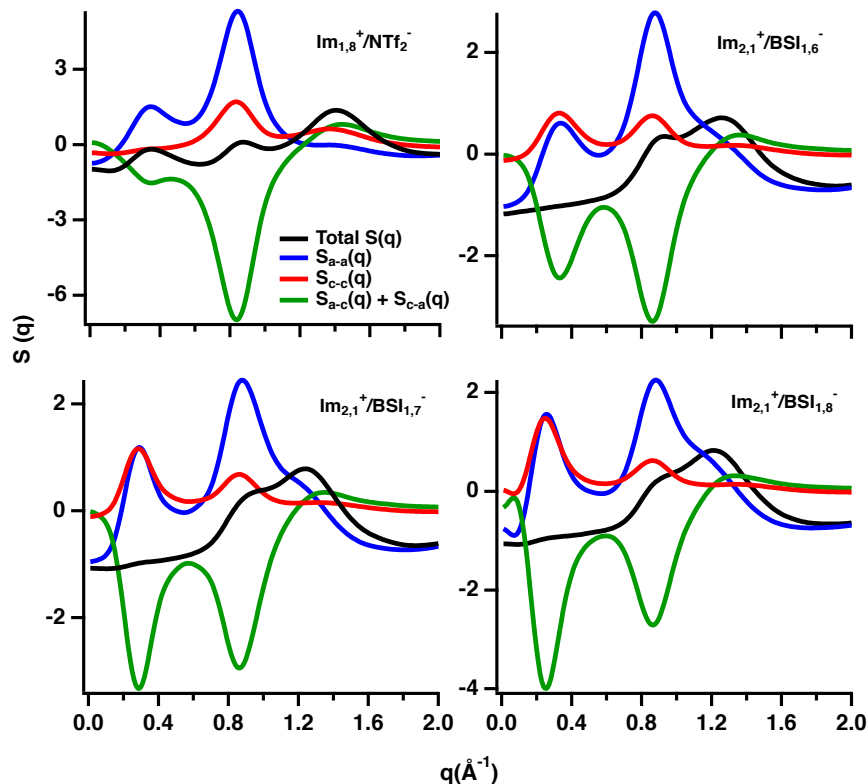


Figure 5.11: Total structure functions $S(q)$ and its ionic partitioning for the set of four ILs in Fig. 5.1. The ionic components add up to the black total $S(q)$ profile.

region completely cancel out and can not be appreciated by X-ray scattering measurement. This is quite common for fluorinated ILs.(13; 90) As the fluorinated tails become longer, the ionic FSDPs shift to lower q values with increasing amplitude. A lower q value corresponds to larger domain size ($2\pi/q$) due to the increased volume of nonpolar species, as can be seen in Fig. 5.12.

5.2.2 Interfacial structures of the salts

The equilibrated boxes from the bulk simulations were placed in vacuum to obtain the interfacial structure of the studied ILs. After 100 ns equilibration at 425 K, the liquid-vacuum structures of the ILs were obtained. The approximate distance between the two vacuum interfaces is 9 nm. Figure. 5.13 shows the snapshots of the boxes (viewing along x axis) from the last frame of the production run.

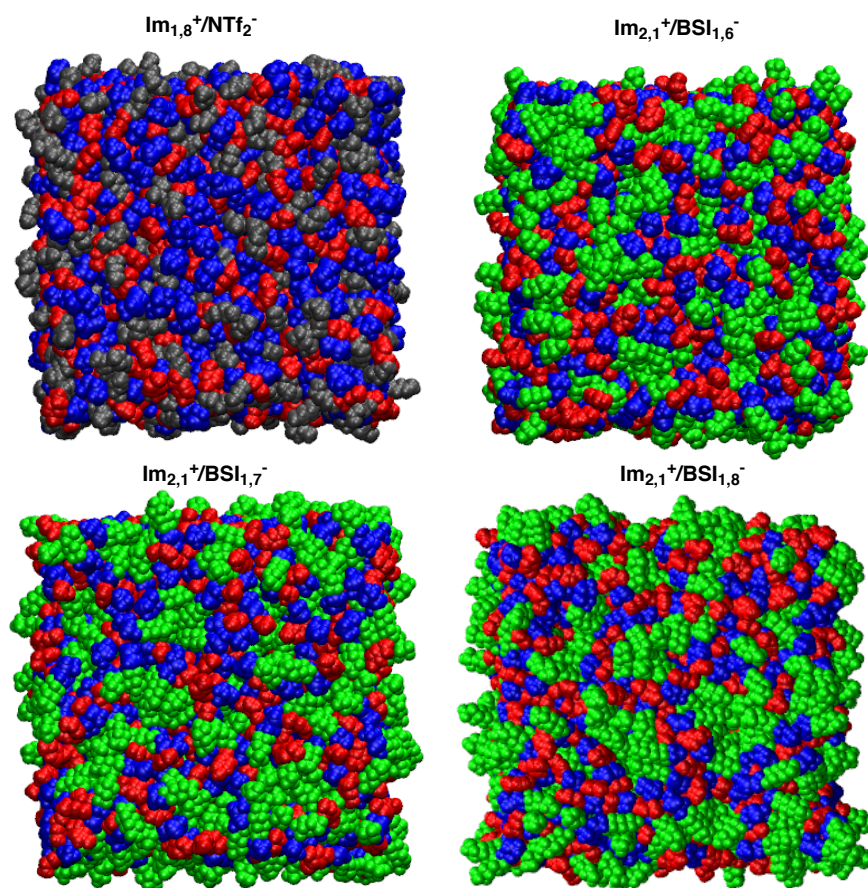


Figure 5.12: Snapshots of the equilibrated systems in bulk. The production runs were carried out at 298 K and 1 bar.

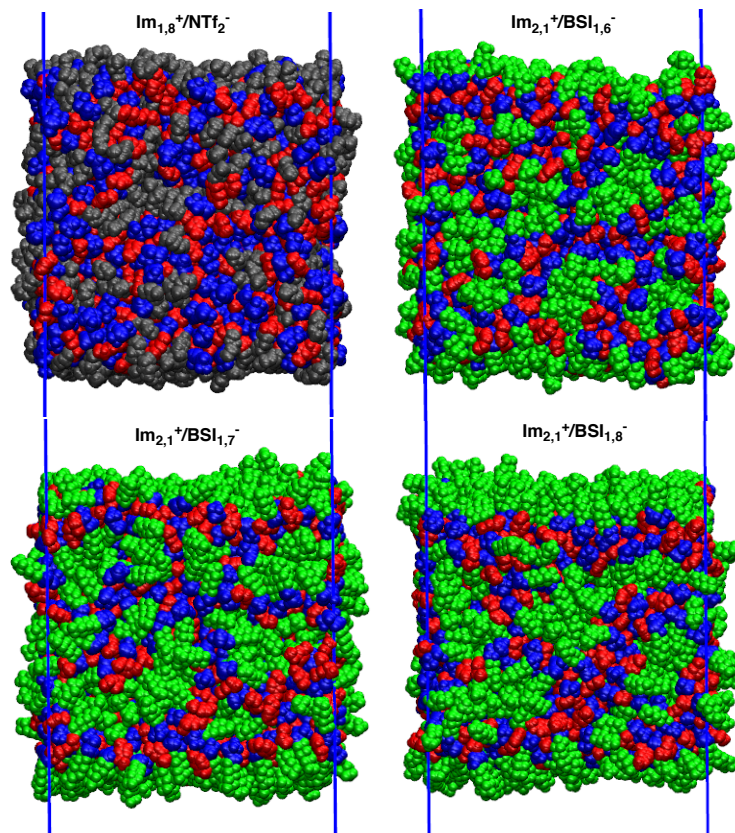


Figure 5.13: Snapshots of the equilibrated systems in vacuum. The coloring scheme is the same as in Fig. 5.1. The cubic box length is around 9 nm.

We can see that the interfaces are covered by hydrophobic tails pointing towards the vacuum. Though the cationic tail on $\text{Im}_{1,8}^+$ (C_6H_{13}) has the same number of carbon atoms as in the anionic tail on $\text{BSI}_{1,7}^-$ anion (C_6F_{13}), the nonpolar interfaces for $\text{Im}_{2,1}^+/\text{BSI}_{1,7}^-$ is thicker than the interfaces for $\text{Im}_{1,8}^+/\text{NTf}_2^-$ due to their volume difference. Following the interfaces, we can see a clear layer of charged heads into the slab for $\text{Im}_{2,1}^+/\text{BSI}_{1,n}^-$ ILs, but there is no such clear definition of a charged layer for $\text{Im}_{1,8}^+/\text{NTf}_2^-$. From $\text{Im}_{2,1}^+/\text{BSI}_{1,6}^-$ to $\text{Im}_{2,1}^+/\text{BSI}_{1,8}^-$, the thickness of the tail layer at the interface increases as the fluorinated tail becomes longer. In the middle of the slab, both $\text{Im}_{1,8}^+/\text{NTf}_2^-$ and $\text{Im}_{2,1}^+/\text{BSI}_{1,6}^-$ show a sponge-like structure like the bulk liquid state. For $\text{Im}_{2,1}^+/\text{BSI}_{1,7}^-$ and $\text{Im}_{2,1}^+/\text{BSI}_{1,8}^-$, the influence of introducing vacuum interfaces persists into the middle of the slab, where the structure is highly ordered.

To analyze the liquid-vacuum structure of the systems quantitatively, Fig. 5.14 shows the molecular number density per unit volume for the cationic head (cation), the anionic head (anion) and the hydrophobic tail across the slab for the set of four ILs along z axis. For $\text{Im}_{1,8}^+/\text{NTf}_2^-$, there is a peak of cationic tails at the interfaces followed by peaks of cationic and anionic heads. After that, the density profiles flatten going into the middle of the slab, where the IL is in a liquid phase. The “tails - charged heads” double layer lasts about 2 nm. For $\text{Im}_{2,1}^+/\text{BSI}_{1,n}^-$ ILs, there is a peak of fluorinated tails followed by peaks of charged heads, corresponding to the double layer of “fluorinated tails - charged heads” at the interfaces. From the density profiles, we can see that the structure in the middle of the slab is still affected by the introduction of vacuum interfaces. The double layer on each side of the interface is not able to relax completely before meeting in the middle, thus the peaks in the middle of the density profiles. There is no bulk liquid structure evident in between the interfaces, as shown by the highly ordered network in Fig. 5.13. From $\text{Im}_{2,1}^+/\text{BSI}_{1,6}^-$ to $\text{Im}_{2,1}^+/\text{BSI}_{1,8}^-$, we see that the two peaks at the middle of the box are merging into one. The double layer for $\text{Im}_{2,1}^+/\text{BSI}_{1,8}^-$ lasts about 4 nm while the interfaces are only 9 nm apart. We can expect that as the fluorinated tails get longer, the second layer of fluorinated tails from each side of the interface will occupy the middle of the box, separated by one layer of cationic and anionic charge heads. From the above analysis, we can see that the introduction of vacuum interfaces has more effect on the structure of fluorinated ILs. As the fluorinated tails become longer, the middle of the box will transfer from a liquid like structure to a highly ordered state.

5.2.3 Structure of the $[\text{Im}_{1,8}^+, \text{Im}_{2,1}^+, \text{NTf}_2^-, \text{BSI}_{1,8}^-]$ mixture

In our previous work on the liquid-vacuum interfacial structure of ILs, it is found that $\text{Im}_{1,8}^+/\text{BSI}_{1,8}^-$, when put in a cubic box with a length of about 10 nm, a lamellar structure is established across the whole slab. If the box length along the z direction is increased, the lamellar structure will return to bulk liquid state in the middle. In this work, we added 1,000 ion pairs of $\text{Im}_{2,1}^+/\text{NTf}_2^-$ to the 1,000 ion pairs of $\text{Im}_{1,8}^+/\text{BSI}_{1,8}^-$,

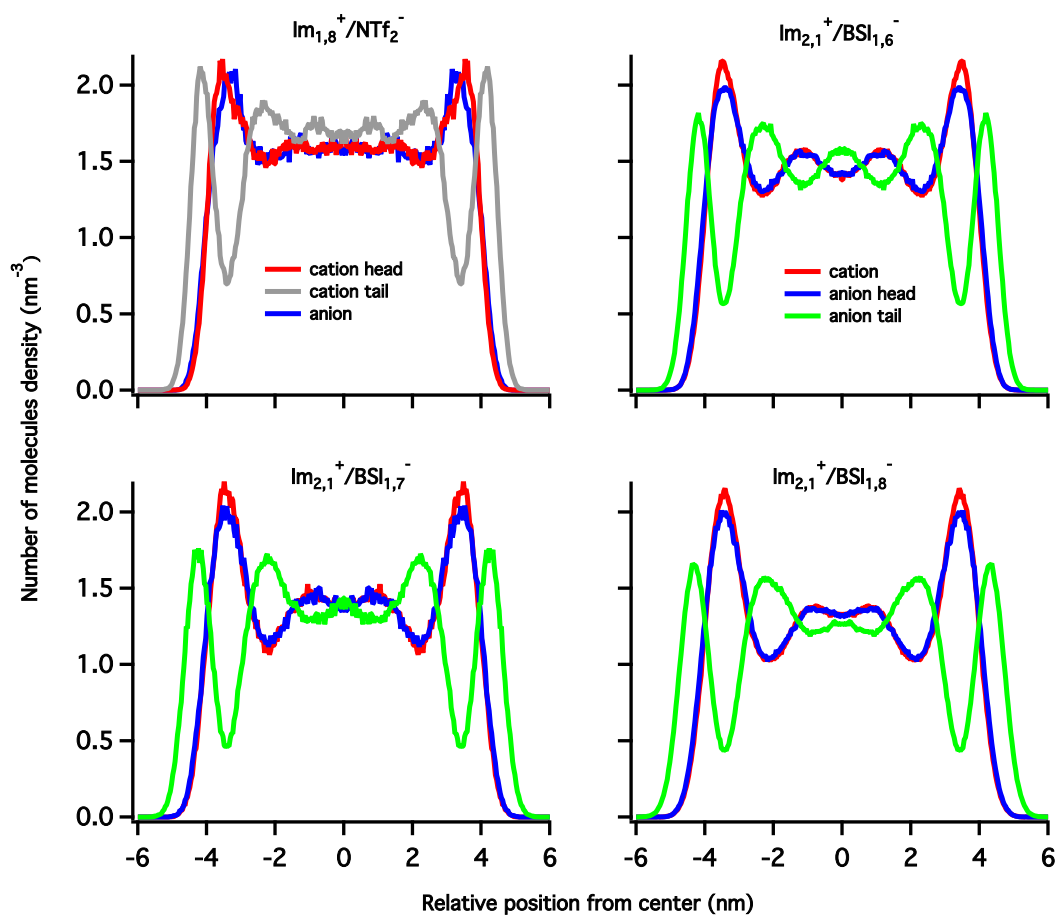


Figure 5.14: Molecular number density profiles for the set of four ILs in the slab configuration. Each line represents the group or molecular number density per unit volume for different groups in the system along the Z axis of the extended simulation box. The density profiles are calculated using the 100 ns equilibration process. The center of the slab is noted as origin.

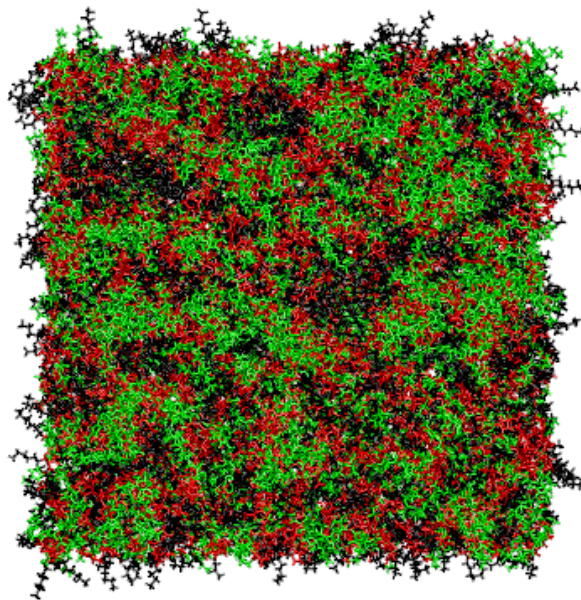


Figure 5.15: Snapshots of the 1:1 mixture of $\text{Im}_{1,8}^+/\text{BSI}_{1,8}^-$ and $\text{Im}_{2,1}^+/\text{NTf}_2^-$ in bulk. The coloring scheme is the same as shown in Fig. 5.17.

in order to see how the added ions (with no nonpolar part) affect the lamellar structure that will otherwise be formed by pure $\text{Im}_{1,8}^+/\text{BSI}_{1,8}^-$.

Fig. 5.16 shows a plot of $S(q)$ in the bulk for each of the two liquids and their mixture. From it we see that the $S(q)$ for $\text{Im}_{1,8}^+/\text{BSI}_{1,8}^-$ has a FSDP for $q < 0.5 \text{ \AA}^{-1}$, characteristic of polar-apolar heterogeneity; this peak is absent in the case of $\text{Im}_{2,1}^+/\text{NTf}_2^-$. Both liquids show typical charge alternation regions at $q \sim 0.9 \text{ \AA}^{-1}$ and the usual adjacency peak for $1.27 \leq q \leq 1.44 \text{ \AA}^{-1}$. The adjacency peak for $\text{Im}_{2,1}^+/\text{NTf}_2^-$ is at a higher q value due to the small size of the $\text{Im}_{2,1}^+$ and NTf_2^- ions. Their mixture has a FSDP of lower intensity. A snapshot of the box from the last frame of the production run is shown in Fig. 5.15. The nonpolar domains (colored black) are formed by both the alkyl tails and fluorinated tails.

Next, the box of the mixture was placed in vacuum and went through sufficient equilibration. Fig. 5.17 shows color-coded density profiles highlighting polar and apolar subcomponents with the polar subcomponent further divided into the contribution

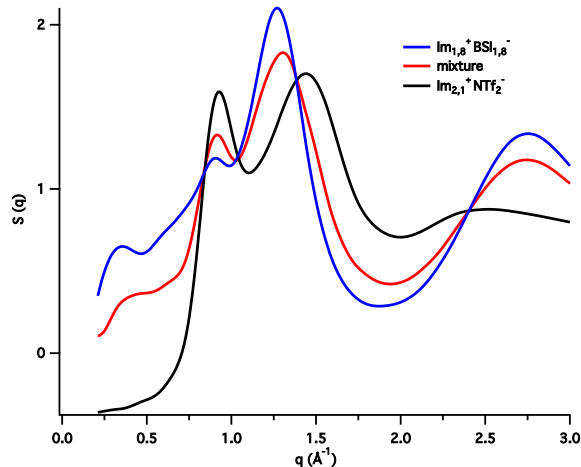


Figure 5.16: Total structure functions $S(q)$ for $\text{Im}_{1,8}^+/\text{BSI}_{1,8}^-$, $\text{Im}_{2,1}^+/\text{NTf}_2^-$, and their 1:1 mixture.

of larger and smaller ions. Associated with the profiles, we also show composite snapshots of our system consisting of 100 frames each spanning from the last 100 ns in the equilibration run.

For this 11 nm thick film, after only one oscillation cycles of the subcomponent density profiles, the density profiles go mostly flat, indicating a complete decay lengthscale of about 4 nm. The outermost layer is apolar followed by charged contribution of the larger ions and then from the smaller ions. Recall that when the system contains pure $\text{Im}_{1,8}^+/\text{BSI}_{1,8}^-$ with a box size of 9 nm, the lamellar structure is formed throughout the slab. Now that the box size increased to 11 nm, the lamellar structure only exists at the interfaces, while the middle of the simulation box returns to sponge-like structure. The addition of $\text{Im}_{2,1}^+/\text{NTf}_2^-$ interrupts the ordering of the $\text{Im}_{1,8}^+/\text{BSI}_{1,8}^-$ ions in the middle of the box.

Figure. 5.18 shows the density profiles for each of the positive, negative, and apolar sub-ionic components of the film. Approaching the system from the vacuum interface, we find first the apolar layer composed of the tails of $\text{Im}_{1,8}^+/\text{BSI}_{1,8}^-$. The peaks of the alkyl and fluorinated are on top of each other, showing that the vacuum has the same preference for the nonpolar tails. Next, it reveals that the polar layer is actually two different adjacent layers that partially overlap. Approaching from the interface to the

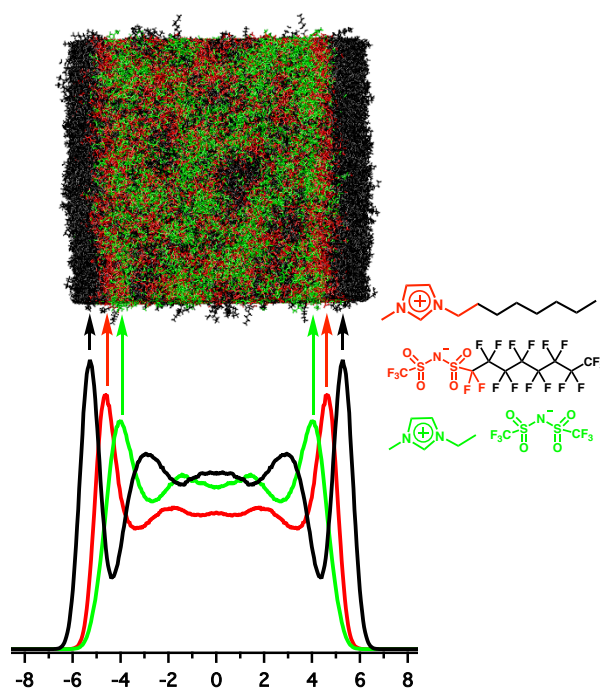


Figure 5.17: For the mixture system, the graph shows atomic density profiles. The profile for apolar tails is in black, for the polar Im_{1,8}⁺ cationic heads and BSI_{1,8}⁻ anionic heads is in red, and for the Im_{2,1}⁺ and NTf₂⁻ ions is in green. On top of the density profiles, an overlay of 100 frames across the full 100 ns production run trajectory is shown. The position along the Z-direction where the individual density maxima occurs is highlighted. The box size is around 11 nm.

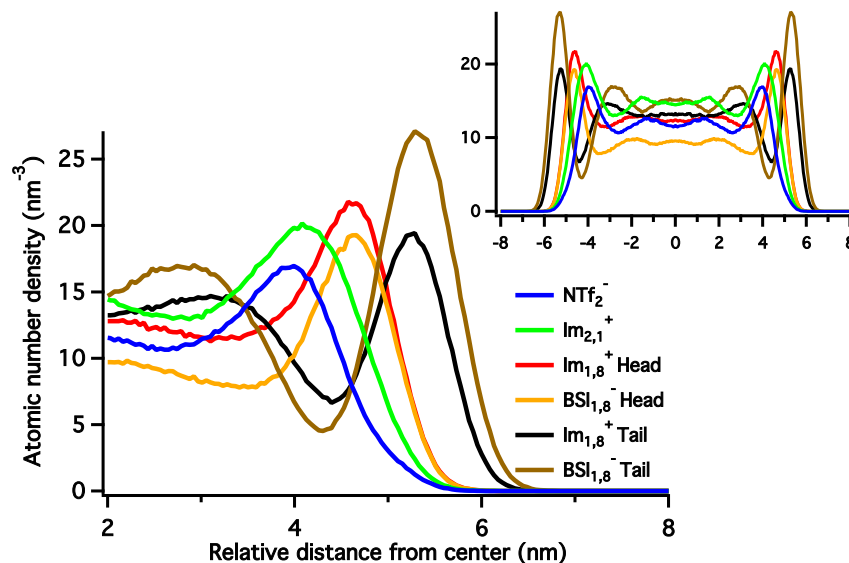


Figure 5.18: Color-coded symmetrized (about the center of the box) density profiles in the vicinity of the interface for positive, negative, and apolar sub-ionic components for the film. Inset shows corresponding symmetrized full density profiles. For the film, we find first an apolar monolayer, followed by the charged heads of the larger ions and then by those of the smaller ions.

middle of the simulation box, we find first the peaks of the $\text{Im}_{1,8}^+$ -head and $\text{BSI}_{1,8}^-$ -head at the same relative distance from center. This is to be expected since the charged head groups are attached to the nonpolar tails, which are pointing towards the vacuum. Next we found the peaks for $\text{Im}_{2,1}^+$ cations and NTf_2^- anions, and the peak of $\text{Im}_{2,1}^+$ cations is slightly outside that of the NTf_2^- anions. This shows that the smaller ions are not in the polar layer composed of the charged heads of $\text{Im}_{1,8}^+/\text{BSI}_{1,8}^-$. Otherwise the smaller ions will interrupt the ordering of nonpolar tails at the outermost layer. Overall, this results in an apolar layer of 2 nm at the liquid-vacuum interface adjacent to a polar layer of 3 nm.

5.2.4 Summary of interfacial structures for fluorinated-anion ILs

In this work, we study the liquid-vacuum structure of ILs with long hydrophobic tails on either the cation or the anion. For $\text{Im}_{1,8}^+/\text{NTf}_2^-$ with nonpolar alkyl tails, the

introduction of vacuum only affects the outermost layer, formed by the alkyl tails. The middle of the slab is in sponge-like liquid phase. For $\text{Im}_{2,1}^+/\text{BSI}_{1,n}^-$ ILs with fluorinated tails, the effect of vacuum-IL interfaces would persist deeper into the slab (away from the surface), where no liquid phase exists due to the structure recurrence. For a mixture of $\text{Im}_{1,8}^+/\text{BSI}_{1,8}^-$ and $\text{Im}_{2,1}^+/\text{NTf}_2^-$, approaching from the vacuum interface, we first find a layer of apolar tails, then a polar layer of charged heads of the larger ions, followed by a polar layer of small ions. After only one oscillation cycle of density peaks, the density profiles mostly go flat in the middle of the slab. The structure of ILs in a slab configuration is affected by many factor including molecular structure and the composition of ILs in a mixture.

5.3 Conclusions

As shown in this chapter, the structure of ILs in vacuum is very different from their bulk structures. For ILs in vacuum, if the cations/anions include nonpolar tails, the nonpolar tails point to the vacuum, forming a nonpolar tail-charge head double layer structure at the liquid-vacuum interfaces. The structure in the middle of the slab can be affected by the nonpolar tail length and electric fields. By controlling these factors, a lamellar structure up to 20 nm can be established across the slab by applying electric fields. The lamellar structure is stable after removing the electric field for up to 100 ns used in this work. This may be useful in electrochemistry applications and separation processes.

Bibliography

- [1] H.-P. Steinrueck and P. Wasserscheid. “Ionic Liquids in Catalysis.” *Catal. Lett.*, 145, 380–397, 2014. doi:10.1007/s10562-014-1435-x.
- [2] J. P. Hallett and T. Welton. “Room-temperature ionic liquids: solvents for synthesis and catalysis. 2.” *Chem. Rev.*, 111, 3508–3576, 2011. doi:10.1021/cr1003248.
- [3] Z. Ma, J. Yu, and S. Dai. “Preparation of Inorganic Materials Using Ionic Liquids.” *Adv. Mater.*, 22, 261–285, 2010. doi:10.1002/adma.200900603.

- [4] Y. Zhou and J. Qu. “Ionic liquids as lubricant additives: A review.” *ACS Appl. Mater. Interfaces*, 9, 3209–3222, 2017. doi:10.1021/acsami.6b12489.
- [5] E. L. Smith, A. P. Abbott, and K. S. Ryder. “Deep Eutectic Solvents (DESS) and Their Applications.” *Chem. Rev.*, 114, 11060–11082, 2014. doi:10.1021/cr300162p.
- [6] F. Zhou, Y. Liang, and W. Liu. “Ionic liquid lubricants: designed chemistry for engineering applications.” *Chem. Soc. Rev.*, 38, 2590–2599, 2009. doi:10.1039/B817899M.
- [7] J. Qin, Q. Lan, N. Liu, F. Men, X. Wang, Z. Song, and H. Zhan. “A metal-free battery with pure ionic liquid electrolyte.” *iScience*, 15, 16 – 27, 2019. doi:10.1016/j.isci.2019.04.010.
- [8] A. Eftekhari. “Supercapacitors utilising ionic liquids.” *Energy Storage Mater.*, 9, 47–69, 2017. doi:10.1016/j.ensm.2017.06.009.
- [9] R. Kido, K. Ueno, K. Iwata, Y. Kitazawa, S. Imaizumi, T. Mandai, K. Dokko, and M. Watanabe. “Li⁺ Ion Transport in Polymer Electrolytes Based on a Glyme-Li Salt Solvate Ionic Liquid.” *Electrochim. Acta*, 175, 5–12, 2015. doi:10.1016/j.electacta.2015.01.067.
- [10] D. M. Piper, T. Evans, K. Leung, T. Watkins, J. Olson, S. C. Kim, S. S. Han, V. Bhat, K. H. Oh, D. A. Buttry, and S.-H. Lee. “Stable silicon-ionic liquid interface for next-generation lithium-ion batteries.” *Nat. Commun.*, 6, 6230, 2015. doi:10.1038/ncomms7230.
- [11] J. F. Wishart. “Energy applications of ionic liquids.” *Energy Environ. Sci.*, 2, 956–961, 2009. doi:10.1039/b906273d.
- [12] J. D. Holbrey, R. D. Rogers, R. A. Mantz, P. C. Trulove, V. A. Cocalia, A. E. Visser, J. L. Anderson, J. L. Anthony, J. F. Brennecke, E. J. Maginn, T. Welton, and R. A. Mantz. *Physicochemical Properties*, 57–174. 2008. doi:10.1002/9783527621194.ch3.
- [13] M. Zhao, B. Wu, S. I. Lall-Ramnarine, J. D. Ramdihal, K. A. Papacostas, E. D. Fernandez, R. A. Sumner, C. J. Margulis, J. F. Wishart, and E. W. Castner.

- “Structural analysis of ionic liquids with symmetric and asymmetric fluorinated anions.” *J. Chem. Phys.*, 151, 074504, 2019. doi:10.1063/1.5111643.
- [14] F. Lo Celso, Y. Yoshida, R. Lombardo, C. Jafta, L. Gontrani, A. Triolo, and O. Russina. “Mesoscopic structural organization in fluorinated room temperature ionic liquids.” *C. R. Chim.*, 21, 757–770, 2018. doi:10.1016/j.crci.2018.02.001.
- [15] F. Lo Celso, Y. Yoshida, F. Castiglione, M. Ferro, A. Mele, C. J. Jafta, A. Triolo, and O. Russina. “Direct experimental observation of mesoscopic fluorine domains in fluorinated room temperature ionic liquids.” *Phys. Chem. Chem. Phys.*, 19, 13101–13110, 2017. doi:10.1039/C7CP01971H.
- [16] K. Shimizu, A. A. Freitas, and J. N. Canongia Lopes. “Structural characterization of the $[C_nC_{1im}][C_4F_9SO_3]$ ionic liquid series: Alkyl versus perfluoroalkyl side chains.” *J. Mol. Liq.*, 226, 28–34, 2017. doi:10.1016/j.molliq.2016.08.014.
- [17] M. V. Fedorov and A. A. Kornyshev. “Ionic Liquids at Electrified Interfaces.” *Chem. Rev.*, 114, 2978–3036, 2014. doi:10.1021/cr400374x.
- [18] S. Perkin, M. Salanne, P. Madden, and R. Lynden-Bell. “Is a Stern and diffuse layer model appropriate to ionic liquids at surfaces?” *Proceedings of the National Academy of Sciences*, 110, E4121, 2013. doi:10.1073/pnas.1314188110.
- [19] R. M. Lynden-Bell, A. I. Frolov, and M. V. Fedorov. “Electrode screening by ionic liquids.” *Phys. Chem. Chem. Phys.*, 14, 2693–2701, 2012. doi:10.1039/C2CP23267G.
- [20] V. Halka, R. Tsekov, and W. Freyland. “Peculiarity of the liquid/vapour interface of an ionic liquid: study of surface tension and viscoelasticity of liquid bmimpf6 at various temperatures.” *Phys. Chem. Chem. Phys.*, 7, 2038–2043, 2005. doi:10.1039/B501760M.
- [21] V. Halka, R. Tsekov, and W. Freyland. “Interfacial phase transitions in imidazolium-based ionic liquids.” *J. Phys. Condens. Matter*, 17, S3325, 2005.

- [22] G. Law, P. R. Watson, A. J. Carmichael, and K. R. Seddon. “Molecular composition and orientation at the surface of room-temperature ionic liquids: Effect of molecular structure.” *Phys. Chem. Chem. Phys.*, 2879–2885, 2001. doi:10.1039/B101952J.
- [23] A. B. Biedron, E. L. Garfunkel, E. W. Castner, Jr., and S. Rangan. “Ionic Liquid Ultrathin Films at the surface of Cu(100) and Au(111).” *J. Chem. Phys.*, 146, 054704, 2017. doi:10.1063/1.4975101.
- [24] R. Wen, B. Rahn, and O. M. Magnussen. “Potential-Dependent Adlayer Structure and Dynamics at the Ionic Liquid/Au(111) Interface: A Molecular-Scale In Situ Video-STM Study.” *Angew. Chem. Int. Ed.*, 54, 6062–6066, 2015. doi:10.1002/anie.201501715.
- [25] T. Iimori, T. Iwahashi, H. Ishii, K. Seki, Y. Ouchi, R. Ozawa, H.-o. Hamaguchi, and D. Kim. “Orientational ordering of alkyl chain at the air/liquid interface of ionic liquids studied by sum frequency vibrational spectroscopy.” *Chem. Phys. Lett.*, 389, 321–326, 2004. doi:10.1016/j.cplett.2004.03.099.
- [26] I. S. Martinez, C. Santos, and S. Baldelli. “Structural Study at the Gas-Liquid Interface of 1-Alkyl-3-Methylimidazolium Alkylsulfates Using Surface Potential Measurements.” *ChemPhysChem*, 13, 1818–1824, 2012. doi:10.1002/cphc.201100985.
- [27] S. Rivera-Rubero and S. Baldelli. “Surface spectroscopy of room-temperature ionic liquids on a platinum electrode: a sum frequency generation study.” *J. Phys. Chem. B*, 108, 15133–15140, 2004. doi:10.1021/jp048260g.
- [28] J. Bowers, , M. C. Vergara-Gutierrez, and J. R. P. Webster. “Surface Ordering of Amphiphilic Ionic Liquids.” *Langmuir*, 20, 309–312, 2004. doi:10.1021/la035495v.
- [29] M. Mezger, B. M. Ocko, H. Reichert, and M. Deutsch. “Surface layering and melting in an ionic liquid studied by resonant soft X-ray reflectivity.” *Proc. Natl. Acad. Sci. U. S. A.*, 110, 3733–3737, 2013. doi:10.1073/pnas.1211749110.

- [30] M. Mezger, B. Jérôme, J. B. Kortright, M. Valvidares, E. M. Gullikson, A. Giglia, N. Mahne, and S. Nannarone. “Molecular orientation in soft matter thin films studied by resonant soft x-ray reflectivity.” *Phys. Rev. B*, 83, 155406, 2011. doi:10.1103/PhysRevB.83.155406.
- [31] M. Mezger, R. Roth, H. Schroeder, P. Reichert, D. Pontoni, and H. Reichert. “Solid-liquid interfaces of ionic liquid solutions-interfacial layering and bulk correlations.” *J. Chem. Phys.*, 142, 164707, 2015. doi:10.1063/1.4918742.
- [32] C. Rodenbücher, K. Wippermann, and C. Korte. “Atomic force spectroscopy on ionic liquids.” *Appl. Sci.*, 9, 2019. doi:10.3390/app9112207.
- [33] D. Wang, D. H. de Jong, A. Rühling, V. Lesch, K. Shimizu, S. Wulff, A. Heuer, F. Glorius, and H.-J. Galla. “Imidazolium-based lipid analogues and their interaction with phosphatidylcholine membranes.” *Langmuir*, 32, 12579–12592, 2016. doi:10.1021/acs.langmuir.6b02496.
- [34] A. Lahiri, T. Carstens, R. Atkin, N. Borisenko, and F. Endres. “In situ atomic force microscopic studies of the interfacial multilayer nanostructure of LiTFSI-[Py1,4]TFSI on Au(111): Influence of Li⁺ ion concentration on the Au(111)/il interface.” *J. Phys. Chem. C*, 119, 16734–16742, 2015. doi:10.1021/acs.jpcc.5b04562.
- [35] A. Elbourne, K. Voitchovsky, G. G. Warr, and R. Atkin. “Ion structure controls ionic liquid near-surface and interfacial nanostructure.” *Chem. Sci.*, 6, 527–536, 2015. doi:10.1039/C4SC02727B.
- [36] R. Hayes, N. Borisenko, M. K. Tam, P. C. Howlett, F. Endres, and R. Atkin. “Double Layer Structure of Ionic Liquids at the Au(111) Electrode Interface: An Atomic Force Microscopy Investigation.” *J. Phys Chem. C*, 115, 6855–6863, 2011. doi:10.1021/jp200544b.
- [37] R. Hayes, G. G. Warr, and R. Atkin. “Structure and Nanostructure in Ionic Liquids.” *Chem. Rev.*, 115, 6357–6426, 2015. doi:10.1021/cr500411q.

- [38] R. Hayes, G. G. Warr, and R. Atkin. “At the interface: solvation and designing ionic liquids.” *Phys. Chem. Chem. Phys.*, 12, 1709–1723, 2010. doi:10.1039/b920393a.
- [39] T. Yan, C. J. Burnham, M. G. D. Pópolo, and G. A. Voth. “Molecular Dynamics Simulation of Ionic Liquids: The Effect of Electronic Polarizability.” *J. Phys. Chem. B*, 108, 11877–11881, 2004. doi:10.1021/jp047619y.
- [40] T. Yan, S. Li, W. Jiang, X. Gao, B. Xiang, and G. A. Voth. “Structure of the Liquid-Vacuum Interface of Room-Temperature Ionic Liquids: A Molecular Dynamics Study.” *J. Phys. Chem. B*, 110, 1800–1806, 2006. doi:10.1021/jp055890p.
- [41] S. S. Sarangi, S. G. Raju, and S. Balasubramanian. “Molecular dynamics simulations of ionic liquid-vapour interfaces: effect of cation symmetry on structure at the interface.” *Phys. Chem. Chem. Phys.*, 13, 2714–2722, 2011. doi:10.1039/C0CP01272F.
- [42] N. Sieffert and G. Wipff. “Ordering of imidazolium-based ionic liquids at the α -quartz(001) surface: A molecular dynamics study.” *J. Phys. Chem. C*, 112, 19590–19603, 2008. doi:10.1021/jp806882e.
- [43] A. S. Pensado, M. F. C. Gomes, J. N. C. Lopes, P. Malfreyt, and A. A. H. Padua. “Effect of alkyl chain length and hydroxyl group functionalization on the surface properties of imidazolium ionic liquids.” *Phys. Chem. Chem. Phys.*, 13, 13518–13526, 2011. doi:10.1039/C1CP20563C.
- [44] X. Paredes, J. Fernández, A. A. H. Pádua, P. Malfreyt, F. Malberg, B. Kirchner, and A. S. Pensado. “Using molecular simulation to understand the structure of [c2c1im]+alkylsulfate ionic liquids: Bulk and liquid-vapor interfaces.” *J. Phys. Chem. B*, 116, 14159–14170, 2012. doi:10.1021/jp309532t.
- [45] J. K. Konieczny and B. Szefczyk. “Structure of alkylimidazolium-based ionic liquids at the interface with vacuum and water- molecular dynamics study.” *J. Phys. Chem. B*, 119, 3795–3807, 2015. doi:10.1021/jp510843m.

- [46] B. Coasne, L. Viau, and A. Vioux. “Loading-controlled stiffening in nanoconfined ionic liquids.” *J. Phys. Chem. Lett.*, 2, 1150–1154, 2011. doi:10.1021/jz200411a.
- [47] Q. Dou, M. L. Sha, H. Y. Fu, and G. Z. Wu. “Molecular dynamics simulation of the interfacial structure of [Cnmim][PF₆] adsorbed on a graphite surface: effects of temperature and alkyl chain length.” *J. Phys. Condens. Matter*, 23, 175001, 2011. doi:10.1088/0953-8984/23/17/175001.
- [48] M. Mezger, S. Schramm, H. Schroeder, H. Reichert, M. Deutsch, E. J. De Souza, J. S. Okasinski, B. M. Ocko, V. Honkimaki, and H. Dosch. “Layering Of [Bmim](+)-Based Ionic Liquids At A Charged Sapphire Interface.” *J. Chem. Phys.*, 131, 94701, 2009. doi:10.1063/1.3212613.
- [49] G. Hantal, M. N. D. S. Cordeiro, and M. Jorge. “What does an ionic liquid surface really look like? unprecedented details from molecular simulations.” *Phys. Chem. Chem. Phys.*, 13, 21230–21232, 2011. doi:10.1039/C1CP22639H.
- [50] S. Bovio, A. Podestà, C. Lenardi, and P. Milani. “Evidence of Extended Solidlike Layering in [Bmim][NTf₂] Ionic Liquid Thin Films at Room-Temperature.” *J. Phys. Chem. B*, 113, 6600–6603, 2009. doi:10.1021/jp9022234.
- [51] I. S. Martinez and S. Baldelli. “On the arrangement of ions in imidazolium-based room temperature ionic liquids at the gas-liquid interface, using sum frequency generation, surface potential, and surface tension measurements.” *J. Phys. Chem. C*, 114, 11564–11575, 2010. doi:10.1021/jp1039095.
- [52] C. S. Santos and S. Baldelli. “Surface Orientation of 1-Methyl-, 1-Ethyl-, and 1-Butyl-3-methylimidazolium Methyl Sulfate as Probed by Sum-Frequency Generation Vibrational Spectroscopy.” *J. Phys. Chem. B*, 111, 4715–4723, 2007. doi:10.1021/jp067056l.
- [53] X. Paredes, J. Fernández, A. A. H. Pádua, P. Malfreyt, F. Malberg, B. Kirchner, and A. S. Pensado. “Bulk and liquid-vapor interface of pyrrolidinium-based ionic liquids: A molecular simulation study.” *J. Phys. Chem. B*, 118, 731–742, 2014. doi:10.1021/jp406651f.

- [54] B. L. Bhargava and S. Balasubramanian. “Layering at an ionic liquid-vapor interface: a molecular dynamics simulation study of [Bmim][PF₆].” *J. Am. Chem. Soc.*, 128, 10073–10078, 2006. doi:10.1021/ja060035k.
- [55] R. M. Lynden-Bell and M. Del Popolo. “Simulation of the surface structure of butylmethylimidazolium ionic liquids.” *Phys. Chem. Chem. Phys.*, 8, 949–954, 2006. doi:10.1039/B514848K.
- [56] R. M. Lynden-Bell, M. G. Del Pópolo, T. G. A. Youngs, J. Kohanoff, C. G. Hanke, J. B. Harper, and C. C. Pinilla. “Simulations of ionic liquids, solutions, and surfaces.” *Acc. Chem. Res.*, 40, 1138–1145, 2007. doi:10.1021/ar700065s.
- [57] L. A. Jurado, H. Kim, A. Arcifa, A. Rossi, C. Leal, N. D. Spencer, and R. M. Espinosa-Marzal. “Irreversible structural change of a dry ionic liquid under nanoconfinement.” *Phys. Chem. Chem. Phys.*, 17, 13613–13624, 2015. doi:10.1039/c4cp05592f.
- [58] R. S. Anareddy and S. K. Shaw. “Long-Range Ordering of Ionic Liquid Fluid Films.” *Langmuir*, 32, 5147–5154, 2016. doi:10.1021/acs.langmuir.6b00304.
- [59] W. D. Amith, J. J. Hettige, E. W. Castner, Jr., and C. J. Margulis. “Structures of Ionic Liquids Having Both Anionic and Cationic Octyl Tails: Lamellar Vacuum Interface vs Sponge-Like Bulk Order.” *J. Phys. Chem. Lett.*, 7, 3785–3790, 2016. doi:10.1021/acs.jpcllett.6b01763.
- [60] J. J. Hettige, W. D. Amith, E. W. Castner, and C. J. Margulis. “Ionic liquids with symmetric diether tails: Bulk and vacuum-liquid interfacial structures.” *J. Phys. Chem. B*, 121, 174–179, 2017. doi:10.1021/acs.jpcb.6b09148.
- [61] F. Wu, W. V. Karunaratne, and C. J. Margulis. “Ionic liquid mixture at the vacuum interface and the peaks and antipeaks analysis of x-ray reflectivity.” *J. Phys. Chem. C*, 123, 4914–4925, 2019. doi:10.1021/acs.jpcc.8b11958.
- [62] M. L. Ferreira, M. J. Pastoriza-Gallego, J. a. M. M. Araújo, J. N. Canongia Lopes, L. P. N. Rebelo, M. M. Piñeiro, K. Shimizu, and A. B. Pereiro. “Influence of

- nanosegregation on the phase behavior of fluorinated ionic liquids.” *J. Phys. Chem. C*, 121, 5415–5427, 2017. doi:10.1021/acs.jpcc.7b00516.
- [63] Y. Shen, D. F. Kennedy, T. L. Greaves, A. Weerawardena, R. J. Mulder, N. Kirby, G. Song, and C. J. Drummond. “Protic ionic liquids with fluorous anions: physicochemical properties and self-assembly nanostructure.” *Phys. Chem. Chem. Phys.*, 14, 7981–7992, 2012. doi:10.1039/C2CP40463J.
- [64] D. O’Hagan. “Understanding organofluorine chemistry. an introduction to the c-f bond.” *Chem. Soc. Rev.*, 37, 308–319, 2008. doi:10.1039/B711844A.
- [65] M. F. Costa Gomes and A. A. H. Pádua. “Interactions of carbon dioxide with liquid fluorocarbons.” *J. Phys. Chem. B*, 107, 14020–14024, 2003. doi:10.1021/jp0356564.
- [66] O. Holloczki, M. Macchiagodena, H. Weber, M. Thomas, M. Brehm, A. Stark, O. Russina, A. Triolo, and B. Kirchner. “Triphilic ionic-liquid mixtures: Fluorinated and non-fluorinated aprotic ionic-liquid mixtures.” *ChemPhysChem*, 16, 3325–3333, 2015. doi:10.1002/cphc.201500473.
- [67] J. G. Riess. “Highly fluorinated amphiphilic molecules and self-assemblies with biomedical potential.” *Curr. Opin. Colloid Interface Sci.*, 14, 294 – 304, 2009. doi:10.1016/j.cocis.2009.05.008.
- [68] M. P. Krafft and J. G. Riess. “Chemistry, physical chemistry, and uses of molecular fluorocarbon-hydrocarbon diblocks, triblocks, and related compounds-unique “apolar” components for self-assembled colloid and interface engineering.” *Chem. Rev.*, 109, 1714–1792, 2009. doi:10.1021/cr800260k.
- [69] A. M. A. Dias, R. P. Bonifácio, I. M. Marrucho, A. A. H. Pádua, and M. F. Costa Gomes. “Solubility of oxygen in n-hexane and in n-perfluorohexane. experimental determination and prediction by molecular simulation.” *Phys. Chem. Chem. Phys.*, 5, 543–549, 2003.

- [70] A. M. A. Dias, J. C. Pàmies, J. a. A. P. Coutinho, I. M. Marrucho, and L. F. Vega. “Saft modeling of the solubility of gases in perfluoroalkanes.” *J. Phys. Chem. B*, 108, 1450–1457, 2004. doi:10.1021/jp036225o.
- [71] C. Yang, X. Wang, and M. A. Omary. “Fluorous metal-organic frameworks for high-density gas adsorption.” *J. Am. Chem. Soc.*, 129, 15454–15455, 2007. doi:10.1021/ja0775265.
- [72] R. Berger, G. Resnati, P. Metrangolo, E. Weber, and J. Hulliger. “Organic fluorine compounds: a great opportunity for enhanced materials properties.” *Chem. Soc. Rev.*, 40, 3496–3508, 2011. doi:10.1039/C0CS00221F.
- [73] F. Lo Celso, G. B. Appetecchi, E. Simonetti, M. Zhao, E. W. Castner, Jr., U. Keiderling, L. Gontrani, A. Triolo, and O. Russina. “Microscopic Structural and Dynamic Features in Triphilic Room Temperature Ionic Liquids.” *Front. Chem.*, 7, 285, 2019. doi:10.3389/fchem.2019.00285.
- [74] T. L. Greaves and C. J. Drummond. “Solvent nanostructure, the solvophobic effect and amphiphile self-assembly in ionic liquids.” *Chem. Soc. Rev.*, 42, 1096–1120, 2013. doi:10.1039/C2CS35339C.
- [75] T. L. Greaves, D. F. Kennedy, Y. Shen, A. Weerawardena, A. Hawley, G. Song, and C. J. Drummond. “Fluorous protic ionic liquid exhibits a series of lyotropic liquid crystalline mesophases upon water addition.” *J. Mol. Liq.*, 210, 279–285, 2015. doi:10.1016/j.molliq.2015.03.037.
- [76] E. W. Castner, Jr., C. J. Margulis, M. Maroncelli, and J. F. Wishart. “Ionic Liquids: Structure and Photochemical Reactions.” *Annu. Rev. Phys. Chem.*, 62, 85–105, 2011. doi:10.1146/annurev-physchem-032210-103421.
- [77] H. K. Kashyap, C. S. Santos, R. P. Daly, J. J. Hettige, N. S. Murthy, H. Shirota, E. W. Castner, Jr., and C. J. Margulis. “How Does the Ionic Liquid Organizational Landscape Change when Nonpolar Cationic Alkyl Groups Are Replaced by Polar Isoelectronic Diethers?” *J. Phys. Chem. B*, 117, 1130–1135, 2013. doi:10.1021/jp311032p.

- [78] C. S. Santos, H. V. R. Annapureddy, N. S. Murthy, H. K. Kashyap, E. W. Castner, Jr., and C. J. Margulis. “Temperature-dependent structure of methyltributylammonium bis(trifluoromethylsulfonyl)amide: X ray scattering and simulations.” *J. Chem. Phys.*, 134, 064517, 2011. doi:10.1063/1.3526958.
- [79] J. C. Araque, S. K. Yadav, M. Shadeck, M. Maroncelli, and C. J. Margulis. “How Is Diffusion of Neutral and Charged Tracers Related to the Structure and Dynamics of a Room-Temperature Ionic Liquid? Large Deviations from Stokes-Einstein Behavior Explained.” *J. Phys. Chem. B*, 119, 7015–7029, 2015. doi:10.1021/acs.jpcb.5b01093.
- [80] A. Triolo, O. Russina, H.-J. Bleif, and E. Di Cola. “Nanoscale segregation in room temperature ionic liquids.” *J. Phys. Chem. B*, 111, 4641–4644, 2007. doi:10.1021/jp067705t.
- [81] A. Triolo, O. Russina, B. Fazio, R. Triolo, and E. Di Cola. “Morphology of 1-alkyl-3-methylimidazolium hexafluorophosphate room temperature ionic liquids.” *Chem. Phys. Lett.*, 457, 362–365, 2008.
- [82] O. Russina, A. Triolo, L. Gontrani, R. Caminiti, D. Xiao, J. Hines, Larry G., R. A. Bartsch, E. L. Quitevis, N. Pleckhova, and K. R. Seddon. “Morphology and intermolecular dynamics of 1-alkyl-3-methylimidazolium bis(trifluoromethane)sulfonylamide ionic liquids: structural and dynamic evidence of nanoscale segregation.” *J. Phys.: Condens. Matter*, 21, 424121, 2009. doi:10.1088/0953-8984/21/42/424121.
- [83] K. Shimizu, C. E. S. Bernardes, A. Triolo, and J. N. Canongia Lopes. “Nanoscale segregation in ionic liquids: scorpions and vanishing chains.” *Phys. Chem. Chem. Phys.*, 15, 16256–16262, 2013. doi:10.1039/C3CP52357H.
- [84] J. C. Araque, R. P. Daly, and C. J. Margulis. “A Link Between Structure, Diffusion and Rotations of Hydrogen Bonding Tracers in Ionic Liquids.” *J. Chem. Phys.*, 144, 204504, 2016. doi:10.1063/1.4951012.

- [85] H. K. Kashyap, C. S. Santos, N. S. Murthy, J. J. Hettige, K. Kerr, S. Ramati, J. Gwon, M. Gohdo, S. I. Lall-Ramnarin, J. F. Wishart, C. J. Margulis, and E. W. Castner, Jr. “Structure of 1-Alkyl-1-methylpyrrolidinium Bis(trifluoromethylsulfonyl)amide Ionic Liquids with Linear, Branched, and Cyclic Alkyl Groups.” *J. Phys. Chem. B*, 117, 15328–15337, 2013. doi:10.1021/jp403518j.
- [86] J. C. Araque, J. J. Hettige, and C. J. Margulis. “Modern Room Temperature Ionic Liquids, a Simple Guide to Understanding Their Structure and How It May Relate to Dynamics.” *J. Phys. Chem. B*, 119, 12727–12740, 2015. doi:10.1021/acs.jpcb.5b05506.
- [87] W. Humphrey, A. Dalke, and K. Schulten. “VMD – Visual Molecular Dynamics.” *J. Mol. Graph. Model.*, 14, 33–38, 1996. doi:10.1016/0263-7855(96)00018-5.
- [88] M. J. Abraham, T. Murtola, R. Schulz, S. Páll, J. C. Smith, B. Hess, and E. Lindahl. “GROMACS: High performance molecular simulations through multi-level parallelism from laptops to supercomputers.” *SoftwareX*, 1-2, 19–25, 2015. doi:10.1016/j.softx.2015.06.001.
- [89] H. J. C. Berendsen, D. van der Spoel, and R. van Drunen. “GROMACS: A message-passing parallel molecular dynamics implementation.” *Comp. Phys. Comm.*, 91, 43–56, 1995. doi:10.1016/0010-4655(95)00042-E.
- [90] F. L. Celso, G. Appetecchi, E. Simonetti, U. Keiderling, L. Gontrani, A. Triolo, and O. Russina. “Mesoscopic structural organization in fluorinated pyrrolidinium-based room temperature ionic liquids.” *J. Mol. Liq.*, 289, 111110, 2019. doi:10.1016/j.molliq.2019.111110.

Chapter 6

Conclusions

Ionic liquids have great potential for many applications. In this work, we studied the bulk structure of ionic liquids, including fluorinated-anion ILs and ILs with cationic ether tails, (1; 2) the diffusion coefficients in pure ILs and IL-octanol mixtures, and the liquid-vacuum interfacial structure of ILs using MD simulations.

6.1 Bulk structure of ILs

Using high-energy X-ray scattering and MD simulations, the total liquid structure functions $S(q)$ were obtained for 20 fluorinated-anion ILs: $\text{Im}_{2,1}^+$, $\text{Im}_{1,8}^+$, $\text{Pyrr}_{1,8}^+$, and $\text{P}_{6,6,6,14}^+$ cations paired with the FSI^- , $\text{BSI}_{0,1}^-$, NTf_2^- , BETI^- , and $\text{BSI}_{1,4}^-$ anions. Good agreement was observed between the experimental and simulated $S(q)$. We learned that long fluorinated tails lead to aggregation into fluorine domains in the bulk, just as is the case for hydrocarbon tails. When both long hydrocarbon tails and fluorinated tails are present, they form into nonpolar domains together. The charge heads decorating alkylated and fluorinated tails cannot be separated due to the charge alternation of cationic and anionic heads.

The bulk structures of ILs with long cationic alkyl tails and their ether homologs were examined: $\text{Im}_{1,8}^+$, $\text{Im}_{1,\text{EOEOE}}^+$, $\text{Im}_{1,10}^+$, and $\text{Im}_{1,\text{EOEOEOM}}^+$ paired with NTf_2^- ; $\text{Pyrr}_{1,8}^+$, $\text{Pyrr}_{1,\text{EOEOE}}^+$, $\text{Pyrr}_{1,10}^+$, and $\text{Pyrr}_{1,\text{EOEOEOM}}^+$ paired with NTf_2^- . ILs with ether tails have lower viscosity than their alkyl analogues. The ether chains curl and form hydrogen bonds with the cationic heads, thus disrupting the polar networks of both IL families.

6.2 Diffusivities in ILs and IL-octanol mixtures

Using the PG-SE NMR method, we measured the self-diffusivities of ions and/or molecules in ILs. Low viscosity ILs show higher diffusivities than high viscosity ILs. In a pure IL system, small ions diffuse faster than the large ions. The self-diffusion coefficients are affected by the molecular structure of ions as well. Ions in general diffuse faster than the hydrodynamic predictions based on the Stokes-Einstein equation. However, for ILs like $\text{P}_{6,6,6,14}^+/\text{NTf}_2^-$, where the cations are extremely large and the anions are embedded in the cations, the ions diffuse slower than the predictions.

Adding a low viscosity neutral solvent to the viscous IL can greatly decrease the viscosity of the solution, which in turn increases the diffusivities of the molecules. In the octanol- $\text{P}_{6,6,6,14}^+/\text{BSI}_{1,4}^-$ mixtures, the relationship between viscosity and temperature is fitted well by both the VFT(3; 4) and Arrhenius equations in the measured temperature range. The structure of $\text{P}_{6,6,6,14}^+/\text{NTf}_2^-$ system is sponge-like with charge network and non-polar domains form by the alkyl tails on the $\text{P}_{6,6,6,14}^+$ cation. There are heterogeneous frictions between the charged and non-polar regions, with a reduced microviscosity for neutral solutions. The neutral 1-octanol molecules reside in the non-polar domains and experience less frictions. As a result, the diffusivity of 1-octanol in $\text{P}_{6,6,6,14}^+/\text{NTf}_2^-$ is three times faster than the Stokes-Einstein predictions. Compared to the diffusivity of hexane in $\text{P}_{6,6,6,14}^+/\text{NTf}_2^-$, however, the diffusivity of 1-octanol is significantly reduced due to the hydroxide group. Hydrogen bonding among the hydroxide groups and NTf_2^- anions slows down the diffusivities of 1-octanol and NTf_2^- anion.

6.3 Liquid-vacuum interfacial structure of ILs

The interfacial structure of ILs is quite different from their bulk structure. We have studied the vacuum-IL interface using MD simulations. For a model interface consisting of a box of ions with periodic boundaries on the four sides and vacuum interfaces at the top and bottom, one or multiple amellae comprising nonpolar tail-charge head double layers can form near the surfaces before relaxing into sponge-like structure in

the middle of the slab. If there is not enough space for the lamellar structure at each side of the slab to relax before meeting in the middle, a lamellar structure up to 10 nm can be formed.⁽⁵⁾ This usually happens for ILs with long nonpolar tails on both the cations and anions. The structure of ILs can be influenced by the electric field. In our case of $\text{Im}_{1,8}^+/\text{BSI}_{1,8}^-$ in a 20 nm slab, a lamellar structure throughout the slab was established after applying electric fields. The 20 nm lamellar structure is very stable after removing the electric field.

6.4 Future directions

The heterogeneity of IL structure and dynamics has been well demonstrated. Future study should focus on studying the transport behavior of molecules in ILs and IL mixtures, and the applications of ILs that take advantage of the transport heterogeneity in ILs, like separation, water purification, and gas absorption.

We have done some work on the interfacial structure of ILs on mica surface by atomic force spectroscopy (AFM) experiments. Several organized layers of ions were detected near the surface by measuring force-distance curves. It would be interesting to look at the IL-mica interfacial structure using MD simulations, where the structure can be studied at an atomic level. Next, we can charge the mica surface and see how the interfacial structure of ILs changes, using AFM or MD simulations.

In the case of ILs in vacuum, lamellar structure forms near the interfaces while structure in the middle of the slab depends on the slab thickness. If a neutral molecule is put in the slab, its diffusion behavior should differ in the bulk liquid region and lamellar structure region. If the neutral molecule diffuses into the lamellar structure region, it may stay in the nonpolar tail layer and move horizontally within the layer, or it may push through the layer of charge heads and diffuse vertically. The diffusivities in the nonpolar tail layer and charged head layer should be different. Assuming that the ILs can retain its structure and we put two or more kinds of molecules in the system, the diffusion differences of molecules in different regions and layers may allow us to separate the molecules.

We learned that the structure of ILs can be affected by applying electric fields. With an electric field, a lamellar structure can be established across the slab. We can place neutral molecules or charged molecules near one end of the slab and observe the diffusion behavior of molecules across the slab. For the charged molecule, its diffusion direction may be affected by the electric field. The diffusion behavior of molecules in nonpolar layer and charged layer should also be different. We can control the diffusivity of molecules in IL systems based on their diffusion differences.

Finally, the intermediate range order domains in the IL systems can be engineered more nonpolar with fluorinated tails only or more polar with ether tails. The diffusion behavior of molecules may be affected by the polarity of domains, which is interesting to study. Moreover, for IL mixtures domains with different polarities can be formed in the same system, where the molecules have different diffusion behaviors.

Bibliography

- [1] M. Zhao, B. Wu, S. I. Lall-Ramnarine, J. D. Ramdihal, K. A. Papacostas, E. D. Fernandez, R. A. Sumner, C. J. Margulis, J. F. Wishart, and E. W. Castner. “Structural analysis of ionic liquids with symmetric and asymmetric fluorinated anions.” *J. Chem. Phys.*, 151, 074504, 2019. doi:10.1063/1.5111643.
- [2] S. I. Lall-Ramnarine, M. Zhao, C. Rodriguez, R. Fernandez, N. Zmich, E. D. Fernandez, S. B. Dhiman, E. W. Castner, Jr., and J. F. Wishart. “Connecting structural and transport properties of ionic liquids with cationic oligoether chains.” *J. Electrochem. Soc.*, 164, H5247–H5262, 2017. doi:10.1149/2.0371708jes.
- [3] G. S. Fulcher. “Analysis of recent measurements of the viscosity of glasses.” *J. Am. Ceram. Soc.*, 8, 339–355, 1925. doi:10.1111/j.1151-2916.1925.tb16731.x.
- [4] G. Tammann and W. Hesse. “Die abhängigkeit der viscosität von der temperatur bei unterkühlten flüssigkeiten.” *Z. Anorg. Allg. Chem.*, 156, 245–257, 1926. doi:10.1002/zaac.19261560121.

- [5] W. D. Amith, J. J. Hettige, E. W. Castner, Jr., and C. J. Margulis. “Structures of Ionic Liquids Having Both Anionic and Cationic Octyl Tails: Lamellar Vacuum Interface vs Sponge-Like Bulk Order.” *J. Phys. Chem. Lett.*, 7, 3785–3790, 2016. doi:10.1021/acs.jpcllett.6b01763.

List of Publications

- (3) M. Zhao, B. Wu, S. I. Lall-Ramnarine, C. J. Margulis, J. F. Wishart, E. W. Castner, Jr., “Structural Analysis of Ionic Liquids With Symmetric and Asymmetric Fluorinated Anions”, *J. Chem. Phys.*, **2019**, **151**, 074504, doi: 10.1063/1.5111643.
- (2) F. Lo Celso, G. B. Appetecchi, E. Simonetti, M. Zhao, E. W. Castner, Jr., U. Keiderling, L. Gontrani, A. Triolo, and O. Russina, “Dynamic Features in Triphilic Room Temperature Ionic Liquids”, *Front Chem.*, **2019**, **7**, 285, doi: 10.3389/fchem.2019.00285.
- (1) S. I. Lall-Ramnarine, M. Zhao, C. Rodriguez, R. Fernandez, N. Zmich, E. D. Fernandez, S. B. Dhiman, E. W. Castner, Jr. and J. F. Wishart, “Connecting Structural and Transport Properties of Ionic Liquids with Cationic Oligoether Chains”, *J. Electrochem. Soc.*, **2017**, **164**, H5247-H5262, doi: 10.1149/2.0371708jes